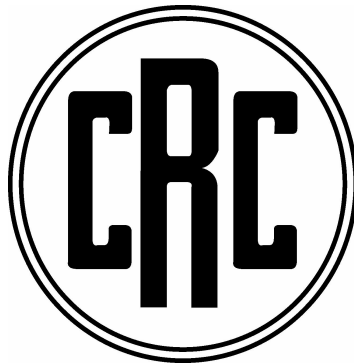


# **EVALUATION OF A METEOROLOGICAL MODEL FOR INTER-REGIONAL TRANSPORT**

**Final Report  
CRC Project No. A-28**

**Prepared by:  
Nelson L. Seaman  
Aijun Deng  
and  
David R. Stauffer**

**Department of Meteorology  
503 Walker Building  
The Pennsylvania State University  
University Park, PA 16802**



**July 31, 2002**

**Prepared for:  
COORDINATING RESEARCH COUNCIL, INC.  
3650 Mansell Road, Suite 140 - Alpharetta, Georgia 30022**

## **DISCLAIMER**

The statements and conclusions in this report are those of the contractor and not necessarily those of the Coordinating Research Council. The mention of commercial products, their source or their use in connection with material reported herein is not to be construed as either an actual or implied endorsement of such products.

## ABSTRACT

A better understanding of transport issues and source-receptor relationships on the inter-regional scale is dependent on reducing the uncertainties in our ability to define complex three-dimensional wind fields evolving in time. Observations are generally too sparse to allow accurate analysis of mesoscale wind circulations. Dynamical mesoscale meteorological models with four-dimensional data assimilation (FDDA), on the other hand, generally have much better horizontal and temporal resolution than do the observations, even during special field programs. Although these models are certainly imperfect, they have been improved substantially in recent years. Some improvements most important for air-quality studies involve finer grid resolutions, practical FDDA techniques to reduce the accumulation of model errors over time, and better representation of sub-grid scale physics (radiation, turbulence, convection, etc).

While improvements in model skill have been demonstrated time and again on nested fine-mesh domains, the accuracy of the simultaneous solutions produced on coarser model domains has received much less attention in recent years. *Because the finest domains cover areas only a few hundred kilometers on a side, however, it is the coarser domains in these nested-grid mesoscale models that control the inter-regional transport of airborne pollutants over distances of 1000-3000 km.* Thus, a gap exists in our current modeling skill at the mesoalpha, or inter-regional scale, and it is no longer clear what the state of the science is for representing longer-range sub-continental transport. The *primary objective* of this study supported by CRC under Contract A-28, then, is *to evaluate an advanced meteorological model for its skill in simulating transport and mixing on inter-regional scales as a function of grid resolution, model physics and FDDA.*

The CAPTEX-83 Episode 1 on 18-19 September 1983 was chosen for study because the meteorology of this case was fairly similar to synoptic conditions known to be associated with poor air quality in the Northeast U.S. and because tracer data collected for this case was relatively complete. The MM5 mesoscale model was applied in many numerical experiments conducted by Penn State, six of which are presented here in detail. The original scope of work for Study A-28 was expanded by Penn State to include plume dispersion modeling runs using the ARAP-Titan Corp. SCIPUFF model. By adding the SCIPUFF runs, it became possible to verify predicted surface tracer concentrations against observed surface concentrations collected during the CAPTEX-83 study. In this way, the combined effects of diffusion and advection acting over time to produce inter-regional plume transport could be verified against the observed tracer.

Specific conclusions about the use of mesoscale meteorological models for inter-regional transport that resulted from this study are as follows. (1) A model configuration reflecting capabilities of the late 1980s (70-km horizontal grid, 15 layers, older sub-grid physics, and no FDDA) was shown to produce large errors in the simulated meteorology that severely degraded the accuracy of the surface tracer concentrations predicted by SCIPUFF. (2) Improving the horizontal and vertical resolution of the mesoscale model to 12 km and 32 layers led to some modest improvements in the MM5 performance, but the further addition of more advanced physical parameterizations produced much greater reductions of simulation errors. (3) Use of FDDA, along with 12-km resolution and improved physics, produced the overall best performance of all experiments in both MM5 and SCIPUFF. (4) Further reduction of horizontal grid size to 4 km had a detrimental effect on meteorological and plume dispersion solutions in the case of 18-19 September 1983 due to misrepresentation by the MM5's explicit moist physics of the extensive convection associated with a cold front crossing the lower Great Lakes.

## EXECUTIVE SUMMARY

Our ability to define the complex three-dimensional (3-D) wind fields in real atmospheric cases remains uncertain because of our inability to observe the atmosphere at spatial scales much finer than that provided by the synoptic data network. Consequently, better understanding of transport issues and source-receptor relationships on the inter-regional scale is dependent on reducing these uncertainties. Wind fields can be diagnosed directly from observations, or simulated by dynamical models (with or without FDDA). Although diagnostic analysis tools have an advantage in that they create representations of the atmospheric fields that are based solely on the observations, they do have limitations. Standard observing networks, such as those operated by the National Weather Service (NWS), are too coarse to resolve many mesoscale features, even over the continents. Supplemental observations, especially above the surface, can be very costly to obtain even for special field programs (*intensive observing periods*, or IOPs). Even during IOPs, the observation base generally is insufficient to resolve important variables, such as the vertical velocity and the divergence fields, and the special data are usually concentrated over a relatively small area.

Dynamical mesoscale meteorological models, on the other hand, generally have much better horizontal and temporal resolution than do the observations, even in the case of special field programs. They also generate complete data sets that include vertical velocity, divergence and clouds, and can produce inter-variable consistency based on the full Navier-Stokes equations (scaled for atmospheric applications). Although these models are certainly imperfect, they have been improved in recent years. Some of the improvements most important for air-quality related studies involve finer grid resolutions, practical four-dimensional data assimilation (FDDA)

techniques help to reduce the accumulation of model errors over time, and better representation of sub-grid scale physics (radiation, turbulence, convection, etc.). Consequently, high-resolution, data-assimilating dynamical models with advanced physics have become widely accepted as the best approach for generating mesoscale meteorological fields for many air-quality investigations.

However, most of the air-quality modeling research over the past decade has focused on two extremes: the local scales and continental to global scales. At the local scales, the focus has been primarily on understanding and controlling one-hour peak ozone, especially in and near urban centers. This has led to a great emphasis on the simulation of meteorological features at the mesobeta scale (20 - 200 km) using finer and finer mesh sizes and limited-area domains. These mesobeta-scale domains generally are nested within larger and coarser domains that typically have resolutions of ~10-40 km. While the improvement in model skill has been demonstrated time and again on these nested fine-mesh domains, the accuracy of the solutions produced simultaneously on coarser model domains has received much less attention in recent years. *Because the finest domains only cover areas a few hundred kilometers on a side, however, it is the coarser domains in these nested-grid mesoscale models that control the inter-regional transport of pollutants over distances of 1000-3000 km.*

Thus, a gap exists in our current modeling skill at the mesoalpha, or inter-regional scale, and it is no longer clear what the state of the science is for representing longer-range sub-continental transport. The last major modeling studies to replicate measurements from inter-regional tracer releases were performed over a decade ago (e.g., Haagenson et al. 1987, 1990; Chock and Kuo 1990). Those regional models had much more coarse horizontal and vertical resolutions than today's models (often, only ~60-80 km in the horizontal and ~15 vertical layers),

no FDDA and generally less sophisticated atmospheric physics. Since the regional-scale outer domains have such an important influence on the nested fine-domain solutions, and the importance of inter-regional transport has been enhanced by the introduction of new 8-h air-quality standards, it is appropriate to revisit the question of model accuracy at the inter-regional scale.

Therefore, the *primary objective* of this study supported by CRC under Contract A-28 is *to evaluate an advanced meteorological model for its skill in simulating transport and mixing on inter-regional scales as a function of grid resolution, model physics and FDDA*. Specific goals are:

- To evaluate the current state of the science for simulating inter-regional transport and diffusion of a tracer when using a particular numerical mesoscale model, the Penn State/NCAR MM5, to represent the meteorology (wind, turbulence, convective processes, etc.) and a regional plume model, the ARAP/Titan SCIPUFF, to represent dispersion.
- To identify which of the meteorological model's attributes introduced or enhanced over the past decade (finer resolution, better physics, FDDA), if any, are most effective for improving the skill of inter-regional transport.

The original investigation, as described in the proposal, envisioned using the MM5 mesoscale model and the TRAJEC parcel trajectory post-processor to estimate the transport of material parcels due to advection by the model's 3-D wind field. The CAPTEX-83 Episode 1 on 18-19 September 1983 was chosen for numerical experimentation because the meteorology of this case was fairly similar to synoptic conditions known to be associated with poor air quality in

the Northeast U.S. and because the tracer data collected for this case was relatively complete. Of the many numerical experiments conducted by Penn State during this study, six are presented in detail in this report.

However, as the investigation proceeded, it became clear that the meteorological observations alone would be insufficient to evaluate certain details of the mesoscale model simulations and how they are related to inter-regional transport. Advection by the resolved-scale winds is only part of the information needed to understand inter-regional transport of airborne constituents. Diffusion by turbulence is also extremely important. Examination of the meteorology in the 18-19 September case soon made it very clear that sub-grid vertical and horizontal mixing must have interacted strongly with major resolvable mesoscale features (fronts and a low-level jet) to yield the observed downwind distributions of surface tracer concentrations. Upper-air measurements taken by aircraft during CAPTEX-83 were ineffective for revealing the 3-D morphology of the tracer in this case because the plume aloft traveled so rapidly that it had passed the area of the pre-planned research flight paths before the airborne measurements were taken. Previous analysis and modeling studies in the literature acknowledged that complex scale interactions were likely to have occurred in this case, but they were unable to address these issues in any meaningful way.

Thus, the original scope of work for Study A-28 was expanded by Penn State to include plume dispersion modeling runs using the ARAP-Titan Corp. SCIPUFF model. By adding the SCIPUFF runs, it became possible to verify predicted surface tracer concentrations against observed surface concentrations collected during the CAPTEX-83 study. In this way the combined effects of diffusion and advection acting over time to produce inter-regional plume transport could be verified. Also, by combining results from MM5, TRAJEC and SCIPUFF, a

much more complete picture emerged of the fate of the 3-D tracer plume as it traveled over 1200 km in less than 24 h.

The analysis of model solutions and observations revealed that most of the tracer mass had left the region of the monitoring network much earlier than anticipated by the CAPTEX field-study team. Some of the surface-level tracer material was swept northeastward along the northern shore of Lake Erie on the evening of 18 September and then back southeastward across Lake Ontario during the night of September 18-19 as the cold front advanced across the lower Great Lakes. The cold front became the effective northern boundary of the surface tracer plume very early on 19 September. More importantly, in advance of the front, a nocturnal low-level jet was responsible for rapid advection of the upper portions of the plume mass that had been carried aloft by turbulence in the convective boundary layer over OH on the afternoon of 18 September. Observed surface concentrations early on 19 September over northern NY and New England were primarily the result of shear-induced turbulence that mixed portions of the elevated jet-level plume down to the surface, especially over the higher elevations of the Adirondack, Green and White Mountains. In this respect, more advanced turbulence schemes such as the TKE-predicting scheme used here can be crucial because they are better able to simulate shear-induced turbulence than some of the older parameterizations available 15 years ago. The leading part of the plume appears to have been lifted over a warm frontal band moving through New England at this time (although the exact position of the front during the night was indistinct). By 1200 UTC, 19 September, only the rearward portion of the elevated plume remained over the CAPTEX monitoring network, so that observed and modeled surface concentrations late in the episode did not appear consistent with the large mass of tracer that had been released from

Dayton, OH. Thus, this more comprehensive modeling approach revealed important aspects of the inter-regional transport that would otherwise have remained unclear.

The study has resulted in a number of important specific conclusions about the use of mesoscale meteorological models for inter-regional transport problems:

- (1) The original model configuration (to be introduced later as Exp. 1A) that reflected modeling capabilities of the late 1980s (70-km horizontal resolution, 15 layers, older sub-grid physics, and no FDDA) was shown to produce very important errors in the simulated meteorology for the 18-19 September 1983 case. These errors included much slower-than-observed frontal speeds and a weakened representation of the nocturnal low-level jet over the lower Great Lakes. The resultant surface tracer concentrations produced by the SCIPUFF dispersion model using the MM5 meteorology of Exp. 1A were consistently too large, averaging 2.65 times the observed concentrations.
- (2) In Exp. 2A, simply improving the horizontal and vertical resolution of the mesoscale model to 12 km (almost by a factor of six) and 32 layers (more than by a factor of 2) led to some improvements in the MM5 model performance. Notably, the phase speed error of the fronts in Exp. 1A was reduced. But overall, the improvements in the mesoscale meteorology and in the dispersion calculations were fairly modest in this complex case. In particular, the over-predictions of surface concentrations in the simulated tracer plume were reduced, but on average they remained about 2.18 times the observed maximums. It is clear from this test that higher grid resolution alone may not be very effective for producing

meteorological data sets with the accuracy needed for air-quality applications involving inter-regional transport.

- (3) The addition of more advanced physical parameterizations for boundary-layer turbulence, resolved-scale moist microphysics and sub-grid convection, coupled with finer 12-km grid resolution (Exp. 2B) produced much greater reductions of errors in the MM5 mesoscale model and the SCIPUFF plume dispersion model than using finer grid resolution alone (Exp. 2A). Surface tracer concentrations and distributions became much like those observed.
- (4) Use of FDDA (surface and upper-air analysis nudging), along with 12-km resolution and improved physics in Exps. 2C and 2D produced the overall best performance of all experiments. Frontal and low-level jet characteristics were represented fairly well and simulated tracer concentrations were in reasonably good agreement with observations. Maximum surface concentrations in Exp. 2D averaged about 0.93 times the observed maximums, while the mean absolute error of the model's maximums was only 0.31 when normalized by the observed maximums. This result, as well as other aspects of the meteorological and dispersion evaluations, showed that modeling capabilities for inter-regional transport indeed have improved substantially as a consequence of all three main factors introduced into mesoscale models over the past 10-15 years.
- (5) Further reduction of the horizontal grid size in Exp. 3A to 4 km had a detrimental effect on meteorological and plume dispersion solutions in the case of 18-19 September 1983. The primary cause of the poor mesoscale model performance was traced to the explicit representation of extensive convection associated with

the cold front advancing across the lower Great Lakes and into New England. Since no convective parameterization was used at this grid size, the convective updrafts were forced onto coarser than normal scales so that rainfall became too intense. This led cold downdrafts to be too vigorous also, causing widespread disruption of the low-level wind field and spurious advection of the simulated tracer. Much more of the tracer was carried aloft by the vertical winds in Exp. 3A than in the other experiments, so that the surface tracer concentrations in SCIPUFF became much too small (averaging only 0.36 times the observed maximum concentrations).

- (6) The results of Exp. 3A (4-km horizontal resolution) demonstrate that use of very fine grid resolution in mesoscale models sometimes can be counter-productive. This result should not be interpreted to mean that 4-km grids are unsuitable for air-quality studies in general. However, model applications at grid sizes of 4 km or less cannot be assumed automatically to be superior for all situations, especially if widespread deep convective is possible. Use of such fine resolutions may be more practical for predominantly dry cases. It is recommended that, when producing meteorological model solutions on a nested fine grid (say, a 4-km mesh), a comparison should be made between statistics calculated for that fine grid and similar statistics for its parent intermediate grid (say, a 12-km mesh). This comparison should be made on a case-by-case basis before using the meteorological fields in air-quality models.
- (7) Future research is recommended to broaden the applicability of very fine scale models (grids of 4 km or less) for cases in which widespread convection is

possible. Improvements are necessary in the representation of boundary layer turbulence at fine scales so that spurious low-level convective instability does not develop so easily, causing excessive thunderstorm development by the explicit moist physics. It actually may be less problematic to use even finer grids, on the order of 1 km, in cases with moist convection, since updrafts and downdrafts could be better represented at approximately their correct scales. However, further experimentation is required before this option can be considered reliable for use in air-quality studies.

## TABLE OF CONTENTS

	<u>Page</u>
Disclaimer	2
ABSTRACT	3
EXECUTIVE SUMMARY	5
List of Tables	16
List of Figures	18
1. INTRODUCTION	27
1.1 Background	27
1.2 Objectives	32
1.3 Organization of the Report	33
2. OVERVIEW OF THE 18-19 SEPTEMBER 1983 CAPTEX CASE	34
2.1 CAPTEX Tracer Release and Measurements	34
2.2 Meteorology	38
3. MODEL DESCRIPTIONS	60
3.1 The Penn State/NCAR MM5 Meteorological Model	62
3.1.1 Basic Structure	62
3.1.2 Physics	63
3.1.3 Four-Dimensional Data Assimilation	66
3.2 The ARAP/Titan SCIPUFF Dispersion Model	67
3.3 The Penn State TRAJEC Trajectory Model	70
4. EXPERIMENT DESIGN	72
4.1 MM5 Model Domains	72

4.1.1	Configuration 1: Unnested 70-km Domain	72
4.1.2	Configuration 2: Triply Nested Domains	76
4.1.3	Configuration 3: Quadruply Nested Domains	79
4.2	Initialization and Lateral Boundary Conditions	83
4.3	Model Experiments	84
4.4	Evaluation Procedures	88
4.4.1	Approach for Evaluating Mesoscale Features	89
4.4.2	Statistical Evaluation Approach	89
4.4.3	Transport Evaluation Approach	93
4.4.4	Dispersion Evaluation Approach	94
5.	MODEL RESULTS	96
5.1	Evaluation of the Simulated Mesoscale Features	96
5.1.1	Configuration 1	96
5.1.2	Configuration 2	104
5.1.3	Configuration 3	137
5.2	Evaluation of the MM5 Statistical Performance	156
5.3	Evaluation of the Simulated Transport	171
5.4	Evaluation of the Simulated Plume Dispersion	183
6.	CONCLUSIONS	207
	REFERENCES	213

## LIST OF TABLES

		<u>Page</u>
Table 1.	Vertical distribution of sigma levels (half layers) and model-layer heights (m above ground level, AGL) for Configuration 1.	73
Table 2.	Vertical distribution of sigma levels (half layers) and model-layer heights (m AGL) for Configuration 2 (also used for Configuration 3).	80
Table 3.	Summary of experimental design. BLKDR refers to the Blackadar PBL scheme (Zhang and Anthes 1982), while TKE PBL refers to the scheme of Shafran et al. (2000). Anthes-Kuo convection scheme refers to Anthes (1977), and Kain-Fritsch refers to Kain and Fritsch (1990). The radiation scheme is that of Dudhia (1989).	86
Table 4.	Summary of analysis-nudging parameters. Temperature is $T$ , moisture is $q$ , and $u$ and $v$ are the east-west and north-south horizontal wind components, respectively.	87
Table 5.	Critical thresholds chosen for desired accuracy of meteorological variables.	93
Table 6.	Statistical summary of MM5 performance for wind speed and direction in CAPTEX-83 Episode 1 (1200 UTC, 18 Sept. - 0000 UTC, 20 Sept. 1983) on the 70-km verification domain of Exp. 1A.	157
Table 7.	Statistical summary of MM5 performance for wind speed and direction in CAPTEX-83 Episode 1 (1200 UTC, 18 Sept. - 0000 UTC, 20 Sept. 1983) on the 12-km verification domain of Exp. 2A.	160
Table 8.	Statistical summary of MM5 performance for wind speed and direction in CAPTEX-83 Episode 1 (1200 UTC, 18 Sept. - 0000 UTC, 20 Sept. 1983) on the 12-km verification domain of Exp. 2B.	163
Table 9.	Statistical summary of MM5 performance for wind speed and direction in CAPTEX-83 Episode 1 (1200 UTC, 18 Sept. - 0000 UTC, 20 Sept. 1983) on the 12-km verification domain of Exp. 2C.	165
Table 10.	Statistical summary of MM5 performance for wind speed and direction in CAPTEX-83 Episode 1 (1200 UTC, 18 Sept. - 0000 UTC, 20 Sept. 1983) on the 12-km verification domain of Exp. 2D.	167
Table 11.	Statistical summary of MM5 performance for wind speed and direction in CAPTEX-83 Episode 1 (1200 UTC, 18 Sept. - 0000 UTC, 20 Sept. 1983) on the 4-km verification domain of Exp. 3A.	170

Table 12. Maximum concentrations ( $\text{fl } \Gamma^1$ ) of  $\text{C}_7\text{F}_{14}$  tracer at the surface during the CAPTEX-83 Episode 1. Numbers in parentheses are the ratio of modeled to observed concentrations at the specified times. Case-averaged ratios of modeled to observed concentrations (perfect score = 1.0) and mean absolute errors of the ratios (perfect score = 0.0) are shown in the two right-hand columns.

184

## LIST OF FIGURES

		<u>Page</u>
Figure 1.	Location of CAPTEX-83 surface sampling sites (black dots). Release locations are designated with an "R" (after Haagenson et al. 1987).	36
Figure 2.	Objective analysis of sea-level pressure (mb) for 1200 UTC, 18 September 1983 at the beginning of CAPTEX Episode 1. Isobar interval is 2 mb. Grid resolution is 36 km.	39
Figure 3.	Objective analysis of sea-level pressure (mb) for 0000 UTC, 19 September 1983 during CAPTEX Episode 1. Isobar interval is 2 mb. Grid resolution is 36 km.	41
Figure 4.	Objective analysis of 850-mb winds ( $\text{m s}^{-1}$ ) for 0000 UTC, 19 September 1983 during CAPTEX Episode 1. Isotach interval is $10 \text{ m s}^{-1}$ . Grid resolution is 36 km.	42
Figure 5.	Objective analysis of sea-level pressure (mb) for 1200 UTC, 19 September 1983 during CAPTEX Episode 1. Isobar interval is 2 mb. Grid resolution is 36 km.	43
Figure 6.	Objective analysis of sea-level pressure (mb) for 0000 UTC, 20 September 1983 during CAPTEX Episode 1. Isobar interval is 2 mb. Grid resolution is 36 km.	44
Figure 7.	Manual analysis of sea-level pressure (mb) for 1200 UTC, 18 September 1983 during CAPTEX Episode 1 on the area of the 12-km domain (Configuration 2). Isobar interval is 2 mb. Winds are plotted in kts.	46
Figure 8.	Manual analysis of sea-level pressure (mb) for 1800 UTC, 18 September 1983 during CAPTEX Episode 1 on the area of the 12-km domain (Configuration 2). Isobar interval is 2 mb. Winds are plotted in kts.	47
Figure 9.	Manual analysis of sea-level pressure (mb) for 0000 UTC, 19 September 1983 during CAPTEX Episode 1 on the area of the 12-km domain (Configuration 2). Isobar interval is 2 mb. Winds are plotted in kts.	48
Figure 10.	Manual analysis of sea-level pressure (mb) for 0600 UTC, 19 September 1983 during CAPTEX Episode 1 on the area of the 12-km domain (Configuration 2). Isobar interval is 2 mb. Winds are plotted in kts.	49

Figure 11.	Manual analysis of sea-level pressure (mb) for 1200 UTC, 19 September 1983 during CAPTEX Episode 1 on the area of the 12-km domain (Configuration 2). Isobar interval is 2 mb. Winds are plotted in kts.	50
Figure 12.	Manual analysis of sea-level pressure (mb) for 1800 UTC, 19 September 1983 during CAPTEX Episode 1 on the area of the 12-km domain (Configuration 2). Isobar interval is 2 mb. Winds are plotted in kts.	51
Figure 13.	Manual analysis of sea-level pressure (mb) for 0000 UTC, 20 September 1983 during CAPTEX Episode 1 on the area of the 12-km domain (Configuration 2). Isobar interval is 2 mb. Winds are plotted in kts.	52
Figure 14.	Observed tracer concentrations (parts of perfluorocarbon per 10 <sup>15</sup> parts of air by volume, or femtoliters/liter) at the CAPTEX-83 surface sampling sites. Concentrations are for six-hour samples assumed to apply at the mid-point of the sampling periods, defined at: (a) 2200 UTC, 18 Sept., (b) 0400 UTC, 19 Sept., (c) 1000 UTC, 19 Sept., and (d) 1600 UTC, 19 Sept. 1983. "R" is the release point at Dayton, OH. Positions of the cold and warm fronts are added.	55
Figure 15.	Location of 70-km domain for MM5 Configuration 1.	74
Figure 16.	Terrain (m) for 70-km domain of MM5 Configuration 1. Contour interval is 100 m.	75
Figure 17.	Location of 108-km, 36-km, and 12-km nested domains for MM5 Configuration 2.	77
Figure 18.	Terrain (m) for 12-km inner domain of MM5 Configuration 2. Contour interval is 100 m.	78
Figure 19.	Location of 108-km, 36-km, 12-km and 4-km nested domains for MM5 Configuration 3.	81
Figure 20.	Terrain (m) for 4-km inner domain of MM5 Configuration 3. Contour interval is 100 m.	82
Figure 21.	MM5 simulation of sea-level pressure (mb) on the 70-km domain at 1800 UTC, 19 September 1983, 30 h into CAPTEX Experiment 1A. Isobar interval is 2 mb.	98

Figure 22.	MM5 simulation of surface-layer winds ( $\text{m s}^{-1}$ ) on the 70-km domain at 1800 UTC, 19 September 1983, 30 h into CAPTEX Experiment 1A. Contour interval is $5 \text{ m s}^{-1}$ .	99
Figure 23.	MM5 simulation of 850-mb wind ( $\text{ms}^{-1}$ ) on the 70-km domain at 1800 UTC, 19 September 1983, 30 h into CAPTEX Experiment 1A. Isotach interval is $5 \text{ ms}^{-1}$ .	102
Figure 24.	MM5 sounding simulated at Albany, NY, 1800 UTC, 19 September 1983, 30 h into CAPTEX Experiment 1A. Winds are plotted in kts.	103
Figure 25.	MM5 simulation of 850-mb temperature (C) on the 70-km domain at 1800 UTC, 19 September 1983, 30 h into CAPTEX Experiment 1A. Isotherm interval is 2 C.	105
Figure 26.	MM5 simulation of sea-level pressure (mb) on the 12-km domain at 0000 UTC, 19 September 1983, 12 h into CAPTEX Experiment 2B. Isobar interval is 2 mb.	107
Figure 27.	MM5 simulation of surface-layer winds ( $\text{m s}^{-1}$ ) on the 12-km domain at 0000 UTC, 19 September 1983, 12 h into CAPTEX Experiment 2B. Contour interval is $5 \text{ m s}^{-1}$ .	108
Figure 28.	MM5 simulation of 6-h rainfall (mm) on the 12-km domain for the period ending at 0000 UTC, 19 September 1983, 12 h into CAPTEX Experiment 2B. Contours are at 1, 5, 10, and 20 mm.	109
Figure 29.	MM5 simulation of 850-mb wind ( $\text{ms}^{-1}$ ) on the 12-km domain at 0000 UTC, 19 September 1983, 12 h into CAPTEX Experiment 2B. Isotach interval is $5 \text{ ms}^{-1}$ .	111
Figure 30.	Location of southwest to northeast cross section on the 12-km domain for CAPTEX Episode 1. The cross section is oriented to lie approximately along the centerline of the surface plume for this case.	113
Figure 31.	Cross section of MM5 simulated potential temperature (K) on the 12-km domain at 0000 UTC, 19 September 1983, 12 h into CAPTEX Experiment 2B. Isentrope interval is 1 K. Dashed line indicates depth of the surface-based turbulent layer. Position of the warm front surface is superimposed. Location of the southwest-northeast cross section is shown in Figure 30. Line segments just below 1050 mb level each indicate 100 km distance from left.	114

Figure 32.	Cross section of MM5 simulated horizontal wind speed ( $\text{ms}^{-1}$ ) and wind vectors in the plane on the 12-km domain at 0000 UTC, 19 September 1983, 12 h into CAPTEX Experiment 2B. Isotach interval is $5 \text{ ms}^{-1}$ . Vectors are exaggerated in the vertical by 100:1. Dashed line indicates depth of the surface-based turbulent layer. Position of the warm front surface is superimposed. Location of the southwest-northeast cross section is shown in Figure 30. Line segments just below 1050-mb level each indicate 100 km distance from left.	116
Figure 33.	MM5 simulation of 900-mb water vapor mixing ratio ( $\text{g kg}^{-1}$ ) on the 12-km domain at 0000 UTC, 19 September 1983, 12 h into CAPTEX Experiment 2B. Contour interval is $1 \text{ g kg}^{-1}$ .	118
Figure 34.	MM5 simulation of sea-level pressure (mb) on the 12-km domain at 1800 UTC, 19 September 1983, 30 h into CAPTEX Experiment 2B. Isobar interval is 2 mb. Location of a cross section identical to that shown in Figure 30 is indicated by the straight line from OH to ME.	119
Figure 35.	MM5 simulation of surface-layer winds ( $\text{m s}^{-1}$ ) on the 12-km domain at 1800 UTC, 19 September 1983, 30 h into CAPTEX Experiment 2B. Contour interval is $5 \text{ m s}^{-1}$ .	120
Figure 36.	MM5 simulation of 6-h rainfall (mm) on the 12-km domain for the period ending at 1800 UTC, 19 September 1983, 30 h into CAPTEX Experiment 2B. Contours are at 1, 5, 10, and 20 mm.	122
Figure 37.	MM5 simulation of 850-mb wind ( $\text{ms}^{-1}$ ) on the 12-km domain at 1800 UTC, 19 September 1983, 30 h into CAPTEX Experiment 2B. Isotach interval is $5 \text{ ms}^{-1}$ .	123
Figure 38.	MM5 sounding simulated at Albany, NY, 1800 UTC, 19 September 1983, 30 h into CAPTEX Experiment 2B. Winds are plotted in kts.	124
Figure 39.	MM5 simulation of 900-mb temperature (C) on the 12-km domain at 1800 UTC, 19 September 1983, 30 h into CAPTEX Experiment 2B. Isotherm interval is 2 C.	126
Figure 40.	Cross section of MM5 simulated potential temperature (K) on the 12-km domain at 1800 UTC, 19 September 1983, 30 h into CAPTEX Experiment 2B. Isentrope interval is 1 K. Dashed line indicates depth of the surface-based turbulent layer. Position of the warm and cold frontal surfaces are superimposed. Location of the southwest-northeast cross section is shown in Figure 34. Line segments just below 1050-mb level each indicate 100 km distance from left.	127

Figure 41.	Cross section of MM5 simulated cloud liquid water ( $\text{g kg}^{-1}$ ) on the 12-km domain at 1800 UTC, 19 September 1983, 30 h into CAPTEX Experiment 2B. Contour interval is $0.1 \text{ g kg}^{-1}$ . Dashed line indicates depth of the surface-based turbulent layer. Location of the southwest-northeast cross section is shown in Figure 34. Line segments just below 1050-mb level each indicate 100 km distance from left.	128
Figure 42.	MM5 simulation of sea-level pressure (mb) on the 12-km domain at 0000 UTC, 19 September 1983, 12 h into CAPTEX Experiment 2D. Isobar interval is 2 mb.	130
Figure 43.	Cross section of MM5 simulated potential temperature (K) on the 12-km domain at 0000 UTC, 19 September 1983, 12 h into CAPTEX Experiment 2D. Isentrope interval is 1 K. Dashed line indicates depth of the surface-based turbulent layer. Position of the warm front surface is superimposed. Location of the southwest-northeast cross section is shown in Figure 30. Line segments just below 1050 mb level each indicate 100 km distance from left.	132
Figure 44.	MM5 simulation of sea-level pressure (mb) on the 12-km domain at 1800 UTC, 19 September 1983, 30 h into CAPTEX Experiment 2D. Isobar interval is 2 mb. Location of the a cross section identical to that shown in Figure 30 is indicated by the straight line from OH to ME.	134
Figure 45.	Cross section of MM5 simulated potential temperature (K) on the 12-km domain at 1800 UTC, 19 September 1983, 30 h into CAPTEX Experiment 2D. Isentrope interval is 1 K. Dashed line indicates depth of the surface-based turbulent layer. Position of the warm and cold frontal surfaces are superimposed. Location of the southwest-northeast cross section is shown in Figure 44. Line segments just below 1050-mb level each indicate 100 km distance from left.	136
Figure 46.	MM5 simulation of sea-level pressure (mb) on the 4-km domain at 0000 UTC, 19 September 1983, 12 h into CAPTEX Experiment 3A. Isobar interval is 2 mb.	139
Figure 47.	MM5 simulation of surface-layer winds ( $\text{m s}^{-1}$ ) on the 4-km domain at 0000 UTC, 19 September 1983, 12 h into CAPTEX Experiment 3A. Contour interval is $5 \text{ m s}^{-1}$ .	140
Figure 48.	MM5 simulation of 6-h rainfall (mm) on the 4-km domain for the period ending at 0000 UTC, 19 September 1983, 12 h into CAPTEX Experiment 3A. Contours are at 1, 5, 10, and 20 mm.	141

- Figure 49. Location of southwest to northeast cross section on the 4-km domain for CAPTEX Episode 1. The cross section is oriented to lie approximately along the centerline of the surface plume for this case. 143
- Figure 50. Cross section of MM5 simulated potential temperature (K) on the 4-km domain at 0000 UTC, 19 September 1983, 12 h into CAPTEX Experiment 3A. Isentrope interval is 1 K. Dashed line indicates depth of the surface-based turbulent layer. Position of the warm front surface is superimposed. Location of the southwest-northeast cross section is shown in Figure 49. Line segments just below 1050 mb level each indicate 100 km distance from left. 144
- Figure 51. Cross section of MM5 simulated horizontal wind speed ( $\text{ms}^{-1}$ ) and wind vectors in the plane on the 4-km domain at 0000 UTC, 19 September 1983, 12 h into CAPTEX Experiment 3A. Isotach interval is  $5 \text{ ms}^{-1}$ . Vectors are exaggerated in the vertical by 100:1. Dashed line indicates depth of the surface-based turbulent layer. Position of the warm front surface is superimposed. Location of the southwest-northeast cross section is shown in Figure 50. Line segments just below 1050-mb level each indicate 100 km distance from left. 146
- Figure 52. MM5 simulation of sea-level pressure (mb) on the 4-km domain at 1800 UTC, 19 September 1983, 30 h into CAPTEX Experiment 3A. Isobar interval is 2 mb. Location of the a cross section identical to that shown in Figure 49 is indicated by the straight line from OH to ME. Heavy dashed-dotted line denotes cold outflow boundary. 148
- Figure 53. MM5 simulation of 6-h rainfall (mm) on the 4-km domain for the period ending at 1800 UTC, 19 September 1983, 30 h into CAPTEX Experiment 3A. Contours are at 1, 5, 10, and 20 mm. Heavy dashed-dotted line denotes cold outflow boundary. 149
- Figure 54. MM5 simulation of surface-layer temperatures (C) on the 4-km domain at 1800 UTC, 19 September 1983, 30 h into CAPTEX Experiment 3A. Isotherm interval is 2 C. Heavy dashed-dotted line denotes cold outflow boundary. 151
- Figure 55. MM5 simulation of surface-layer winds ( $\text{m s}^{-1}$ ) on the 4-km domain at 1800 UTC, 19 September 1983, 30 h into CAPTEX Experiment 3A. Contour interval is  $5 \text{ m s}^{-1}$ . Heavy dashed-dotted line denotes cold outflow boundary. 152

- Figure 56. Cross section of MM5 simulated potential temperature (K) on the 4-km domain at 1800 UTC, 19 September 1983, 30 h into CAPTEX Experiment 3A. Isentrope interval is 1 K. Dashed line indicates depth of the surface-based turbulent layer. Positions of the cold frontal surface (standard symbols) and cold convective downdraft (heavy dashed-dotted line) are superimposed. Location of the southwest-northeast cross section is shown in Figure 52. Line segments just below 1050-mb level each indicate 100 km distance from left. 154
- Figure 57. Cross section of MM5 simulated turbulent kinetic energy ( $\text{J kg}^{-1}$ ) on the 4-km domain at 1800 UTC, 19 September 1983, 30 h into CAPTEX Experiment 3A. Contour interval is  $0.1 \text{ J kg}^{-1}$ . Dashed line indicates depth of the surface-based turbulent layer. Location of the southwest-northeast cross section is shown in Figure 52. Line segments just below 1050-mb level each indicate 100 km distance from left. 155
- Figure 58. Parcel trajectories calculated for Exp. 1A using TRAJEC. Release time at Dayton is 1700 UTC, 18 September; termination time is 1100 UTC, 19 September 1983. Release heights as follows: Parcel 1 = 36 m, Parcel 2 = 143 m, Parcel 3 = 326 m, Parcel 4 = 540 m, Parcel 5 = 777 m, Parcel 6 = 1012 m, Parcel 7 = 1308 m, and Parcel 8 = 1725 m. All trajectories are plotted with two lines, the separation of which corresponds to the pressure level following the parcel (key is at lower right of the figure). Tick marks along the trajectories represent 1 h intervals. 174
- Figure 59. Parcel trajectories calculated for Exp. 2B using TRAJEC. Release time at Dayton is 1700 UTC, 18 September; termination time is 1700 UTC, 19 September 1983. Release heights as follows: Parcel 1 = 29 m, Parcel 2 = 86 m, Parcel 3 = 143 m, Parcel 4 = 472 m, Parcel 5 = 1047 m, Parcel 6 = 1206 m, Parcel 7 = 1368 m, and Parcel 8 = 1533 m. All trajectories are plotted with two lines, the separation of which corresponds to the pressure level following the parcel (key is at lower right of the figure). Tick marks along the trajectories represent 1 h intervals. 177
- Figure 60. Parcel trajectories calculated for Exp. 2D using TRAJEC. Release time at Dayton is 1700 UTC, 18 September; termination time is 1700 UTC, 19 September 1983. Release heights as follows: Parcel 1 = 29 m, Parcel 2 = 86 m, Parcel 3 = 143 m, Parcel 4 = 472 m, Parcel 5 = 1047 m, Parcel 6 = 1206 m, Parcel 7 = 1368 m, and Parcel 8 = 1533 m. All trajectories are plotted with two lines, the separation of which corresponds to the pressure level following the parcel (key is at lower right of the figure). Tick marks along the trajectories represent 1 h intervals. 180

Figure 61.	Parcel trajectories calculated for Exp. 3A using TRAJEC. Release time at Dayton is 1700 UTC, 18 September; termination time is 1200 UTC, 19 September 1983. Release heights as follows: Parcel 1 = 29 m, Parcel 2 = 86 m, Parcel 3 = 143 m, Parcel 4 = 472 m, Parcel 5 = 1047 m, Parcel 6 = 1206 m, Parcel 7 = 1368 m, and Parcel 8 = 1533 m. All trajectories are plotted with two lines, the separation of which corresponds to the pressure level following the parcel (key is at lower right of the figure). Tick marks along the trajectories represent 1 h intervals.	182
Figure 62.	SCIPUFF surface concentrations of inert tracer ( $\text{fl } \Gamma^1$ ) released from Dayton, OH, on the 70-km domain of Exp. 1A during CAPTEX-83, Episode 1. Concentrations are valid at 1000 UTC, 19 September 1983 (+17 h).	188
Figure 63.	SCIPUFF surface concentrations of inert tracer ( $\text{fl } \Gamma^1$ ) released from Dayton, OH, on the 70-km domain of Exp. 1A during CAPTEX-83, Episode 1. Concentrations are valid at 1600 UTC, 19 September 1983 (+23 h).	189
Figure 64.	SCIPUFF surface concentrations of inert tracer ( $\text{fl } \Gamma^1$ ) released from Dayton, OH, on the 12-km domain of Exp. 2B during CAPTEX-83, Episode 1. Concentrations are valid at 1000 UTC, 19 September 1983 (+17 h).	190
Figure 65.	SCIPUFF surface concentrations of inert tracer ( $\text{fl } \Gamma^1$ ) released from Dayton, OH, on the 12-km domain of Exp. 2B during CAPTEX-83, Episode 1. Concentrations are valid at 1600 UTC, 19 September 1983 (+23 h).	191
Figure 66.	SCIPUFF surface concentrations of inert tracer ( $\text{fl } \Gamma^1$ ) released from Dayton, OH, on the 12-km domain of Exp. 2D during CAPTEX-83, Episode 1. Concentrations are valid at 1000 UTC, 19 September 1983 (+17 h).	193
Figure 67.	SCIPUFF surface concentrations of inert tracer ( $\text{fl } \Gamma^1$ ) released from Dayton, OH, on the 12-km domain of Exp. 2D during CAPTEX-83, Episode 1. Concentrations are valid at 1600 UTC, 19 September 1983 (+23 h).	194
Figure 68.	SCIPUFF surface concentrations of inert tracer ( $\text{fl } \Gamma^1$ ) released from Dayton, OH, on the 4-km domain of Exp. 3A during CAPTEX-83, Episode 1. Concentrations are valid at 0400 UTC, 19 September 1983 (+11 h).	196

Figure 69.	SCIPUFF surface concentrations of inert tracer ( $\text{fl } \Gamma^1$ ) released from Dayton, OH, shown along cross section A (Lake Ontario) on the 12-km domain of Exp. 2D during CAPTEX-83, Episode 1. Concentrations are valid at 1000 UTC, 19 September 1983 (+17 h).	198
Figure 70.	SCIPUFF surface concentrations of inert tracer ( $\text{fl } \Gamma^1$ ) released from Dayton, OH, shown along cross section B (Adirondack Mountains) on the 12-km domain of Exp. 2D during CAPTEX-83, Episode 1. Concentrations are valid at 1000 UTC, 19 September 1983 (+17 h).	199
Figure 71.	SCIPUFF surface concentrations of inert tracer ( $\text{fl } \Gamma^1$ ) released from Dayton, OH, shown along cross section C (White Mountains) on the 12-km domain of Exp. 2D during CAPTEX-83, Episode 1. Concentrations are valid at 1000 UTC, 19 September 1983 (+17 h).	200
Figure 72.	SCIPUFF surface concentrations of inert tracer ( $\text{fl } \Gamma^1$ ) released from Dayton, OH, shown along cross section A (Lake Ontario) on the 12-km domain of Exp. 2D during CAPTEX-83, Episode 1. Concentrations are valid at 1600 UTC, 19 September 1983 (+23 h).	203
Figure 73.	SCIPUFF surface concentrations of inert tracer ( $\text{fl } \Gamma^1$ ) released from Dayton, OH, shown along cross section B (Adirondack Mountains) on the 12-km domain of Exp. 2D during CAPTEX-83, Episode 1. Concentrations are valid at 1600 UTC, 19 September 1983 (+23 h).	204
Figure 74.	SCIPUFF surface concentrations of inert tracer ( $\text{fl } \Gamma^1$ ) released from Dayton, OH, shown along cross section C (White Mountains) on the 12-km domain of Exp. 2D during CAPTEX-83, Episode 1. Concentrations are valid at 1600 UTC, 19 September 1983 (+23 h).	205

# 1. INTRODUCTION

## 1.1 Background

In the late 1990s, the U.S. Environmental Protection Agency mandated revised federal clean-air standards that include a maximum allowable eight-hour-average exposure to ozone of no more than 85 ppb. This mid-term exposure<sup>1</sup> limit is to be applied in addition to the original hourly peak dosage of 125 ppb. Studies are also underway to set new short-term and mid-term limits for fine-scale particulate matter (PM<sub>2.5</sub>) that is suspected to contribute to lung ailments, such as asthma and emphysema. The new air-quality standards were recently upheld by the U.S. Supreme Court and are expected to have wide-ranging impacts as they are implemented.

One implication of these changes is that, in many areas, local sources of pollutants cannot be assumed to dominate the relevant chemistry leading to exceedances of the 8-h standards. Of course, even when concerns were limited primarily to reducing the one-hour peak concentrations in or immediately downwind of a large urban center, it was necessary to consider long-range transport of ozone and its precursors. However, when considering of 8-h dosages, ozone concentrations measured locally could very easily be dominated by longer-range transport mechanisms, necessitating closer scrutiny of the atmospheric chemistry over broader areas. Thus, for example, emissions originating in the Midwest could contribute to exceedances over wide regions of the Northeast a day later (including rural areas). Even with a mean wind speed of only 10 ms<sup>-1</sup>, parcels can be transported over 850 km/day. Moreover, for that speed and time,

---

<sup>1</sup> For the purpose of this report "short-term" will refer to a time scale of about 1-4 h, "mid-term" will refer to about 4-48 h, and "long-term" will refer to periods longer than two days but less than a month. Beyond "long-term", one could discuss climatological time scales of months, seasons and years.

a change in the mean wind direction of just 10 degrees can shift the 24-h position of the plume centerline by nearly 150 km.

Over the past decade, many of the observational and numerical studies of episodes having poor air quality have focused primarily on understanding short-term exposure to certain species. Daily one-hour peak ozone concentrations and the diurnal cycle of local ozone and precursor concentrations were given a high priority. Meteorological modeling studies in support of this type of air-quality assessment have been carried out in diverse regions including central California (Seaman et al. 1995), Los Angeles (Bornstein et al. 2001), the upper Midwest (Lyons et al. 1995, Shafran et al. 2000) and the Northeast U.S. (Seaman and Michelson 2000). To be sure, this work has included important elements of inter-regional transport on the mid- to long-term time scales, but the meteorological focus generally has been on improving the representation of local mesoscale features by using finer grid resolutions, improved model physics and data-assimilation techniques. It is now fairly common for meteorological models used in support of air-quality investigations to be applied with grids of 4 km or less (on domains extending at least several hundred kilometers on a side) and to use four-dimensional data assimilation (FDDA) to reduce the accumulation of modeling errors. Such advancements have made it possible to do a better job of simulating the meteorology of air-quality events (Seaman 2000, Hogrefe et al. 2001a) and local ozone concentrations (e.g., Hogrefe et al. 2001b). However, with the extension of the federal clean-air mandates to include standards for mid-term exposures, it is important to re-examine our understanding of inter-regional transport and the ability of meteorological models to accurately represent the wind and stability fields that control transport and dispersion on that scale.

For our purposes the inter-regional-scale (mesoalpha-scale) is defined here to include distances of 200 - 2000 km. That is, the inter-regional scale stretches beyond any single large metropolitan area and may span several states. Transport on the inter-regional scale is a product of atmospheric motions acting over a range of spatial scales from the synoptic scale ( $> 2000$  km) to turbulence scales ( $\sim 0.1$  m -  $\sim 2$  km). At the small end of the range, turbulence is understood to mix surface emissions and pollutants vertically through the planetary boundary layer (PBL) and to spread plumes laterally as they move downwind. Meanwhile, synoptic-scale anticyclones often provide stable weakly forced environments that are ideal for producing air-stagnation, enhanced photochemistry (especially in summer), suppressed mixed-layer depths, reduced precipitation and weakening of other deposition and removal processes.

Embedded within these quasi-stagnant synoptic systems, mesoscale circulations (fronts, troughs, sea-breezes, low-level jets, etc.) can generate convergence zones that help generate or intensify concentration gradients of airborne species. For example, McNider et al. (1998) reported that enhanced ozone concentrations could be found in the vicinity of old quasi-stationary fronts due to convergence and reduced winds in the frontal-boundary zone, despite enhanced cloudiness. Moreover, Seaman and Michelson (2000) found that vertical circulations associated with the convergence zone of the Appalachian Lee Trough were able to lift pollutants above the mixed layer in New Jersey during the 12-15 July 1995 NARSTO-Northeast episode. Once aloft, ozone and other contaminants were transported rapidly northeastward by a low-level jet to New England, where they later were mixed downward to the surface (Ray et al. 1998). Thus, mesoscale features embedded in the synoptic wind field must be considered important for understanding inter-regional transport.

Our ability to define the complex three-dimensional (3-D) wind fields in real atmospheric cases remains uncertain because of our inability to observe the atmosphere at spatial scales much finer than that provided by the synoptic data network. Consequently, better understanding of transport issues and source-receptor relationships on the inter-regional scale is dependent on reducing these uncertainties. Wind fields can be diagnosed directly from observations, or simulated by dynamical models (with or without FDDA) (Seaman 2000). Although diagnostic analysis tools have an advantage in that they create representations of the atmospheric fields that are based solely on the observations, they do have limitations. Standard observing networks, such as those operated by the National Weather Service (NWS), are too coarse to resolve most mesoscale features, even over the continents. Supplemental observations, especially above the surface, can be very costly to obtain even for special field programs (intensive observing periods, or IOPs). Even during IOPs, the observation base generally is insufficient to resolve important variables, such as the vertical velocity and the divergence fields, and the special data are usually concentrated over a relatively small area.

Dynamical mesoscale meteorological models, on the other hand, generally have much better horizontal and temporal resolution than do the observations, even in the case of special field programs. They also generate complete data sets that include vertical velocity, divergence and clouds, and can produce inter-variable consistency based on the full Navier-Stokes equations (scaled for atmospheric applications). Although these models are certainly imperfect, they have been improved in recent years. The availability of faster computers and cheaper random-access memory has allowed grid resolutions for small regional areas (hundred kilometers on a side) to be reduced to ~1-5 km. Practical FDDA techniques help to reduce the accumulation of model errors over time (e.g., Stauffer and Seaman 1994), so that simulations for episodes lasting 5-10

days are now routine. Better representation of sub-grid scale physics (radiation, turbulence, convection, etc.) and improved numerics have further reduced meteorological model errors. Recent development of shallow-convection parameterizations (e.g., Deng et al. 2002a,b) offer the promise of more accurate simulations of the low-level clouds that are common in air-quality episodes and can transport pollutants in the vertical. Consequently, high-resolution, data-assimilating dynamical models with advanced physics have become widely accepted as the best approach for generating mesoscale meteorological fields for many air-quality investigations (Seaman 2000).

However, most of the air-quality modeling research over the past decade has focused on two extremes: the local scales and continental scales. At the continental scales, global models are being used to understand how, for example, emissions from rapidly industrializing Asian nations may affect atmospheric aerosol loading over the Pacific Ocean and North America and its impact on air quality and climate. At the local scales, the focus has been primarily on understanding and controlling one-hour peak ozone, especially in and near urban centers. This has led to a great emphasis on the simulation of meteorological features at the mesobeta scale (20 - 200 km) using finer and finer mesh sizes and limited-area domains. These mesobeta-scale domains generally are nested within larger and coarser domains that typically have resolutions of ~10-40 km. While the improvement in model skill on nested fine-mesh domains has been demonstrated time and again, the accuracy of the solutions produced simultaneously on coarser model domains has received much less attention in recent years. *Because the finest domains only cover areas a few hundred kilometers on a side, however, it is the coarser domains in these nested-grid mesoscale models that control the inter-regional transport of pollutants.* Moreover, these coarser regional domains have considerable impact on local concentrations in the fine-grid

domains by controlling the winds and mass-field advection imposed through the grid interfaces (Warner et al. 1997). In many recent studies, however, the accuracy of the model solutions on the coarser mesoalpha-scale domains has been virtually ignored. It is not uncommon to find that no statistical evaluations of model skill are made on the coarser grids and in many cases only brief visual inspections are performed to ensure that no very serious errors have occurred.

Thus, a gap in our understanding of current model skill has developed at the mesoalpha, or inter-regional scale. While the improvement in skill of numerical meteorological models for simulating transport and mixing at very fine scales (grids of 1 - 5 km) has been demonstrated, it is no longer clear what is the state of the science for representing longer-range sub-continental transport. The last major modeling studies to replicate measurements from inter-regional tracer releases were performed over a decade ago (e.g., Haagenson et al. 1987, 1990; Chock and Kuo 1990). Those regional models had much more coarse horizontal and vertical resolutions than today's models (generally, only ~60-80 km in the horizontal and ~15 vertical layers), no FDDA and generally less sophisticated atmospheric physics. Since the regional-scale outer domains have such an important influence on the nested fine-domain solutions, and the importance of inter-regional transport has been enhanced by the new 8-h air-quality standards, it is appropriate to revisit the question of model accuracy at the inter-regional scale.

## 1.2 Objectives

The *primary objective* of this study supported by CRC under Contract A-28 is *to evaluate the skill of an advanced meteorological model for transport and mixing on inter-regional scales as a function of grid resolution, model physics and FDDA*. Specific goals are:

- To evaluate the current state of the science for simulating inter-regional transport and diffusion of a tracer when using a particular numerical mesoscale model, the Penn State/NCAR MM5, to represent the meteorology (wind, turbulence, convective processes, etc.) and a regional plume model, the ARAP/Titan SCIPUFF, to represent dispersion.
- To identify which of the meteorological model's attributes introduced or enhanced over the past decade (finer resolution, better physics, FDDA), if any, are most effective for improving the skill of inter-regional transport.

### **1.3 Organization of the Report**

Section 2 of this report describes the meteorology of the case selected for the study of inter-regional transport. The case-selection approach, involving issues related to the meteorology and tracer-data availability, is reviewed. An overview of the tracer-measurement program is also provided. In Section 3 the numerical modeling tools are described. These include the Penn State/NCAR MM5 mesoscale meteorological model, the ARAP/Titan SCIPUFF dispersion model, and the Penn State TRAJEC trajectory model. The design of the numerical experiments is described in Section 4, and the model results are presented in Section 5. Finally, a summary of the study and its most important findings are given in Section 6.

## **2. OVERVIEW OF THE 18-19 SEPTEMBER CAPTEX CASE**

The case chosen for experimentation in this study is the 18-19 September episode from the Cross Appalachian Tracer Experiment of 1983 (CAPTEX-83). This episode was selected because it produced fairly complete tracer measurements that provide an independent set of data suitable for evaluating the inter-regional transport simulated by the numerical model. Details of the tracer experiment design and the meteorological conditions for this case are given below.

### **2.1 CAPTEX Tracer Release and Measurements**

In CAPTEX-83, an inert perfluorocarbon tracer gas (perfluoro-monomethyl-cyclohexane, or  $C_7F_{14}$ ) was released for seven individual cases during September and October 1983. Five of the releases were made from Dayton, OH and two were from Sudbury, Ontario. Following each release, concentrations of the tracer gas were measured over an array of 82 ground-based sites in OH, WV, NY, PA, NJ, New England and southern Ontario and Quebec (Figure 1) using automated sequential air samplers. Sampling was also done using seven instrumented aircraft, which flew more or less simultaneously across the path of each plume at different altitudes to provide a vertical cross section of its structure. These aircraft data were sometimes helpful, although they were often unavailable at the times and places that later proved most important for understanding the interactions between the meteorology and the tracer plumes.

The sites closest to the release point (those in Ohio, in the case of the releases from Dayton) were programmed to take six consecutive 3-h samples (duration of 18 h), while those farther downwind were programmed to take six longer 6-h samples (duration of 36 h).

Following Haagenson et al. (1987), pairs of the 3-h samples were combined into effective mean 6-h samples to be consistent with the majority of the measurements and the goal of focusing on longer-range transport. The average spacing of the surface sites was on the order of 80-90 km. The most distant arc of sites, in NH and MA, lay approximately 1200 km from the Dayton release site. The detection threshold at which the automatic sequential air samplers could distinguish between the tracer plume and the background level of the perfluorocarbon used in the field study was  $\sim 1$  part per  $10^{15}$  parts of air by volume (i.e., 1 femtoliters/liter).

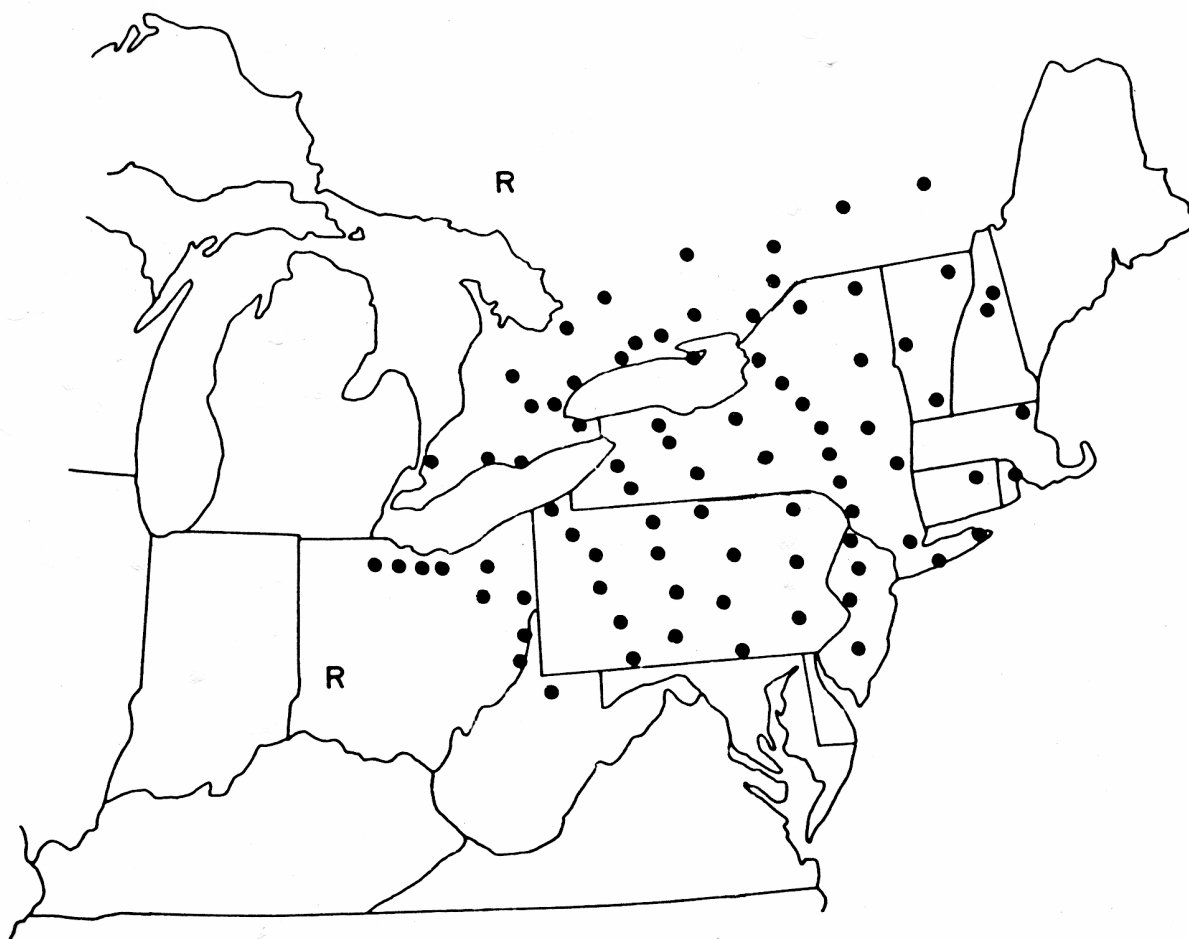


**Figure 1.** Location of CAPTEX-83 surface sampling sites (black dots). Release locations are designated with an "R" (after Haagensohn et al. 1987).

For all of the CAPTEX-83 Dayton releases, cases were selected that exhibited a broad anticyclonic circulation centered over the Southeast U.S. This produced west to southwesterly synoptic-scale flow on the northern flank of the anticyclones that carried the tracer material over the monitoring network (see Section 2.2 for details of the 18-19 September episode). The two releases from Sudbury, on the other hand, were made following the passage of a cold front and therefore they produced northwesterly winds across the network. An anticyclonic event with southwesterly flow is considered generally advantageous for the present study because it is representative of many situations commonly associated with poor air quality over the Midwest and Northeast U.S. Therefore, the first CAPTEX episode, 18-19 September 1983, was chosen for use in the A-28 study because it had the most complete tracer measurements, had a favorable anticyclonic synoptic-scale pattern, and it already has been the subject of a prior investigation by Haagenson et al. (1987).

For the 18-19 September episode, 208 kg of the perfluorocarbon tracer were released from Dayton, OH, at ground level over a 3-h period (1700-2000 UTC, 18 September). Thus, the period when the monitoring network was active extended from about 1800 UTC, 18 September to 0600 UTC, 20 September. However, because the mean advective speed in the layers between the surface and 850 mb was rather high during this episode (see Sec. 2.2), the focus of the modeling study is primarily on the 24-h period from 1800 UTC, 18 September to 1800 UTC, 19 September.

By releasing the tracer during the middle of the day (1200-1500 LST), the CAPTEX-83 forecasters expected that the tracer would rapidly become well mixed through the depth of the daytime convective planetary boundary layer (PBL). This is an ideal experiment design for learning about inter-regional transport because it should prevent substantial quantities of the

tracer from becoming trapped in shallow stagnant layers near the surface during the first 6-12 hours, as might occur with a nocturnal release in a stable air mass over irregular terrain. A total of 273 six-hour surface tracer samples were available from 68 of the 82 monitoring sites (after the 3-h samples were combined, as described above). The other 14 monitors were not operational during this case. The missing information included data from five sites northwest of Lake Ontario and four sites in central NY, which lay in or near the path of the tracer plume for the 18-19 September case. Many other samples show zero concentration through most or all of the period, indicating that the plume remains less broad than the monitoring network (see Sections 2.2 and 5.4).

## **2.2 Meteorology**

The first CAPTEX case of 18-19 September 1983 was characterized by a large anticyclone centered over the Mid-Atlantic Coast, with broad southwesterly wind flow over the Midwest and Northeast U.S. Figure 2 shows this anticyclone at 1200 UTC, 18 September (5 h before the beginning of the tracer release from Dayton). To the northwest of the high, warm and cold fronts (associated with a deep 982-mb occluded storm located in central Canada) were approaching the Northeast, but still lay well to the west. The Canadian storm and the pressure gradient in the Midwest ahead of the cold front were rather strong for this early in the autumn. Consistent with the strength of the deep baroclinic storm, the frontal system was propagating rapidly through the western Great Lakes at nearly  $15 \text{ m s}^{-1}$ . Meanwhile, ahead of the cold front in southern MI, a warm-sector low-level jet (LLJ) at 850 mb contained wind speeds of  $30 \text{ m s}^{-1}$  at 1200 UTC, 18 September (not shown).

Title:

Creator:

CorelDRAW

Preview:

This EPS picture was not saved  
with a preview included in it.

Comment:

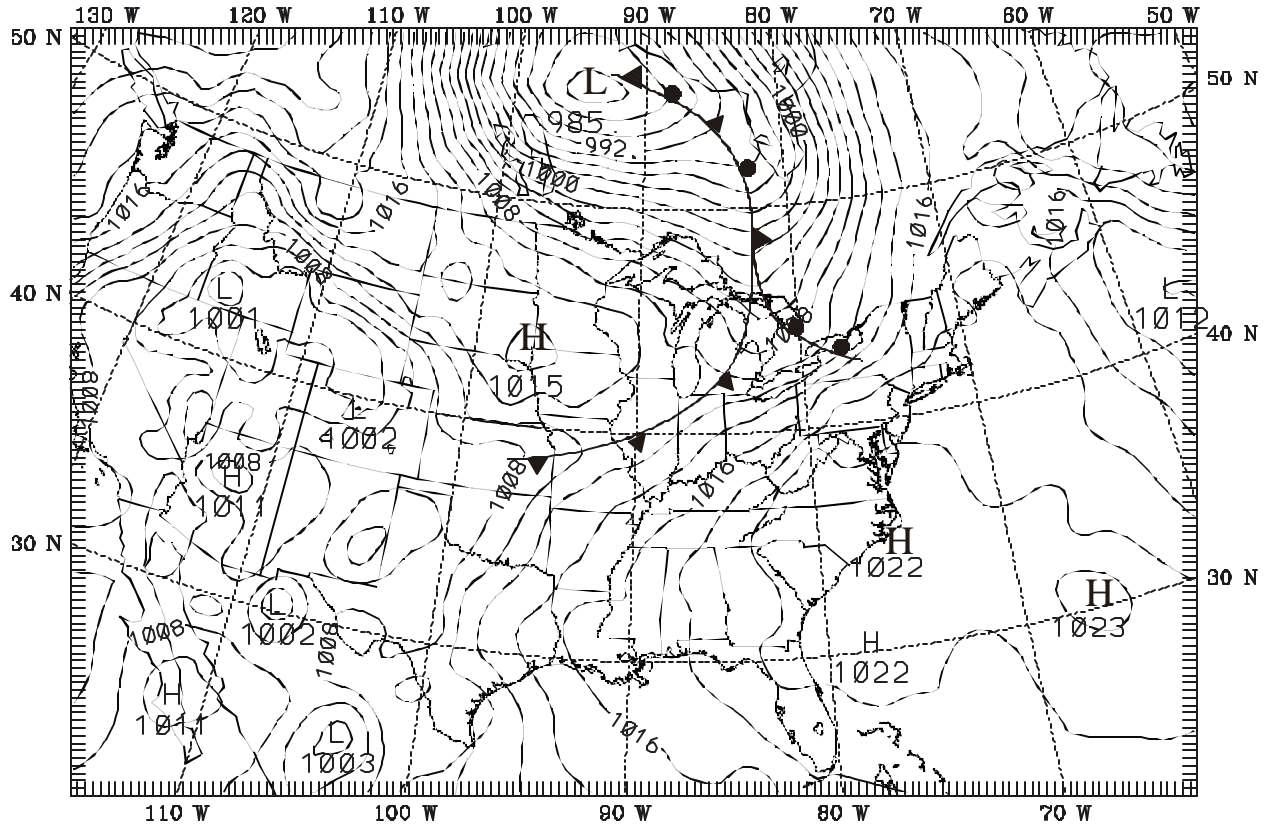
This EPS picture will print to a  
PostScript printer, but not to  
other types of printers.

**Figure 2. Objective analysis of sea-level pressure (mb) for 1200 UTC, 18 September 1983 at the beginning of CAPTEX Episode 1. Isobar interval is 2 mb. Grid resolution is 36 km.**

As the cold front approached the Northeast from the Great Lakes, the strongest surface pressure gradient had shifted eastward by 0000 UTC on 19 September to the vicinity of Buffalo, NY (Figure 3). At this time the center of the 850-mb LLJ was analyzed just west of Niagara Falls with maximum winds of  $\sim 26 \text{ m s}^{-1}$  (Figure 4). This LLJ led to rapid transport of air from the Midwest to northern New England between 0000-1200 UTC, 19 September, when the tracer cloud had already reached the lower Great Lakes. Clouds and rain showers also accompanied the cold front during this period as it crossed the lower Lakes and approached the St. Lawrence Valley (to be discussed below). By 1200 UTC, 19 September, the occlusion point of the frontal system was north of ME in the province of Quebec, while the trailing cold front had decelerated and was just beginning to push into northern NY from Lake Ontario (Figure 5). Notice that even in the synoptic-scale analysis (Figure 5), a modest surface trough can be detected at this time over New England in the warm sector ahead of the front. Also, the pressure gradient ahead of the cold front had relaxed by 1200 UTC, September 19, so that winds in the 850-mb LLJ had weakened to  $\sim 20 \text{ m s}^{-1}$  from the west (not shown). Despite this weakening of the mid-level winds in the warm sector, the tracer material was certainly undergoing rapid advection above the surface throughout the period of interest.

The final synoptic-scale objective analysis for sea-level pressure in CAPTEX Episode 1, at 0000 UTC, 20 September, is shown in Figure 6. It indicates that the original Canadian storm had become quasi-stationary over Hudson Bay, while a secondary 999-mb cyclone had formed along the occluded front in Labrador. Since upper-level dynamic support for the Labrador storm was by this time far to the northeast of New England, the cold front had been able to push southward into central ME, but had made only slow progress into NY. Farther to the west, from IA to MI, the frontal boundary had reversed direction toward the north as a warm front. In CO,

SIGMA -1.000 SEA PRES (mb) | 1983-09-19\_00.00.00



MM5V3-CAPTEX,EXP2=> MMINPUT  
CONTOUR FROM 984.00 TO 1024.0 CONTOUR INTERVAL OF 2.0000 PT(3,3)= 1008.3

**Figure 3.** Objective analysis of sea-level pressure (mb) for 0000 UTC, 19 September 1983 during CAPTEX Episode 1. Isobar interval is 2 mb. Grid resolution is 36 km.

PRESSURE=850. mb WIND UV (m/s } 1983-09-19\_00.00.00  
 PRESSURE=850. mb BARB UV (m/s } 1983-09-19\_00.00.00

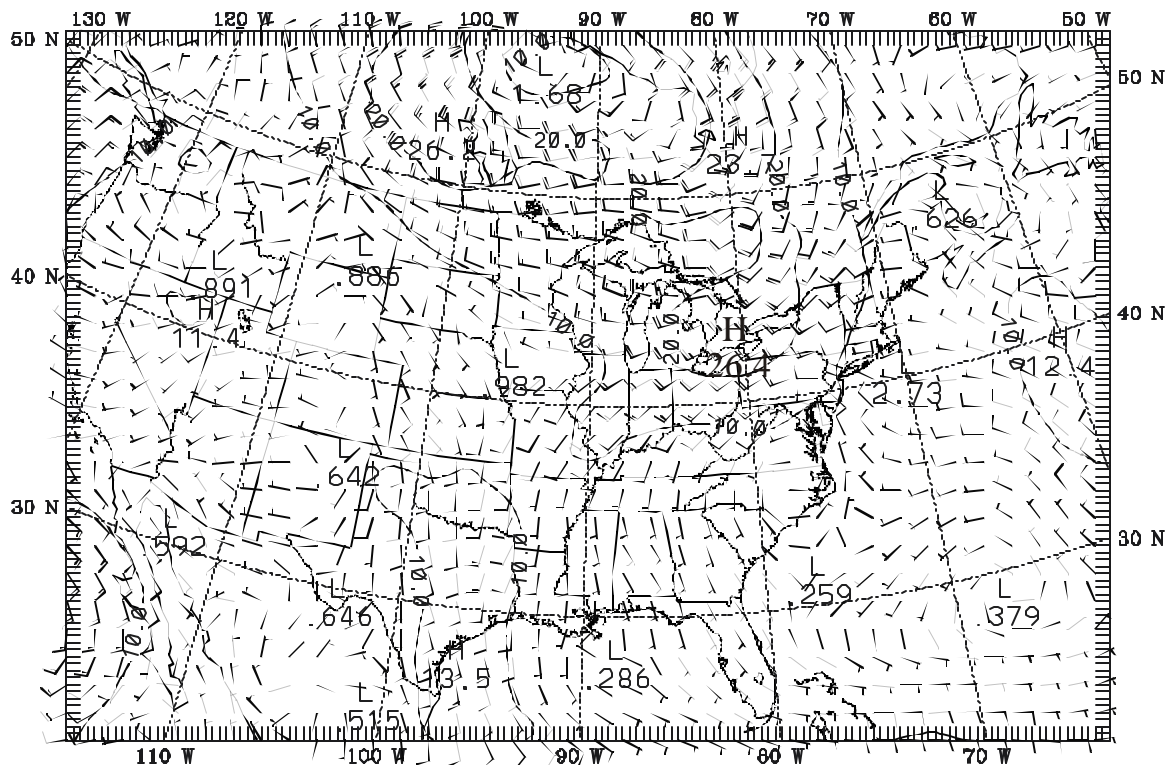
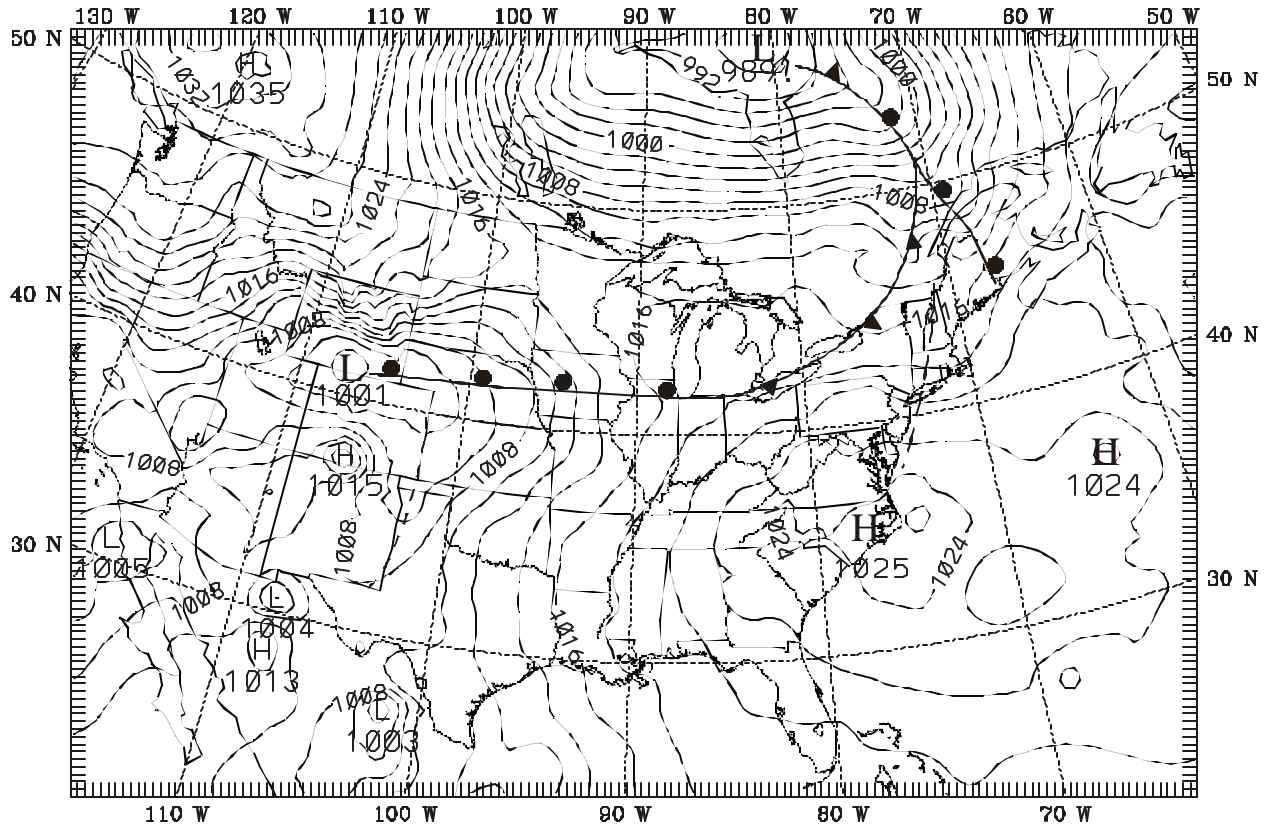


**Figure 4.** Objective analysis of 850-mb winds ( $\text{m s}^{-1}$ ) for 0000 UTC, 19 September 1983 during CAPTEX Episode 1. Isotach interval is  $10 \text{ m s}^{-1}$ . Grid resolution is 36 km.

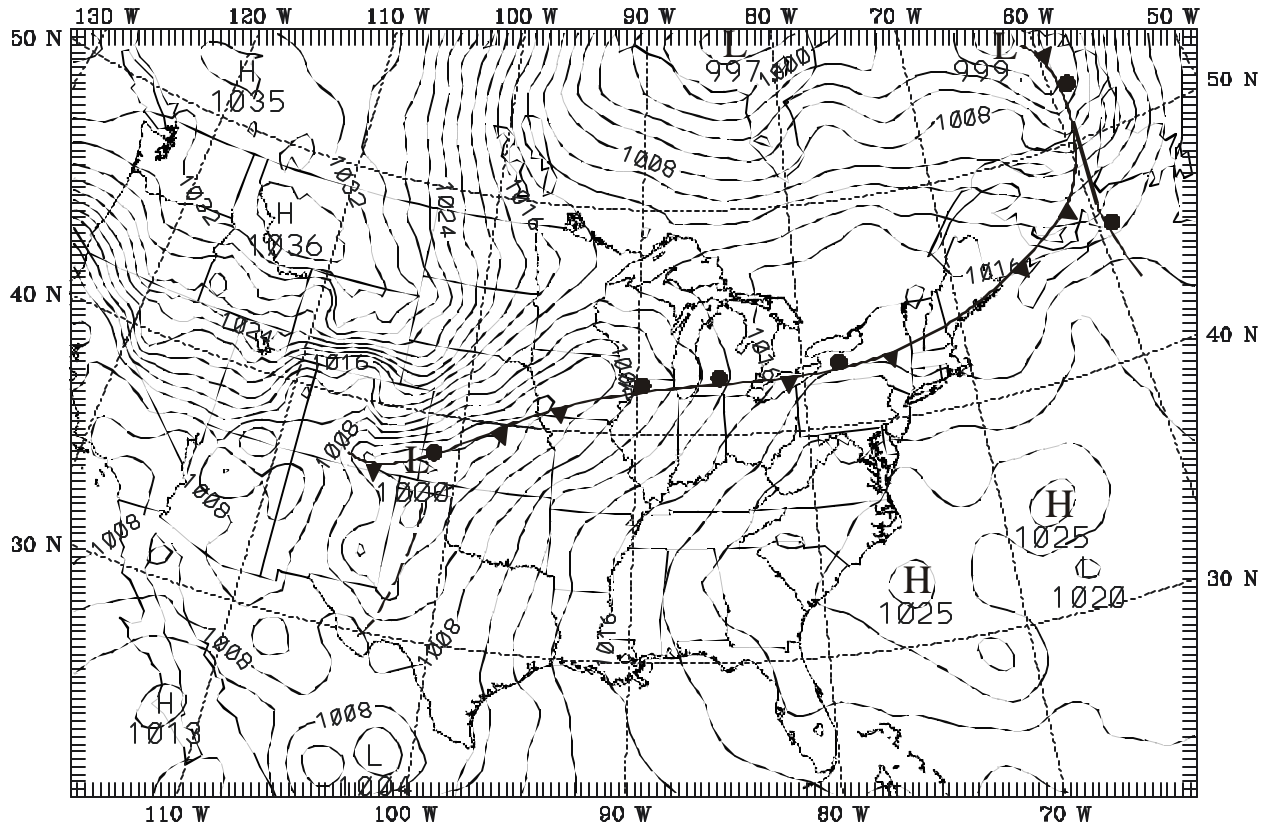
SIGMA -1.000 SEA PRES (mb) | 1983-09-19\_12.00.00



MM5V3-CAPTEX,EXP2=> MMINPUT  
CONTOUR FROM 998.00 TO 1034.0 CONTOUR INTERVAL OF 2.0000 PT(3,3)= 1010.7

**Figure 5. Objective analysis of sea-level pressure (mb) for 1200 UTC, 19 September 1983 during CAPTEX Episode 1. Isobar interval is 2 mb. Grid resolution is 36 km.**

SIGMA -1.000 SEA PRES (mb) | 1983-09-20\_00.00.00



MM5V3-CAPTEX,EXP2=> MMINPUT  
CNTOUR FRDM 996.00 TO 1034.0 CNTDLR INTERVAL OF 2.0000 PT(3,3)= 1011.2

**Figure 6.** Objective analysis of sea-level pressure (mb) for 0000 UTC, 20 September 1983 during CAPTEX Episode 1. Isobar interval is 2 mb. Grid resolution is 36 km.

another new baroclinic storm was gathering strength as a strong high-pressure system pushed southward from western Canada into the central Rocky Mountains. Notice from the position of the cold front in NY and New England in Figures 5 and 6 that, by the end of Episode 1, the front could easily impact the tracer plume released ~24 h earlier at Dayton in the southwesterly flow on the north side of the large East-Coast anticyclone.

Next, Figures 7-13 present a series of manual analyses of sea-level pressure over the Midwest and Northeast U.S. These analyses are shown at 6-h intervals from 1200 UTC, 18 September through 0000 UTC, 20 September 1983, during Episode 1. Mesoscale details become evident in these figures that are not resolved easily in the synoptic-scale objective analyses presented above. For example, the figures show bands of cloudiness and convective precipitation along the warm and cold fronts as they traverse the region. In Figure 7, at 1200 UTC on 18 September, there are many thunderstorms close to the warm front from southeastern WI to southern MI, with widespread showers throughout the rest of MI. The rain then shifts eastward with the advancing warm front, so that by 1800 UTC, the thunderstorms are mostly around Lake Ontario (Figure 8) before weakening at 0000 UTC, 19 September (Figure 9). Later during the evening, by 0600 UTC, thunderstorm activity again becomes widespread all along the frontal boundaries from northern IL to Montreal in southwestern Quebec (Figure 10). These reinvigorated storms were likely triggered by the ageostrophic wind circulations associated with the acceleration of the nocturnal LLJ just ahead of the cold front. Figure 11 shows that the convective storms persisted through the night, mostly along the cold front, but weakened toward morning, especially from Lake Erie to Montreal. As on the previous day, Figure 12 indicates that the frontal showers in the Northeast were weakest around early afternoon (1800 UTC).

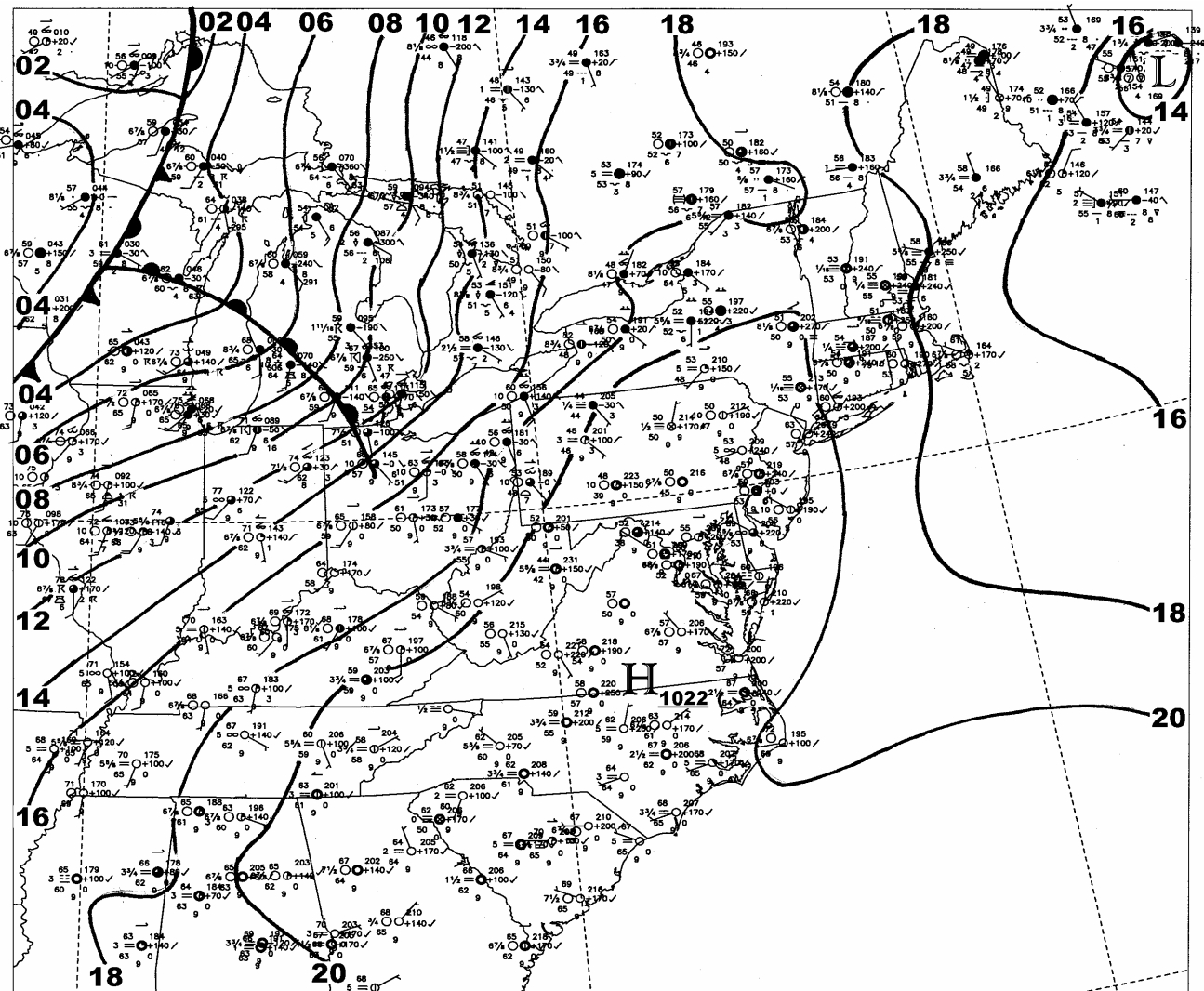


Figure 7. Manual analysis of sea-level pressure (mb) for 1200 UTC, 18 September 1983 during CAPTEX Episode 1 on the area of the 12-km domain (Configuration 2). Isobar interval is 2 mb. Winds are plotted in kts.

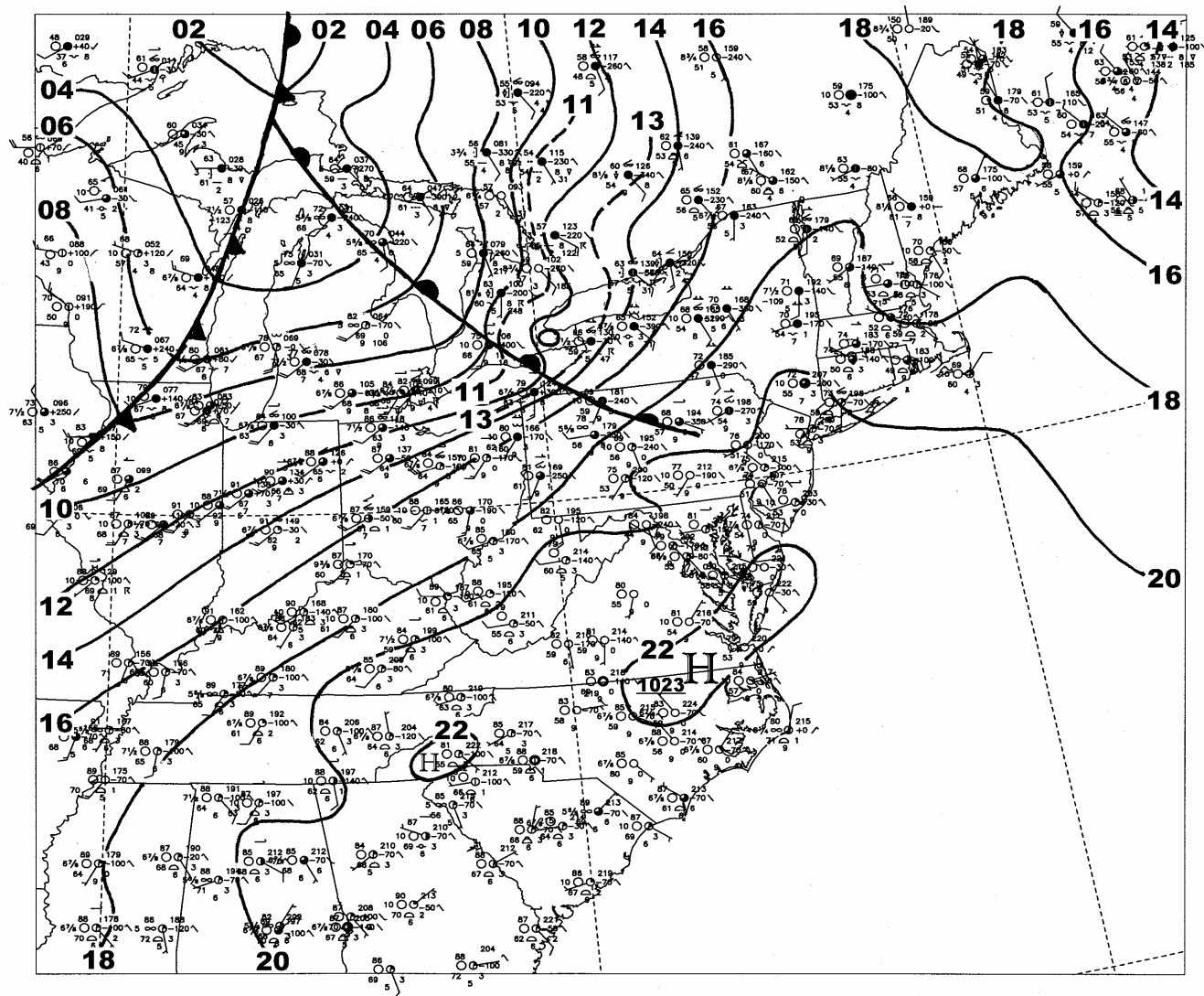


Figure 8. Manual analysis of sea-level pressure (mb) for 1800 UTC, 18 September 1983 during CAPTEX Episode 1 on the area of the 12-km domain (Configuration 2). Isobar interval is 2 mb. Winds are plotted in kts.

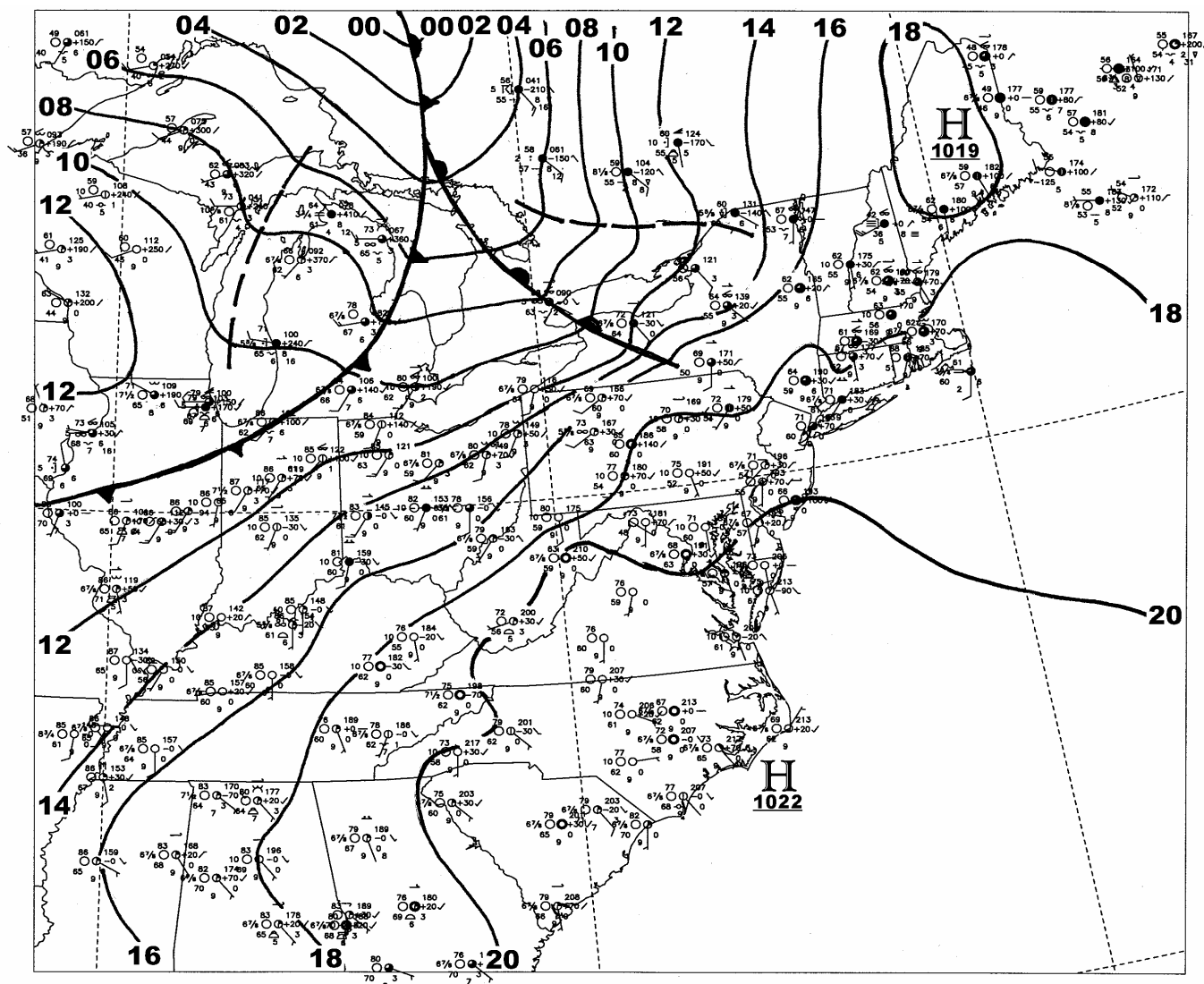


Figure 9. Manual analysis of sea-level pressure (mb) for 0000 UTC, 19 September 1983 during CAPTEX Episode 1 on the area of the 12-km domain (Configuration 2). Isobar interval is 2 mb. Winds are plotted in kts.

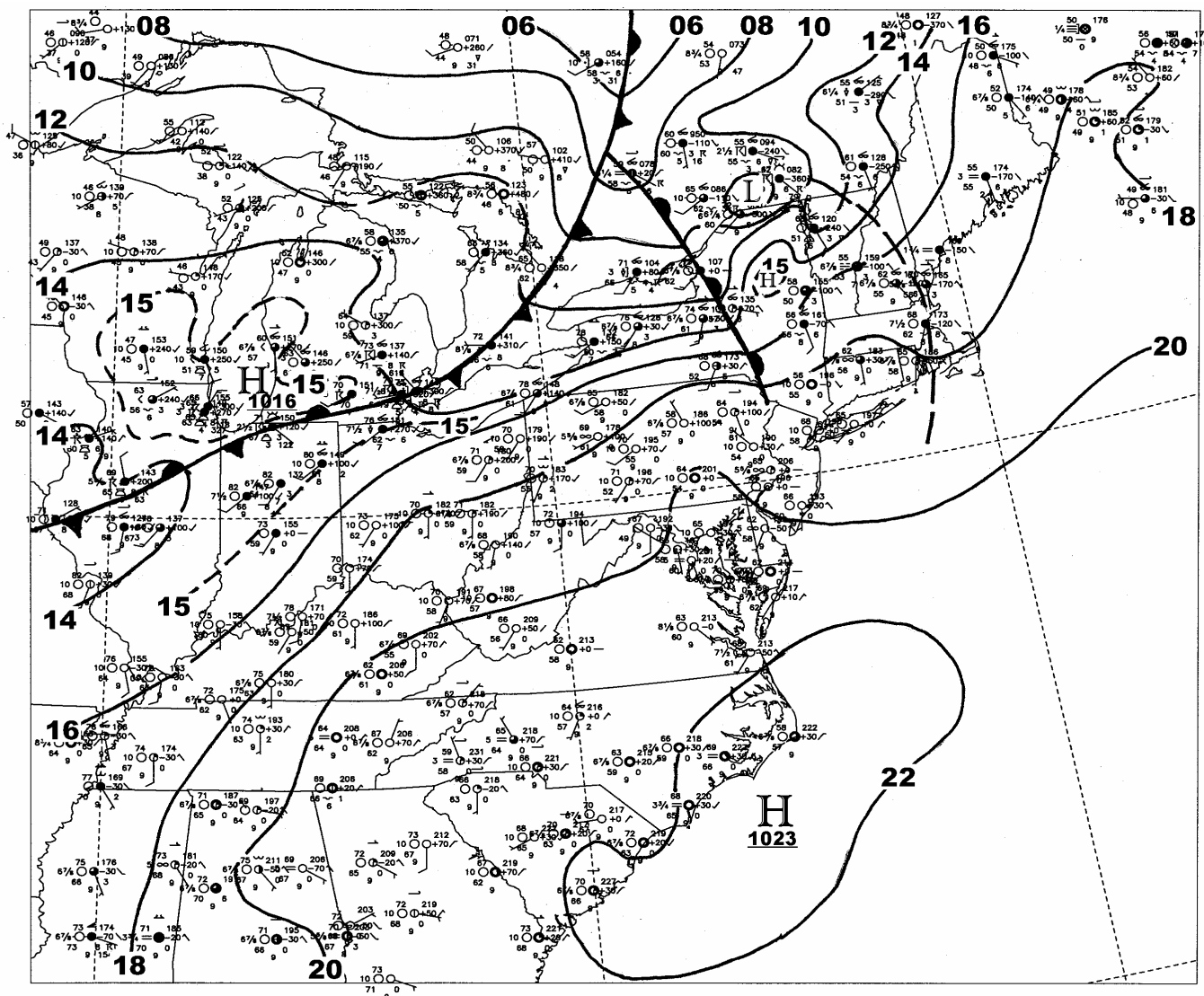


Figure 10. Manual analysis of sea-level pressure (mb) for 0600 UTC, 19 September 1983 during CAPTEX Episode 1 on the area of the 12-km domain (Configuration 2). Isobar interval is 2 mb. Winds are plotted in kts.

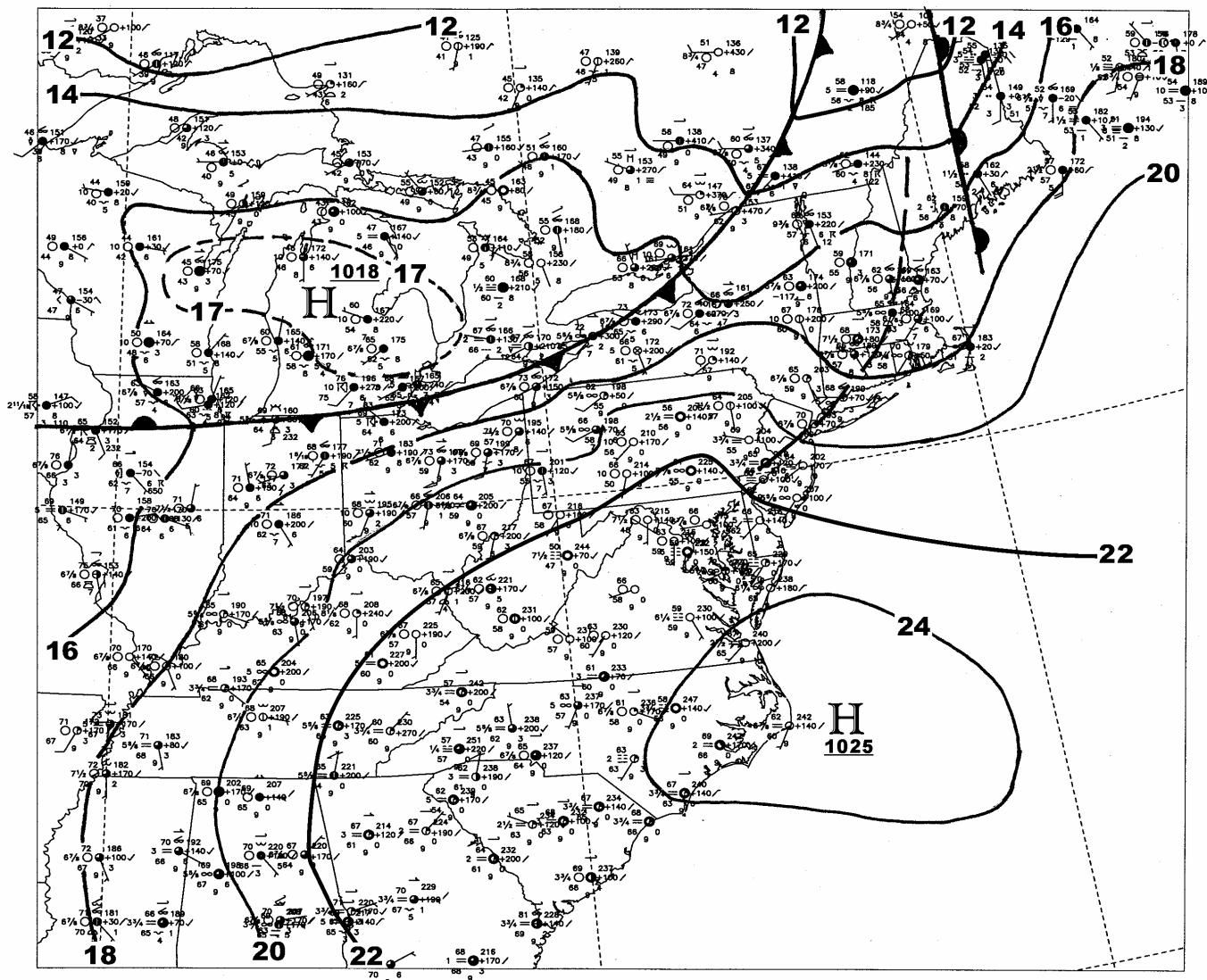


Figure 11. Manual analysis of sea-level pressure (mb) for 1200 UTC, 19 September 1983 during CAPTEX Episode 1 on the area of the 12-km domain (Configuration 2). Isobar interval is 2 mb. Winds are plotted in kts.

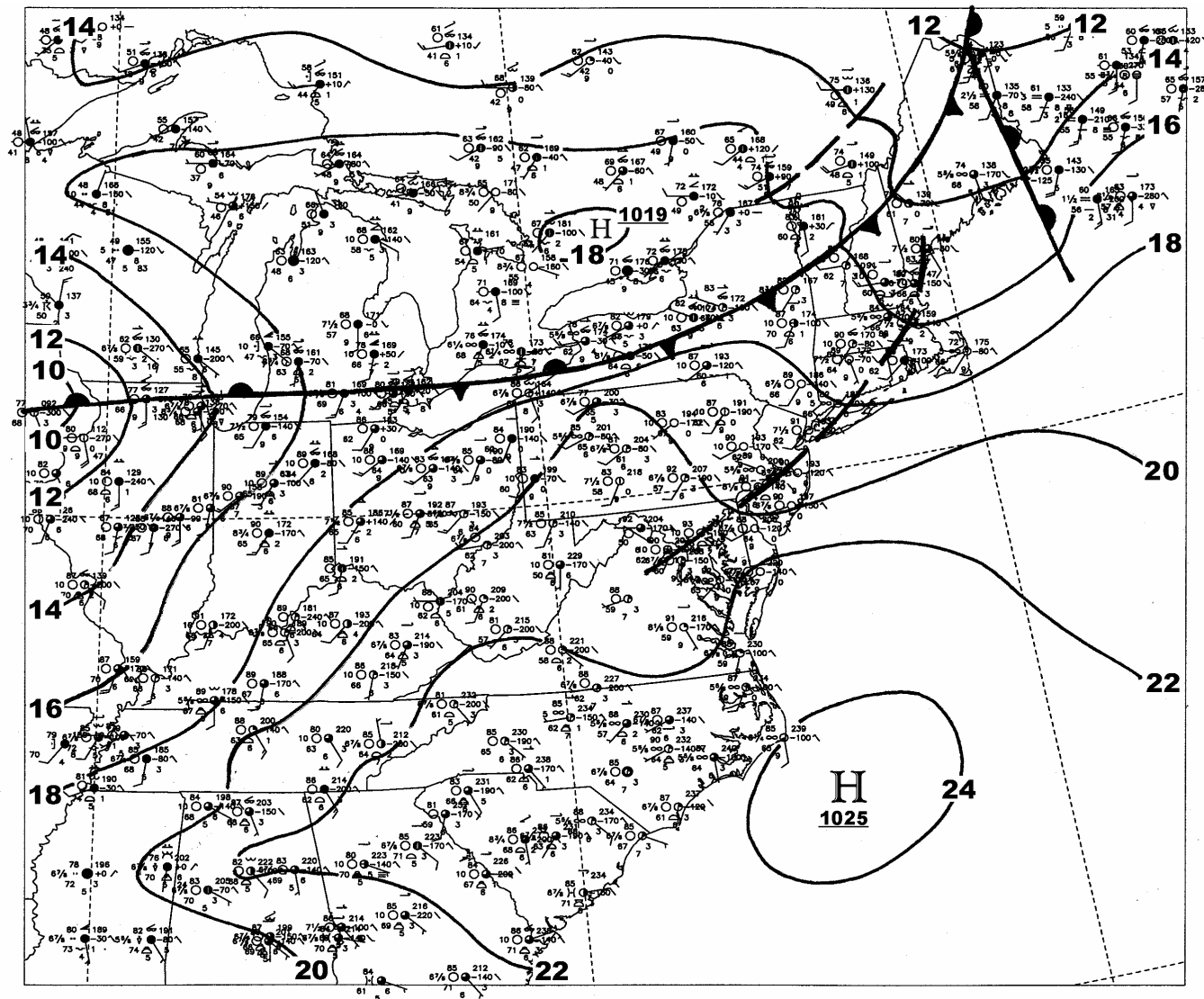


Figure 12. Manual analysis of sea-level pressure (mb) for 1800 UTC, 19 September 1983 during CAPTEX Episode 1 on the area of the 12-km domain (Configuration 2). Isobar interval is 2 mb. Winds are plotted in kts.

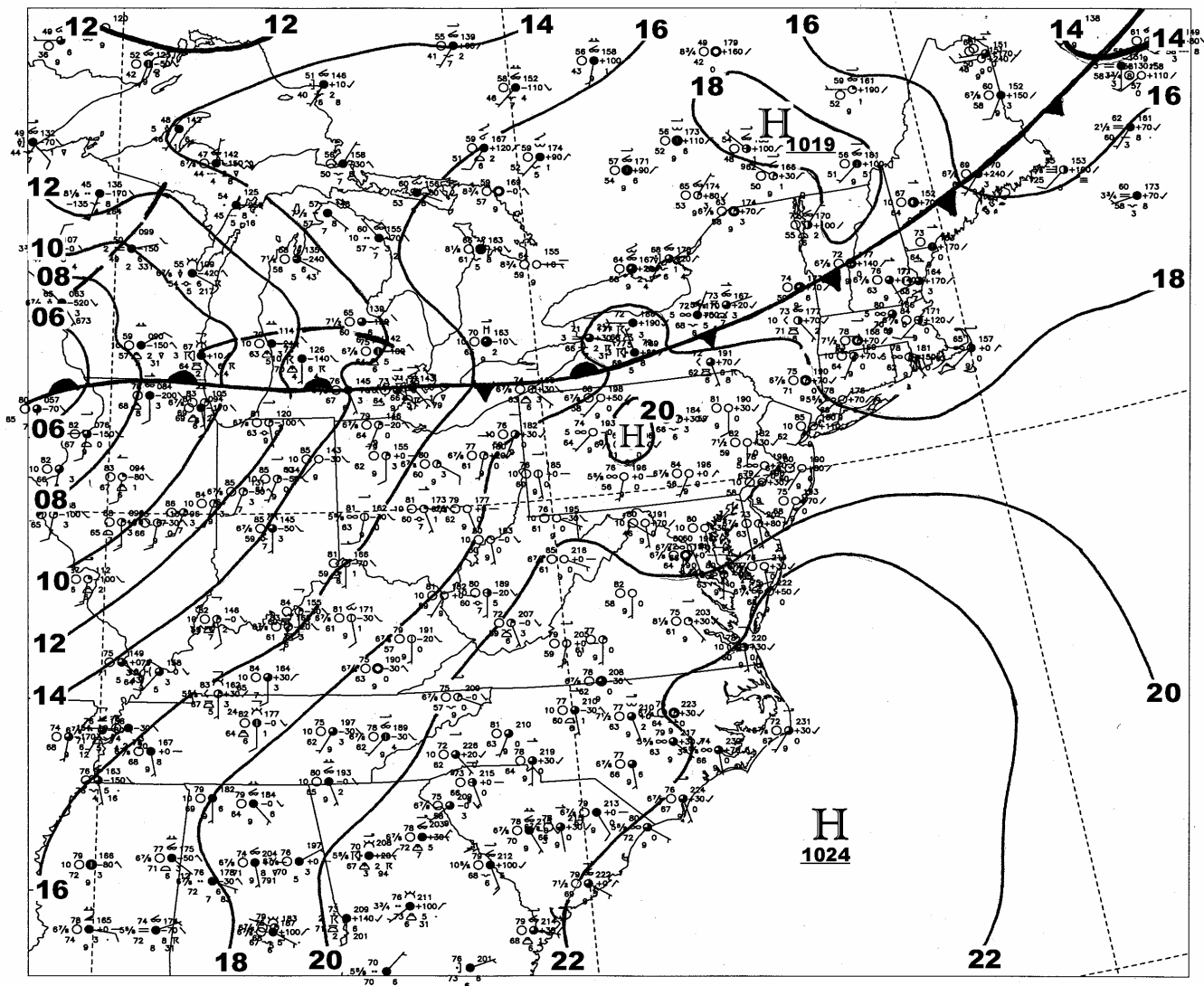


Figure 13. Manual analysis of sea-level pressure (mb) for 0000 UTC, 20 September 1983 during CAPTEX Episode 1 on the area of the 12-km domain (Configuration 2). Isobar interval is 2 mb. Winds are plotted in kts.

Even though the surface reports at this time failed to show frontal rain at the observing stations from Detroit to Maine (Figure 12), renewed thunderstorms and showers were evident once more by 0000 UTC, 20 September (Figure 13).

During many mid-summer episodes with poor air quality, convective outbreaks occur in synoptic environments that have relatively weak baroclinicity (i.e., weak dynamic forcing). In that type of situation, it is not unusual for an outbreak of thunderstorms to grow and consolidate into a mesoscale convective system. These fairly well organized thunderstorm clusters often generate mesoscale high- and low-pressure centers and outflow boundaries, accompanied by strong gusty winds. They can distort the synoptic wind pattern over hundreds of kilometers and can last for 6-18 h (sometimes longer). Thus, the mesoscale patterns analyzed in mid-summer cases can be quite distinct.

In the CAPTEX-83 study, however, Episode 1 differed from a mid-summer case in that it took place in the middle of September, when a relatively strong baroclinic frontal system was in the area. At this time of year, large high-pressure systems along the Mid-Atlantic coast (westward extensions of the quasi-permanent Bermuda High) can cause enhanced advection of warm moist air from the Gulf of Mexico to the northern states. A quick review of the pressure gradient and 850-mb winds in Figures 2-6 indicates that this scenario was the primary source of moisture for the convective rainfall that accompanied the fronts shown in Figures 7-13. Also, afternoon temperatures just south of the fronts reached into the mid-80s F (28-30 C) during Episode 1, so that conditions were ideal for thunderstorm development when the warm moist air was lifted over the frontal surfaces. At the same time, strong subsidence in the broad interior of the Bermuda High suppressed rain through most of the area covered by the anticyclone.

Due to the stronger dynamic forcing at this season, compared to mid-summer, the thunderstorms in this case did not generate intense long-lasting meso-highs and meso-lows. That is, the strong mid-level wind shear in this case tended to rip apart the thermal perturbations aloft (associated with the convective release of latent heat and the formation of cold downdrafts) that induce the surface pressure anomalies. Thus, although the mesoscale analyses for this case reveal some local distortions of the wind pattern due to the spreading of cold downdrafts, only a few weak short-lived surface pressure perturbations and trough features formed in the vicinity of thunderstorm clusters. Examples of these can be seen in Figure 8 near Toronto, and in Figure 10 near Montreal, but they do not persist to the next 6-h analyses.

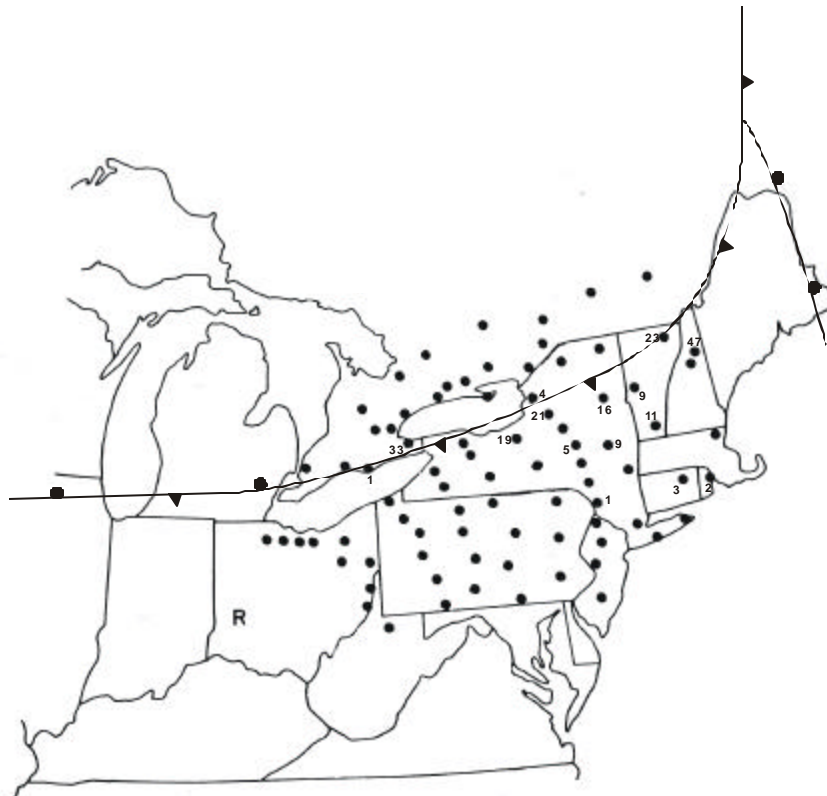
To complete the meteorological overview of the 18-19 September case, Figure 14 shows the 6-h average concentrations measured at the CAPTEX surface monitoring sites as the tracer plume was advected northeastward by the winds. Times shown in the figure represent the middle of the sampling periods. Frontal positions have been overlaid for reference. The time of the first panel (Figure 14a, 2200 UTC) is 3.5 h after the mid-point of the tracer-release period (1700-2000 UTC). Haagenson et al. (1987) present smoothed analyses for the time segments shown in Figure 14, but here we choose to show the actual measurements. Comparison between these measurements and the analyses of Haagenson et al. indicates that the latter contained considerable smoothing that could further complicate interpretation.

Consistent with the winds ahead of the advancing cold front, the initial transport of the tracer was northeastward from Dayton late on 18 September (Figure 14a). During this first afternoon period, skies were mostly sunny over OH (see Figure 8), so that strong vertical mixing should occur in the convective boundary layer of the warm sector, resulting in a plume depth on the order of a kilometer or so. Early on 19 September (nocturnal period), the high-speed west-





(c)



(d)

Figure 14. (Continued)

southwesterly flow over Lake Erie and Lake Ontario (see Figs. 3 and 4) steered the tracer plume toward the east-northeast with its leading edge in western NY by 0400 UTC (Figure 14b). Since the beginning of the tracer-release period was at 1700 UTC on 18 September, this represents a mean speed for the plume's leading edge *at the surface* of  $\sim 21\text{-}22\text{ ms}^{-1}$ . That speed is roughly consistent with the LLJ speeds observed at 850 mb ( $\sim 1500\text{ m MSL}$ ), but it is much faster than can be explained by surface advection alone. Thus, the plume movement detected during the evening hours at the surface must result from rapid advection aloft, coupled with downward mixing to the ground level by turbulence in the strong wind shear beneath the jet. The role of shear in generating the turbulence, rather than convective buoyancy, is probable because these events occur at night. The more westerly wind directions above the surface help to account for the turning of the plume's leading edge to the east-northeast, following the initial northeastward track observed during the first six hours (compare Figures 14a and 14b).

Moreover, it appears that the speeds in the nocturnal LLJ between 0000 UTC and 1200 UTC, 19 September, became faster than the rate at which the surface warm front was propagating northeastward. That means that the leading edge of the tracer plume could have been lifted over the frontal surface. Once above the front, the plume would lose contact with the ground because of the high stability typically found within a sloping frontal surface. This hypothesis is supported by Figure 14b, which shows that the leading edge of the surface plume had already reached the surface warm front not later than 0400 UTC, but no surface monitors ahead of the front reported tracer concentrations above the background level.

Finally, the advance of the front into northern NY around 1200 UTC, 19 September, suggests that pre-cold-frontal vertical circulations could have interacted with the tracer on the second day of the episode. Figures 14c and 14d indicate that the surface plume continued to race

eastward into northern New England during the pre-dawn hours and then began to exit the monitoring network between 1000 UTC and 1800 UTC, 19 September (or perhaps even before 1000 UTC, if the warm-frontal position is considered as a likely leading edge for the surface-plume "footprint"). Meanwhile, the cold front had reached the left (northern) flank of the surface plume by 1000 UTC, and thereafter appears to define the position of that flank, as clean Canadian air advances from the northwest. A hypothesis for the interaction with the cold front is that the warm-sector air containing the tracer is progressively lifted from the surface by the front as the cold air pushes southward. As in the case of the warm front, the frontal boundary above the surface should be thermally quite stable, even though the cold air beneath the front can be turbulent. Thus, the stable frontal zone could prevent the lifted left flank of the plume from re-establishing contact with the surface, despite solar heating on 19 September. The conclusion of this hypothesis is that, once the fronts begin interacting with the tracer plume, the extent of the plume aloft in this case may become very much different and more complex to understand than would otherwise be the case. The tracer measurements supplied by the surface monitors must be considered to give useful, but very incomplete information in this case. Unfortunately, the aircraft flights taken across the plume's path during Episode 1 were limited to western NY on the morning of 19 September shortly before the arrival of the cold front, so they provide little additional insight into the complex structure of the plume.

Another mechanism that also could affect the surface concentrations observed by the CAPTEX monitoring network, but which has not been mentioned, is the possible role of vertical transport of the tracer due to convective motions associated with clouds and precipitation. Because the tracer material is highly insoluble, the clouds and showers associated with the front should not be an effective removal mechanism through wet deposition to the surface. However,

vertical motions in sub-grid scale convective clouds could transport a significant quantity of tracer from the boundary layer into the middle or upper troposphere. The result would be a greater decrease of concentrations in the boundary layer than could be explained solely due to resolved-scale advection and turbulent mixing.

### 3. MODEL DESCRIPTIONS

The conditions on 18-19 September provide an interesting and complex case for studying mesoscale inter-regional transport and diffusion in a meteorological model. To be able to capture the transport and diffusion correctly, a model must simulate realistically the PBL mixing, the low-level jet transport, and the resolved-scale vertical circulations associated with the frontal system. Clearly, the broad features of the anticyclone itself exist on the synoptic scale. The frontal band and the pre-front LLJ dynamics, however, are mesoscale features. Thus, *model resolution* can be expected to play an important role. Moreover, the precipitation associated with the cold front occurred mostly in the form of convective showers, so the model's treatment of sub-grid *parameterized moist convection* is also of interest.

Furthermore, as implied above, it is expected that turbulence generation in this case can be related to several processes. First, surface sensible and latent heat fluxes due to solar radiation should lead to buoyant production of turbulent energy and growth of the PBL, especially in the sunny regions ahead of the frontal cloud bands. Second, the low-level jet should lead to strong vertical shear in the warm sector between the jet and the surface. Therefore considerable shear-induced production of turbulent energy may exist with the LLJ along a mesoscale band just ahead of the cold front. Since the LLJ should accelerate to its maximum speed during the night when the daytime convectively unstable boundary layer has collapsed, due to frictional decoupling of the jet layer from the surface (Blackadar 1957), the shear production of turbulence may be maximized at night, as well. Third, the rapid advection of cold air aloft over a warmer surface behind the front can lead to destabilization in the lower levels of the atmosphere, which in turn can trigger additional buoyant production of turbulent energy,

even at night. Thus, improvement of the *model physics for representing turbulence processes and the PBL* also could have important effects on the accuracy of the transport and diffusion calculations in the model.

Finally, we note that the speed of eastward propagation of the baroclinic storm and its accompanying frontal systems predicted by the numerical model could be in error. It is not uncommon for such models to exhibit a slow bias (an error in the phase speed) for these features due to the numerics of finite differencing methods. The phase speed errors generally become greater as the mesh size increases. Thus, FDDA could be important for correcting possible model phase-speed errors.

Each of the atmospheric features and processes discussed in Section 2.2 can be evaluated directly by comparing the meteorological model outputs to observations and by calculating statistical skill scores for the primary simulated variables. However, the impact of the model solutions on the net transport and diffusion may remain unclear because dispersion is an integrated result of 3-D motions acting through those various features at different scales and over many hours. Therefore, it is useful to make additional evaluations by examining the model's 3-D net transport using a parcel trajectory model driven by the MM5's wind field. Lastly, the combined effects of the model's advection and mixing processes on atmospheric trace-constituent concentrations can be estimated by feeding the meteorological solutions into a plume dispersion model and by comparing the simulated concentrations with those observed in the CAPTEX-83 experiment. The models necessary to carry out these comparisons will be discussed below.

## 3.1 The Penn State/NCAR MM5 Meteorological Model

### 3.1.1 Basic Structure

The meteorological model used in this study is the non-hydrostatic version of the Pennsylvania State University/National Center for Atmospheric Research (PSU/NCAR) mesoscale model, known as MM5. The MM5 is a 3-D nested-grid, primitive-equation model with a terrain-following  $\sigma$  (non-dimensionalized pressure) vertical coordinate, given by

$$\sigma = \frac{p - p_t}{p_s - p_t} \quad (1)$$

where,  $p$  is the pressure,  $p_s$  is the surface pressure, and  $p_t$  is the pressure at the top of the model. All the sigma layers are defined using a time-invariant "background" pressure field, based on a standard atmospheric lapse rate, while a much smaller prognostic pressure perturbation field ( $p' = p'(x, y, \sigma, t)$ ) represents the 3-D departure from the background. The MM5 also contains prognostic equations for the three wind components ( $u, v, w$ ), temperature ( $T$ ) and water-vapor mixing ratio ( $q_v$ ), each of which are written in the flux form. The model uses a split semi-implicit temporal integration scheme to increase computational efficiency. The MM5 is flexible enough to be applied to a wide range of synoptic and mesoscale phenomena, including baroclinic storm development, tropical cyclones, and the role of physical processes, such as convection and planetary boundary layer (PBL) influences. For a more complete description of the MM5 formalism, see Dudhia (1993) and Grell et al. (1994).

The horizontal grid system of the MM5 domains is based on the staggered Arakawa-B grid described by Arakawa and Lamb (1977). In this grid configuration, the wind components,  $u$  and  $v$ , are defined on the so-called "dot points" at the corners of a grid box, while all the other variables are defined on the "cross points" at the center of the boxes. The vertical structure of the model's grid is such that vertical motion,  $w$ , and the  $TKE$  are defined on the full sigma-layer boundaries, while the other variables ( $u$ ,  $v$ ,  $T$ , and  $q_v$ ) are defined on the half levels (middle of the layers) (also see Grell et al. 1994).

### ***3.1.2 Physics***

For this study three separate grid configurations were used (see Section 4). The experimental design and the various grid resolutions in these configurations required the use of different physics options. In this sub-section, the particular physics choices selected for these experiments are identified and their principal characteristics are described briefly.

Taken together, the three grid configurations described in Section 4 encompass five domains having horizontal resolutions of 108, 70, 36, 12, and 4 km. On all of these domains, resolved-scale moist processes were represented using explicit prognostic equations for cloud water or ice ( $q_c$ ) and rain water or snow ( $q_r$ ) according to a formulation described by Dudhia (1989). No mixed-phase moist processes (ice and water existing simultaneously in a grid cell) were included in the experiments run for this study. On all but the finest domain (i.e., all except the 4-km grid), deep convection cannot be resolved explicitly, but was handled separately through a sub-grid parameterization. Two different convective parameterization schemes (CPSs) were used in this study, depending on the design of the individual experiments: (1) the Anthes-

Kuo scheme (Kuo 1965, 1974; Anthes 1977), and (2) the Kain-Fritsch scheme (Fritsch and Chappell 1980, Kain and Fritsch 1990). The Anthes-Kuo deep-convection scheme is most appropriate for grid sizes greater than  $\sim 30$  km (Wang and Seaman 1997) and has a trigger function that depends on the vertically integrated moisture convergence in a grid column. Convection is initiated when the moisture convergence exceeds a prescribed critical threshold value. On the other hand, the Kain-Fritsch scheme is generally more accurate for grid sizes on the order of 10-40 km. It has a fully entraining/detraining cloud model and uses an energy-equilibrium closure. First, the potential for convective clouds is diagnosed by lifting low-level parcels to their saturation levels. Then, a convection-forming parcel is initiated from the saturated parcel below 700 mb having the highest  $q_e$  (equivalent potential temperature). Rain is triggered when the cloud exceeds a critical depth (3-4 km). Once convection is initiated in a grid column, it continues until all convective available potential energy (CAPE) has been eliminated.

No convective parameterization is needed on the 4-km domain because it is assumed to be fine enough to resolve explicitly the main aspects of the convection (Weisman et al. 1997). This is equivalent to saying that the deep convective updrafts are about the same size or larger than the grid. However, for a 4-km mesh, this assumption may not be true universally, which can lead to some distortions in the propagation speed and vertical structure of the convective precipitation. When there is an external mechanism controlling the propagation of the convection, such as the frontal system in the 18-19 September case, the explicit representation of all precipitation should be reasonably accurate on this fine grid.

Two kinds of PBL parameterizations are used for this study, depending on the individual experiment design (also see Section 4). The Blackadar PBL parameterization (Zhang and Anthes 1982) uses a non-local closure for convectively unstable boundary layers and a local K-theory

closure for all other conditions. The Blackadar scheme has been in use for nearly 25 years. It can be reasonably accurate in many cases, but has a tendency to mix a convectively unstable boundary layer too thoroughly and it often underestimates turbulent mixing in shear-driven or cloudy situations. The other turbulence scheme used in the study is a 1.5-order closure approach developed by Gayno et al. (1994) and described by Shafran et al. (2000). The scheme of Shafran et al. has a 2<sup>nd</sup>-order predictive equation for turbulent kinetic energy (TKE), while the eddy viscosity is a function of the predicted TKE and several stability-dependent mixing lengths. Turbulent fluxes of momentum, moisture and virtual potential temperature ( $q_v$ ) are parameterized using K-theory in which the turbulent transfer occurs down gradient. However, since basic K-theory fails under certain convective situations (Moeng and Wyngaard, 1989), countergradient flux terms are included to correct the turbulent transport terms near the surface and near the top of the convective mixed layer (Gayno et al. 1994). The TKE-predicting scheme is representative of newer higher-order PBL physics and has been shown to generate both shear-driven turbulence and in-cloud mixing associated with cloud-top radiative flux divergence (Stauffer and Seaman 1999). It has also been shown to predict more accurate boundary-layer structure for convectively unstable conditions, compared to the Blackadar scheme (Shafran et al. 2000). In addition, Stauffer et al. (1999) added the capability to account for the effects of saturation on the buoyancy production of TKE, which makes this 1.5-order scheme more accurate in cloudy or foggy conditions than the other turbulence parameterizations available in MM5.

In addition, the atmospheric and surface temperature tendencies due to short-wave and long-wave radiation flux divergences are calculated with a column radiation parameterization

(Dudhia 1989). The Dudhia radiation scheme is based on a two-stream, single-band approach. It is fully interactive with dry air, water vapor and cloud liquid/ice.

### ***3.1.3 Four Dimensional Data Assimilation***

Four-dimensional data assimilation (FDDA) is a process in which observations are used to correct for numerical forecast errors in a model simulation, instead of using data only at the initial time. It has been shown to reduce error accumulation during the assimilation period (e.g., Seaman et al. 1995, Michelson and Seaman 2000). The FDDA approach used in this study is based on a "nudging" or Newtonian relaxation method developed by Stauffer and Seaman (1990, 1994). In this method, the model state is relaxed continuously at each time step toward the observed state by adding to the prognostic equations an artificial tendency term, which is based on the difference between the two states. The assimilation can be accomplished by nudging the model solutions towards gridded analyses based on observations (analysis nudging) or directly toward the individual observations (obs-nudging). In the present study, only analysis nudging is used.

The *analysis-nudging* term for a given variable is proportional to the difference between the model state and the observed analysis at each grid point. The general form of the FDDA term for the non-hydrostatic version of the MM5 predictive equations in flux form for any prognostic variable  $\tilde{\mathbf{a}}(x, t)$  is given by the last term in the following tendency equation:

$$\frac{\partial p^* \mathbf{a}}{\partial t} = F(\mathbf{a}, \tilde{x}, t) + G_a \cdot W_a(\tilde{x}, t) \cdot \mathbf{e}_a \cdot p^* \cdot (\hat{\mathbf{a}}_0 - \mathbf{a}) \quad (2)$$

where  $p^*$  is defined as

$$p^* = p_s - p_t \quad (3)$$

and where  $p_s$  is the surface pressure and  $p_t$  is the pressure at the top of the model's reference state. The function  $F$  represents the model's physical and dynamical forcing terms, such as advection, friction or Coriolis force. The term  $G_a$  is the nudging factor and  $W_a(\tilde{x}, t)$  is the four-dimensional weighting function that specifies the horizontal, vertical and temporal weighting applied to the analysis. Typical values for  $G_a$  are between  $10^{-4} \text{ s}^{-1}$  to  $10^{-3} \text{ s}^{-1}$  (Stauffer and Seaman 1990). The analysis confidence factor,  $\mathbf{e}_a$ , ranges between 0 and 1, and depends on both the quality of the observations and the spatial distribution of the observations that are used to create the analysis. The analyzed (observed) field at each grid point is represented by  $\hat{\mathbf{a}}_0$ .

### 3.2 The ARAP/Titan SCIPUFF Dispersion Model

The SCIPUFF (Second-order Closure Integrated Puff) model is an advanced Gaussian-puff model developed at ARAP/Titan Corporation (Sykes et al. 1996, Sykes et al. 1998). The dispersion model is based on a collection of 3-D Lagrangian "puffs" emitted from one or more sources, each having Gaussian concentrations that change over time as the puffs undergo

transport and diffusion. SCIPUFF uses second-order closure turbulence techniques to relate measurable velocity statistics to the predicted dispersion rates. Together, these puffs describe the evolution of the three-dimensional concentration field over a range of spatial scales downwind of the source location. An important aspect of SCIPUFF is that the closure model provides a direct prediction of the statistical variance in the concentration field, so that the inherent uncertainty in the turbulent wind field can be used to estimate the uncertainty in the predicted plume dispersion.

SCIPUFF can make use of inhomogeneous velocity fields, such as produced through objective analysis or numerical predictions, by including a complete moment-tensor description for shear distortions and turbulent transport. The Lagrangian framework of SCIPUFF avoids the artificial diffusion problems that are associated with dispersion calculations performed on an Eulerian grid. The individual puffs increase in size due to shear distortions and turbulent dispersion and may grow in scale from a few meters to thousands of kilometers across. The puff method is very robust under coarse-resolution conditions (Sykes et al. 1998), but as a puff grows, local conditions at its centroid may no longer be representative of the entire puff. Therefore, SCIPUFF uses a splitting algorithm to divide the original puff into two smaller puffs whenever the puff size exceeds a critical value that depends on the resolution of the velocity field. By maintaining smaller puffs as the plume broadens with time, the dispersion model minimizes errors by avoiding highly inhomogeneous large puffs. On the other hand, over time the splitting algorithm could produce a very large number of puffs that would eventually cripple model efficiency. To prevent this, a merging algorithm combines overlapping puffs using a mass-conserving adaptive multi-grid approach. The efficiency of SCIPUFF also is aided by an adaptive time-stepping scheme that depends on the turbulence time scale, advection velocity,

shear distortion rates and other physical processes. Each puff determines its own time step, that lengthens as the puff becomes larger and the relevant time scales grow.

While it is possible to uniquely describe the statistical mean value of concentrations in a turbulent environment (i.e., deterministic solutions for the means), the randomness within the turbulent fields produces uncertainty in the instantaneous solutions for dispersion problems. SCIPUFF also provides a quantitative value of the random variations in the concentrations due to the stochastic nature of the turbulent diffusion process (Sykes et al. 1998). The key aspect of the fluctuation variance prediction is the dissipation time-scale based on the internal fluctuation scale (Sykes et al. 1984, 1996). The variance prediction provides a quantitative probability distribution for the local concentration using the assumption of a clipped normal shape function (Lewellen and Sykes 1986). This probabilistic description of concentrations is the only meaningful way to describe and quantify the uncertainties in the field due to the randomness of the turbulence.

The mesoscale and synoptic-scale meteorological inputs to SCIPUFF (primarily winds and temperatures) can be specified as 3-D gridded fields, or the dispersion model can analyze these fields from a set of surface and upper-air data using an interpolation based on inverse-square distance weighting. The dispersion model also can accommodate irregular topography with a terrain-following vertical coordinate, similar to the MM5. Boundary-layer turbulence profiles can be specified directly, as from LES, but are usually diagnosed based on estimates of the surface heat flux and the shear stress, much like the turbulence source terms in the predictive equation for TKE used by Shafran et al. (2000). Source material can be introduced into the meteorological environment three ways: (a) as an instantaneous release, (b) as a steady plume over a specified time period, or (c) as a moving source. Thus, SCIPUFF can easily represent

conditions encountered in a variety of cases, such as an explosion, a stack plume, or a moving ship plume.

### **3.3 The Penn State TRAJEC Trajectory Model**

The Penn State TRAJEC program is designed to calculate the trajectories of one or more particles (or, parcels) based on a set of gridded 3-D wind data ( $u$ ,  $v$  and  $w$ ) distributed in space and time. TRAJEC operates with wind fields supplied by the MM5 mesoscale model (or analyses on a MM5-compatible grid) at uniform time intervals of, say, 1 hour. Both forward and backward trajectories can be calculated. If vertical velocities are not available, TRAJEC can move parcels along surfaces at a constant height above the ground, or quasi-horizontally along constant-pressure or constant-potential temperature surfaces. In any case, the movement of particles is diagnosed through a series of small time steps using a two-step iterative process based on a user-specified time step of perhaps five minutes. The two-step iterative approach is designed to reduce transport error that can occur in curved flow when the wind at the beginning of a time step is assumed to apply throughout the interval. By using the iterative approach the trajectory calculations remain quite accurate, even without reducing the time step to very short intervals.

Parcels can be defined three ways: (a) individually, (b) as a series of particles released at specified time intervals from a given point (simulating continuous point emissions), or (c) as a cloud of regularly spaced points over a specified sub-region of the domain. Particles are

deactivated if they leave the domain through the lateral boundaries, but no deposition is allowed to the surface. TRAJEC includes a simple plotting package that shows the motion of the parcels in either the X-Y plane or the S-Z plane (where S is the horizontal distance downwind from the release point, following the flow).

TRAJEC provides a useful complement to a plume dispersion model, such as SCIPUFF, because it isolates the role of transport while ignoring diffusion. Thus, by using both TRAJEC and SCIPUFF, it is possible to investigate more thoroughly how important organized mesoscale circulations are to the dispersion of a plume over many hours. For example, in the case of inter-regional transport over 24 - 48 h, a plume may undergo shearing from multiple mesoscale features in succession (sea-breezes, troughs, LLJs, fronts, etc.). In this hypothetical case it can be difficult to isolate the role of the individual processes when using a dispersion model because diffusion of the plume eventually broadens it so much that its response to a particular mesoscale feature can be indistinct. However, a particle trajectory based only on the 3-D resolved-scale wind field can be used to identify the role of local changes in the transport speed or direction that occur along specific boundaries in the atmosphere. This aids in the interpretation of the overall dispersion represented in a plume model such as SCIPUFF.

## 4. EXPERIMENT DESIGN

### 4.1 MM5 Model Domains

For this study three different grid configurations were selected. In the first, a single (unnested) domain was defined with a horizontal resolution of 70 km. In the second, three nested-grid domains were chosen, with resolutions of 108, 36, and 12 km. The third configuration also used 108, 36, and 12 km domains, but added an inner domain having 4-km resolution.

#### *4.1.1 Configuration 1: Unnested 70-km Domain*

Configuration 1 was designed to approximate a typical model domain used for inter-regional transport studies during the mid-1980s (e.g., Haagenson et al. 1987). The purpose of this configuration in the present study was to establish a benchmark level of performance for the MM5 model against which changes introduced over the past 15 years could be evaluated for their impact on model skill. Configuration 1 uses a single unnested domain of 70-km horizontal resolution, shown in Figure 15, which has 55 X 69 grid points. The terrain on this mesoalpha scale domain is shown in Figure 16. A comparable land-use array (not shown) was generated at the same resolution, based on the 13-category land-use database described by Grell et al. (1994). Physical parameters at the lower boundary are assigned to each land-use category using a look-up table. These parameters include albedo, moisture availability, emissivity, roughness length and thermal inertia (see Grell et al, 1994 for more details).

Although the size of the 70-km domain easily covers the entire region of interest for the CAPTEX study, a glance at the terrain field in Figure 16 reveals that very few details of the individual mountain ranges in the northern Appalachian region can be resolved by this grid. For example, there is no distinction between the Adirondack Mountains of northern NY and the Green and White Mountains of VT and NH. The highest model terrain shown in this area is only 510 m, while the actual highest peaks in these three regional mountain ranges are about 1600, 1300 and 1900 m, respectively.

To be consistent with typical model designs used in the mid-1980s, Configuration 1 used 15 layers in the vertical direction (see Table 1). Seven of the model layers lie below 850 mb. The surface layer has a thickness of about 36 m, while the model top is placed at 100 mb for the experiment based on Configuration 1 (also see Section 4.3).

**Table 1. Vertical distribution of  $\sigma$  levels (half layers) and model-layer heights (m above ground level, AGL) for Configuration 1.**

Layer	$\sigma$	Height (m)
15	0.995	36.0
14	0.980	143.7
13	0.955	325.9
12	0.925	540.0
11	0.895	777.5
10	0.865	1011.5
9	0.828	1308.2
8	0.778	1724.5
7	0.709	2330.8
6	0.612	3256.0
5	0.500	4455.5
4	0.389	5828.1
3	0.278	7460.2
2	0.167	9492.9
1	0.056	12242.4

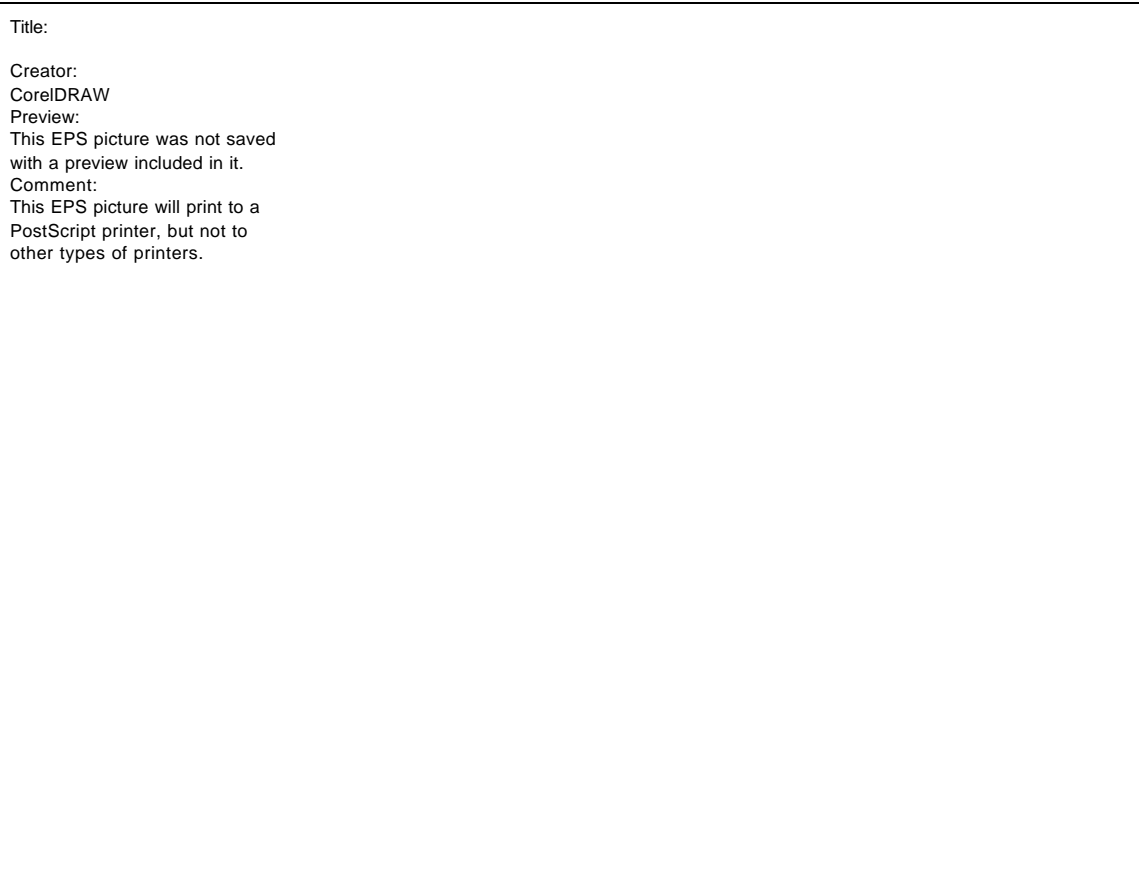


**Figure 15. Location of 70-km domain for MM5 Configuration 1.**

Title:

Creator:

CorelDRAW

Preview:

This EPS picture was not saved  
with a preview included in it.

Comment:

This EPS picture will print to a  
PostScript printer, but not to  
other types of printers.

**Figure 16. Terrain (m) for 70-km domain of MM5 Configuration 1. Contour interval is 100 m.**

### ***4.1.2 Configuration 2: Triply Nested Domains***

In contrast to the mid-1980's domain described in Section 4.1.1, Configuration 2 uses a set of three nested domains, as shown in Figure 17. The purpose of Configuration 2 is to represent the approximate resolution of regional-scale domains used in mesoscale atmospheric models during the late 1990s. Note that, although grid resolutions on the order of 4 km became common during that decade, they were generally sub-regional in scale (usually a few hundred kilometers on each side) and generally failed to cover an area similar to that of the CAPTEX study. The coarsest domain in Configuration 2 has a resolution of 108 km and covers most of the North America with a mesh of 55 X 69 points. The middle domain covers the continental United States (CONUS), southern Canada and northern Mexico at 36-km resolution with a mesh of 104 X 151 points. Finally, the innermost regional domain in Figure 17 has a resolution of 12 km and covers the eastern U.S. and parts of southeastern Canada with a mesh of 163 X 181 points. The 12-km domain is designed to represent comfortably the inter-regional transport from the Midwest to the Northeast U.S. that was encountered during CAPTEX-83 Episode 1.

The terrain field for the 12-km inner domain of Configuration 2 is shown in Figure 18. Notice that this field represents far more of the details in the Appalachian Mountains than was possible with the 70-km grid mesh used in Configuration 1 (compare to Figure 16). For example, the individual ranges in the northern part of the Appalachians emerge at this resolution, with maximum heights of the Adirondack, Green, and White Mountains represented at 764, 610, and 755 m, respectively. While these remain well below the actual height of the highest individual peaks, it represents a considerable improvement over the single maximum of 510 m found in this region in Figure 16. Also, note that additional local mountain ranges begin to emerge, such as the Catskill Mountains of southern NY, the Allegheny Mountains of western PA



Title:

Creator:

CorelDRAW

Preview:

This EPS picture was not saved  
with a preview included in it.

Comment:

This EPS picture will print to a  
PostScript printer, but not to  
other types of printers.

**Figure 17. Location of 108-km, 36-km, and 12-km nested domains for MM5 Configuration 2.**

Title:

Creator:

CorelDRAW

Preview:

This EPS picture was not saved  
with a preview included in it.

Comment:

This EPS picture will print to a  
PostScript printer, but not to  
other types of printers.

**Figure 18. Terrain (m) for 12-km inner domain of MM5 Configuration 2. Contour interval is 100 m.**

and the Laurentian Highlands of Quebec. As reported for Configuration 1, land-use arrays were generated for each of the three domains in Configuration 2. Consistent with the greater horizontal resolution, all three of the domains had 32 layers in the vertical direction for Configuration 2 (Table 2). The lowest layer is located at ~29 m above ground level (AGL). The thickness of the layers increases gradually with height, with 16 layers below 850 m (~1560 m AGL). Again, the top of the model was set at 100 mb.

#### ***4.1.3 Configuration 3: Quadruply Nested Domains***

Finally, Configuration 3 uses a set of four nested domains (Figure 19). The purpose of Configuration 3 is to explore the potential for future improvements in the modeling of inter-regional transport of atmospheric pollutants that will undoubtedly become possible quite soon as computational resources continue to become less expensive. In Configuration 3, the 108, 36, and 12 km meshes of Configuration 2 are retained, while a new 4-km domain is embedded over the Northeast U.S. Inspection of Figure 19 indicates that the area of this 4-km domain covers the entire monitoring network of CAPTEX-83, while the area of the 12-km domain has been expanded a bit to the north and east to accommodate the new 4-km domain. The 4-km grid has 289 X 306 points, covering an area of 1152 X 1220 km. The expanded 12-km grid has 190 X 208 points. The 108-km and 36-km domains have the same sizes and locations as in Configuration 2. Land-use fields were derived for Configuration 3 from the same database used for the other model configurations (not shown). The number and distribution of vertical levels remained as described in Configuration 2 (see Table 2).

**Table 2. Vertical distribution of  $\epsilon$  levels (half layers) and model-layer heights (m AGL) for Configuration 2 (also used for Configuration 3).**

<b>Layer</b>	<b><math>\epsilon</math></b>	<b>Height (m)</b>
32	0.996	28.9
31	0.988	85.9
30	0.980	143.3
29	0.972	201.0
28	0.964	259.0
27	0.955	324.7
26	0.945	398.3
25	0.935	472.4
24	0.925	547.0
23	0.915	622.3
22	0.900	736.3
21	0.880	890.4
20	0.860	1047.1
19	0.840	1206.4
18	0.820	1368.3
17	0.800	1533.1
16	0.780	1700.8
15	0.760	1871.6
14	0.730	2133.7
13	0.690	2494.9
12	0.650	2870.8
11	0.610	3262.7
10	0.570	3672.1
9	0.525	4156.0
8	0.475	4726.1
7	0.425	5335.4
6	0.375	5990.3
5	0.325	6699.2
4	0.275	7472.8
3	0.225	8325.9
2	0.150	9802.3
1	0.050	12347.4

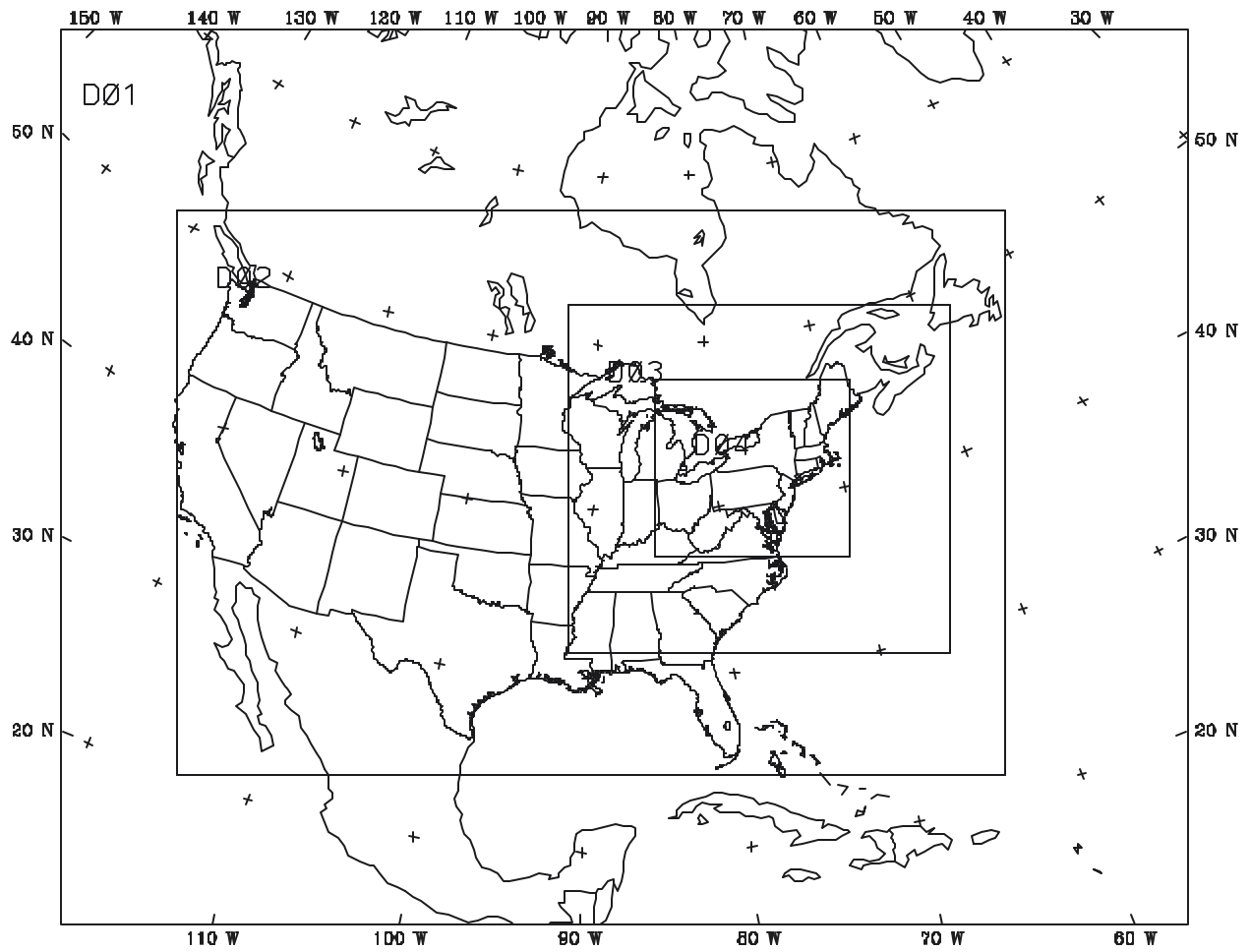


**Figure 19. Location of 108-km, 36-km, 12-km and 4-km nested domains for MM5 Configuration 3.**

# TERRAIN HEIGHT IN B/W

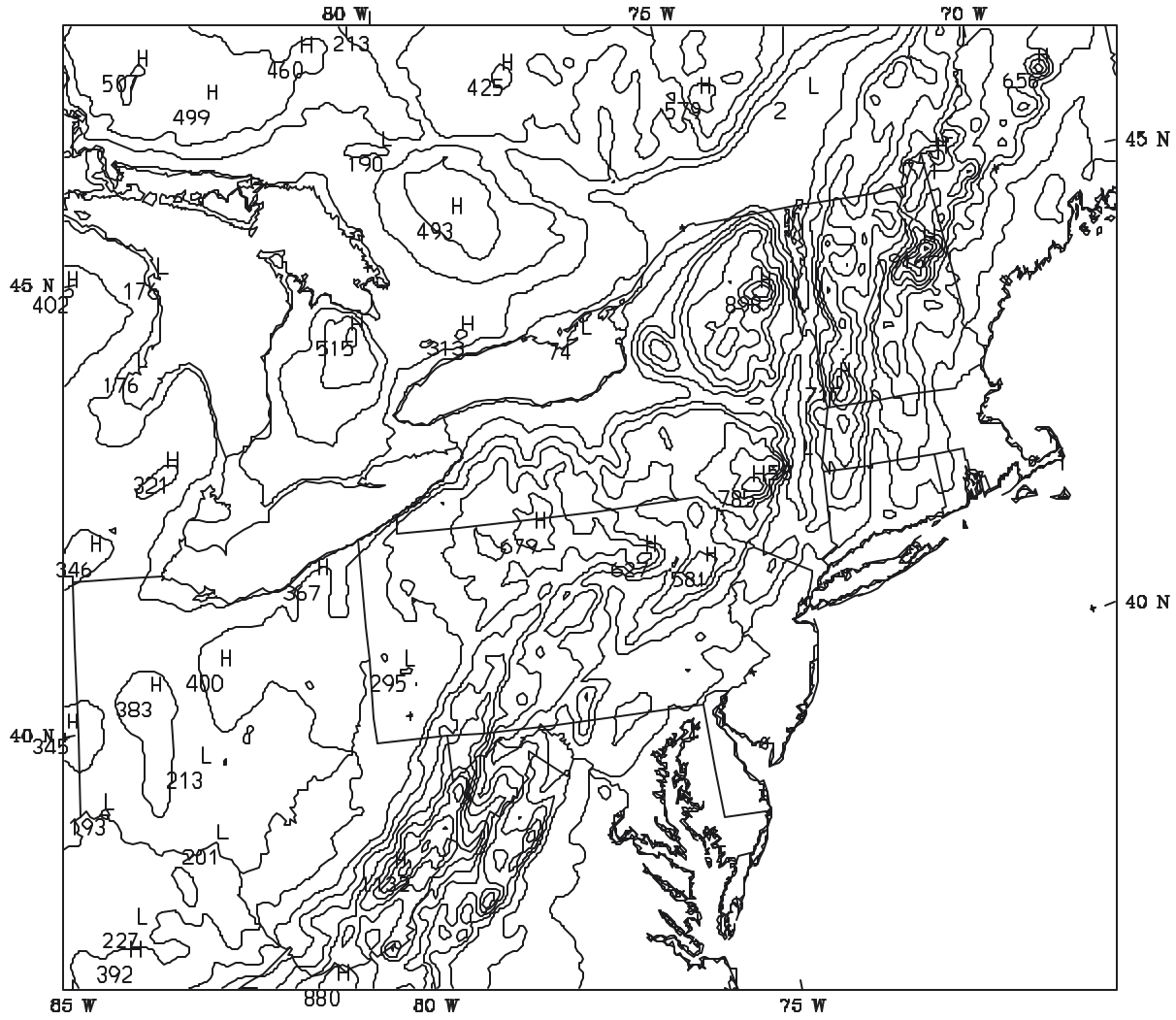


**Figure 20.** Terrain (m) for 4-km inner domain of MM5 Configuration 3. Contour interval is 100 m.

The terrain field for Configuration 3 is shown in Figure 20. No new mountain ranges emerge at 4-km resolution, which indicates that the 12-km terrain described by Figure 18 is adequate to capture the more significant regional features of the topography in the Northeast. However, the 4-km terrain does sharpen the definition of the sub-regional mountains and increases the height to which the peaks can be resolved. Thus, the Adirondack, Green and White Mountains have maximum elevations of 898, 717, and 916 m in Figure 20, respectively. While still not capturing the full height of the actual peaks, as defined in Section 4.1.1, it appears that the 4-km resolution can adequately represent the height of the main ridges. Thus, the blocking effects of the terrain should be represented well, which means that orographic impacts on plume transport should be captured quite reasonably.

## **4.2 Initialization and Lateral Boundary Conditions**

Generation of initial and lateral boundary conditions for the 70-km domain (Configuration 1) and the 108-km domain (Configurations 2 and 3) began with the National Center for Environmental Prediction's (NCEP) 2.5-degree global spectral analyses. The  $1^{\circ} \times 1^{\circ}$  global model fields of temperature, horizontal wind components and relative humidity were accessed at mandatory and supplemental pressure levels (1000, 975, 950, 925, 900, 875, 850, 800, 750, 700, 650, 600, 550, 500, 400, 300, 250, 200, 150, 100 mb), plus sea-level pressure and ground temperature, and were projected onto the outermost MM5 domains to be used as background (first-guess) fields prior to an objective analysis. (Ground temperature is defined as the surface air temperature over land, and sea-surface temperature over water.) Next, in the objective-analysis step, the analyses are enhanced by incorporating standard radiosonde and

surface data through use of an anisotropic successive-correction objective analysis (Benjamin and Seaman 1985). The completed pressure-level analyses then are interpolated to the model's sigma levels to be used as initial conditions. For Configurations 2 and 3, the 108-km analyses also are interpolated to provide initial conditions for the successive nested domains (i.e., 36-km fields are interpolated from the 108-km domain, 12-km fields from the 36-km domain, and 4-km fields from the 12-km domain).

The lateral boundary conditions of the 70-km and 108-km domains are defined at 12-h intervals from analyses generated in a way similar to that used for the initial conditions. The pressure-level analyses were created at 12-h intervals, while surface fields were generated at 3-h intervals throughout Episode 1. For the nested grids, the 36-km domain received its lateral boundary conditions directly from the 108-km domain at every time step, since these two domains are run two-way interactive. However, the one-way lateral boundary conditions of the two finest domains are created by interpolation from the next coarsest grid at one-hour intervals.

### **4.3 Model Experiments**

Six numerical experiments were designed and run in this study. (Several others were performed, but are not described here.) All experiments were initiated at 1200 UTC, 18 September 1983 (5 h before the beginning of the tracer release from Dayton) and were run for 48 h until 1200 UTC, 20 September. However, only the first 36 h of the simulations (ending at 0000 UTC, 20 September) will be discussed in Section 5 to be consistent with the period during which the tracer plume was within the CAPTEX-83 measurement network. The important factors distinguishing these experiments are summarized in Table 3.

The first experiment was a baseline run (Exp. 1A) intended to approximate the conditions that were typical of mesoscale meteorological models used for air-quality applications in the mid-1980s. Experiment 1A is based on MM5 Configuration 1 (see Section 4.1.1). This experiment used the Blackadar PBL scheme described by Zhang and Anthes (1982) and the Anthes-Kuo convection parameterization (Anthes 1977), both of which were used by Haagenson et al. (1987) (also see Section 3.1.2). Similar to that earlier study, Exp. 1A did not include a column radiation model, but did use a simple radiation balance equation at the surface. No FDDA was used in Exp. 1A, and subsequent plume-dispersion calculations (see Section 4.4.4) were made using the MM5 70-km output fields to drive the SCIPUFF model.

The second experiment (Exp. 2A) was designed to isolate the effect of improved horizontal and vertical resolution by introducing the MM5 grid Configuration 2. The model physics were identical to Exp. 1A and no FDDA was used. Subsequent SCIPUFF calculations were made using fields from the 12-km inner MM5 domain of Configuration 2. Next, Exp. 2B was similar to Exp. 2A (Configuration 2) except that up-to-date physical parameterizations were added, of the type that were commonly used in air-quality applications by 2000. Thus, in this experiment, the 1.5-order (TKE-predicting) turbulence scheme of Shafran et al. (2000) and the deep-convection parameterization of Kain and Fritsch (1990) were used. In addition, the single-band two-stream column radiation scheme of Dudhia (1989) was introduced. As in the previous experiments, no FDDA was included. Comparison of results from Exps. 2A and 2B allowed isolation of the effects of the newer physics.

During the 1990s, much attention was been given to the role of FDDA for reducing the accumulation of model errors in case simulations intended for air-quality applications. The fourth experiment (Exp. 2C), therefore, added FDDA using a fairly early FDDA technique developed by

**Table 3. Summary of experimental design. BLKDR refers to the Blackadar PBL scheme (Zhang and Anthes 1982), while TKE PBL refers to the scheme of Shafran et al. (2000). Anthes-Kuo convection scheme refers to Anthes (1977), and Kain-Fritsch refers to Kain and Fritsch (1990). The radiation scheme is that of Dudhia (1989).**

Exp. No.	MM5 Grid Configuration	MM5 Physics	MM5 FDDA	SCIPUFF Resolution
1A	1	BLKDR PBL Anthes-Kuo Conv. W/O Dudhia Radiation	No FDDA	70 km
2A	2	BLKDR PBL Anthes-Kuo Conv. W/O Dudhia Radiation	No FDDA	12 km
2B	2	TKE PBL Kain-Fritsch Conv. With Dudhia Radiation	No FDDA	12 km
2C	2	TKE PBL Kain-Fritsch Conv. With Dudhia Radiation	Assimilate Upper-Air Data Only (Stauffer & Seaman 1990)	12 km
2D	2	TKE PBL Kain-Fritsch Conv. With Dudhia Radiation	Assimilate Sfc. and Upper-Air Data (Shafran et al. 2000)	12 km
3A	3	TKE PBL Kain-Fritsch Conv. With Dudhia Radiation	Assimilate Sfc. and Upper-Air Data (Shafran et al. 2000)	4 km

Stauffer and Seaman (1990). This approach assimilated only the 12-h gridded 3-D analyses based on standard NWS soundings. These are the same analyses that were used for the model's initial and lateral boundary conditions, as described in Section 4.2. Surface-layer analyses of wind and water vapor mixing ratio were not assimilated. The 3-D analysis nudging was applied for wind, temperature and water vapor mixing ratio on the 108-, 36- and 12-km grids. A summary of the nudging parameters is given in Table 4. Table 4 also shows that the nudging coefficient, G, which determines the e-folding time (or rate) of the assimilation, is decreased on the 12-km domain to prevent over-smoothing of mesobeta-scale features that begin to emerge at this model resolution.

**Table 4. Summary of analysis-nudging parameters. Temperature is  $T$ , moisture is  $q$ , and  $u$  and  $v$  are the east-west and north-south horizontal wind components, respectively.**

	3-D data	2-D data	Nudging Factor, $G$
Source	108-km analyses based on NWS radiosondes	108-km analyses based on NWS surface data	
Frequency	12 h	3 h	
Data types	$u, v, T, q$ (limited to region above 850 mb in Exps. 2D, 3A and 3B)	$U, v$ (below $\sigma = 0.950$ , in the PBL)	108 and 36 km domains: $G(U, v, T) = 3 \times 10^{-4}$ $G(q) = 1 \times 10^{-5}$ 12 km domain: $G(U, v, T) = 1 \times 10^{-4} \text{ s}^{-1}$ $G(q) = 1 \times 10^{-5} \text{ s}^{-1}$

Next, in Exp. 2D, a somewhat more advanced version of analysis-nudging, described by Shafran et al. (2000), was used to replace the early FDDA scheme of Stauffer and Seaman (1990). In this nudging approach, surface 2-D wind analyses also were assimilated in the lowest few model layers and at 3-h intervals, in addition to the 3-D analyses discussed for Exp. 2C (summary given in Table 4). Furthermore, the newer analysis-nudging strategy prevented assimilation of the 3-D fields of wind, temperature and moisture below 850 mb (see Table 4). This approach ensures that surface-related mesoscale features generated by the model (e.g., the low-level jet observed in the warm sector of CAPTEX Episode 1, discussed in Section 2.2), do not suffer significant damping as a result of assimilating coarse-grid analyses that may not adequately resolve those circulations. In summary, the purpose of Exp. 2D is to isolate the possible impact of this improved nudging strategy on inter-regional transport.

Finally, Exp. 3A is designed to use the same physics and FDDA strategy as Exp. 2D, but applied on the MM5 grid Configuration 3, which introduces a 4-km domain. As mentioned in

Section 4.1.3, this configuration makes it possible to determine if the accuracy of inter-regional transport may be improved in future air-quality studies by using fine-mesh resolution over much wider regions than have been possible heretofore. No analysis nudging is applied on the 4-km grid because the synoptic-scale analyses, based on radiosonde data, cannot resolve the mesoscale features expected to develop on this domain. However, assimilation of the gridded analyses on the coarser grids of Configuration 3 still can have a positive impact on the 4-km solutions by improving the accuracy of the lateral boundary conditions supplied from the 12-km domain. For this experiment, the SCIPUFF plume-dispersion model uses the 4-km MM5 output fields.

#### **4.4 Evaluation Procedures**

Evaluation of a complex set of output fields generated by a 3-D mesoscale meteorological model is a challenging task. There are several ways to verify the model's accuracy, but no single method is adequate by itself. For example, a statistical analysis of model performance, calculated from the errors between observed and simulated values of key variables, can give very useful insights that help to quantify the level of skill. However, because the statistics are generally calculated over all the observing sites on an entire domain, they also may mask problems regarding how the model treats important mesoscale features, which cover only a portion of the domain. Therefore, comparison of the physical structures of individual mesoscale features is a useful complement to a statistical analysis.

In a similar way, the normal domain-wide statistical evaluations of the important meteorological variables and the comparisons of simulated and observed mesoscale features can overlook an important aspect of plume dispersion, that is, the impact of time. Inter-regional

plume transport and diffusion occur over many hours, during which the meteorological fields often undergo significant evolution. Additional evaluation approaches are necessary in this case. It is our goal to use a variety of approaches so as to develop a thorough evaluation protocol well suited to the objective of this study.

#### ***4.4.1 Approach for Evaluating Mesoscale Features***

Evaluation of simulated meteorological features was done by comparing the model's 12-km surface fields to manual mesoscale surface analyses that cover the area of the 12-km domain defined in Configuration 2. The manual analyses were generated at 6-h intervals for a complete 36-h period of interest in Episode 1, beginning at 1200 UTC, 18 September 1983. These manual analyses capture many of mesoscale details missing from the synoptic-scale objective analyses (see Section 2). Key results from this intercomparison are presented in Section 5.1. In addition, checks were made to compare the objective analyses and simulated fields between the surface and at 850 mb, especially using vertical cross sections. Mesoscale analyses on pressure levels above the surface, however, were not feasible because of the wide spacing between NWS radiosonde stations.

#### ***4.4.2 Statistical Evaluation Approach***

The most effective approach to statistical evaluation of meteorological model fields is to use a variety of measures, instead of relying on one particular statistical score. Here, we use root mean square errors, mean absolute errors, mean errors, an index of agreement, and a threshold

percentage. Generally, these quantities are calculated as domain-wide averages for one or more layers. In addition, displays also can be made showing the evolution of such statistical scores as a function of time or as vertical profiles of the errors. Scatterplots of the errors can be a useful display to reveal certain trends in the errors of particular variable fields.

The mean error (*ME*) and mean absolute error (*MAE*) are given by

$$ME = \left[ \sum_{n=1}^N (\mathbf{a}_n - \mathbf{a}_n^o) \right] / N \quad (4)$$

and

$$MAE = \left[ \sum_{n=1}^N |\mathbf{a}_n - \mathbf{a}_n^o| \right] / N \quad (5)$$

where  $\mathbf{a}_n^o$  is the  $n^{th}$  observation of some scalar variable  $\mathbf{a}$ ,  $N$  is the total number of observations on the verification domain, and  $\mathbf{a}_n$  is the model field for variable  $\mathbf{a}$  interpolated to the site of the observation. The root mean square error (*RMSE*) for  $\mathbf{a}$  is given by

$$RMSE = \left[ \frac{1}{N} \sum_{n=1}^N (\mathbf{a}_n - \mathbf{a}_n^o)^2 \right]^{1/2} \quad (6)$$

The *ME* provides a measure of the bias in the model, where positive and negative errors can cancel each other. For transport calculations performed over time, it is important that this error be as low as possible. The *MAE* gives a measure of the most "typical" error, in the sense that it is the average size of the absolute value of individual errors. Thus, positive and negative errors cannot cancel one another. The *RMSE* is somewhat similar to the *MAE*, but it magnifies the

impact of "outliers". An experiment with comparatively few outliers will have similar scores for the *RMSE* and *MAE*.

Another statistic that can indicate the overall skill of the model in predicting the wind field is the index of agreement (*I*). The value *I* is calculated by taking the ratio of the sum of the squared errors to the sum of the squares of two differences: that between the model estimate and the mean of observations, and that between the individual observations and the mean of observations (Willmott 1982, Willmott et al. 1985). It is calculated as follows:

$$I = 1 - \left[ \frac{\sum_{n=1}^N (\mathbf{a}_n - \mathbf{a}_n^O)^2}{\sum_{n=1}^N (|\mathbf{a}_n'| + |\mathbf{a}_n^{O'}|)^2} \right], \quad 0 \leq I \leq 1 \quad (7)$$

where  $\mathbf{a}_n' = (\mathbf{a}_n - \bar{\mathbf{a}})$ ,  $\mathbf{a}_n^{O'} = (\mathbf{a}_n^O - \bar{\mathbf{a}})$ , and  $\bar{\mathbf{a}}$  is the mean of the observations on the verification domain. The value of *I* ranges from 0 to 1, with a score of 1 representing perfect agreement to the data. This statistic measures how well the variability in the model simulations matches the variability in the data, in a spatially paired manner. In mesoscale model applications, a value of *I* on the order of 0.5-0.6 is considered to be typical for a successful simulation of the wind field (e.g., Seaman et al. 1995, Lyons et al. 1995, Shafran et al. 2000).

Finally, the threshold percentage (*TRP*) is introduced as a measure of how often the model-predicted values on the verification domain fall within some specified threshold of accuracy. It is defined according to

$$TRP = [N_T / N] \times 100 \quad (8)$$

where  $N_T$  is the total number of points on the domain for which  $(\mathbf{a}_n - \mathbf{a}_n^o) \leq TR_a$  and where  $TR_a$  is a specified *critical threshold* for the variable  $\mathbf{a}$ . The value of  $TR_a$  is chosen to represent a tolerable standard level of error for  $\mathbf{a}$ , which in this case is determined by its intended use for air quality applications. For example, if it is necessary that surface air temperature be simulated within 2 C in order for an emissions model to calculate sufficiently accurate biogenic emissions, then one might specify  $TR_a = 2.0$ .

If the  $TR_a$  happens to be about equal to the *MAE*, then the *TRP* generally will be ~50%, because the *MAE* represents the average size of the absolute value of the individual model errors. In this study, we arbitrarily set  $TR_a$  according to the values given in Table 5. Notice that the values in the table for  $TR_a$  of wind direction may appear to be fairly large. Indeed, if these values represented the model's directional *bias* (mean error), the impact on inter-regional transport would become very large over time. However, a comparatively large  $TR_a$  in the case of low-level wind direction may have little impact, if the *ME* is small, because individual local errors between the model and observations often cancel each other. Recall that the effects of turbulence and obstacles (small hills, buildings, trees, etc.) can introduce large uncertainties to the accuracy and representativeness of surface wind measurements, especially in the case of light wind speeds ( $< \sim 2 \text{ ms}^{-1}$ ). Largely for this reason, surface wind observations are only reported to the nearest 10 degrees. Therefore, the value of  $TR_a$  for wind direction can be relatively large without serious impact on plume transport. We also note that other methods could be used to define the threshold criteria. For example, when high winds are encountered (say,  $|V| > 25 \text{ ms}^{-1}$ ), the threshold for wind speed could be defined as a percentage (perhaps 10%) of the observed wind speed. However, that distinction is not introduced in this study.

**Table 5. Critical thresholds chosen for desired accuracy of meteorological variables.**

<b>Variable</b>	<b>Critical Threshold, <math>TR_a</math></b>
Wind Speed ( $\text{ms}^{-1}$ )	2.0 $\text{ms}^{-1}$ (surface & PBL)
	2.5 $\text{ms}^{-1}$ (1000-5000 m)
	3.0 $\text{ms}^{-1}$ (5000-10,000 m)
Wind Direction (deg.)	30 deg. (surface)
	15 deg. (PBL)
	10 deg. (layers above PBL)
Temperature (C)	2.0 C (all levels)
Water Vap. Mix. Ratio ( $\text{g kg}^{-1}$ )	1.0 $\text{g kg}^{-1}$ (below 5 km)
	0.5 $\text{g kg}^{-1}$ (above 5 km)
Sea-Level Pressure (mb)	2.0 mb

#### **4.4.3 Transport Evaluation Approach**

As mentioned in Section 3.3, a trajectory-calculation model (TRAJEC) is applied here to gain additional insight into plume transport. Parcel trajectory calculations, although helpful, have certain limitations and some discussion is appropriate. In the form presented here, the trajectories cannot account for the dispersive effects of turbulence, so that only the resolved-scale vertical motions can advect parcels upwards or downwards. Also, it may be tempting to interpret the trajectory of a parcel in the horizontal direction as revealing the path of the plume centerline. However, this is true only if the 3-D wind field does not evolve in time. Thus, the best interpretation is that a parcel's motion in the trajectory model represents the motion of the *center of mass* of an individual puff advected by the model's evolving resolved-scale wind field. If the puff had a material surface, like a balloon, and was large enough that turbulent effects did not directly affect its motion, then the transport of an observed parcel could be compared directly with that simulated by the TRAJEC model, based solely on the MM5 grid-resolved winds.

However, there is no corresponding measurement against which the parcel trajectories can be verified. Therefore, the value of the trajectory calculations in this case lies in providing an aid for interpreting the net impact of complex resolved-scale wind fields acting in three spatial dimensions and time.

#### ***4.4.4 Dispersion Evaluation Approach***

Of course, the tracer released in CAPTEX-83 Episode 1 from Dayton, OH, was subject to the dispersive effects of turbulence, in addition to being advected by the larger-scale wind field. Using the MM5's simulated winds as inputs to the SCIPUFF model provides a way of evaluating the accuracy of the modeling system's predictions for the full range of atmospheric motions. Since the finest grid scales in the different MM5 experiments are much larger than the size of turbulent eddies, the mesoscale-model solutions cannot represent the turbulent motions directly. They can only include the effects of the sub-grid turbulence on the resolvable-scale fields for each prognostic variable. Thus, the second-order diffusion sub-model in SCIPUFF is used to diagnose the eddy-diffusive effects of turbulent-scale motions on the plume. Nevertheless, all winds between the turbulence scale ( $< 1$  km) and the MM5's smallest resolved scales ( $\sim 8 \Delta x$  in Exp. 3A) are necessarily lost in the plume dispersion calculations. This provides an additional way that the effects of various grid resolutions can become important.

Despite such limitations, coupling of the MM5 and SCIPUFF provides a very useful way of assessing the accuracy of the numerical experiments by comparing simulated tracer concentrations to the observed concentrations. To this end, SCIPUFF was initialized with the same rate of tracer-mass release that was used at Dayton in Episode 1 of CAPTEX-83. If

SCIPUFF could be assumed perfect, then comparison of the concentrations with the observed values would reveal only the errors in the MM5 winds and stability. Since that is unlikely to be true, errors in the simulated concentrations must be considered as due to the limitations of both MM5 and SCIPUFF.

For our purposes, we shall present simulated surface plume concentrations at specific times, which can be compared with the tracer observations plotted in Figure 14. This type of display gives direct validation of the plume's position and intensity as it undergoes dispersion. Vertical cross sections through the plume can be used to gain further insights, in a qualitative sense, although there is inadequate data to validate upper-air concentrations directly.

## 5. MODEL RESULTS

### 5.1 Evaluation of the Simulated Mesoscale Features

We begin by comparing the structure of mesoscale features simulated in the various model experiments to those revealed by the meteorological observations. The differences between the model-generated fields for some of the experiments are rather small, so it is unnecessary to examine all six experiments in this section. Instead, representative results will be presented from the four most important experiments (Exps. A1, 2B, 2D and 3A), which includes at least one from each of the three domain configurations described in Section 4.1.

The statistical evaluations to be presented in Sections 5.2 and 5.4 are better suited for quantifying differences in skill among the six experiments. This is especially true for understanding the changes that result from the different experiment conditions in the four runs using Configuration 2. On the other hand, the direct examination of plotted fields shown here is important for understanding how well the model can reproduce the complex evolving mesoscale structures found in the analyses described in Section 2. Visual inspections are also helpful for distinguishing among possible causes of model error, such as phase-speed errors versus physical parameterization errors. Statistical evaluations often mask these important details.

#### *5.1.1 Configuration 1*

The evolution of the surface fields in Exp. 1A (the benchmark experiment conducted using Configuration 1) can be understood fairly well by examining Figures 21 and 22. These

figures present the simulated sea-level pressure and surface-layer wind fields, respectively, at 1800 UTC, 19 September 1983, which is 30 h into the numerical experiment. By this time, the tracer plume at the surface was detected over northern NY and New England, but was already beginning to leave the CAPTEX monitoring network (see Figures 14c and 14d).

Since the grid used in Exp. 1A is quite coarse ( $\Delta x = 70$  km), the synoptic-scale features are represented well, but finer mesoscale details of the frontal band cannot be resolved with much clarity. As is typical for such cases, the simulated pressure trough associated with the front is well-defined in the vicinity of the large Canadian storm and also to the west of Lake Michigan near the next storm that is already strengthening over the Great Plains (Figure 21). However, in the area of the lower Great Lakes and the St. Lawrence Valley, where the strong Mid-Atlantic ridge extends northwestward, the pressure trough is less distinct. This pattern is confirmed in the corresponding manual analysis at 1800 UTC (Figure 12). The simulated surface-layer winds in the vicinity of the front along the border between NY and Canada (Figure 22) reflect the weakness of the pressure trough by showing very little cyclonic turning of the wind direction across the frontal boundary. The model's quasi-parallel winds on either side of the front suggest an absence of significant convergence and also have resulted in a marked deceleration of the frontal advance in this area over the past 6-12 h. Thus, while it was hypothesized in Sec. 2.2 that the frontal zone may help to define the left-hand (northern) boundary of the tracer plume, the front simulated in Exp. 1 is unlikely to have lifted a substantial part of the plume off the surface into the middle troposphere.

Further comparison of Figures 12, 21 and 22 reveals that perhaps the most serious flaw in the MM5's surface fields for Exp. 1A at 1800 UTC is the failure of the front to propagate fast enough into NY and New England. Slower-than-observed phase speeds are known to be a

Title:

Creator:

CoreIDRAW

Preview:

This EPS picture was not saved  
with a preview included in it.

Comment:

This EPS picture will print to a  
PostScript printer, but not to  
other types of printers.

**Figure 21. MM5 simulation of sea-level pressure (mb) on the 70-km domain at 1800 UTC, 19 September 1983, 30 h into CAPTEX Experiment 1A. Isobar interval is 2 mb.**

Title:

Creator:

CorelDRAW

Preview:

This EPS picture was not saved  
with a preview included in it.

Comment:

This EPS picture will print to a  
PostScript printer, but not to  
other types of printers.

**Figure 22.** MM5 simulation of surface-layer winds ( $\text{m s}^{-1}$ ) on the 70-km domain at 1800 UTC, 19 September 1983, 30 h into CAPTEX Experiment 1A. Contour interval is  $5 \text{ m s}^{-1}$ .

characteristic of models having 2<sup>nd</sup>-order finite-difference numerics, like MM5, especially when applied with rather coarse grids. Also, over northern IL and the southern end of Lake Michigan, the simulated warm front is a bit too far south (again, too slow), compared to the analyzed position in Figure 12. However, despite some frontal errors, the overall strength and position of the synoptic-scale highs and lows are represented adequately by the model, including the northwestward extension of the ridge over the western Great Lakes. Figure 22 indicates that, after 30 h, the winds over OH and western PA remained southwesterly (as observed), while NY and New England have west-southwesterly winds. This is consistent with the observed flow and with right-hand (clockwise) turning of the tracer plume over time (see Figure 14). Notice that the simulated surface winds in Figure 22 are  $\sim 3\text{-}5\text{ ms}^{-1}$  and turn anticyclonically over the Southeast U.S. and from the Northeast U.S. to eastern OH (with some faster winds over the ocean east of the trough in New England and the Mid-Atlantic coast). Over the Midwest (north of the Ohio River and south of the front), simulated winds increase to  $5\text{-}9\text{ ms}^{-1}$  from the south-southwest. These wind speeds match the observed surface wind pattern very well (Figure 12).

As explained in the synoptic overview (Section 2.2), the surface-layer wind speeds simulated in Exp. 1A (Figure 22) are too weak to explain the very rapid advection of the plume from Dayton, OH, to northern New England. Examination of Figure 14c shows that the plume already had reached northern NH (a distance of  $\sim 1200\text{ km}$  from Dayton) by 1000 UTC, 19 September, just 17 h from the beginning of the tracer release. This translates into a mean advective speed of  $\sim 20\text{ ms}^{-1}$ . The surface-layer winds over the CAPTEX network average only  $\sim 4\text{-}5\text{ ms}^{-1}$  for the episode. Thus, it is clear that the speed of the plume's leading edge can only be explained by early injection of tracer material into a higher level through turbulent mixing in the convective boundary layer on 18 September, followed by rapid advection aloft and subsequent

mixing downward to the surface. This explanation was hypothesized by Haagenson et al. (1987), but was not followed by a thorough examination of the data and by mesoscale meteorological and dispersion modeling.

To confirm this theory, we began by examining the advection aloft in the results of the MM5 simulation in Exp. 1A. First, the depth of the PBL in OH was found to be about 1250 m AGL (~ 850 mb) on the afternoon of 18 September (not shown). The MM5-predicted 850-mb winds over northern OH at the same time had a maximum of  $20 \text{ ms}^{-1}$  from the west-southwest (not shown), so that rapid vertical mixing and mid-level transport of the tracer could occur in the model at about the same speed that was observed in Figure 14. The model's 850-mb winds in Exp. 1A increased during the evening to  $24 \text{ ms}^{-1}$  over western NY due to ageostrophic accelerations in the nocturnal LLJ (the observed maximum wind at 850 mb was  $26 \text{ ms}^{-1}$  in Fig. 4). This placed the upper part of the tracer plume in the core of the fastest winds during the night and led to its rapid advection into New England. Thus, the advection during the night should be at least as fast as the speed of the leading edge of the actual surface plume.

By the next afternoon, at 1800 UTC, 19 September, Figure 23 shows that the 850-mb winds over northern New England had weakened substantially to  $\sim 15 \text{ ms}^{-1}$ . Due to increased cloud cover, the boundary layer depth on this second day was a bit more shallow (~1000-1100 m AGL) over the region south of the advancing cold front, which is best shown by the model's sounding at Albany, NY at 1800 UTC, 19 September (Figure 24). Nevertheless, the PBL is deep enough to allow mixing of portions of the previous day's elevated plume downward to the surface. In summary, the time-averaged simulated wind speed at 850 mb in Exp. 1A (from the time of the tracer release to the afternoon of 19 September) was about  $20\text{-}21 \text{ ms}^{-1}$ , which is



Title:

Creator:

CoreIDRAW

Preview:

This EPS picture was not saved  
with a preview included in it.

Comment:

This EPS picture will print to a  
PostScript printer, but not to  
other types of printers.

**Figure 24.** MM5 sounding simulated at Albany, NY, 1800 UTC, 19 September 1983, 30 h into CAPTEX Experiment 1A. Winds are plotted in kts.

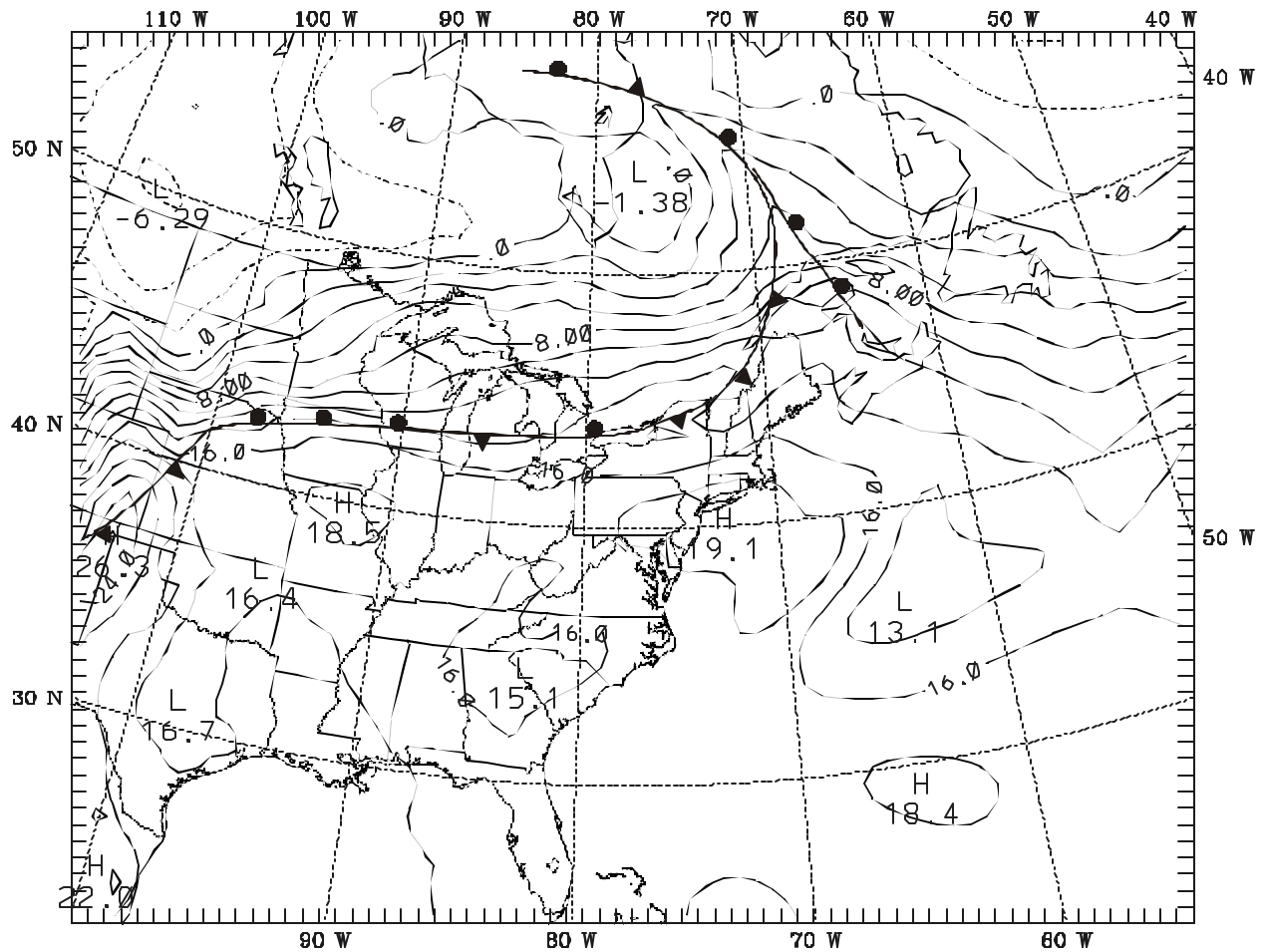
thoroughly consistent with the observed tracer-cloud movement and the mid-level wind analyses available at 12-h intervals.

Meanwhile, Figure 25 shows the 850-mb isotherm pattern in Exp. 1A at 1800 UTC, 19 September. The simulated temperatures aloft are fairly uniform in the warm air mass south of the cold front (~14-18 C), while distinctly colder air and a stronger gradient lie to its north and west. The slightly cooler temperatures simulated just ahead of the front in northern NY and New England are caused by a band of pre-frontal clouds and light showers (not shown). The model generated only about 1-5 mm of rain from New England to Detroit during the 6 h ending at 1800 UTC, 19 September, although heavier rains (10-20 mm in 6 h) were predicted north of the warm front over the Great Plains due to strong overrunning. Examination of the manual analyses indicates that most of the rain occurred shortly after 1200 UTC, after which the showers weakened during the daytime.

### ***5.1.2 Configuration 2***

Next, the results of experiments that used the nested-grid domains of Configuration 2 were examined. The evaluations will focus on the 12-km regional scale grid. Representative results are presented primarily from Exp. 2B (containing improved physics, relative to Exps. 1A and 2A) and from Exp. 2D (with FDDA at the surface and aloft). Only brief comments are added, as necessary, to describe the other two experiments that used this configuration (see Table 3 for details). Although we do not show explicit results from Exp. 2A, inspection of that experiment showed that simply increasing the horizontal resolution to 12 km caused the fronts to advance more rapidly than in Exp. 1, thus leading to generally more accurate positions for these

PRESSURE=850. mb T (C) 1983-09-19\_18.00.00 - 1983-09-18\_12 + 30.00H SMOOTH= 0



MM5V3-CAPTEX EXP1=> 70-KM,KUO CUMU., BLACKADAR PBL, NO FDDA, NO RAD SCHEM  
CONTOUR FROM -6.0000 TO 26.000 CONTOUR INTERVAL OF 2.0000 PT(3,31)= 19.862

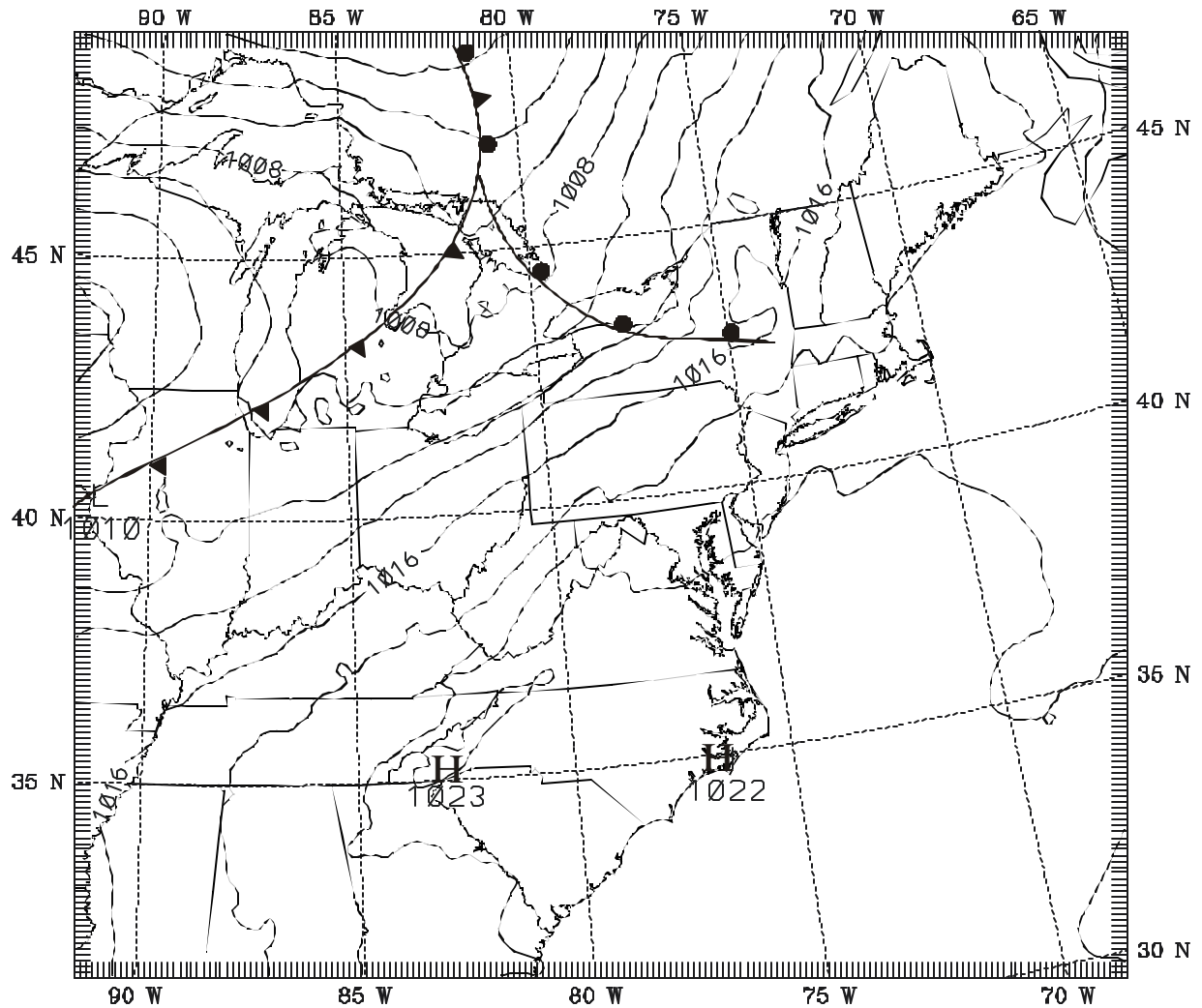
Figure 25. MM5 simulation of 850-mb temperature (C) on the 70-km domain at 1800 UTC, 19 September 1983, 30 h into CAPTEX Experiment 1A. Isotherm interval is 2 C.

boundaries late in the study period. This result is consistent with expectations, given the well-known numerical characteristics of the MM5's 2<sup>nd</sup>-order finite-differencing used to represent the differential equations of motion (Grell et al. 1994). The improvement of the phase speeds for meso-alpha scale features (~200-2000 km) can be significant in this case, since the model grid resolution was increased from 70 km to 12 km, or a factor of almost 6:1.

Figures 26 and 27 show the sea-level pressure and surface wind fields simulated in Exp. 2B (improved physics) after the first 12 h of the model run, at 0000 UTC, 19 September. The figures at this time represent the conditions at the end of the first afternoon, when the tracer plume released from Dayton had been mixed upward through the convectively unstable PBL and advected northeastward across OH to western Lake Erie (see Fig. 14a). Comparison with the manual mesoscale analysis for the same time (Figure 9) indicates that the model has simulated the observed frontal positions reasonably well, although the speed of the cold front remains somewhat slow over IL and IN. (The model's frontal positions are analyzed not only from these two fields, but also by comparison with the surface thermal and moisture fields, which are not shown. Note also that the true positions of the fronts have some uncertainty, on the order of ~20-40 km, due to the spacing of the surface observations.) In addition, the MM5 correctly simulated the strongest pressure gradients, which were observed over western NY and northwestern PA. Meanwhile, the wind directions and speeds are represented rather well across the entire 12-km domain (Figure 27) and clearly reveal the locations of the fronts at this time.

Figure 28 presents the 6-h simulated rainfall totals on the 12-km grid for the period ending at the same time, 0000 UTC, 19 September. As was observed, most of the model's rain occurs as convective showers concentrated along the cold front and occluded front, with some very light overrunning precipitation in advance of the warm front. A few of these convective

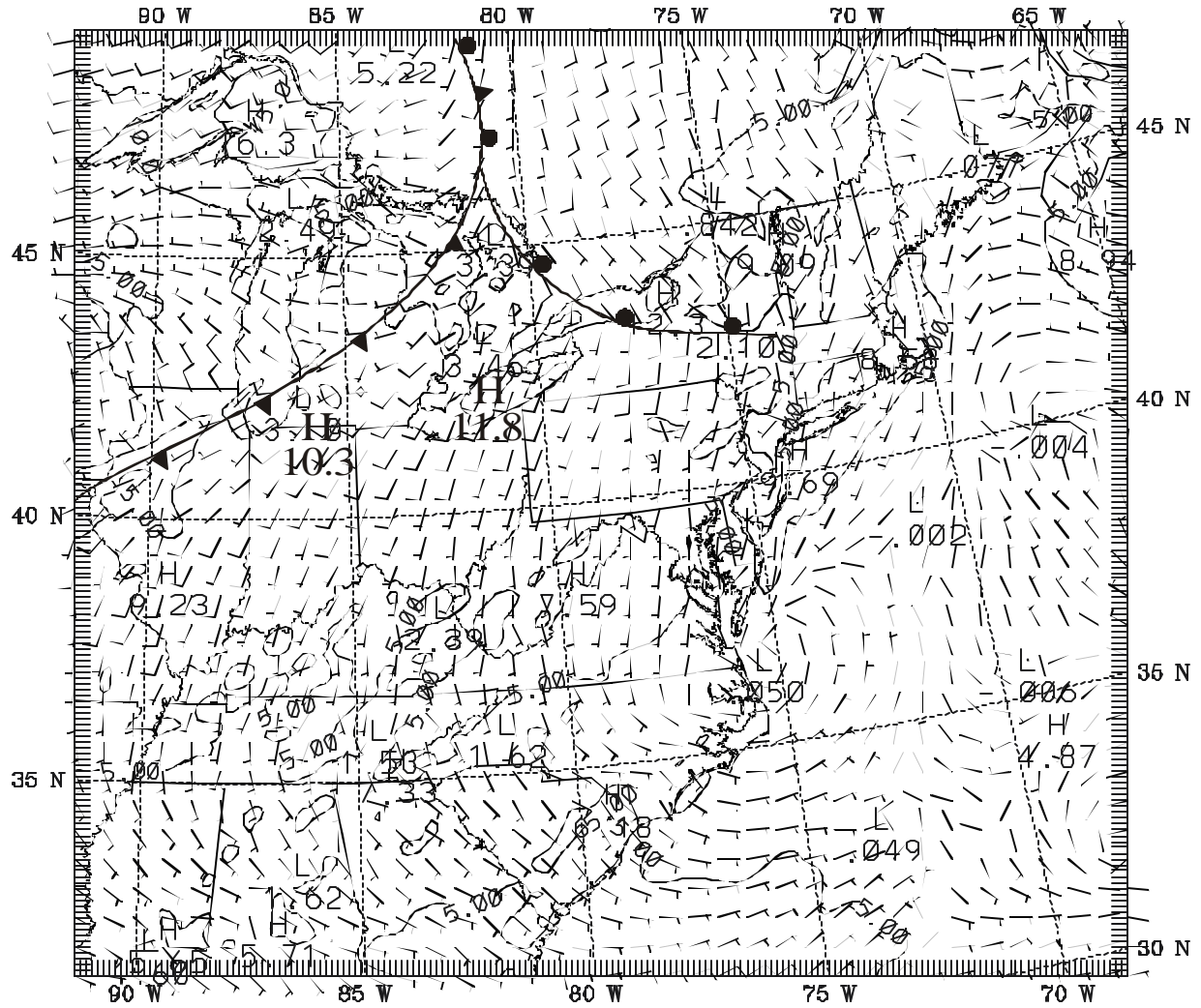
SIGMA =1.000 SEA PRES lmb ) 1983-09-19\_00.00.36 = 1983-09-18\_12 + 12.01H SMOOTH= 0



MM5V3-CAPTEX EXP2=> 12 KM, KF, G-S PBL, DUDHIA RAD., NO FDDA  
CONTOUR FROM 1000.0 TO 1022.0 CONTOUR INTERVAL OF 2.0000 PT(3,31)= 1015.6

**Figure 26.** MM5 simulation of sea-level pressure (mb) on the 12-km domain at 0000 UTC, 19 September 1983, 12 h into CAPTEX Experiment 2B. Isobar interval is 2 mb.

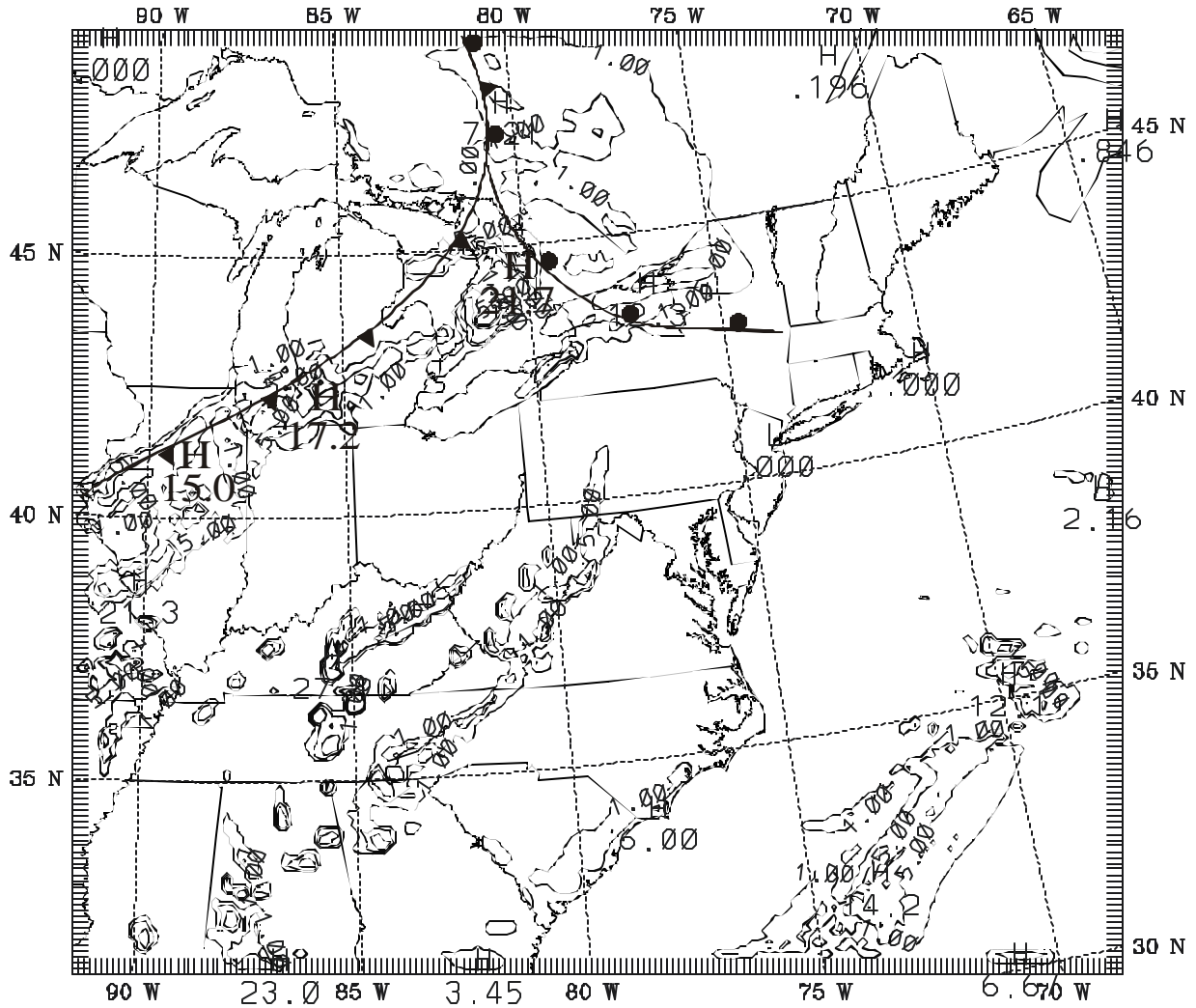
SIGMA =0.996 WIND UV 1m/s ) 1983-09-19\_00.00.36 = 1983-09-18\_12 + 12.01H SMOOTH= 3  
 SIGMA =0.996 BARB UV 1m/s ) 1983-09-19\_00.00.36 = 1983-09-18\_12 + 12.01H SMOOTH= 0



MM5V3-CAPTEX EXP2=> 12 KM, KF, G-S PBL, DUDHIA RAD., NO FDDA  
 CONTOUR FROM 0.0000E+00 TO 15.000 CONTOUR INTERVAL OF 5.0000 PT(3,31)= 3.9514

Figure 27. MM5 simulation of surface-layer winds ( $\text{m s}^{-1}$ ) on the 12-km domain at 0000 UTC, 19 September 1983, 12 h into CAPTEX Experiment 2B. Contour interval is  $5 \text{ m s}^{-1}$ .

SIGMA =1.000 TEND RNT 1mm ) 1983-09-19\_00.00.36 = 1983-09-18\_12 + 12.01H SMOOTH= 0



MM5V3-CAPTEX EXP2=> 12 KM, KF, G-S PBL, DUDHIA RAD., NO FDDA  
CONTOUR FROM 000000 TO 999999 CONTOUR INTERVAL OF 5.0000 PT(3,31)= 0.00000E+00

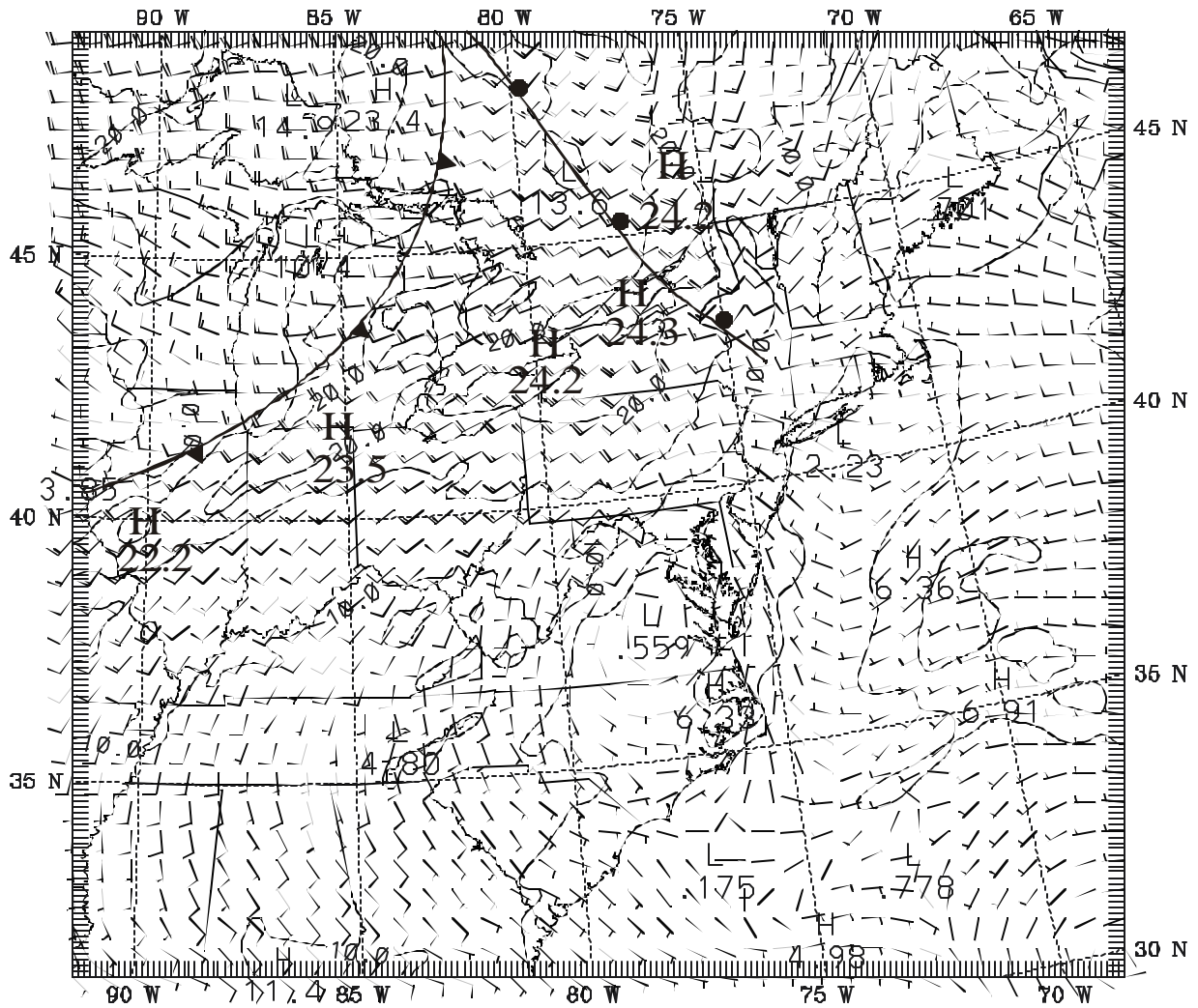
**Figure 28.** MM5 simulation of 6-h rainfall (mm) on the 12-km domain for the period ending at 0000 UTC, 19 September 1983, 12 h into CAPTEX Experiment 2B. Contours are at 1, 5, 10, and 20 mm.

showers deposit 13-22 mm (~0.50-0.75 in.) in the 6-h period, but in most areas the rainfall is considerably less. This is mostly consistent with the observations, although in most areas actual rain was only ~3-6 mm along the cold front. Elsewhere, the model produced some widespread showers farther south in the warm air mass. Although no rain was reported in the NWS reports away from the frontal zones, the observations did indicate cumulonimbus and towering cumulus clouds in southern IL and in AL, so that some light showers actually may have occurred.

Because turbulent mixing is the physical mechanism that initially carries the tracer mass aloft through the convectively unstable daytime PBL, it is important to examine the conditions simulated by the model in that layer at 0000 UTC, 19 September. Figure 29 shows that the model has simulated the LLJ, marked by a series of maxima in the 850-mb wind field (~1250 m AGL) in the warm sector along a line from central IL to Lake Ontario. The fastest winds in Exp. 2B at this time are  $\sim 24 \text{ m s}^{-1}$  in western NY near Buffalo. The position of this LLJ agrees well with the strongest sea-level pressure gradient shown in Figure 26 and with the observed LLJ found in the analyses (Figure 4). Also notice that the position of the fronts at 850 mb reveal a steep cold-front structure and a more gently sloped warm front (compare with Figure 27). (The frontal positions aloft were analyzed by comparing the simulated wind, temperature and moisture fields.) Near the southern end of the warm front, however, the slope must become very steep in the model solutions because the frontal positions are nearly identical in Figures 27 and 29.

As the evening progressed, ageostrophic accelerations in the model intensified the LLJ wind speeds on the 12-km domain, until the maximum reached  $33 \text{ m s}^{-1}$  over Lake Ontario between 900-850 mb at 0600 UTC (not shown). This is roughly the time expected for maximum jet winds in mid-latitudes and is consistent with the very rapid nocturnal advection of the plume noted in Figure 14. The maximum speed in Exp. 2B is substantially stronger than the LLJ winds

PRESSURE=850. mb WIND UV 1m/s ) 1983-09-19\_00.00.36 = 1983-09-18\_12 + 12.01H SMOOTH= 3  
 PRESSURE=850. mb BARB UV 1m/s ) 1983-09-19\_00.00.36 = 1983-09-18\_12 + 12.01H SMOOTH= 0



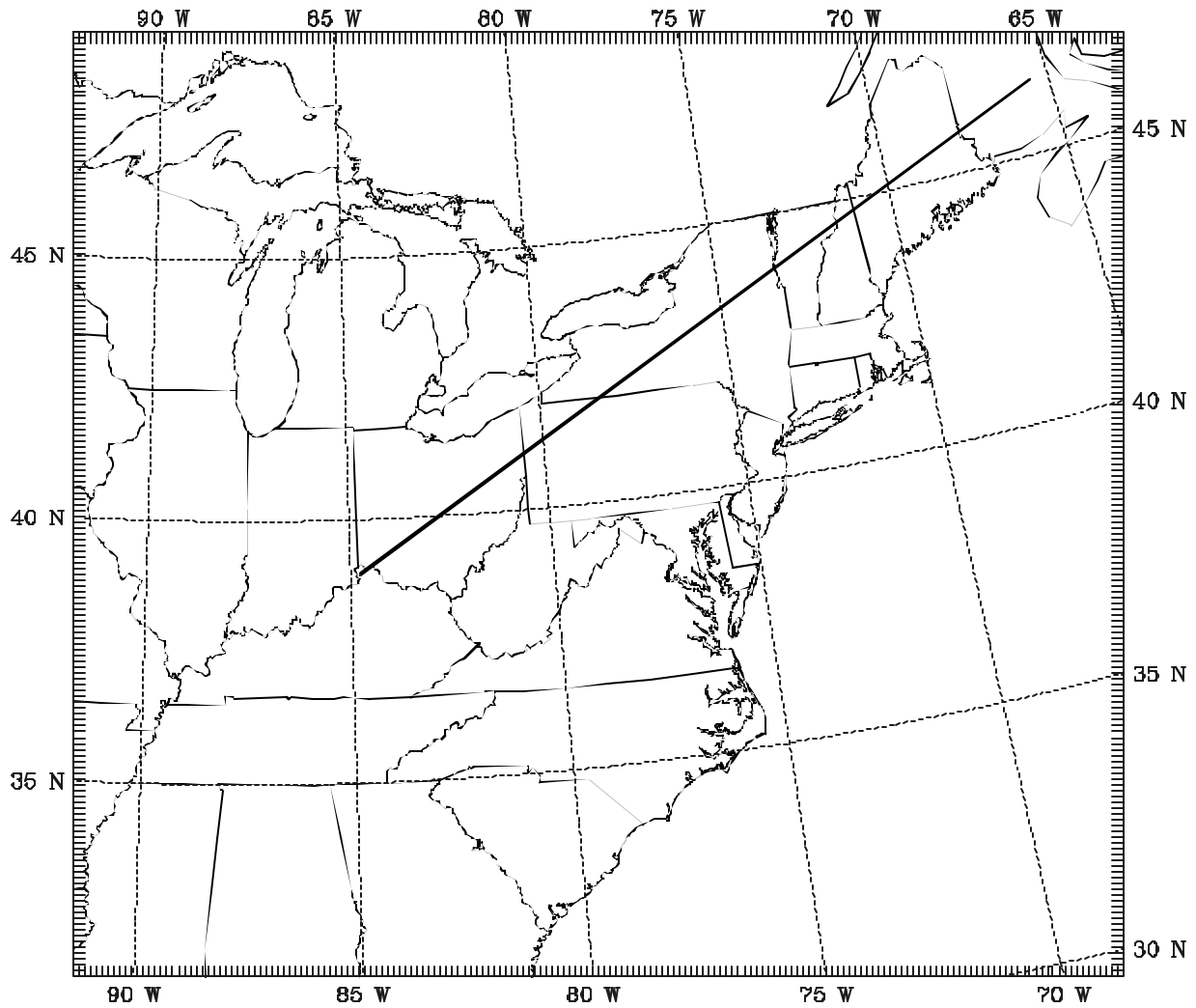
MM5V3-CAPTEX EXP2=> 12 KM, KF, G-S PBL, DUDHIA RAD., NO FDDA  
 CONTOUR FROM 0.00000E+00 TO 20.000 CONTOUR INTERVAL OF 5.0000 PT(3,31)= 4.5933

**Figure 29.** MM5 simulation of 850-mb wind ( $\text{ms}^{-1}$ ) on the 12-km domain at 0000 UTC, 19 September 1983, 12 h into CAPTEX Experiment 2B. Isotach interval is  $5 \text{ ms}^{-1}$ .

produced in Exp. 1A. In fact, if it were sustained, this speed appears to be considerable faster than is necessary to explain the observed speed of advance of the surface tracer plume.

To better understand the role of the LLJ during the nocturnal period, it is important to further assess the vertical structure of the atmosphere in the lowest 1.5 km, where the tracer plume is located. Figures 30 and 31 show a vertical cross section of potential temperature ( $q$ ) along a 1700-km segment stretching from the southwest corner of OH, through Dayton, central NY, northern New England and finally to New Brunswick. This cross section is roughly parallel to the mean direction of the plume over the 30-h period following its release. First, Figure 31 shows the structure of the warm front rising from the surface in central NY and sloping toward the northeast. Aloft, the frontal surface undulates due to mountain-induced gravity waves above the Adirondack and White Mountains.

The  $q$  field also shows the current depth of the turbulent boundary layer (dashed line ~100-300 m above the surface) and the remnants of the previous afternoon's mixed layer (zones of  $\partial q/\partial z \cong 0$  below 850 mb). It is these layers, in the warm sector, that contain the tracer plume. Also, any leading portion of the plume that encounters the warm front is likely to be lifted over the frontal surface, hence losing contact with the ground. This possible scenario is consistent with the acceleration of the LLJ to  $33 \text{ m s}^{-1}$  in Exp. 2B by 0600 UTC (not shown). Once any portion of the plume is lifted over the warm front, it is not likely to be detected (at least during the nighttime) by the surface monitors that lie northeast of the surface warm-front position. Inspection of Figure 14 shows that the observed tracer remains in the analyzed warm sector of each panel as it passes over the monitoring network. Unfortunately, the aircraft flights in Episode 1 began shortly after 0900 UTC, 19 September, well after the warm front had reached ME. Later in Sec. 5.4, we will inspect the vertical structure of the plume during the evening, as



MM5V3-CAPTEX EXP2=> 12 KM, KF, G-S PBL, DUDHIA RAD., NO FDDA

**Figure 30.** Location of southwest to northeast cross section on the 12-km domain for CAPTEX Episode 1. The cross section is oriented to lie approximately along the centerline of the surface plume for this case.

(X1,Y1)=( 50, 70) (X2,Y2)=(165,155) THETA (K | 1983-09-19\_00.00.36 SM= 0

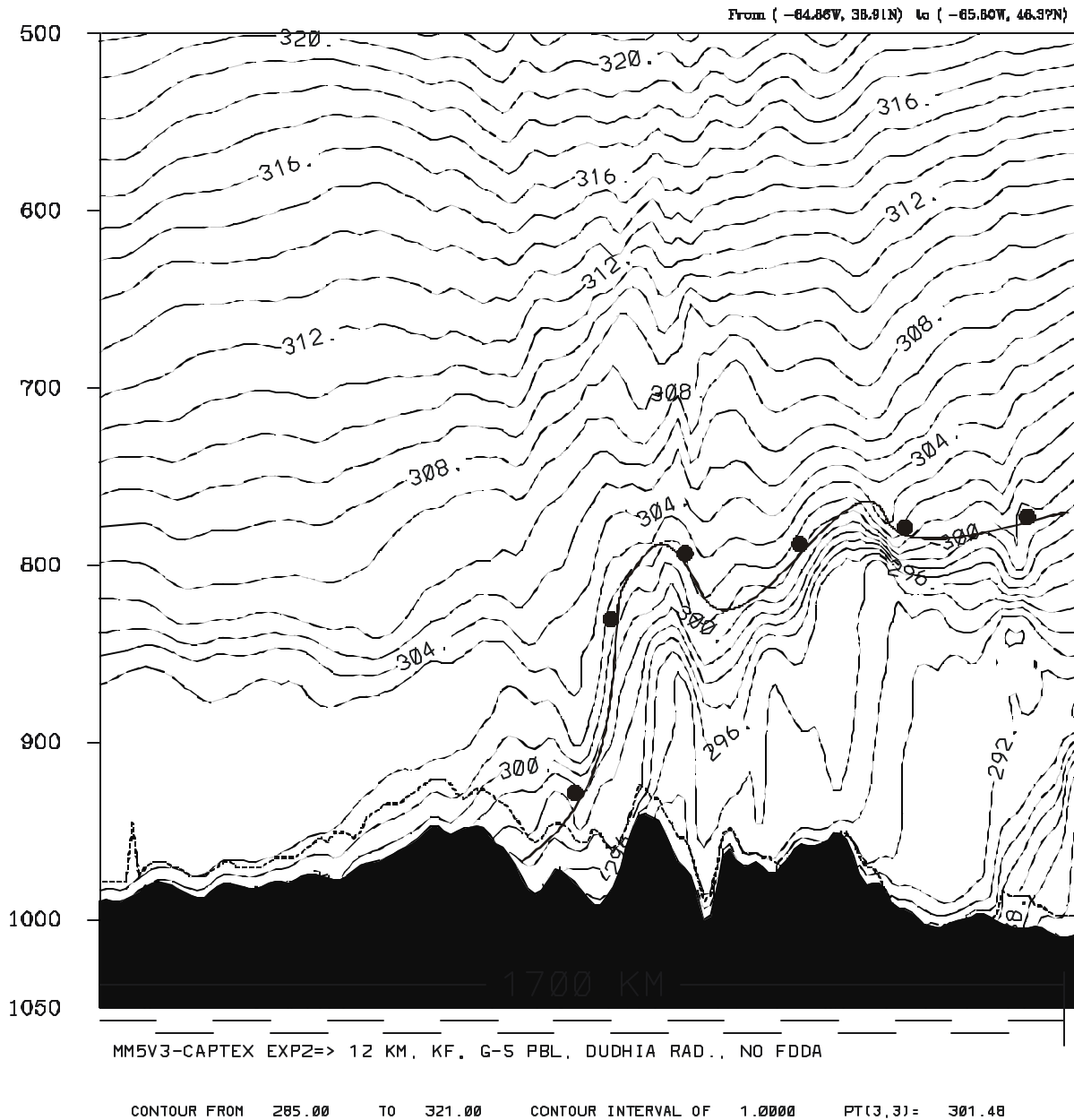


**Figure 31.** Cross section of MM5 simulated potential temperature (K) on the 12-km domain at 0000 UTC, 19 September 1983, 12 h into CAPTEX Experiment 2B. Isentropes interval is 1 K. Dashed line indicates depth of the surface-based turbulent layer. Position of the warm front surface is superimposed. Location of the southwest-northeast cross section is shown in Figure 30. Line segments just below 1050 mb level each indicate 100 km distance from left.

simulated by SCIPUFF using the MM5 meteorology, to learn more about how the warm front may have interacted with the plume.

Notice that the nocturnal turbulent boundary layer at 0000 UTC (Fig. 31) occurs in a shallow zone that is thermally stable (i.e.,  $q$  increases with height), due to longwave radiational cooling of the surface early in the evening. Turbulence in this layer is generated by strong vertical wind shear, rather than by convectively driven buoyancy forces. This is especially true below the LLJ core over the Allegheny Mountains (600-700 km from the left in Fig. 32), where the shear is quite large below 925 mb. However, the turbulence is not confined to the shallow nocturnal boundary layer indicated in these two figures. Sporadic weaker turbulence also occurs above the boundary layer near the level of the LLJ core (in the old daytime PBL). Examination of the TKE fields at 0000 UTC and 0600 UTC (not shown) reveal that the surface-based nocturnal boundary layer deepens during the evening to 300-400 m, developing maximum TKE of 1.5-1.8 J kg<sup>-1</sup>. In the remnant of the old daytime mixed layer near the LLJ, sporadic TKE reaches values of 0.05-0.25 J kg<sup>-1</sup> (not shown). Although not very intense, this elevated turbulence is enough to mix the tracer in the fast-moving plume down to the surface. Thus, the model results in Exp. 2B are consistent with the hypothesis that nocturnal shear-induced turbulence causes vertical transport of the tracer despite low-level thermal stability. This is an important confirmation of the model's fine-grid resolution and physics, especially the 1.5-order TKE-predicting turbulence scheme, for simulating the complex boundary-layer meteorology encountered in real cases and over time scales associated with inter-regional plume transport.

Figure 32 gives additional clues into the possible role of the warm front, as it interacts with the tracer plume above the nocturnal boundary layer. Just to the lee (northeast) of the Allegheny Mountains, the downslope winds below 850 mb appear to be responsible for

(X1, Y1)=( 50, 70) (X2, Y2)=(1165, 155) CXW (m/s) | 1983-09-19\_00.00.36 SM= 0  
 (X1, Y1)=( 50, 70) (X2, Y2)=(1165, 155) WIND UV (m/s) | 1983-09-19\_00.00.36 SM= 0

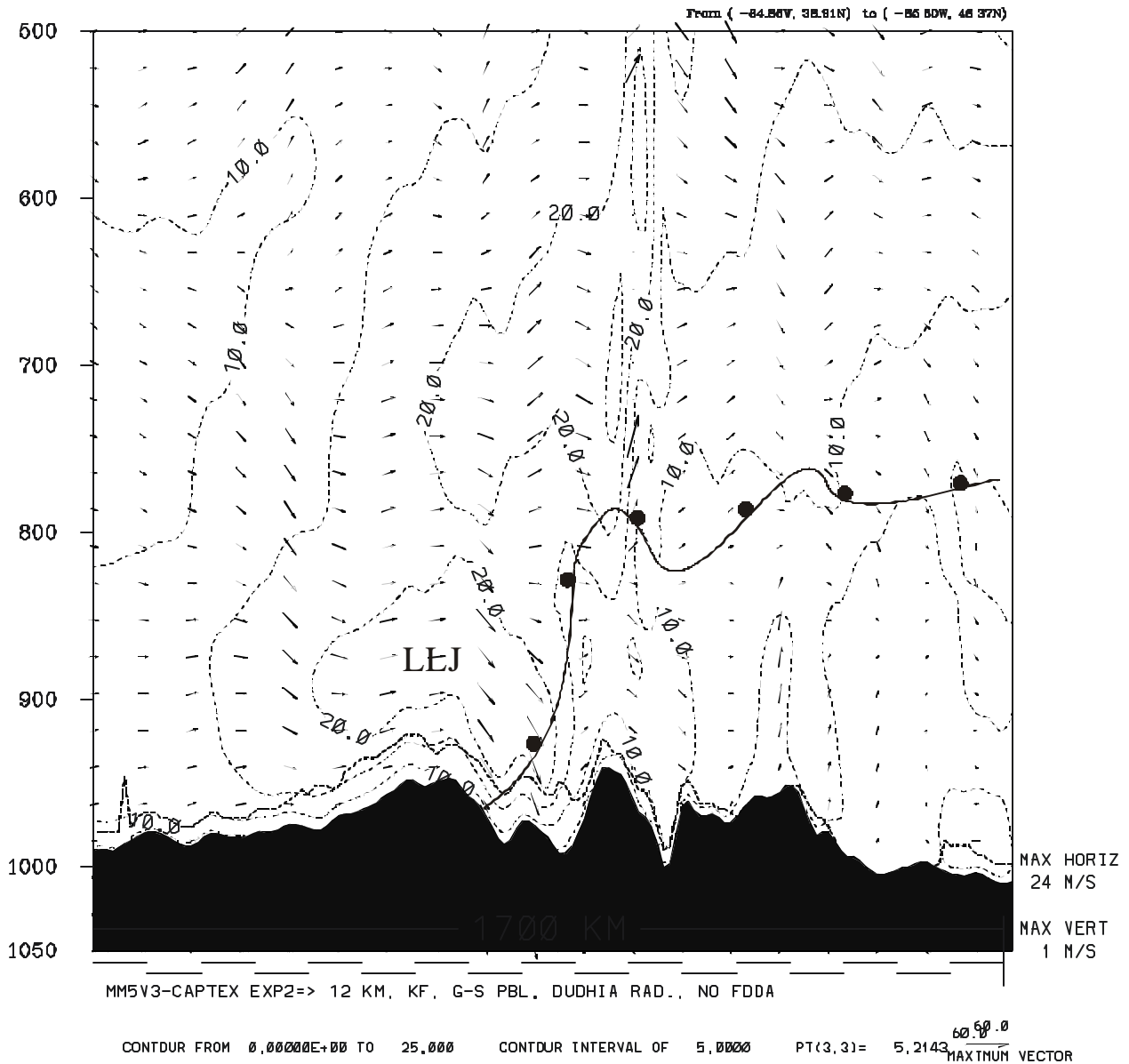


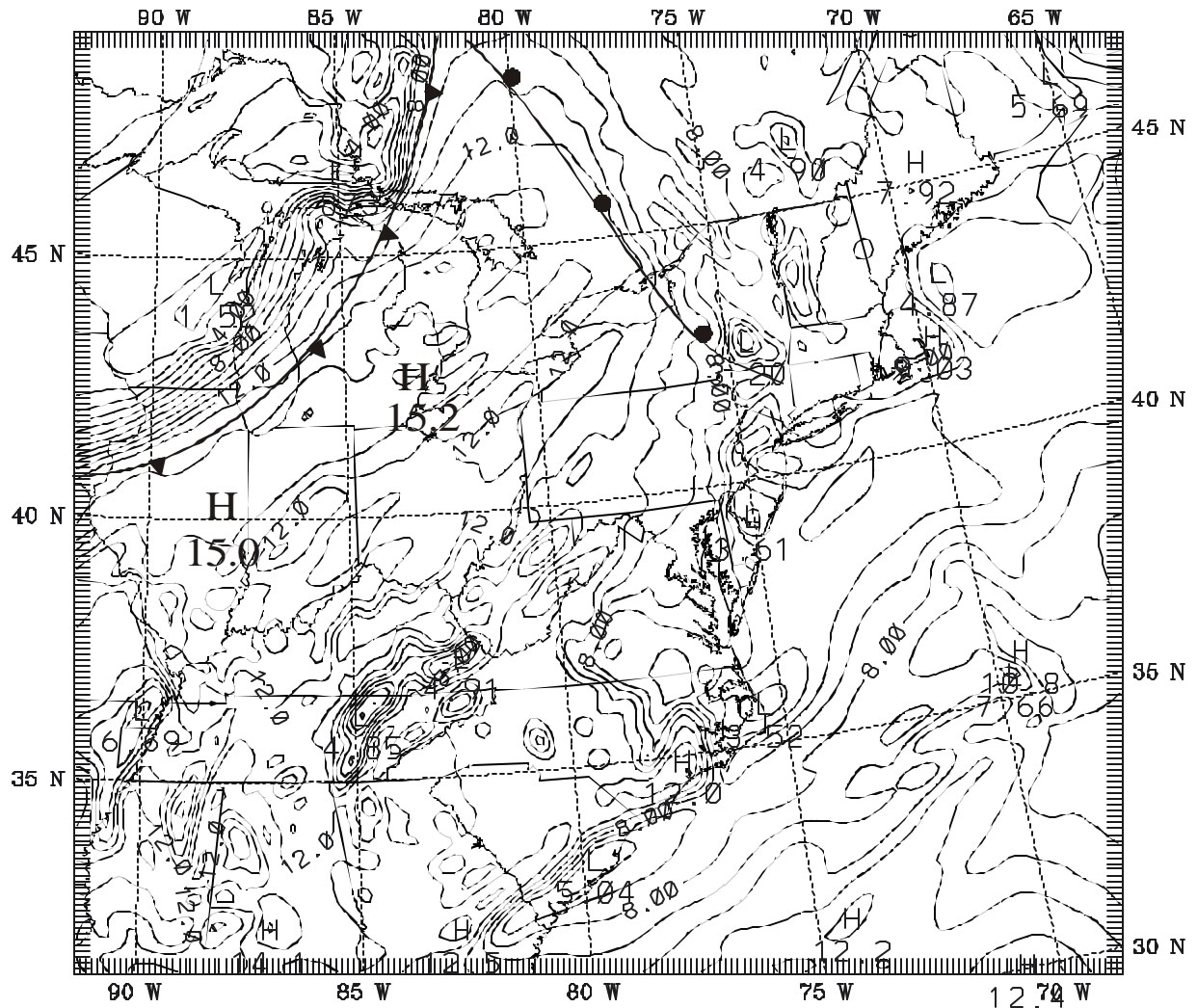
**Figure 32.** Cross section of MM5 simulated horizontal wind speed ( $\text{ms}^{-1}$ ) and wind vectors in the plane on the 12-km domain at 0000 UTC, 19 September 1983, 12 h into CAPTEX Experiment 2B. Isotach interval is  $5 \text{ ms}^{-1}$ . Vectors are exaggerated in the vertical by 100:1. Dashed line indicates depth of the surface-based turbulent layer. Position of the warm front surface is superimposed. Location of the southwest-northeast cross section is shown in Figure 30. Line segments just below 1050 mb level each indicate 100 km distance from left.

steepening the warm front over the Mohawk River Valley because the rapidly sinking air must experience adiabatic warming. However, just above the front between 750-850 mb, it appears that most of the winds from the Mohawk Valley to NH have a mean upward vertical component. This is consistent with the hypothesis that at least part of the forward edge of the plume may be lifted above the warm frontal surface. Figure 32 also shows that the greatest vertical motions in the cross section ( $\sim 1 \text{ m s}^{-1}$ ) occur above the warm front in a gravity wave induced over the Adirondack Mountains.

Lastly for this time, Figure 33 shows the water vapor mixing ratio ( $\text{g kg}^{-1}$ ) at 900 mb. The most obvious features in this field are the strong gradients of water vapor in the vicinity of the fronts, especially along the cold front. In the warm sector, there is a broad band of very moist air ( $\sim 15 \text{ g kg}^{-1}$ ) just ahead of the cold front, which provides an abundant moisture supply for the convective showers induced when this air is lifted by the approaching front. From OH to western NY, however, the warm sector is a bit less moist ( $10\text{-}12 \text{ g kg}^{-1}$ ). Thus, skies should remain mostly cloud free in the vicinity of the tracer plume, at least during the early evening.

By 1800 UTC, 19 September (+30 h), the sea-level pressure field in Figure 34 shows that the cold front in the MM5 Exp. 2B had advanced across northern New England, western and central NY and northern OH. Farther west in IL and IN, the front had first advanced southward, but in the past 6 h, it had begun to surge northward again as a warm front in response to the new storm intensifying in CO. Meanwhile, the original warm front had traveled rapidly northeastward and was leaving eastern ME by this time. Comparison with the manual mesoscale surface analysis (Figure 12) indicates that the simulated frontal positions in northern New England are fairly accurate, but the modeled front is almost 200 km too far south from NY to IL.

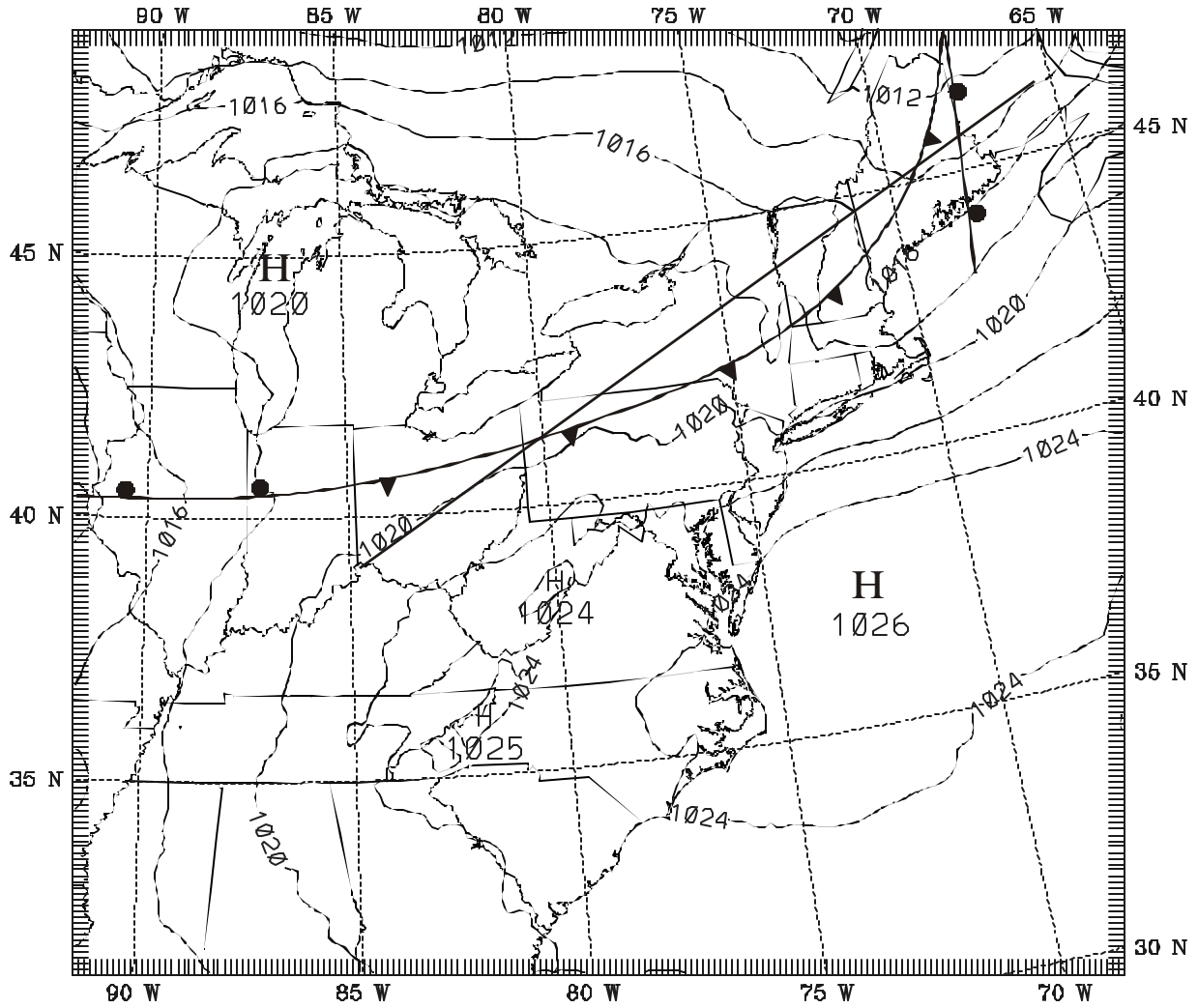
PRESSURE=900. mb QV lg/kg ) 1983-09-19\_00.00.36 = 1983-09-18\_12 + 12.01H SMOOTH= 3



MM5V3-CAPTEX EXP2=> 12 KM, KF, G-S PBL, DUDHIA RAD., NO FDDA  
CONTOUR FROM 0.0000E+00 TO 15.000 CONTOUR INTERVAL OF 1.0000 PT(3,31)= 12.500

Figure 33. MM5 simulation of 900-mb water vapor mixing ratio ( $\text{g kg}^{-1}$ ) on the 12-km domain at 0000 UTC, 19 September 1983, 12 h into CAPTEX Experiment 2B. Contour interval is  $1 \text{ g kg}^{-1}$ .

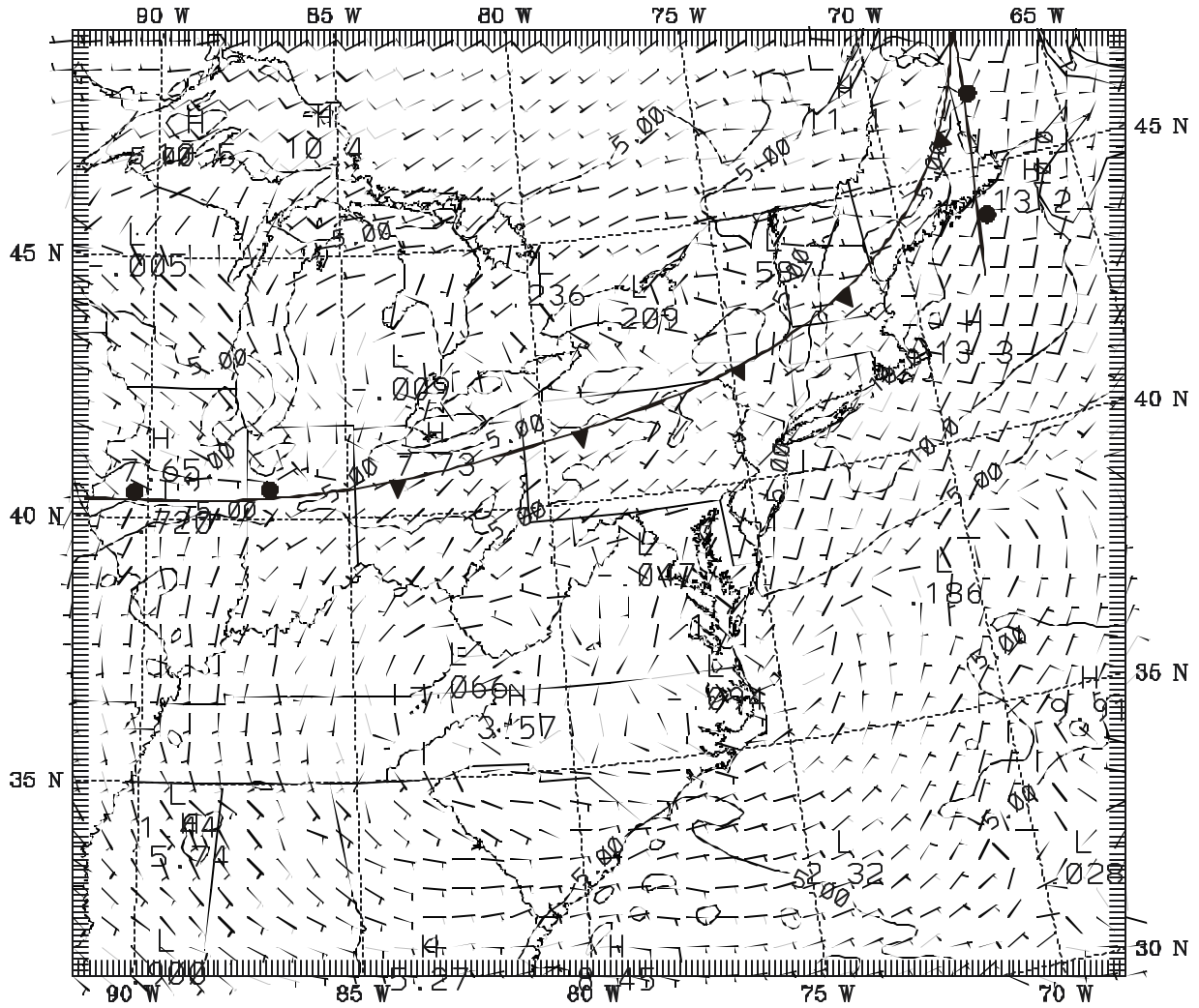
SIGMA =1.000 SEA PRES lmb ) 1983-09-19\_18.00.33 = 1983-09-18\_12 + 30.01H SMOOTH= 0



MM5V3-CAPTEX EXP2=> 12 KM, KF, G-S PBL, DUDHIA RAD., NO FDDA  
 CONTOUR FROM 1008.0 TO 1024.0 CONTOUR INTERVAL OF 2.0000 PT(3,31)= 1017.1

**Figure 34.** MM5 simulation of sea-level pressure (mb) on the 12-km domain at 1800 UTC, 19 September 1983, 30 h into CAPTEX Experiment 2B. Isobar interval is 2 mb. Location of a cross section identical to that shown in Figure 30 is indicated by the straight line from OH to ME.

SIGMA =0.996 WIND UV 1m/s ) 1983-09-19\_18.00.33 = 1983-09-18\_12 + 30.01H SMOOTH= 3  
 SIGMA =0.996 BARB UV 1m/s ) 1983-09-19\_18.00.33 = 1983-09-18\_12 + 30.01H SMOOTH= 0



MM5V3-CAPTEX EXP2=> 12 KM, KF, G-S PBL, DUDHIA RAD., NO FDDA  
 CONTOUR FROM 0.0000E+00 TO 10.000 CONTOUR INTERVAL OF 5.0000 PT(3,31)= 2.4224

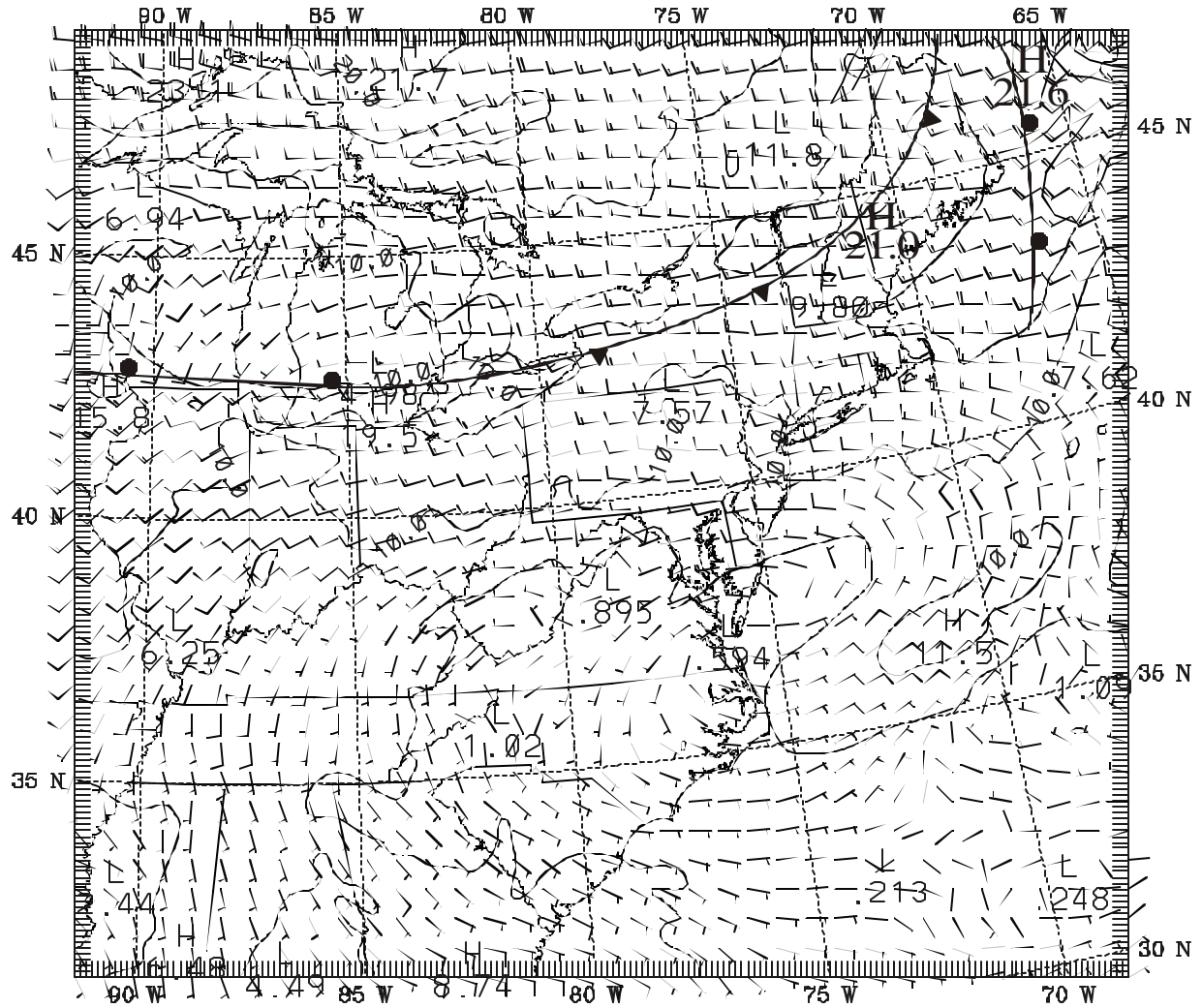
**Figure 35.** MM5 simulation of surface-layer winds ( $\text{m s}^{-1}$ ) on the 12-km domain at 1800 UTC, 19 September 1983, 30 h into CAPTEX Experiment 2B. Contour interval is  $5 \text{ m s}^{-1}$ .

The pressure field has been reproduced reasonably well in the model. At the same time, Figure 35 reveals that the surface-layer winds in Exp. 2B were simulated very well. Unlike Exp. 1A (see Figure 22), the winds behind the front in the western NY in Exp. 2B exhibit a clear convergent component that has kept the front moving slowly southeastward, rather than becoming quasi-stationary over Lake Ontario. These convergent surface winds along the front are confirmed by the observations in Figure 12. The rain showers simulated along the front from NY to ME were very light and widely scattered during the 6-h period ending at 1800 UTC, 19 September (Figure 36). However, from Lake Erie to IL, where warm moist air was overrunning the front, showers were more widespread and produced up to 21.5 mm (~0.82 in) of rain. The heaviest precipitation fell just north of the front in this region, but a few weaker showers were simulated between the Ohio Valley and the front, and also some light rain fell across the South in MS, GA and SC. This pattern is confirmed by the reports of observed rain at 1200 UTC and 1800 UTC (Figures 11 and 12), which indicate that most of the frontal rain occurred near 1200 UTC, while the showers across the deep South appeared close to 1800 UTC.

Next, examination of the mid-level atmosphere at 1800 UTC, 19 September, in Exp. 2B begins with the 850-mb winds shown in Figure 37. As for the 850-mb winds in Exp. 1A (Figure 23), the speeds in the LLJ at this level had decreased significantly from their maximum values at 0600 UTC the night before. However, Figure 37 shows winds of up to 21-22  $\text{ms}^{-1}$  remained in narrow bands just ahead of the cold and warm fronts in Maine and New Brunswick. The accompanying vertical structure of the atmosphere in the vicinity of the cold front is shown in the MM5's simulated sounding at Albany, NY, for 1800 UTC (Figure 38). At this time the surface cold front had almost reached Albany, but the surface winds were still from the southwest. The figure indicates that the depth of the mixed PBL is about 1100 m (slightly



PRESSURE=850. mb WIND UV |m/s ) 1983-09-19\_18.00.33 = 1983-09-18\_12 + 30.01H SMOOTH= 3  
 PRESSURE=850. mb BARB UV |m/s ) 1983-09-19\_18.00.33 = 1983-09-18\_12 + 30.01H SMOOTH= 0



MM5V3-CAPTEX EXP2=> 12 KM, KF, G-S PBL, DUDHIA RAD., NO FDDA  
 CONTOUR FROM 0.0000E+00 TO 20.000 CONTOUR INTERVAL OF 5.0000 PT(3,31)= 4.5644

Figure 37. MM5 simulation of 850-mb wind ( $\text{ms}^{-1}$ ) on the 12-km domain at 1800 UTC, 19 September 1983, 30 h into CAPTEX Experiment 2B. Isotach interval is  $5 \text{ms}^{-1}$ .

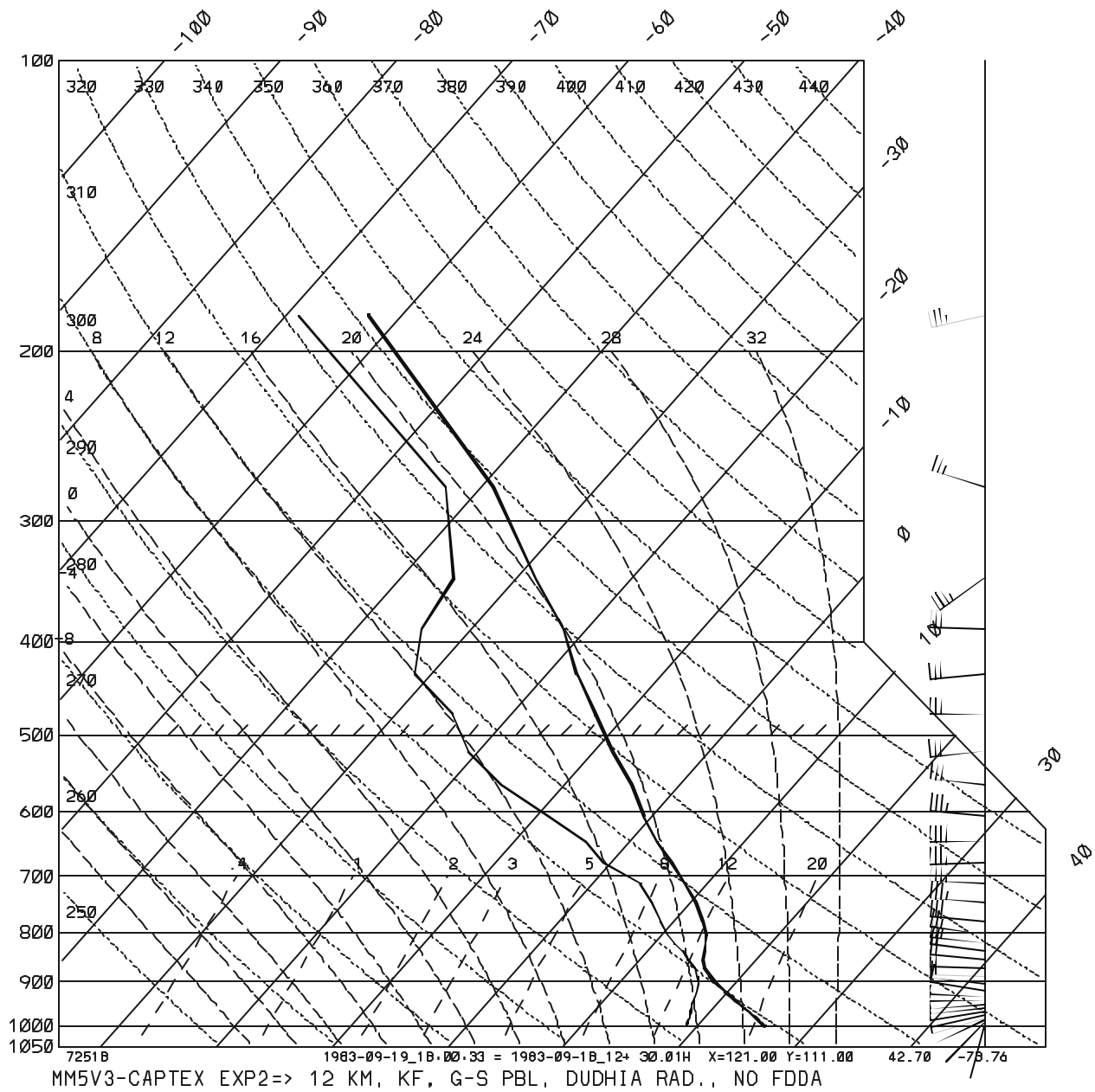
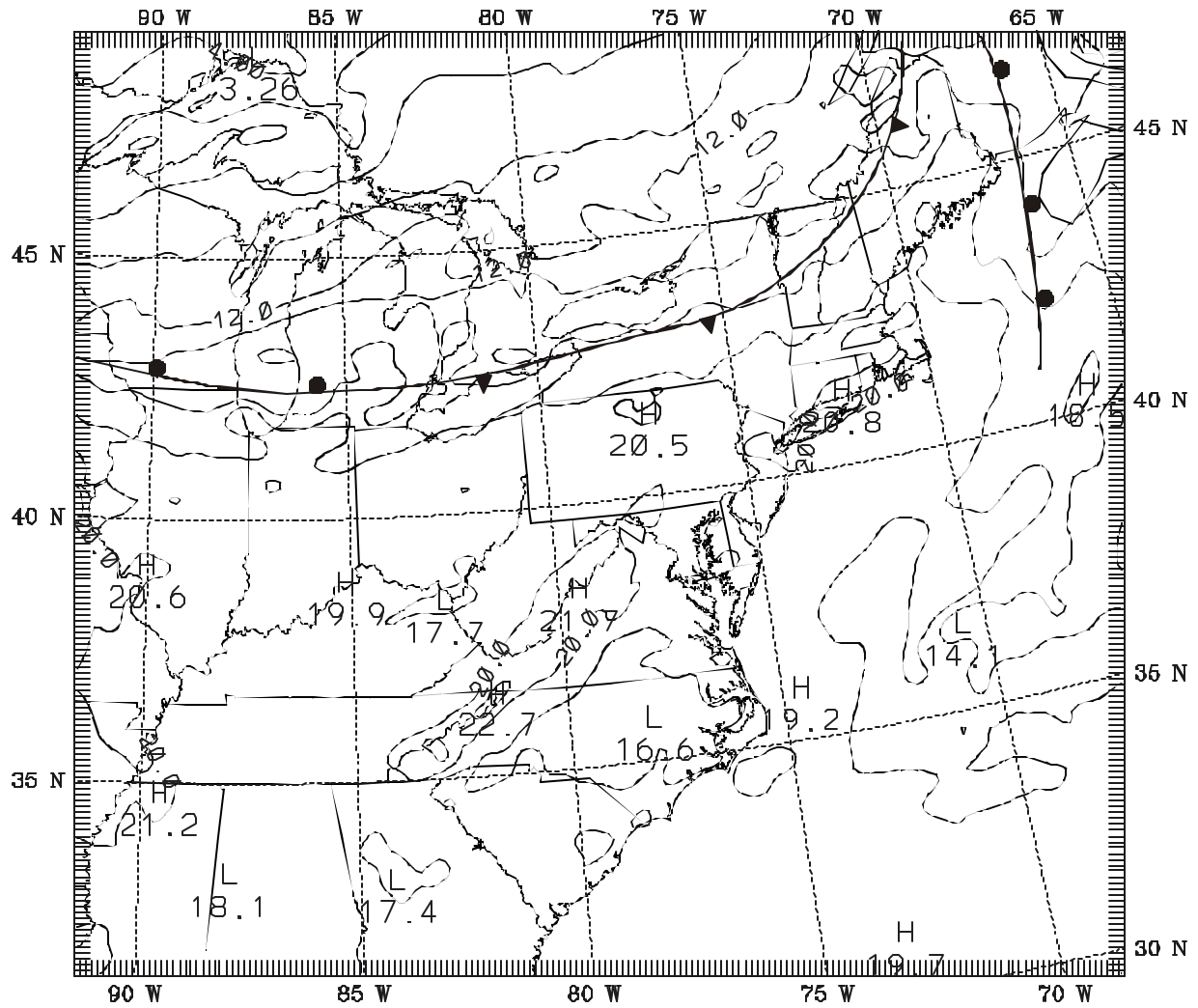


**Figure 38. MM5 sounding simulated at Albany, NY, 1800 UTC, 19 September 1983, 30 h into CAPTEX Experiment 2B. Winds are plotted in kts.**

deeper than in Exp. 1A; see Figure 24), but otherwise, there is little difference between this low-level structure and that found in earlier experiments. The most important differences between the Albany soundings simulated in Exps. 1A and 2B at this time are found above 500 mb. In Exp. 2B, the wind speeds are faster by  $\sim 5\text{-}10\text{ ms}^{-1}$  and the layers above 300 mb are more moist. The high-level moisture is due to the more efficient production of deep convection and the accompanying moist updrafts produced on the 12-km domain by the Kain-Fritsch cumulus parameterization.

The thermal and moisture fields aloft can be better understood by examining Figures 39-41. The 900-mb temperature field simulated in Exp. 2B at 1800 UTC, September 19, is shown in Figure 39. Comparison between the frontal positions at this level and those at the surface (see Figure 35) clearly shows the sloping structure of the fronts, as expected. The narrow wedge of warm air being advected northward in ME just ahead of the cold front is typical of maturing baroclinic systems and is clearly visible in this figure. The vertical cross section of potential temperature,  $q$ , presented in Figure 40, is especially revealing at this time, since it cuts through the leading edge of the cold air from northwestern PA to central ME (refer to Figure 34). This cross section also intersects the warm front in eastern ME. The frontal surfaces are diagnosed easily in the  $q$  field in Figure 40, even though the cross section is roughly parallel to the front and so does not show the full intensity of the thermal gradients. Together with the horizontal temperature, pressure and moisture fields at the surface and 900-mb, the cross section reveals clearly the 3-D atmospheric structure at this time. Notice that the PBL depth is quite deep ( $\sim 900\text{-}1100\text{ m}$ ) in the two segments lying in the warm sector (the left-most 600 km in Figure 40 and the 100 km wedge in ME just east of the White Mts.). Elsewhere, in the two segments lying in the cold air mass (the central 700-km segment from PA to ME and the 200-km segment at the



MM5V3-CAPTEX EXP2=> 12 KM, KF, G-S PBL, DUDHIA RAD., NO FDDA  
CONTOUR FROM 2.0000 TO 22.000 CONTOUR INTERVAL OF 2.0000 PT(3,31)= 20.126

**Figure 39.** MM5 simulation of 900-mb temperature (C) on the 12-km domain at 1800 UTC, 19 September 1983, 30 h into CAPTEX Experiment 2B. Isotherm interval is 2 C.

(X1,Y1)=( 50, 70) (X2,Y2)=(165,155) THETA (K ) 1983-09-19\_18.00.33 SM= 0

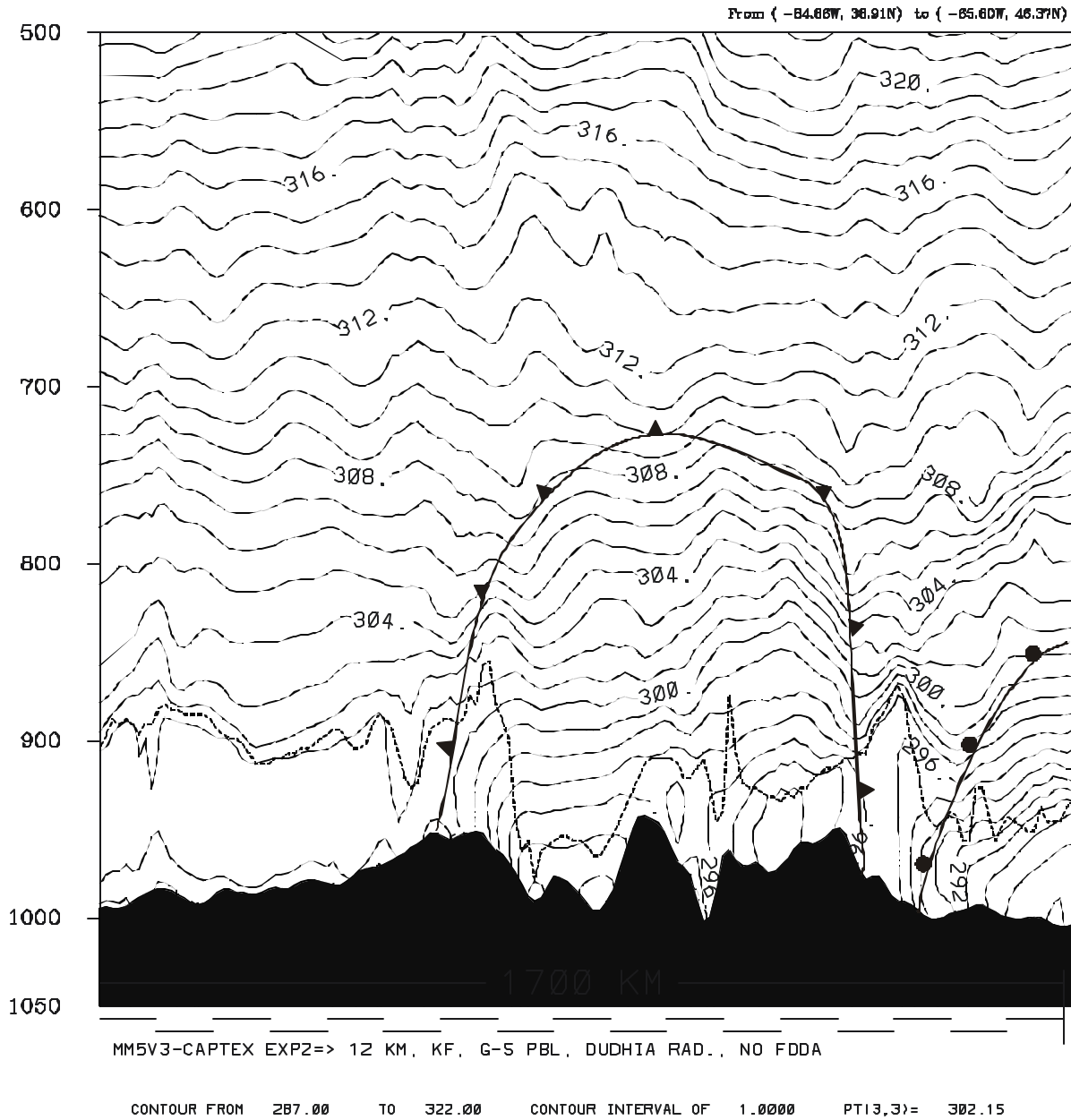


**Figure 40.** Cross section of MM5 simulated potential temperature (K) on the 12-km domain at 1800 UTC, 19 September 1983, 30 h into CAPTEX Experiment 2B. Isentropes interval is 1 K. Dashed line indicates depth of the surface-based turbulent layer. Position of the warm and cold frontal surfaces are superimposed. Location of the southwest-northeast cross section is shown in Figure 34. Line segments just below 1050-mb level each indicate 100 km distance from left.

(X1,Y1)=( 50, 70) (X2,Y2)=(165,155) CL WATER (g/kg ) 1983-09-19\_18.00.33 SM= 0

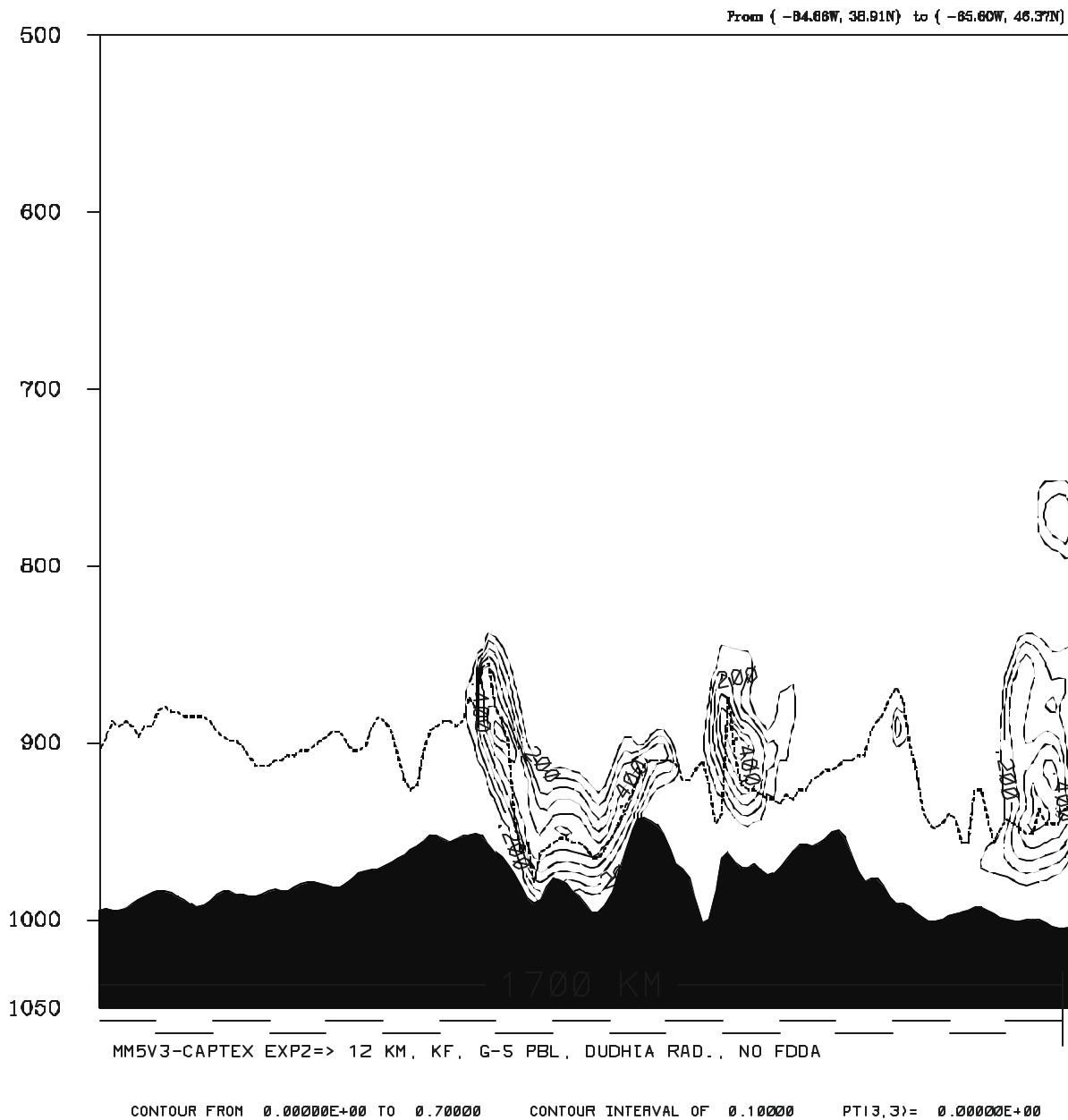


**Figure 41.** Cross section of MM5 simulated cloud liquid water ( $\text{g kg}^{-1}$ ) on the 12-km domain at 1800 UTC, 19 September 1983, 30 h into CAPTEX Experiment 2B. Contour interval is  $0.1 \text{ g kg}^{-1}$ . Dashed line indicates depth of the surface-based turbulent layer. Location of the southwest-northeast cross section is shown in Figure 34. Line segments just below 1050-mb level each indicate 100 km distance from left.

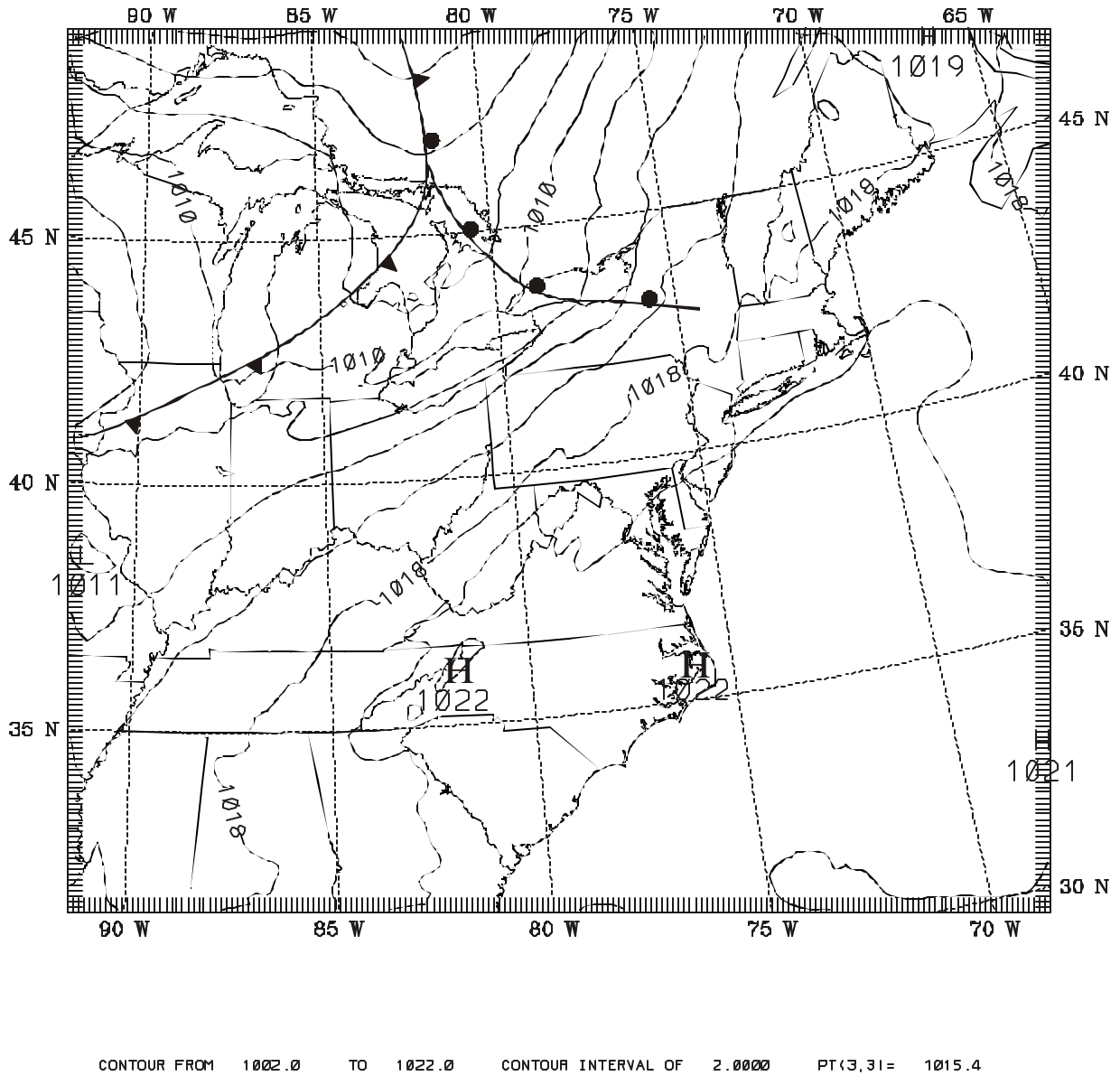
right-most end), the PBL averages about half as deep. The only significant exception is the deep PBL shown in a narrow band over the Allegheny Mts. just behind the cold front in northwestern PA. Finally, Figure 41 shows that the resolved-scale clouds in the cross section at this time are found mostly in the cold sectors and are confined to fairly low levels. However, note that the first contour is  $0.1 \text{ g kg}^{-1}$ , so that there can be extensive areas of visible cloud with low water content that are not shown.

As discussed earlier, this complex frontal structure may play an important role in the dispersion of the tracer plume for Episode 1. The examination of model fields presented here also shows how a numerical model can reveal details of the 3-D mesoscale structure that would normally be difficult or impossible to analyze directly from radiosonde data because of the wide spacing of the observing network.

Having completed the examination of Exp. 2B, we next move forward to inspect the fields produced by MM5 in Exp. 2D, in which FDDA was added to reduce the growth of errors remaining in the earlier experiments using Configuration 2. Since Exp. 2B was discussed in detail, we will concentrate only on describing the most important differences found in Exp. 2D.

First, the sea-level pressure field from Exp. 2D at 0000 UTC, 19 September (+12 h) is shown in Figure 42. Comparison with the corresponding manual analysis in Figure 9 and the MM5 simulation from Exp. 2B in Figure 26 shows that the use of FDDA in Exp. 2D had virtually no effect on the frontal positions at this time. Closer inspection of Figures 9, 26 and 42, however, reveals that the FDDA has improved the accuracy of the pressure field in subtle ways. Specifically, it has lowered the model errors by reducing the intensity of the high pressure system building into WI behind the cold front, by slightly weakening the high pressures over western NC and by slightly intensifying the ridge over ME. Most of the other fields in Exp. 2D

SIGMA =1.000 SEA PRES 1mb ) 1983-09-19\_00.00.36 = 1983-09-18\_12 + 12.01H SMOOTH= 0



at 0000 UTC, 19 September also showed generally similar solutions to those discussed for Exp. 2B. For example, the winds at the surface and 850 mb were very much alike in the two experiments (not shown). The dominant features of the precipitation pattern were the same, although there was more rain over IL in Exp. 2B and less over southern Ontario. The additional rain over IL (up to 39 mm in 6 h) represents an over-prediction of observed rain at this time in Exp. 2D (~3-6 mm in 6 h was observed at most stations reporting rain).

Meanwhile, Figure 43 shows some important changes in Exp. 2D at 0000 UTC in the vertical structure of the potential temperature through the warm front. Comparison of the frontal structure in Exp. 2D with that shown in Figure 31 for Exp. 2B reveals that the front aloft is more diffuse in Figure 43 and the terrain-induced gravity waves have been damped significantly. The low-level thermal structure (below 850 mb) is rather similar in the two figures, which reflects success of the strategy to remove the FDDA below 1.5 km in this experiment (see Table 4). This FDDA strategy prevented weakening of the intense gradients in the layers most important for pollutant transport. Of course, such small-scale features as the frontal gradients and gravity waves could not be resolved by the widespread radiosonde observations on which the analyses are based. This explains the general reduction of mesoscale details in the MM5 solutions above 850 mb in Exp. 2D, despite the overall favorable outcome due to FDDA.

To summarize these results, it appears that assimilation of the synoptic-scale analyses helped to reduce errors in larger-scale features (such as the improvements noted for the sea-level pressure field in Figure 42). However, the data assimilation simultaneously can erode mesoscale features and can weaken mid-level stable layers that tend to inhibit deep convection. Consequently, the FDDA strategy was intentionally designed with a lower nudging coefficient,  $G$ , on the 12-km domain and it eliminated nudging toward the 3-D analyses altogether below 850

(X1,Y1)=( 50, 70) (X2,Y2)=(165,155) THETA (K | 1983-09-19\_00.00.36 SM= 0

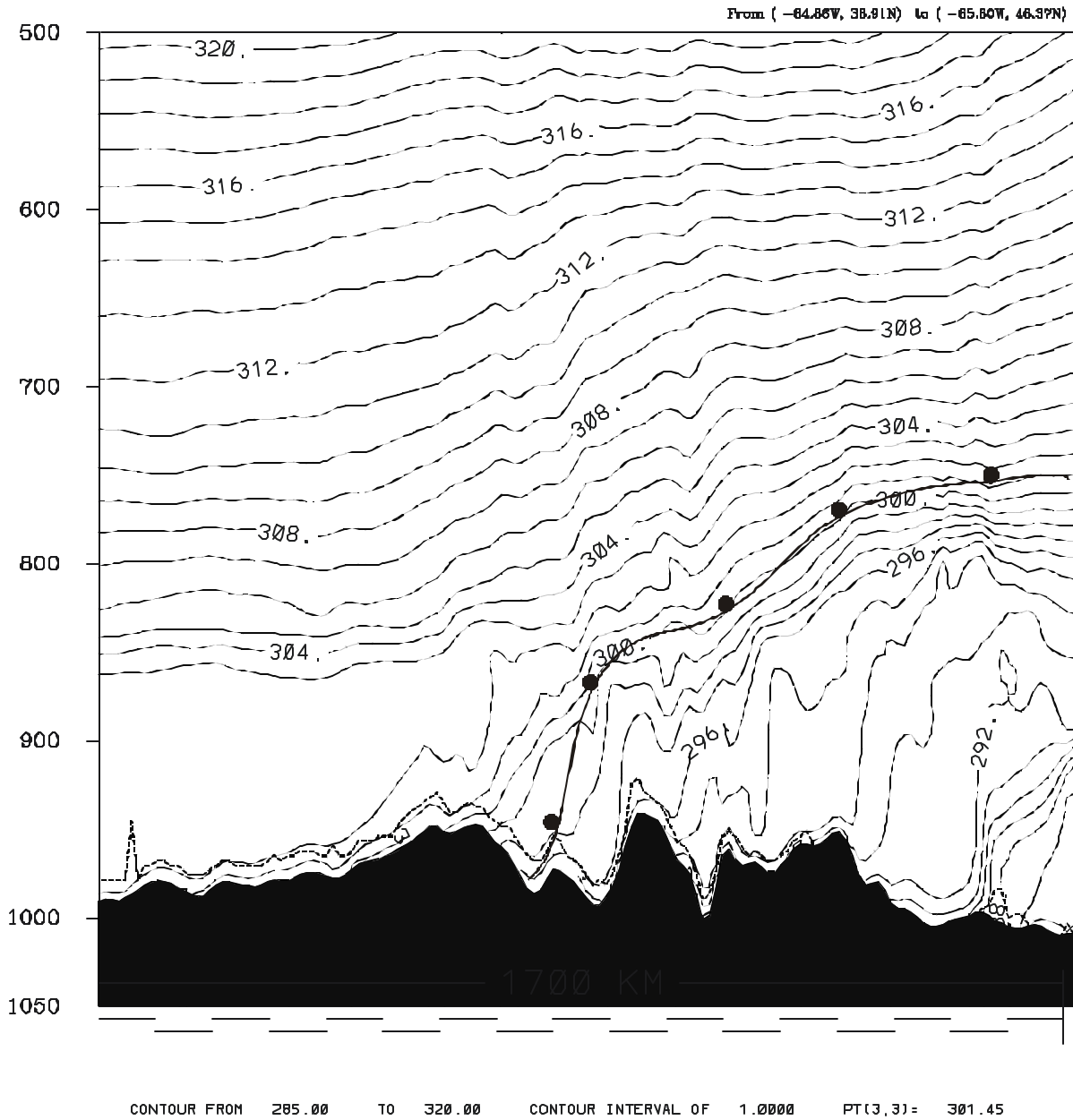
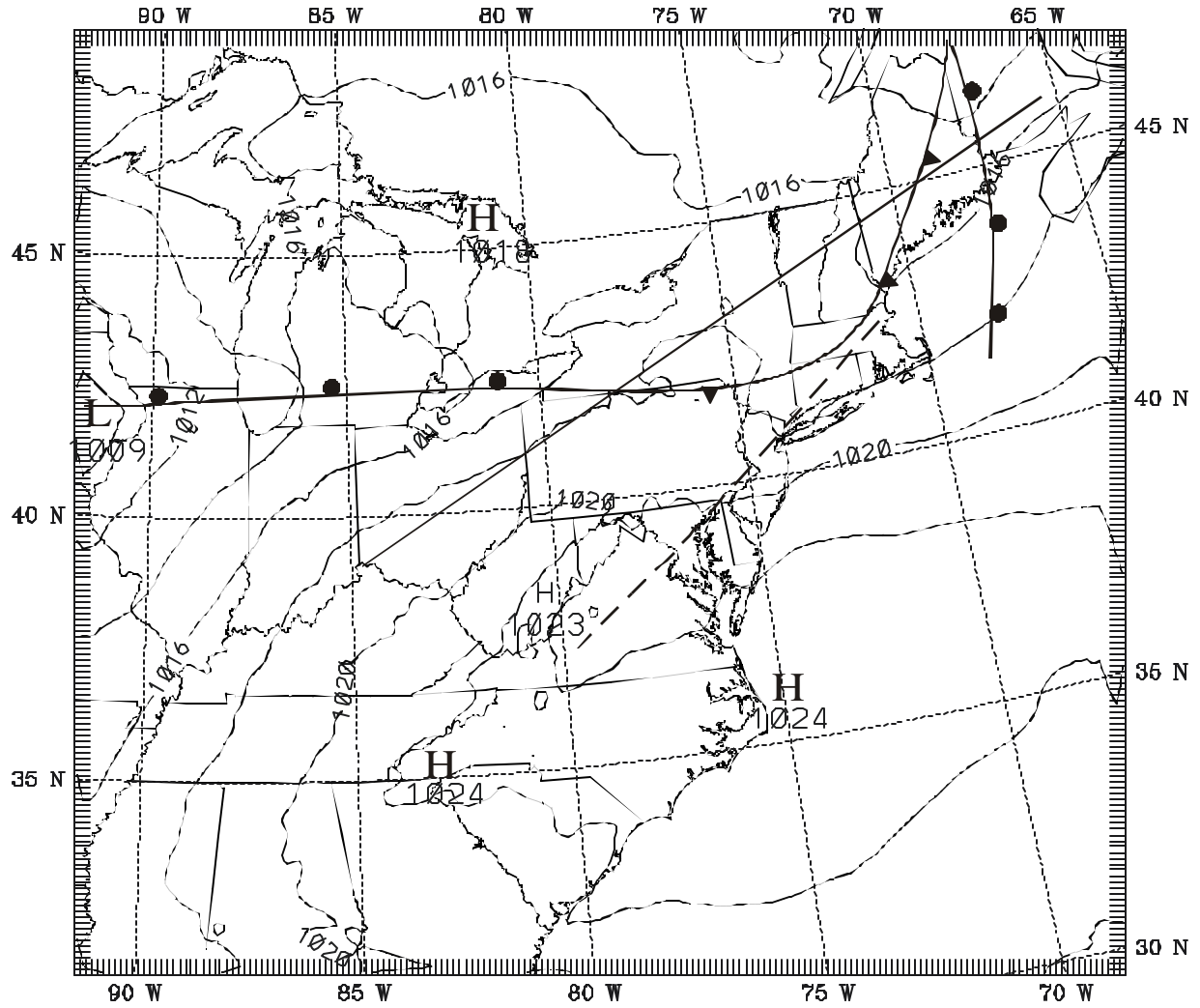


**Figure 43.** Cross section of MM5 simulated potential temperature (K) on the 12-km domain at 0000 UTC, 19 September 1983, 12 h into CAPTEX Experiment 2D. Isentropes interval is 1 K. Dashed line indicates depth of the surface-based turbulent layer. Position of the warm front surface is superimposed. Location of the southwest-northeast cross section is shown in Figure 30. Line segments just below 1050 mb level each indicate 100 km distance from left.

mb, where the tracer plume was expected to be confined. In this case, a change in the amplitude of the gravity waves may be of little importance for the dispersion of the plume (unless breaking gravity waves induce turbulence in otherwise smooth air). However, a significant weakening of the front could affect its ability to lift the warm air mass carrying the tracer above the surface. That could result in an increase in the surface tracer concentrations simulated ahead of the warm front. On the other hand, increased convection could transport tracer material into the upper troposphere in convective updrafts. Therefore, in this case, FDDA could produce both positive and negative changes in the overall ability of the mesoscale model to generate realistic meteorological solutions for inter-regional transport. The examination of the SCIPUFF results in Section 5.4 should help to address these concerns.

Later, at 1800 UTC, 19 September (+30 h), Figure 44 shows that errors in the frontal positions simulated in Exp. 2B have been reduced dramatically in Exp. 2D as a result of the FDDA (compare with Figures 12 and 34). In Figure 44, the data assimilation has caused the warm front over the Midwest to advance northward more rapidly, so that its position now agrees very well with the manual analysis in Figure 12. There have been comparatively few changes in the frontal positions over New England, relative to Exp. 2B, although the surface trough near the Mid-Atlantic coast is more distinct. Thus, even though there was little sign of improvement in the frontal boundaries due to FDDA early in the simulations at 0000 UTC, the cumulative effect of the data assimilation still had desirable effects. Again, the sea-level pressures are also more accurate in Exp. 2D. For example the advancing low-pressure area in eastern IA is deeper by 4 mb and better matches observed pressures, while the Mid-Atlantic ridge has been corrected by decreasing its central pressure by ~2 mb. Although the pattern of accompanying surface-layer winds is mostly similar in Exps. 2B and 2D (not shown), these pressure changes certainly

SIGMA =1.000 SEA PRES lmb ) 1983-09-19\_18.00.33 = 1983-09-18\_12 + 30.01H SMOOTH= 0



CONTOUR FROM 1008.0 TO 1022.0 CONTOUR INTERVAL OF 2.0000 PT(3,31)= 1016.3

**Figure 44.** MM5 simulation of sea-level pressure (mb) on the 12-km domain at 1800 UTC, 19 September 1983, 30 h into CAPTEX Experiment 2D. Isobar interval is 2 mb. Location of the a cross section identical to that shown in Figure 30 is indicated by the straight line from OH to ME.

indicate reductions in the low-level errors that may have non-trivial impacts on the model's ability to represent inter-regional transport in the boundary layer.

Most of the other fields produced in Exp. 2D at 1800 UTC, 19 September (+30 h) show patterns that are basically similar to those noted earlier at 0000 UTC (+12 h), but with some changes in intensity or magnitude. For example, the 6-h rainfall was somewhat less widespread, which represents an improvement at this time. Primarily, the rain was concentrated just north and south of the main frontal band stretching from western New England to IL (not shown). Only a few isolated showers fell elsewhere across the South. Also, as found at 0000 UTC, the 6-h rain maxima were heavier than in Exp. 2B, reaching 33 mm (~1.3 in.) over southern WI, which is more realistic at this time. Both the rain totals and the distribution appear to have been improved by the FDDA in this case. The heavier rainfall along the front in Exp. 2D due to the FDDA, particularly from western NY to IL, was consistent with the 850-mb wind pattern, which showed  $\sim 5 \text{ ms}^{-1}$  stronger overrunning winds in the Midwest carrying moist air above the warm front (not shown). (Recall that there is no assimilation of rain data, so that this change has to occur through assimilation of wind, temperature and water vapor.) At the same time, the 850-mb winds over northern New England were reduced by 3-6  $\text{ms}^{-1}$  in Exp. 2D. Statistical evaluations of these upper-level winds will be used to quantify the net changes in skill, if any, that results from addition of the data assimilation (see Section 5.2).

Next, Figure 45 shows the vertical cross section of potential temperature,  $q$ , in Exp. 2D taken along the southwest-northeast slice through the fronts at 1800 UTC, 19 September. Comparison with the similar cross section from Exp. 2B (Figure 40) reveals the same general pattern for the frontal zones in the vertical plane, except that the gradients of  $q$  have been weakened substantially above 850 mb. This makes it difficult to identify the top of the cold-air

(X1,Y1)=( 50, 70) (X2,Y2)=(165,155) THETA (K ) 1983-09-19\_18.00.33 SM= 0

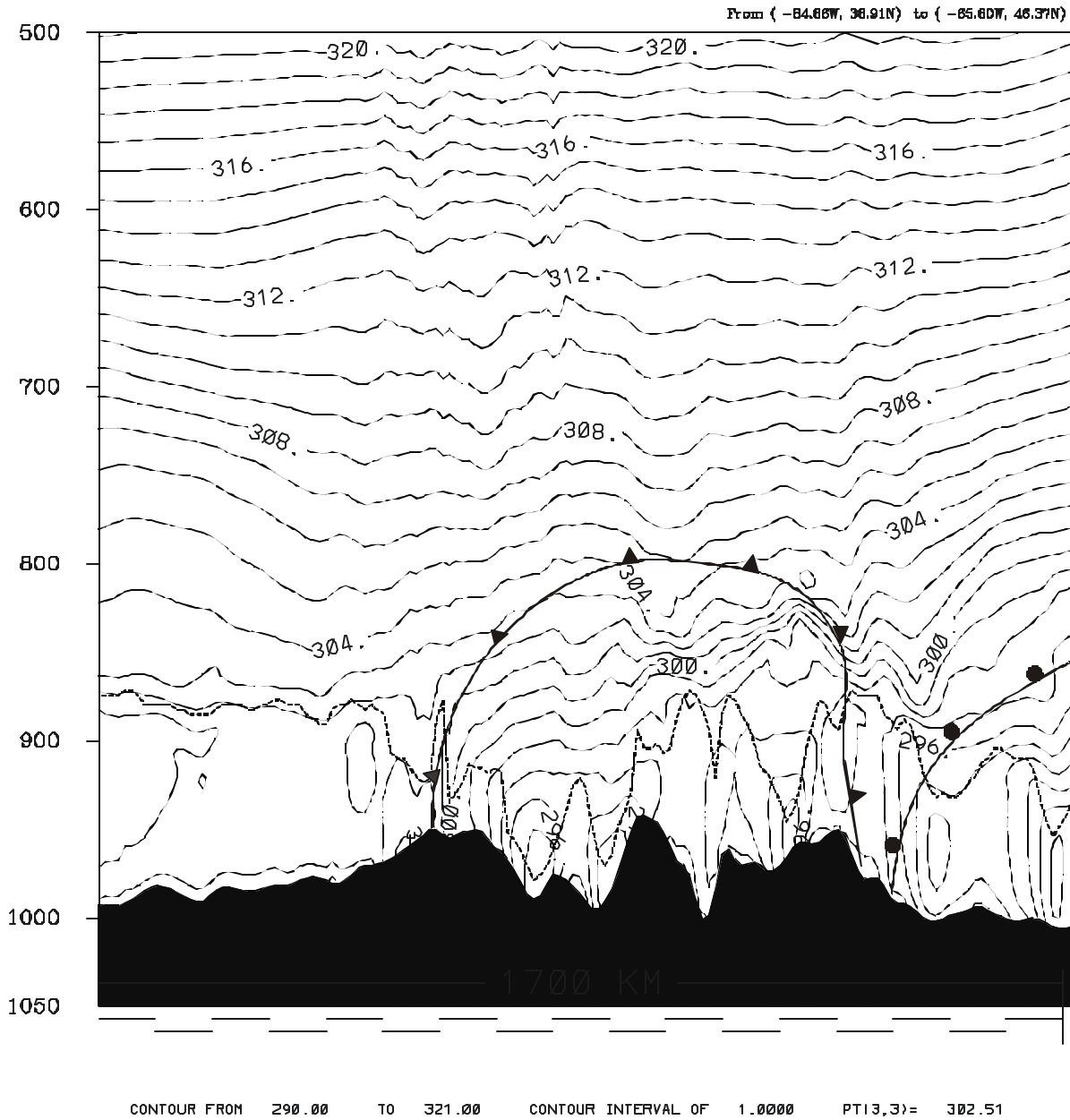


**Figure 45.** Cross section of MM5 simulated potential temperature (K) on the 12-km domain at 1800 UTC, 19 September 1983, 30 h into CAPTEX Experiment 2D. Isentropes interval is 1 K. Dashed line indicates depth of the surface-based turbulent layer. Position of the warm and cold frontal surfaces are superimposed. Location of the southwest-northeast cross section is shown in Figure 44. Line segments just below 1050-mb level each indicate 100 km distance from left.

wedge in Figure 45, especially since this slice is almost parallel to the front. The weakening of the vertical gradient of  $q$  occurs because the 3-D analyses of the thermal field, assimilated by the FDDA scheme, lack adequate resolution and upper-air data to accurately define these gradients. Thus, directly over the Adirondack Mts. in the center of the cross section, the 312 K isentrope is about 50 mb higher in Exp. 2D and the 304 K isentrope is about 20 mb lower. Below 850 mb, where the FDDA strategy prevents nudging toward the synoptic-scale analyses, the gradients remain fairly strong. Therefore, the application of FDDA may reduce the overall statistical error in the upper levels, while at the same time leaving some important mesoscale features weaker if they were poorly resolved in the analyses used in the assimilation (dependent on upper-air data availability). Of course, care needs to be taken when interpreting the results of data-assimilating meteorological models to understand the implications of such effects on inter-regional transport and other air-quality related problems.

### ***5.1.3 Configuration 3***

As described in Table 3, the design of Exp. 3A was similar to that of Exp. 2D (advanced physics, plus FDDA at the surface and aloft), except that a 4-km domain was added over the region covered by the CAPTEX-83 monitoring network. On the 36-km and 12-km domains the data-assimilation strategy was identical to that used in Exp. 2D, but no data assimilation was applied on the 4-km domain. The 4-km domain responds to the data assimilation only through the lateral boundaries where the 12-km solutions are imposed. Therefore, the FDDA strategy in Exp. 3A was designed to correct large-scale errors, such as phase-speed errors in the synoptic-scale systems by nudging the solutions on the outer domains, while allowing the model's

dynamics and physics to act without interference on the inner domain to generate mesoscale structure. This strategy is especially appropriate for modeling the CAPTEX-83 cases because there are insufficient special meteorological observations to resolve the mesoscale details that are expected to develop in the solutions on the 4-km domain.

By 0000 UTC, 19 September (+12 h), the sea-level pressure field in Exp. 3A (Figure 46) indicates that the fronts were moving a bit too rapidly across the 4-km domain (compared to the manual analysis in Figure 9 and the MM5 simulation for Exp. 2D in Figure 42). However, Figure 47 shows that the surface-layer wind field matches reasonably well with the observed winds of the analysis (Figure 9). Next, Figure 48 shows the 6-h rainfall totals on the 4-km domain. This figure indicates that rain was limited almost entirely to the area north of the warm front from northern NY to Ontario, with local maximums of 13 - 20 mm (~0.5 to 0.8 in.). The largely spurious rains that were evident on the 12-km domain in Exp. 2B (see Figure 28) in the northern part of the warm sector (southern Ontario) are completely missing in Exp. 3A. As mentioned earlier, the observed 6-h rain totals in Figure 9 were on the order of 3-6 mm. However, further examination of the manual analysis in Figure 8 reveals that at the beginning of the 6-h period in question, there were quite a few thunderstorms in the vicinity of Lake Ontario. These storms had been producing between 25 and 60 mm of rain. Comparison of Figures 8 and 9 also shows that there was a lot of missing data over Ontario at 0000 UTC. Thus, it is very possible that quite a lot of rain could have fallen north of Lake Ontario between 1800 UTC and 0000 UTC in the temporary data void. The heavy thunderstorm activity in the area just a few hours before seems to support this possibility. Moreover, both the analyses (Figures 8 and 9)

SIGMA =1.000 SEA PRES lmb ) 1983-09-19\_00.00.02 = 1983-09-18\_12 + 12.00H SMOOTH= 0

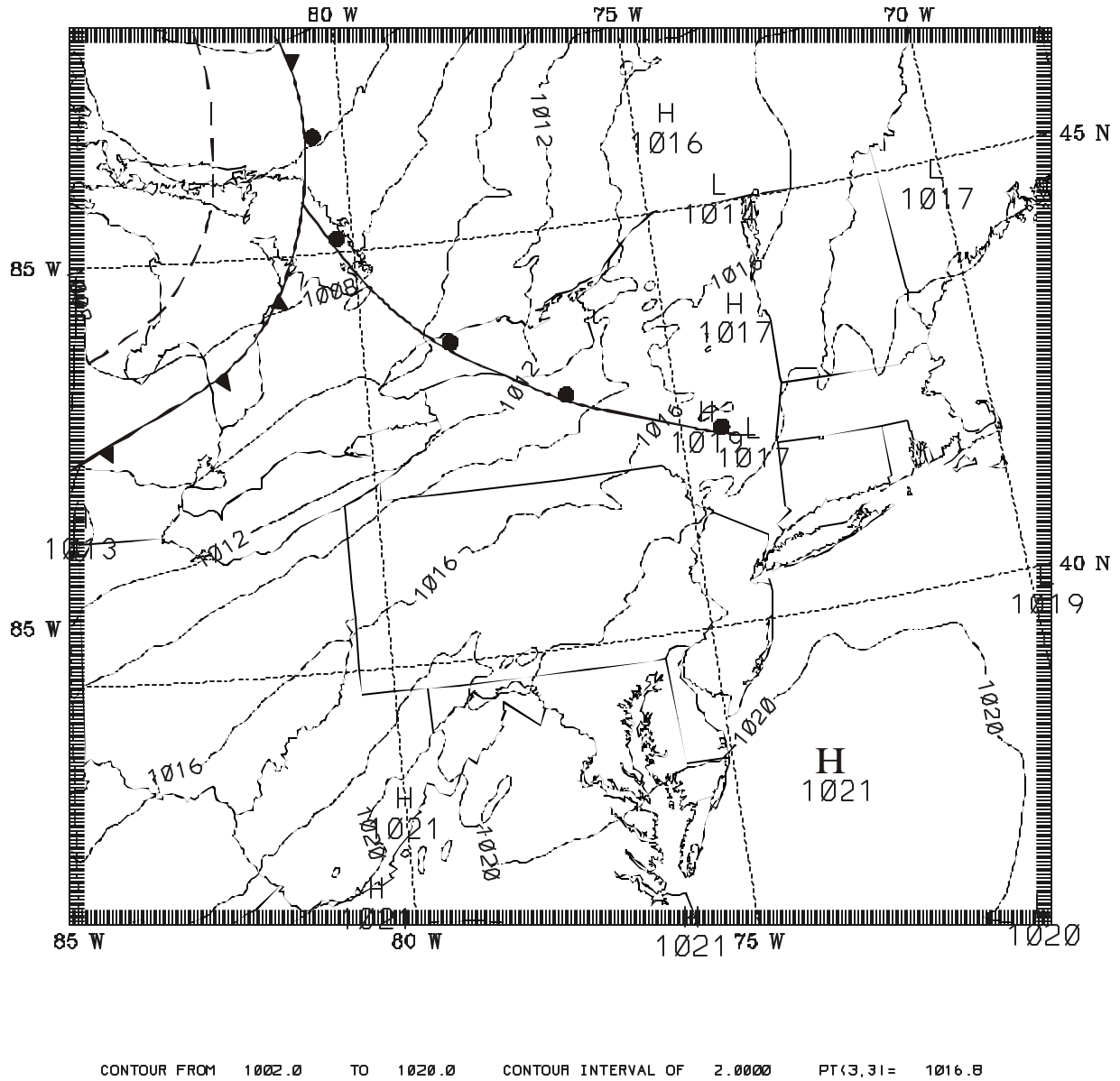
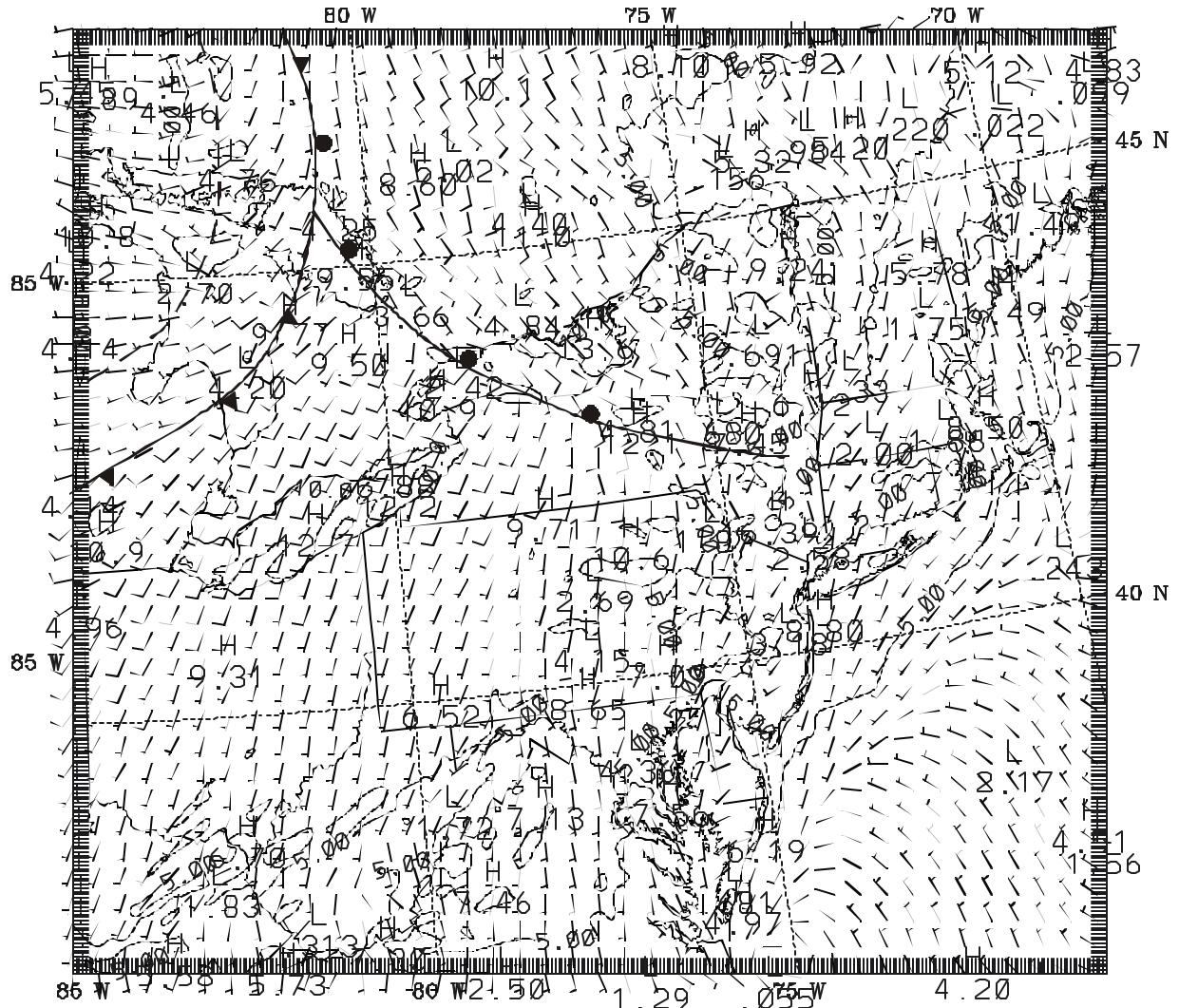


**Figure 46.** MM5 simulation of sea-level pressure (mb) on the 4-km domain at 0000 UTC, 19 September 1983, 12 h into CAPTEX Experiment 3A. Isobar interval is 2 mb.

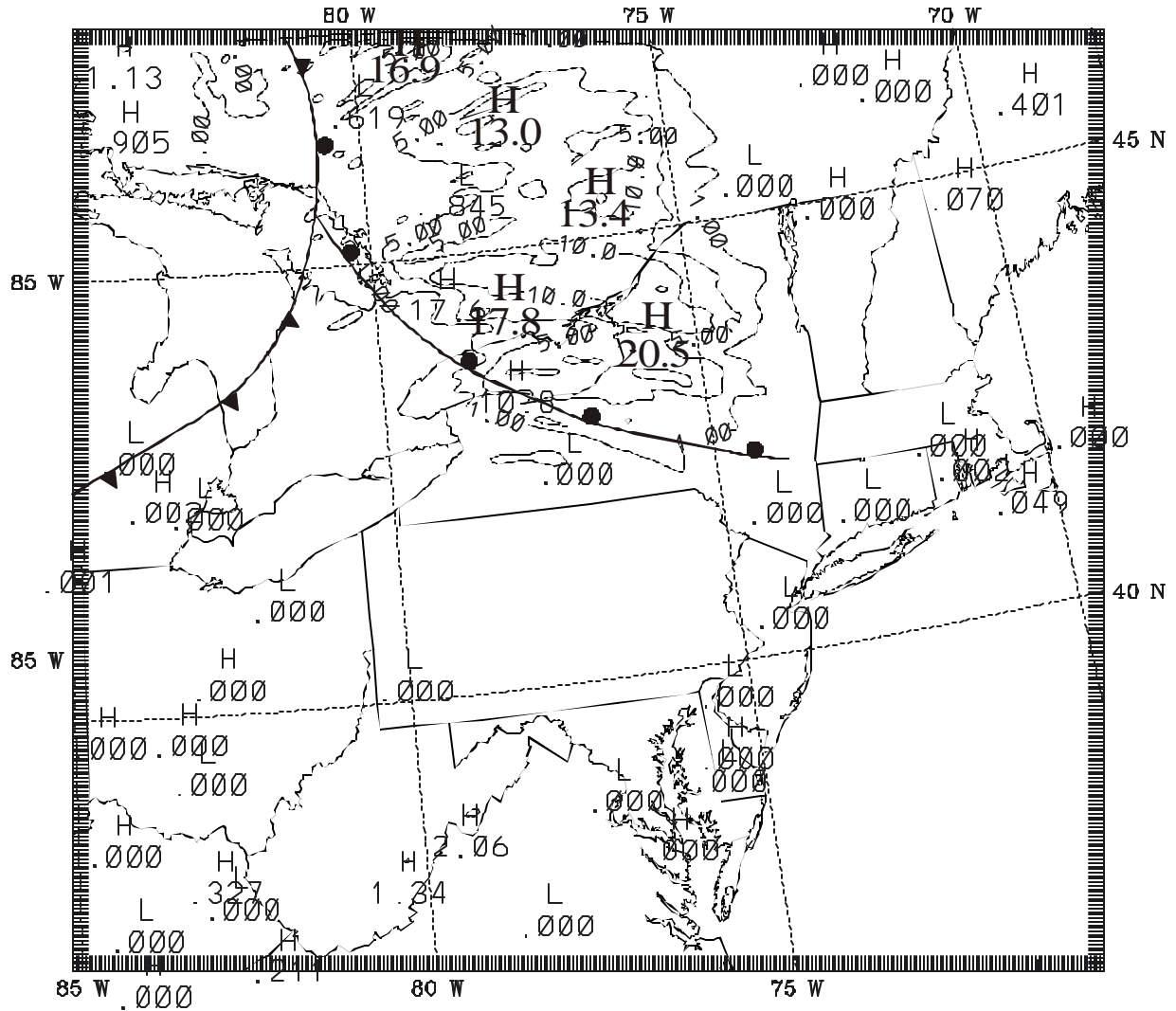
SIGMA =0.996 WIND UV 1m/s ) 1983-09-19\_00.00.02 = 1983-09-18\_12 + 12.00H SMOOTH= 3  
 SIGMA =0.996 BARB UV 1m/s ) 1983-09-19\_00.00.02 = 1983-09-18\_12 + 12.00H SMOOTH= 0



MM5V3-CAPTEX EXP. 3A => 4KM,KF,G-SPBL  
 CONTOUR FROM 0.0000E+00 TO 10.000 CONTOUR INTERVAL OF 5.0000 PT(3,31)= 4.7948

**Figure 47.** MM5 simulation of surface-layer winds ( $\text{m s}^{-1}$ ) on the 4-km domain at 0000 UTC, 19 September 1983, 12 h into CAPTEX Experiment 3A. Contour interval is  $5 \text{ m s}^{-1}$ .

SIGMA =1.000 TEND RNT lmm ) 1983-09-19\_00.00.02 = 1983-09-18\_12 + 12.00H SMOOTH= 0



MM5V3-CAPTEX EXP. 3A => 4KM,KF,G-SPBL  
 CONTOUR FROM 000000 TO 200000 CONTOUR INTERVAL OF 5.0000 PT(3,31)= 0.24696E-26

**Figure 48.** MM5 simulation of 6-h rainfall (mm) on the 4-km domain for the period ending at 0000 UTC, 19 September 1983, 12 h into CAPTEX Experiment 3A. Contours are at 1, 5, 10, and 20 mm.

show little or no rain with the cold front as it passed over Lake Huron and eastern MI. Consequently, it appears that the model's 4-km rainfall, although different from the 12-km rainfall, could be very reasonable during this early stage of the MM5 simulation at 0000 UTC, 19 September.

Visual inspection of the wind field at 850 mb for Exp. 3A (not shown) revealed mostly similar characteristics to those shown in Figure 29 for the 12-km domain in Exp. 2B. The LLJ simulated over Lake Ontario had a maximum speed of almost  $26 \text{ ms}^{-1}$  at 0000 UTC. However, the horizontal extent of the area having winds exceeding  $20 \text{ ms}^{-1}$  was less in Exp. 3A than in Exp. 2B, with somewhat weaker winds over southeast MI and northwest OH. Figures 49-51 give additional insights into the differences in the vertical structure of the 12-km and 4-km model solutions at 0000 UTC. First, for the vertical plane of the cross section identified in Figure 49, the warm front and the potential temperature,  $q$ , are shown at this time in Figure 50. As noted earlier in Exp. 2B, the packing of the isentropes in the frontal zone also is clearly evident in Exp. 3A. Recall that even though data assimilation is used in Exp. 3A, it was not applied on the 4-km domain, so the effects of the data assimilation are felt only through the lateral boundary conditions. This strategy prevented the spurious damping of the mesoscale frontal structure and gravity waves above 850 mb (Figure 50) that had characterized the solutions on the 12-km domain in Exp. 2D (see Figure 43). Thus, this experiment design appears to be a suitable way of preserving most of the mesoscale features in the fine-mesh model solutions, even though many of the mesoscale details on the 12-km domain are likely to be damped by assimilating coarse-mesh analyses.

Further examination of the cross sections for Exp. 3A reveals potentially important vertical processes that were not evident on the 12-km domain. Notice, for example, that the

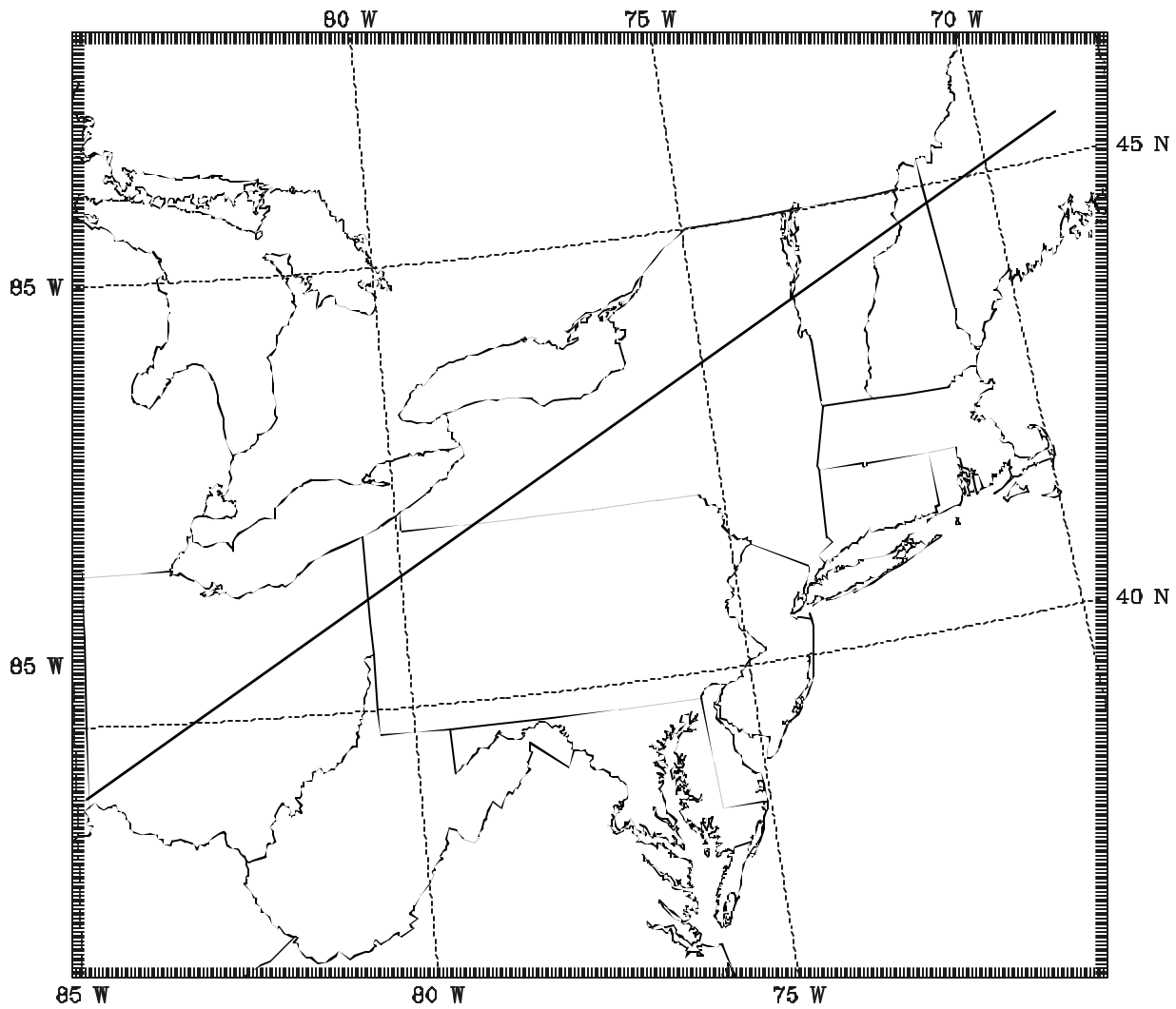


**Figure 49.** Location of southwest to northeast cross section on the 4-km domain for CAPTEX Episode 1. The cross section is oriented to lie approximately along the centerline of the surface plume for this case.

(X1,Y1)=( 5, 55) (X2,Y2)=(300,265) THETA (K ) 1983-09-19\_00.00.02 SM= 0

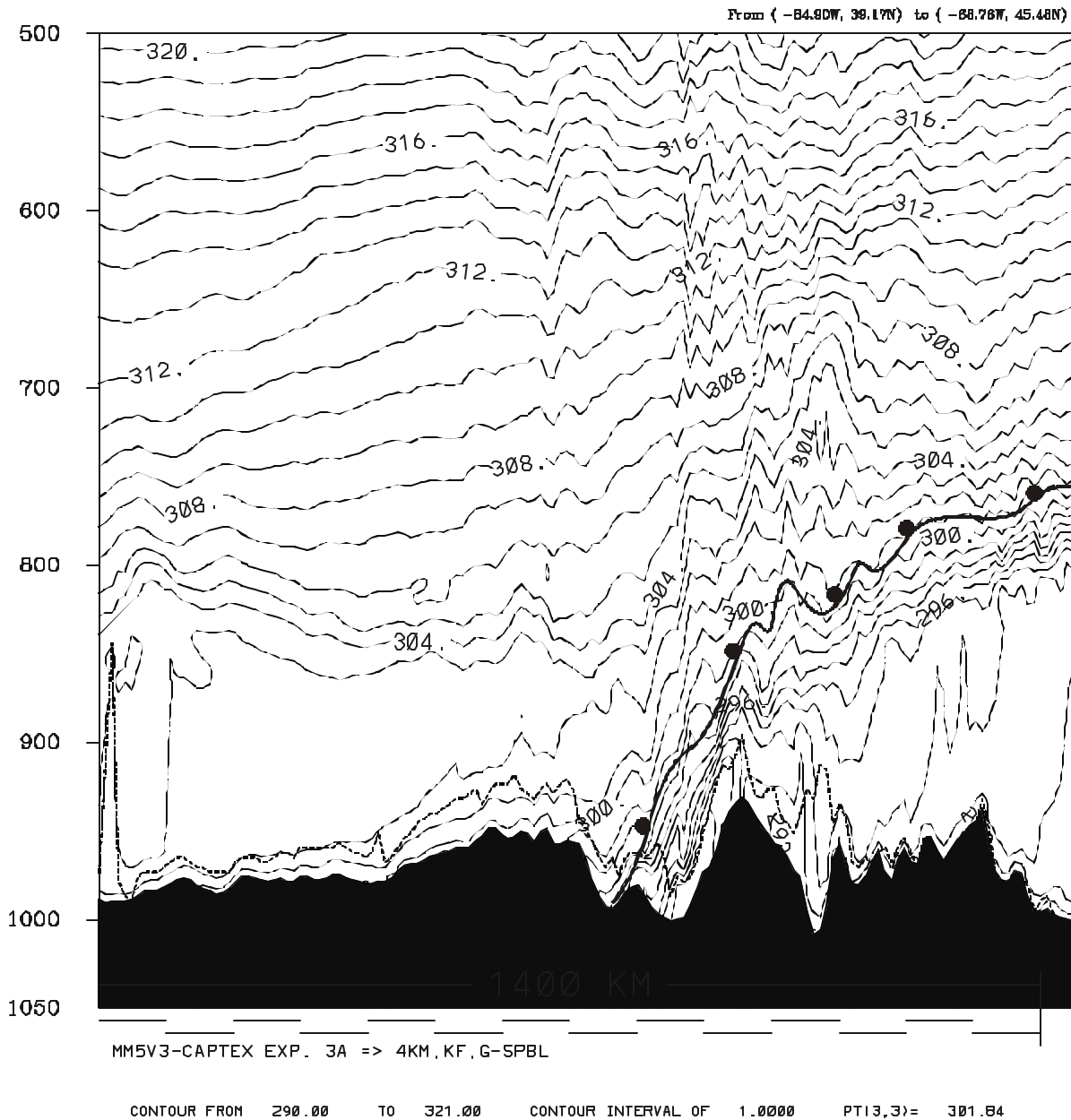


**Figure 50.** Cross section of MM5 simulated potential temperature (K) on the 4-km domain at 0000 UTC, 19 September 1983, 12 h into CAPTEX Experiment 3A. Isentropes interval is 1 K. Dashed line indicates depth of the surface-based turbulent layer. Position of the warm front surface is superimposed. Location of the southwest-northeast cross section is shown in Figure 49. Line segments just below 1050 mb level each indicate 100 km distance from left.

finer grid resolution available in Exp. 3A has allowed the temperature gradients across the front to become generally more intense than on the 12-km grid, especially below 850 mb, and that the mountain-induced gravity waves tend to have shorter wavelengths than were resolvable in Exp. 2B (compare Figures 31 and 50). Otherwise, many of the other features in these cross sections appear to be rather similar, including the boundary layer structure and the elevated mixed layers remaining from the previous afternoon.

Next, Figure 51 shows the winds in the same cross section of Exp. 3A taken through the warm front at 0000 UTC, 19 September. Examination of the figure indicates that the mean slope of the front is about 1:250, while the mean horizontal wind speed of the air encountering the front is  $\sim 20 \text{ ms}^{-1}$ . This implies that, if deceleration and buoyancy effects can be ignored and if the warm front was moving much slower than the wind, then the mean vertical velocity of the warm air as it is lifted by the front must be  $\sim 8 \text{ cm s}^{-1}$ . However, the maximum vertical winds are  $\sim 1 \text{ m s}^{-1}$ , so the mountain-induced gravity waves effectively mask the  $8 \text{ cm s}^{-1}$  mean lifting effect of the frontal boundary. In fact, it is possible that gravity-wave breaking in this strongly sheared zone could act to weaken the frontal gradients and may force at least some of the tracer material to mix through the frontal boundary. Once injected below the frontal zone, it could be mixed downward to the ground by turbulent boundary-layer eddies in the cold air mass. In effect, this would represent an eastern U.S. manifestation of the familiar Chinook winds of the northern and central Rocky Mountains. In Figure 50, the notable weakening of the vertical isentropic gradient over the Champlain Valley just to the northeast of the Adirondack Mts. (about 1/4 of the horizontal distance from the right side of the figure) may give evidence in support of this hypothesis. If it were to occur, this downward "Chinooking" of pollutants through a front due to

(X1,Y1)=( 5, 55) (X2,Y2)=(1300, 265) CXW (m/s) | 1983-09-19\_00.00.02 SM= 0  
 (X1,Y1)=( 5, 55) (X2,Y2)=(1300, 265) WIND UV (m/s) | 1983-09-19\_00.00.02 SM= 0

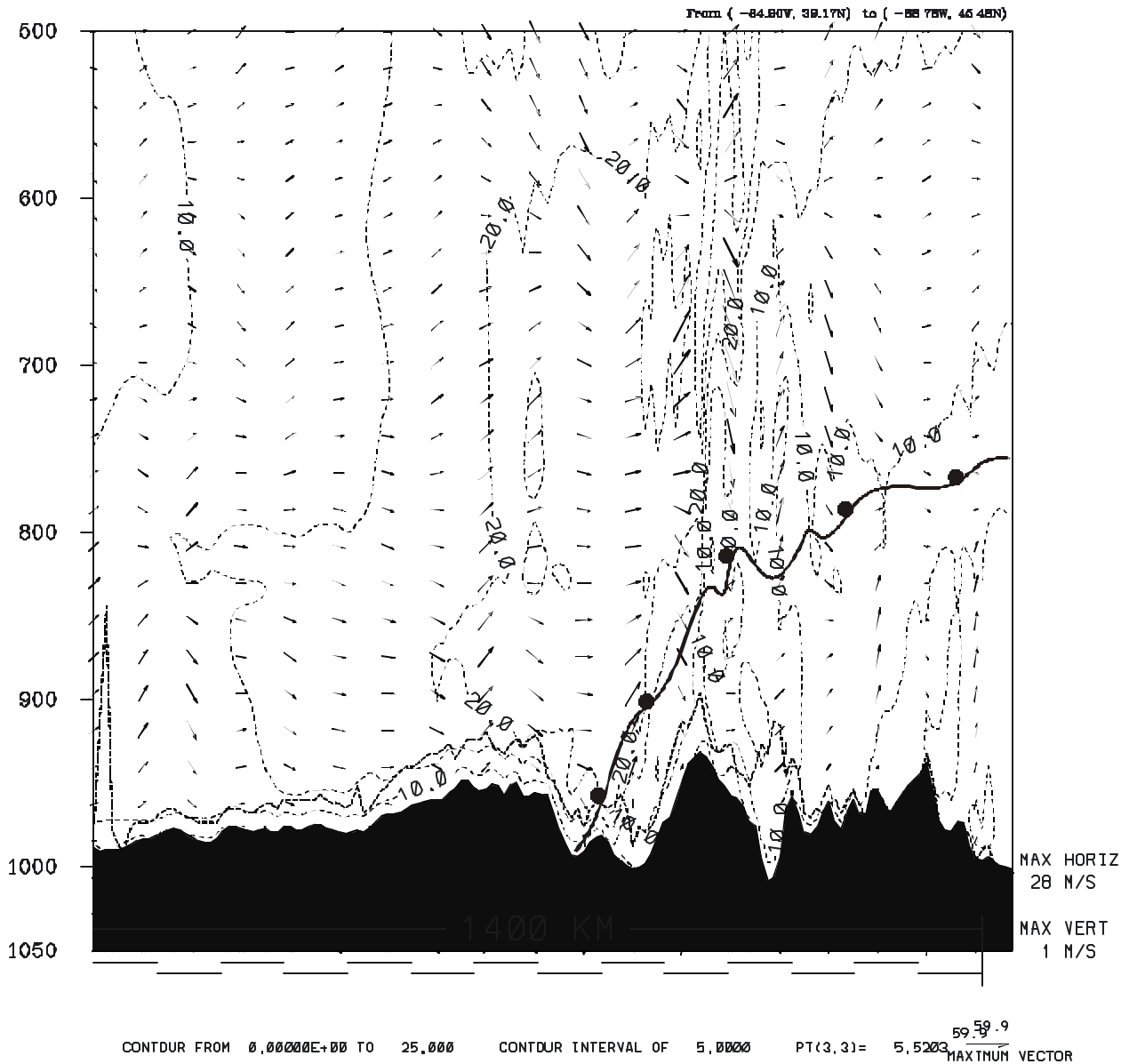
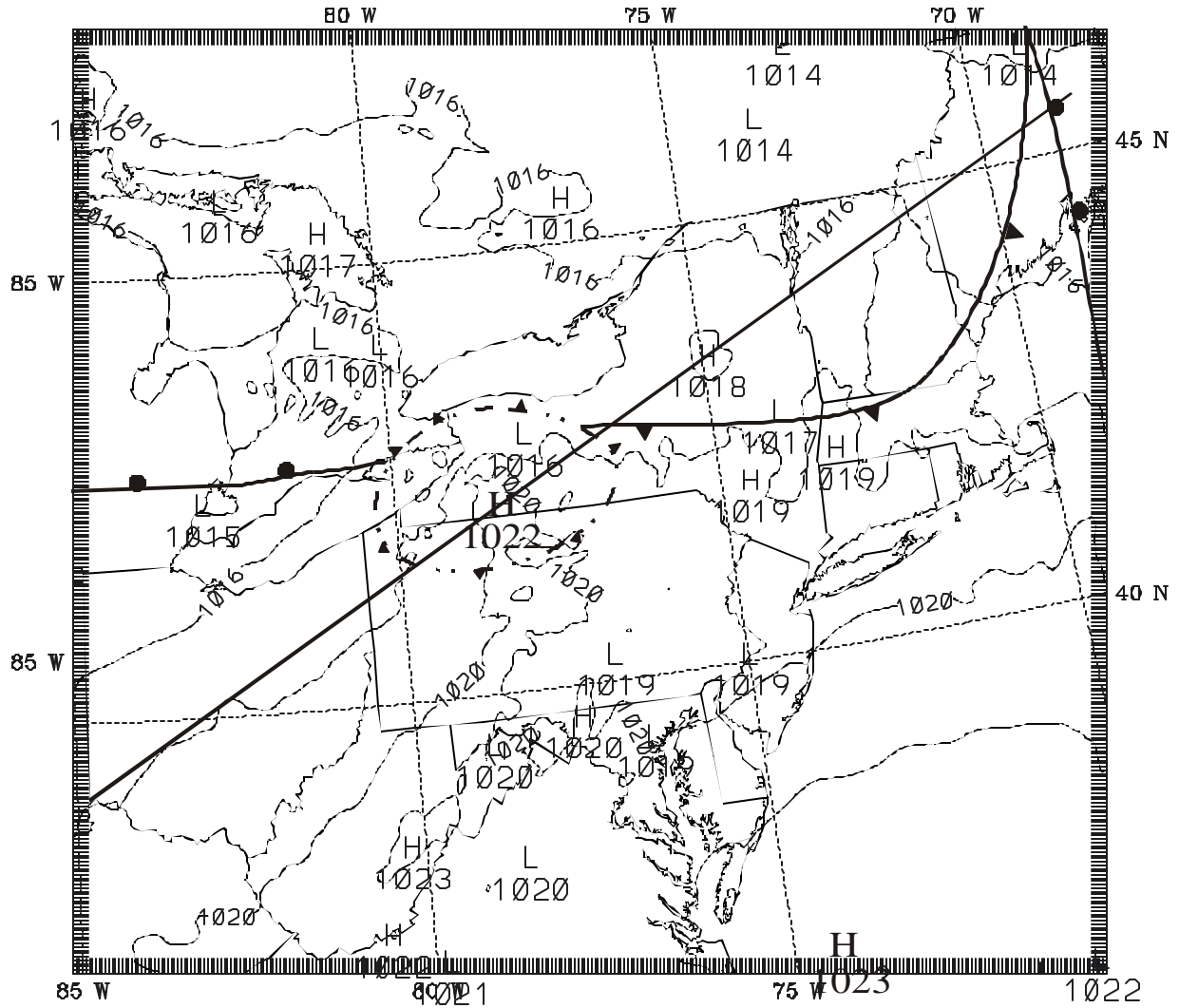


**Figure 51.** Cross section of MM5 simulated horizontal wind speed ( $\text{ms}^{-1}$ ) and wind vectors in the plane on the 4-km domain at 0000 UTC, 19 September 1983, 12 h into CAPTEX Experiment 3A. Isotach interval is  $5 \text{ ms}^{-1}$ . Vectors are exaggerated in the vertical by 100:1. Dashed line indicates depth of the surface-based turbulent layer. Position of the warm front surface is superimposed. Location of the southwest-northeast cross section is shown in Figure 50. Line segments just below 1050-mb level each indicate 100 km distance from left.

breaking gravity waves would represent yet another complex mechanism that could affect inter-regional transport of atmospheric pollutants. SCIPUFF results in Section 5.4 will be interpreted with this possible mechanism in mind, although the analysis of the warm-front positions relative to the surface footprint of the tracer plume shown in Figure 14 do not appear to make this mechanism likely in this case.

Moving forward to 1800 UTC, 19 September (+30 h), Figure 52 shows the sea-level pressure in the latter stage of the MM5 simulation for Exp. 3A. This field can be compared to the corresponding manual analysis in Figure 12 and the MM5 simulation of Exp. 2D in Figure 44. The frontal positions on the 4-km domain in Exp. 3A are mostly similar to those of the 12-km solutions in Exp. 2D. (Recall that both experiments used the same data assimilation strategy on their 36 and 12-km domains.) The warm front in the Midwest is correctly simulated in southern MI and Ontario, while the cold front appears to have advanced a bit too rapidly in NH and ME. However, a new development has appeared at this time in Exp. 3A over western NY and northwestern PA. The superimposed frontal analysis in Figure 52 shows a mesoscale outflow boundary intersecting the front, with a 1022-mb mesohigh near its center. This mesoscale pressure signature, although weak in this case, is typical of the atmosphere's response to a cluster of summertime thunderstorms. Indeed, the manual mesoscale analyses in Figures 8, 10 and 13 showed a number of similar short-lived features in Episode 1 of CAPTEX-83. Figure 53 presents the rainfall total for the 6-h period ending at 1800 UTC, which confirms that the model simulated heavy rainfall in this area (98 mm, or nearly 4 in., in 6 h over northwest PA and 70 mm over eastern Lake Erie). The manual analysis in Figure 12 at this time does not show thunderstorms in this area, although towering cumulus clouds were observed and a cluster of

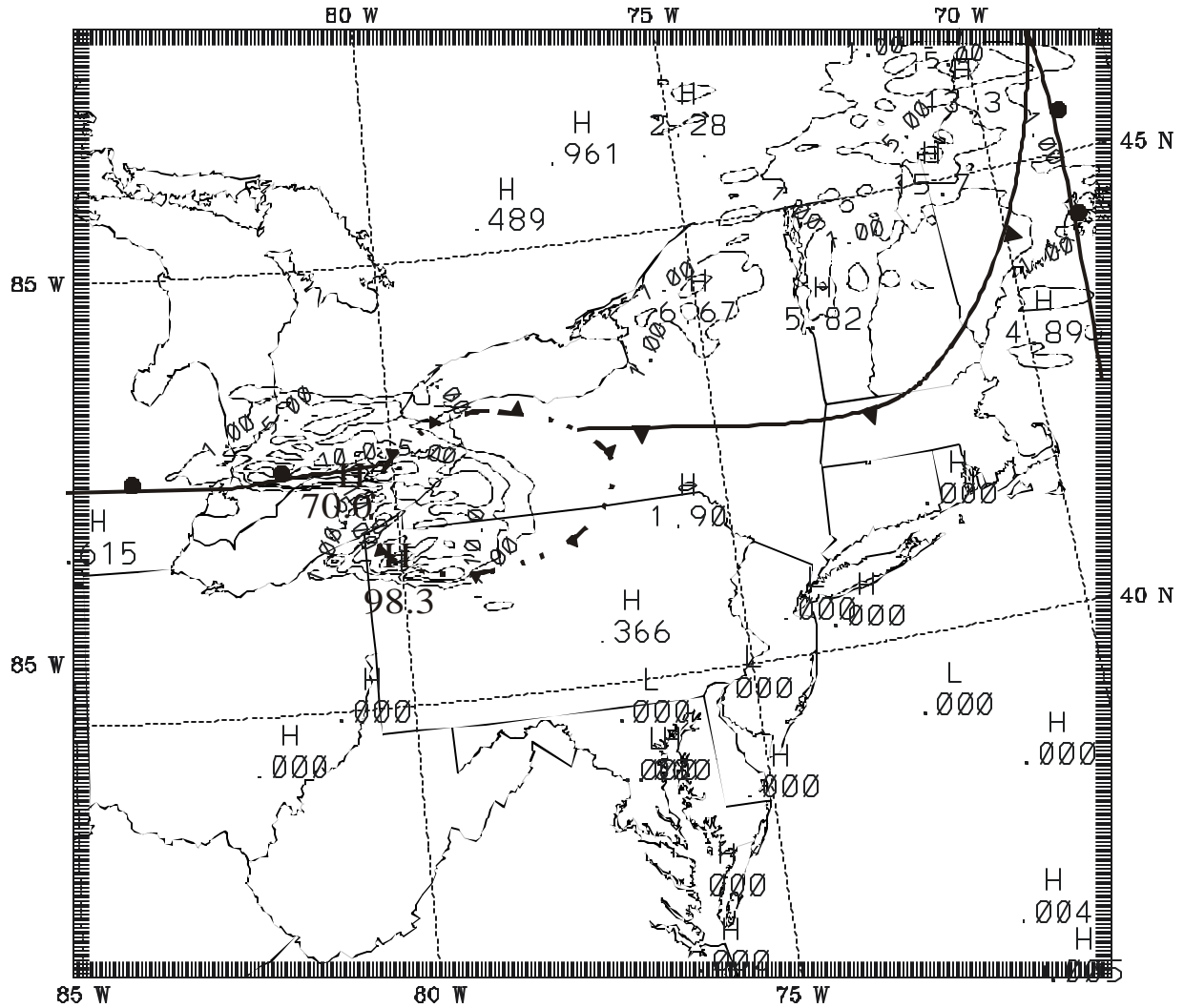
SIGMA =1.000 SEA PRES lmb ) 1983-09-19\_18.00.03 = 1983-09-18\_12 + 30.00H SMOOTH= 0



MM5V3-CAPTEX EXP. 3A => 4KM,KF,G-SPBL  
 CONTOUR FROM 1012.0 TO 1022.0 CONTOUR INTERVAL OF 2.0000 PT(3,31)= 1019.4

**Figure 52.** MM5 simulation of sea-level pressure (mb) on the 4-km domain at 1800 UTC, 19 September 1983, 30 h into CAPTEX Experiment 3A. Isobar interval is 2 mb. Location of the a cross section identical to that shown in Figure 49 is indicated by the straight line from OH to ME. Heavy dashed-dotted line denotes cold outflow boundary.

SIGMA =1.000 TEND RNT 1mm ) 1983-09-19\_18.00.03 = 1983-09-18\_12 + 30.00H SMOOTH= 0



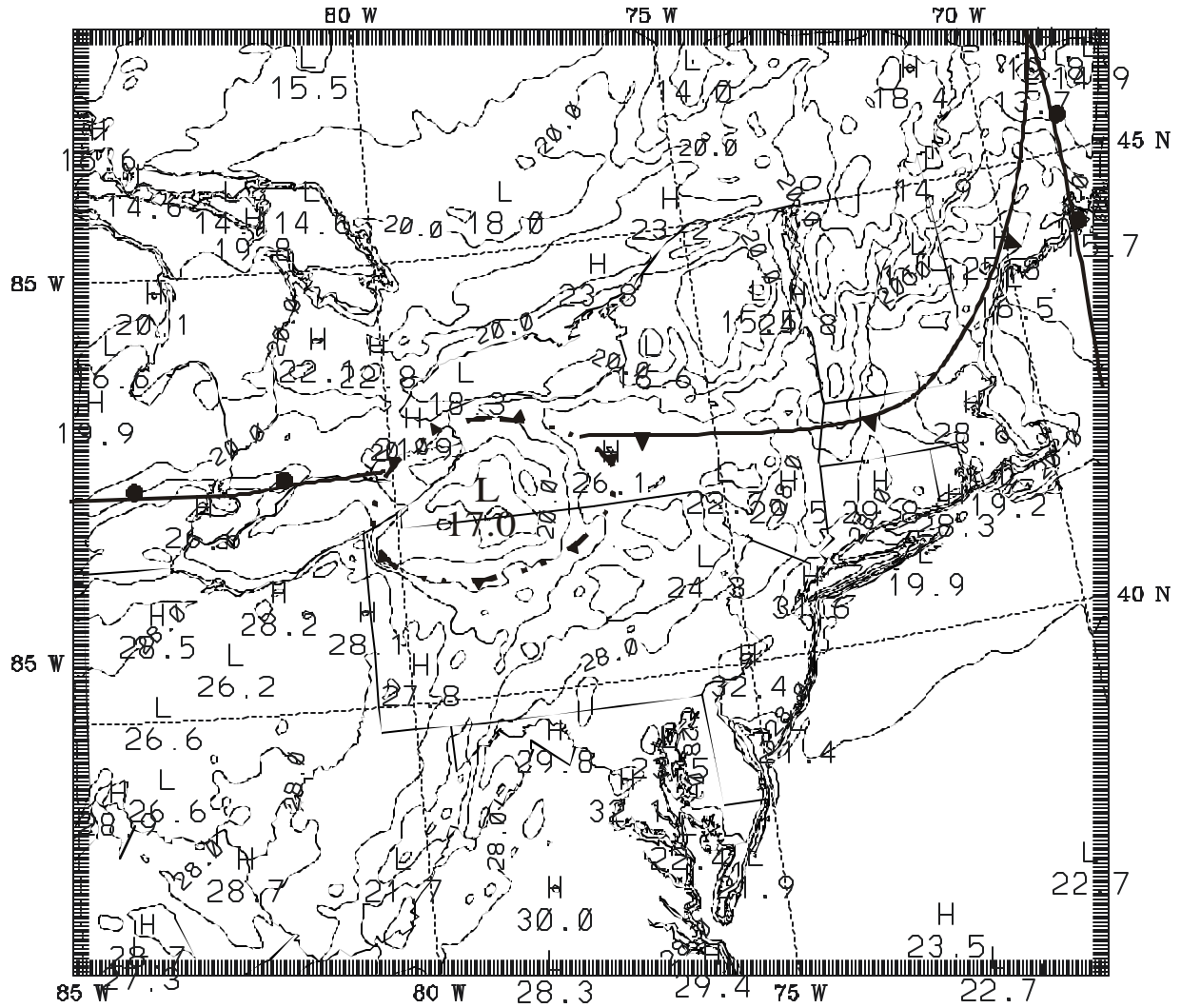
MM5V3-CAPTEX EXP. 3A => 4KM,KF,G-SPBL  
 CONTOUR FROM 000000 TO 999999 CONTOUR INTERVAL OF 5.0000 PT(3,31)= 0.25254E-26

**Figure 53.** MM5 simulation of 6-h rainfall (mm) on the 4-km domain for the period ending at 1800 UTC, 19 September 1983, 30 h into CAPTEX Experiment 3A. Contours are at 1, 5, 10, and 20 mm. Heavy dashed-dotted line denotes cold outflow boundary.

storms did develop near Buffalo, NY during the next several hours. Thus, despite some general similarities to the overall rainfall pattern on this afternoon, it is fairly certain that the model triggered the storms too early and seriously over-predicted the convective rainfall intensity in NY and PA.

The consequences of this early and excessive prediction of convective storms by the model certainly are dramatic in the immediate vicinity (~200 X 150 km), as shown in the figures. However, there is little direct impact on other areas farther away. For example, in the surface-layer temperature field at 1800 UTC (Figure 54), the cause of the surface mesohigh pressure center in Exp. 3A becomes evident. First, when convective rain forms in the mid- and upper-troposphere in the presence of wind shear, it begins falling through unsaturated layers below, which leads to evaporative cooling in the rain shaft. This cold dense air accelerates downward until it hits the surface, where the downdraft spreads out as a cold pool with gusty winds. In this case, the simulated cold pool has a minimum temperature of 17 C, compared to 24-28 C in the surrounding warm air mass. The hydrostatic response of the air column to the cooling and water loading leads to the high surface pressures. The gusty surface winds of 10-15 ms<sup>-1</sup> can be seen diverging from the center of the downdraft cold pool in southwestern NY in Figure 55.

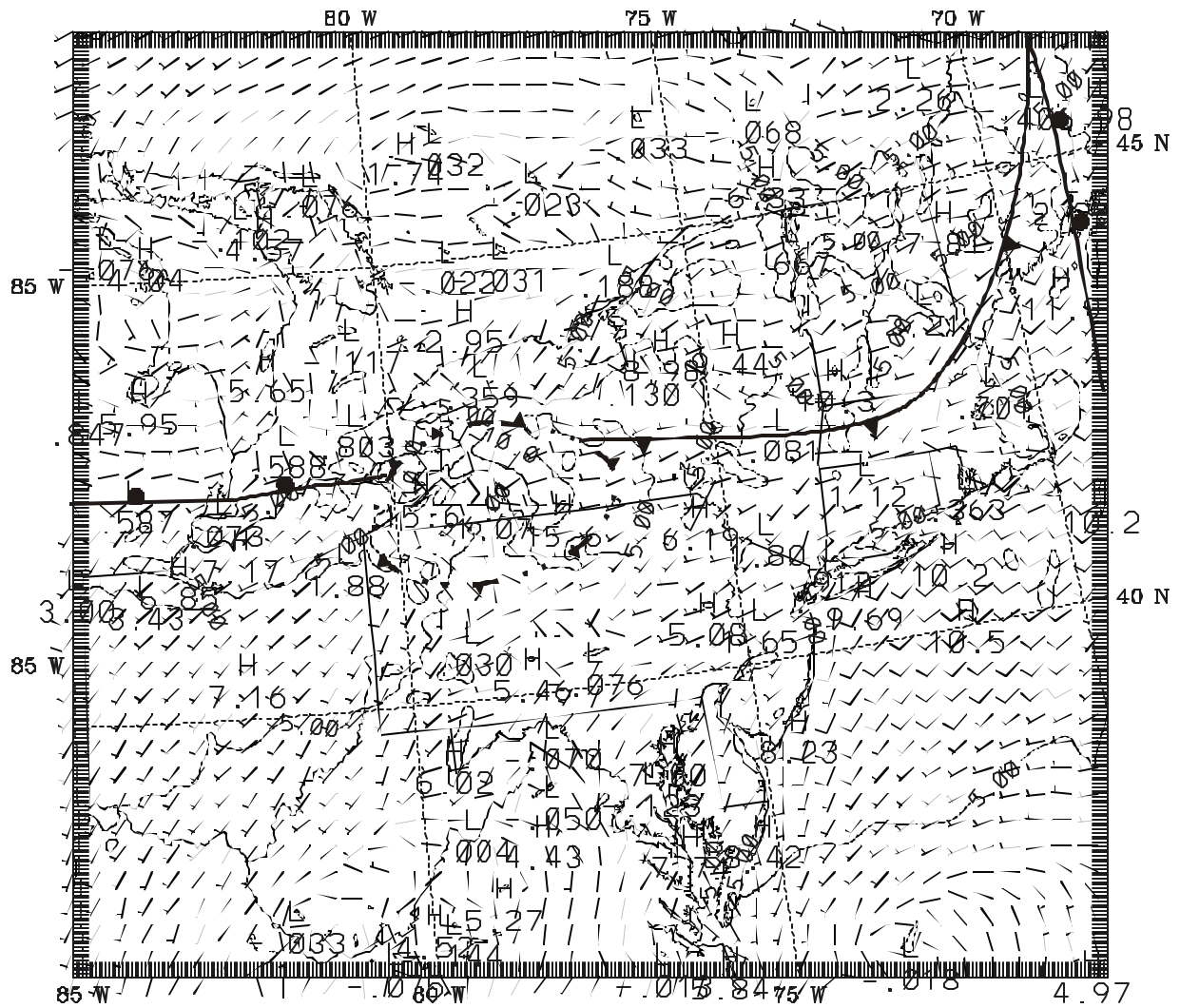
Even though the early outbreak of heavy thunderstorms at 1800 UTC produced some spurious results over western NY and northwestern PA, as shown in Figures 52-55, it is unlikely that the impact on the tracer cloud would be catastrophic in this case. Most of the tracer plume had already traveled east of western NY by this time and its leading portion probably had exited from the far end of the observing network. Thus, the solutions from Exp. 3A remain suitable for further evaluations of inter-regional transport issues in this case, despite the problems noted here.



MM5V3-CAPTEX EXP. 3A => 4KM,KF,G-SPBL  
 CONTOUR FROM 12.000 TO 32.000 CONTOUR INTERVAL OF 2.0000 PT(3,31= 27.810

**Figure 54.** MM5 simulation of surface-layer temperatures (C) on the 4-km domain at 1800 UTC, 19 September 1983, 30 h into CAPTEX Experiment 3A. Isotherm interval is 2 C. Heavy dashed-dotted line denotes cold outflow boundary.

SIGMA =0.996 WIND UV lm/s ) 1983-09-19\_18.00.03 = 1983-09-18\_12 + 30.00H SMOOTH= 3  
 SIGMA =0.996 BARB UV lm/s ) 1983-09-19\_18.00.03 = 1983-09-18\_12 + 30.00H SMOOTH= 0



MM5V3-CAPTEX EXP. 3A => 4KM,KF,G-SPBL  
 CONTOUR FROM 0.0000E+00 TO 15.000 CONTOUR INTERVAL OF 5.0000 PT(3,31)= 3.7095

**Figure 55.** MM5 simulation of surface-layer winds ( $\text{m s}^{-1}$ ) on the 4-km domain at 1800 UTC, 19 September 1983, 30 h into CAPTEX Experiment 3A. Contour interval is  $5 \text{ m s}^{-1}$ . Heavy dashed-dotted line denotes cold outflow boundary.

However, later evaluations involving statistical analysis and plume simulations will be carefully examined for signs that the spurious convection could have affected the results in other ways.

The vertical structure of the model's atmosphere on the 4-km domain at 1800 UTC, 19 September (+30 h) is shown in Figures 56 and 57. (Figure 52 shows the location of the cross section relative to the surface fronts at this time.) In the isentropic cross section (Figure 56), the locations of the intersecting cold front (northern NY and New England) and the convectively induced cold-air downdraft (southwest NY) are both revealed. The cold front to the northeast is fairly weak at this time, possibly due to extensive erosion by turbulent breakdown of the orographic gravity waves. Farther southwest, in the vicinity of the thunderstorm cluster, more gravity waves have been induced by dynamic adjustments to the convective latent-heat release and the evaporative cooling in the downdraft. Figure 57 shows the turbulent kinetic energy (*TKE*) in the cross section. Naturally, there is substantial *TKE* in the boundary layer, but the figure also reveals many areas of substantial turbulence aloft, mainly in the vicinity of the convective cluster and where the cold downdraft air intersects the cross section plane. The vertical motion in convective updrafts (not shown) and the turbulence shown in Figure 57 suggest that portions of a tracer plume originating in the PBL can undergo vertical transport and mixing at least up to 500 mb. In such situations, surface concentrations could become lower than simple horizontal advection and mixing in the PBL would imply.

(X1,Y1)=( 5, 55) (X2,Y2)=(300,265) THETA (K | 1983-09-19\_18.00.03 SM= 0

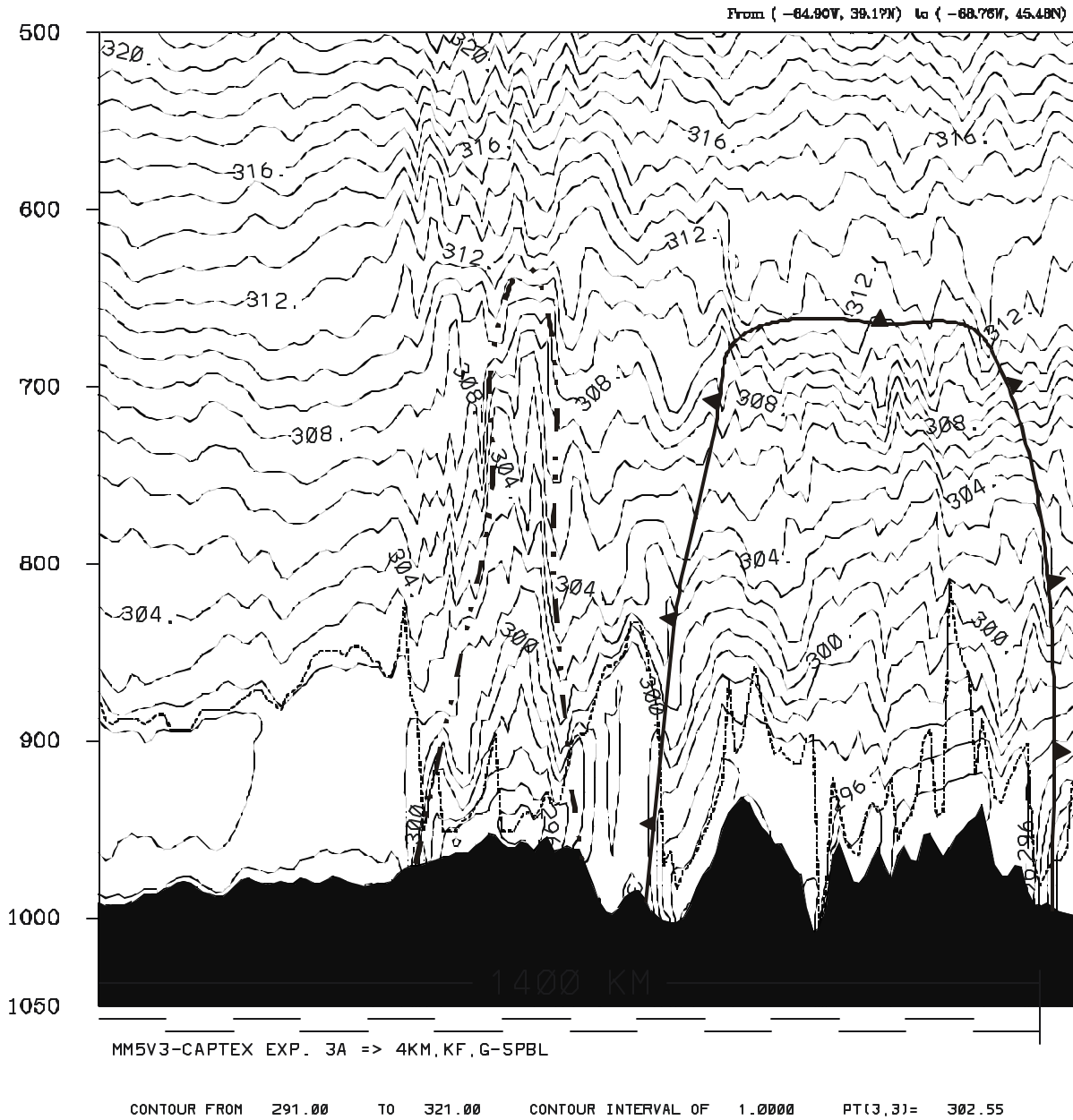


**Figure 56.** Cross section of MM5 simulated potential temperature (K) on the 4-km domain at 1800 UTC, 19 September 1983, 30 h into CAPTEX Experiment 3A. Isentrope interval is 1 K. Dashed line indicates depth of the surface-based turbulent layer. Positions of the cold frontal surface (standard symbols) and cold convective downdraft (heavy dashed-dotted line) are superimposed. Location of the southwest-northeast cross section is shown in Figure 52. Line segments just below 1050-mb level each indicate 100 km distance from left.

(X1,Y1)=( 5, 55) (X2,Y2)=(300,265) TKE (J/kg) | 1983-09-19\_18.00.03 SM= 2

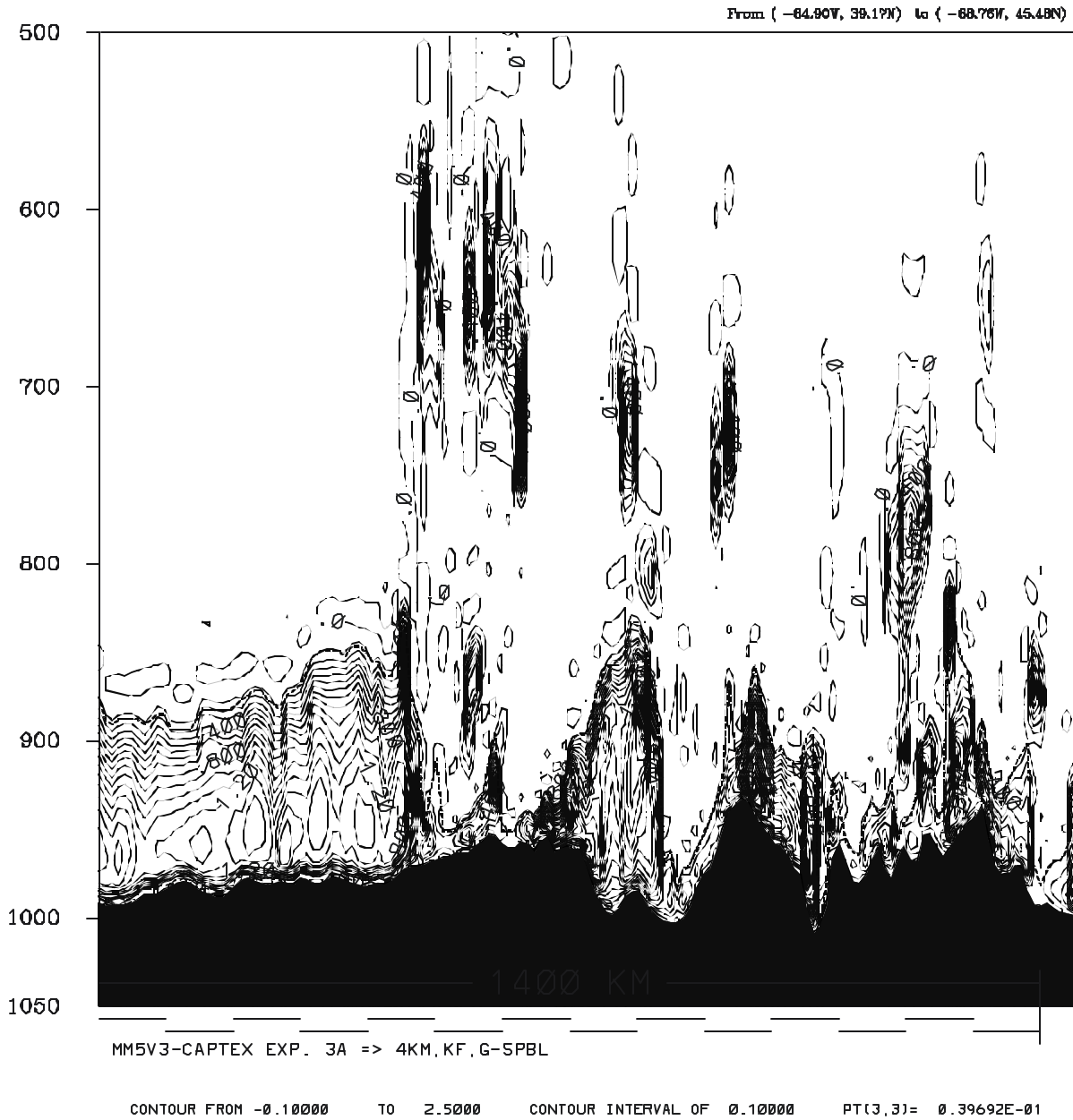


**Figure 57.** Cross section of MM5 simulated turbulent kinetic energy ( $\text{J kg}^{-1}$ ) on the 4-km domain at 1800 UTC, 19 September 1983, 30 h into CAPTEX Experiment 3A. Contour interval is  $0.1 \text{ J kg}^{-1}$ . Dashed line indicates depth of the surface-based turbulent layer. Location of the southwest-northeast cross section is shown in Figure 52. Line segments just below 1050-mb level each indicate 100 km distance from left.

## 5.2 Evaluation of the MM5 Statistical Performance

Moving beyond the examination of mesoscale and synoptic-scale structures simulated by the MM5 model, as presented in Section 5.1, this section examines the model's statistical performance for Episode 1 of the CAPTX-83 study. The statistical measures of accuracy selected for this evaluation were described in Section 4.4.2 and most are common in air-quality meteorology. Since the evaluations are performed for model configurations having different grid resolutions and domain sizes, we first limit the verification region to the 1152 X 1220 km area from KY to ME encompassing the 4-km domain of Configuration 3 (see Fig. 19). Thus, the statistics are calculated only over sub-domains of Configurations 1 and 2, but over the entire 4-km domain of Configuration 3. This approach ensures that the statistics from the various experiments can be compared on an equal footing.

The statistical results for Exp. 1A are summarized in Table 6. Recall that this experiment used 70-km horizontal resolution, 15 layers in the vertical, physical parameterizations typical of the late 1980s, and no FDDA. First, the table shows surface-layer *RMSEs* and *MAEs* for wind speed and direction that are about 50% larger than are typical for more recent cases published for air-quality related studies (e.g., Seaman et al. 1995, Lyons et al. 1995, Shafran et al. 2000, Michelson and Seaman 2000). The *MEs* for surface wind speed ( $+2.37 \text{ ms}^{-1}$ ) and for direction ( $+10.3$  degrees) are also quite large. Thus, the threshold percentages, *TRP* (see Table 5 for critical threshold values), in the surface layer for these two wind variables are rather low (38% and 58%, respectively). The index of agreement (*I*) for wind speed at the surface is 0.57 for Exp. 1A, which is only slightly less than typical values for air-quality episodes.

**Table 6. Statistical summary of MM5 performance for wind speed and direction in CAPTEX-83 Episode 1 (1200 UTC, 18 Sept. - 0000 UTC, 20 Sept. 1983) on the 70-km verification domain of EXP. 1A.**

<b>Wind Speed (ms<sup>-1</sup>)</b>	<b>RMSE (ms<sup>-1</sup>)</b>	<b>MAE (ms<sup>-1</sup>)</b>	<b>ME (ms<sup>-1</sup>)</b>	<b>I</b>	<b>TRP (%)</b>
5000 - 10000 m AGL	4.01	3.28	-1.02	0.95	53.4
1000 - 5000 m AGL	2.64	2.06	+0.18	0.92	66.4
72 - 1000 m AGL	3.05	2.65	+1.72	0.72	37.2
Sfc. Layer (36 m AGL)	3.36	2.88	+2.37	0.57	38.0
<b>Wind Direction (deg.)</b>	<b>RMSE (deg.)</b>	<b>MAE (deg.)</b>	<b>ME (deg.)</b>		<b>TRP (%)</b>
5000 - 10000 m AGL	34.7	25.2	+ 0.4		41.7
1000 - 5000 m AGL	14.2	11.5	- 1.5		50.9
72 - 1000 m AGL	26.7	18.8	+ 6.9		60.0
Sfc. Layer (36 m AGL)	49.5	35.6	+10.3		58.0
<b>Temperature (C)</b>	<b>RMSE (C)</b>	<b>MAE (C)</b>	<b>ME (C)</b>		<b>TRP (%)</b>
5000 - 10000 m AGL	1.32	1.07	+0.39		87.2
1000 - 5000 m AGL	1.56	1.34	+0.83		77.6
72 - 1000 m AGL	1.86	1.48	- 0.54		70.4
Sfc. Layer (36 m AGL)	2.79	2.25	- 0.56		52.1
<b>Mixing Ratio (g kg<sup>-1</sup>)</b>	<b>RMSE (g kg<sup>-1</sup>)</b>	<b>MAE (g kg<sup>-1</sup>)</b>	<b>ME (g kg<sup>-1</sup>)</b>		<b>TRP (%)</b>
5000 - 10000 m AGL	0.27	0.19	+0.03		89.9
1000 - 5000 m AGL	1.35	1.06	- 0.16		53.1
72 - 1000 m AGL	1.86	1.56	+1.12		36.8
Sfc. Layer (36 m AGL)	1.93	1.55	+0.45		39.8
<b>Pressure (mb)</b>	<b>RMSE (mb)</b>	<b>MAE (mb)</b>	<b>ME (mb)</b>		<b>TRP (%)</b>
Sfc. Layer (36 m AGL)	1.19	0.95	-0.29		89.4

Table 6 also shows statistical performance for Exp. 1 above the surface layer. For brevity, the individual model layers have been grouped together into three regions. These averaged layers represent the approximate depth of the daytime PBL (~60-1000 m), the lower free troposphere (1000 - 5000 m) and the upper troposphere (5000 - 10,000 m)]. Notice that Table 6 shows that *MEs* for wind speed generally decrease with height and *I* increases (higher skill), while the *RMSEs* and *MAEs* remain rather large (reflecting greater wind speeds toward the level of the upper-tropospheric jet stream). This is a normal response for a strongly baroclinic atmosphere. Wind direction errors given by the *RMSE*, *MAE*, *ME* and *TRP* tend to be lower aloft where the influences of PBL turbulence and irregular terrain forcing are decreased. Based on these statistics, it is unlikely that winds simulated in Exp. 1A would be considered by most investigators today as suitable for inputs to air-quality models.

There are at least two reasons for the comparatively large statistical wind errors in Exp. 1A. First, the experiment design purposely excludes many of the advantageous model developments introduced over the past 10-15 years. Second, the 18-20 September 1983 episode has much greater baroclinic forcing than is typical for mid-summer air-quality studies. For example, winds of more than  $70 \text{ ms}^{-1}$  were observed at  $\sim 300 \text{ mb}$  in the jet stream associated with the deep storm sweeping across Canada during this case (see Sec. 2.2). By contrast, in more typical mid-summer cases having poor air quality (e.g., Seaman et al. 1995, Lyons et al. 1995, Shafran et al. 2000, Michelson and Seaman 2000), the synoptic-scale environment tends to be mostly barotropic so that jet-level winds may be  $\sim 30 \text{ ms}^{-1}$  or less. This translates into stronger surface winds and greater vertical shear in the lowest 1.5 km, especially near frontal zones.

Table 6 also gives the errors for the mass-field variables. The *RMSEs* for temperature in the surface layer are  $\sim 0.5\text{-}1.0 \text{ C}$  greater than is typical for most air-quality cases, although the

*ME* is about normal and the *TRP* is about average (slightly above 50%). As expected, the temperature errors expressed by the *RMSE*, *MAE* and *TRP* tend to decrease with height due to lessened influence of the strong irregular thermal forcing at the surface. The *RMSE*, *MAE* and *ME* for mixing ratio near the surface are fairly normal. The positive *ME* of  $+0.45 \text{ g kg}^{-1}$  at the surface suggests a somewhat moist bias in the evaporation rate, which contributes to a rather low *TRP* of ~40%. Finally, the sea-level pressure errors are fairly small in this case, which suggests that the geostrophic forcing is reasonably accurate.

Next, a summary of the statistical results for Exp. 2A is given in Table 7. Exp. 2A was designed to use two nested-grid domains with a fine mesh of 12 km, but the same physics as in Exp. 1A and no FDDA. Comparison of the statistical performance in Exps. 1A and 2A isolates the benefit of finer grid resolutions that have typically been used for regional-scale model domains (1000-2000 km) in recent years.

First, the *RMSEs*, *MAEs* and *TRPs* for the surface-layer wind speeds in Table 7 indicate some improvement (~9-14%) in Exp. 2A, compared to Exp. 1A. While not having a dramatic impact, any improvement of this magnitude due to a single change in model characteristics is generally regarded as rather successful. Above the surface, however, the reduction of the wind-speed errors in Exp. 2A is less dramatic in the PBL, and then it reverses to produce greater errors in the free troposphere (above 1000 m AGL). The boundary-layer speed bias is slightly greater in Exp. 2A than in the 70-km domain of Exp. 1A. On the other hand, inspection of the wind direction errors shows no significant trend in the size of individual errors. (It should be noted that the wind directions in surface meteorological observations are reported only to the nearest 10 degrees, so that it is virtually impossible for the *RMSE* and *MAE* to ever fall below that level. The reporting threshold for upper-air wind directions is 5 degrees.)

**Table 7. Statistical summary of MM5 performance for wind speed and direction in CAPTEX-83 Episode 1 (1200 UTC, 18 Sept. - 0000 UTC, 20 Sept. 1983) on the 12-km verification domain of EXP. 2A.**

<b>Wind Speed (ms<sup>-1</sup>)</b>	<b>RMSE (ms<sup>-1</sup>)</b>	<b>MAE (ms<sup>-1</sup>)</b>	<b>ME (ms<sup>-1</sup>)</b>	<b>I</b>	<b>TRP (%)</b>
5000 - 10000 m AGL	4.46	3.63	- 0.44	0.95	51.7
1000 - 5000 m AGL	3.29	2.56	+0.47	0.89	61.4
58 - 1000 m AGL	2.98	2.46	+1.78	0.74	42.3
Sfc. Layer (29 m AGL)	3.06	2.61	+2.04	0.62	42.1
<b>Wind Direction (deg.)</b>	<b>RMSE (deg.)</b>	<b>MAE (deg.)</b>	<b>ME (deg.)</b>		<b>TRP (%)</b>
5000 - 10000 m AGL	33.0	22.9	+6.9		43.0
1000 - 5000 m AGL	13.4	10.9	- 0.0		52.8
58 - 1000 m AGL	26.7	19.1	+6.5		60.8
Sfc. Layer (29 m AGL)	48.0	34.2	+7.9		58.6
<b>Temperature (C)</b>	<b>RMSE (C)</b>	<b>MAE (C)</b>	<b>ME (C)</b>		<b>TRP (%)</b>
5000 - 10000 m AGL	1.62	1.38	+1.18		80.0
1000 - 5000 m AGL	1.75	1.54	+1.13		72.1
58 - 1000 m AGL	1.71	1.34	- 0.63		72.0
Sfc. Layer (29 m AGL)	2.52	2.04	- 0.74		58.2
<b>Mixing Ratio (g kg<sup>-1</sup>)</b>	<b>RMSE (g kg<sup>-1</sup>)</b>	<b>MAE (g kg<sup>-1</sup>)</b>	<b>ME (g kg<sup>-1</sup>)</b>		<b>TRP (%)</b>
5000 - 10000 m AGL	0.38	0.28	+0.08		80.5
1000 - 5000 m AGL	1.52	1.16	- 0.35		51.6
58 - 1000 m AGL	1.83	1.49	+0.76		40.9
Sfc. Layer (29 m AGL)	2.03	1.62	+0.30		38.3
<b>Pressure (mb)</b>	<b>RMSE (mb)</b>	<b>MAE (mb)</b>	<b>ME (mb)</b>		<b>TRP (%)</b>
Sfc. Layer (29 m AGL)	1.52	1.30	-1.00		75.1

Meanwhile, Table 7 reveals that the introduction of the a 12-km regional-scale domain in Exp. 2A caused a reduction of the *RMSE* and *MAE* for surface temperature errors by ~10%, while the temperature bias expressed by the *ME* rose by nearly a third. Despite the larger cold bias, these statistics reveal an overall improvement in the model simulated temperatures due to the grid resolution, which is also reflected by the rise of surface-layer *TRP* to ~58%. Above the surface, the temperature errors also are reduced in the PBL. However, in the free troposphere a fairly strong warm bias exists in Exp. 2A, which leads to reduced accuracy in the other statistical scores for temperature, as well. Table 7 indicates that mixing ratio errors are a bit worse in Exp. 2A at all levels, likely due to more vigorous convective precipitation on the finer mesh. Sea-level pressure errors also are degraded in accuracy in this experiment.

It is clear from the comparison of Tables 6 and 7 that simply using finer grid resolution does not lead automatically to consistent improvement in the model performance. Naturally, as computational resources expanded and meteorological research proceeded during the 1990s, better physics parameterizations were developed for use with finer model grids. Exp. 2B was designed to isolate the role of this improved physics, when compared to Exp. 2A. Table 8 shows the statistical performance in Exp. 2B. Immediately, a significant improvement is noticeable in the accuracy of the surface-layer wind speeds, relative to those of Exp. 2A shown in Table 7. Since Exp. 2B does not include FDDA, its design is very similar to 12-km "Control" experiments (no FDDA) of many recent meteorological model applications performed for air-quality studies. Indeed, the speed errors for the surface layer shown in Table 8 are just about typical of other such experiments at this resolution (e.g., Shafran et al. 2000). Thus, comparing Tables 6-8, it appears that the introduction of improved physics (mostly due to the TKE-predictive turbulence

scheme and the Kain-Fritsch deep convection) has had a greater impact on the accuracy of the surface wind speed than the grid size, at least in this case.

However, this picture reverses above the surface, where the *RMSE* and *MAE* show ~10-15% larger errors in the PBL and lower troposphere, even though the model bias (*ME*) is smaller. Even so, the speed bias in the PBL (58-1000 m) remains fairly large at  $\sim 1.5 \text{ ms}^{-1}$  in Exp. 2B. This result has important implications for air-quality studies because the bulk of airborne trace constituents are transported in this layer. Statistical analysis of recent independent applications of the MM5 model using several different turbulence parameterizations and without FDDA (Prof. Da-lin Zhang, U. of MD, 2002, personal communication) have confirmed that this is a persistent characteristic of the MM5's PBL, especially at night. Penn State has also found this behavior in a number of its own recent modeling studies and it appears that this is a consistent problem for all of the model's PBL schemes. These results indicate that additional research is needed to correct the vertical momentum flux in the MM5 boundary layer schemes. Examination of the wind-direction statistics in Table 8, compared to those of Table 7, reveal that Exp. 2B led to a reduction of the surface wind-direction bias (*ME*). However, the other measures of accuracy show no significant changes for this case in any of the layers, indicating that the magnitude of individual wind errors did not change very much.

Unlike the wind-field statistics, Table 8 shows that the addition of more advanced physics in Exp. 2B led to fairly substantial improvements in the model's temperature solutions as revealed in the statistics, especially at the surface and in the free troposphere above 1000 m. Surface temperature errors in this experiment are similar to or lower than what is typical of many MM5 "Control" experiments of similar design. However, above the surface, PBL temperatures have developed a strong cold bias of -1.3 C, which contributes to larger errors in the other

**Table 8. Statistical summary of MM5 performance for wind speed and direction in CAPTEX-83 Episode 1 (1200 UTC, 18 Sept. - 0000 UTC, 20 Sept. 1983) on the 12-km verification domain of EXP. 2B.**

<b>Wind Speed (ms<sup>-1</sup>)</b>	<b>RMSE (ms<sup>-1</sup>)</b>	<b>MAE (ms<sup>-1</sup>)</b>	<b>ME (ms<sup>-1</sup>)</b>	<b>I</b>	<b>TRP (%)</b>
5000 - 10000 m AGL	4.30	3.47	+0.34	0.95	53.1
1000 - 5000 m AGL	3.57	2.95	- 0.31	0.87	47.0
58 - 1000 m AGL	3.40	2.76	+1.48	0.72	41.8
Sfc. Layer (29 m AGL)	2.69	2.24	+1.08	0.63	48.9
<b>Wind Direction (deg.)</b>	<b>RMSE (deg.)</b>	<b>MAE (deg.)</b>	<b>ME (deg.)</b>		<b>TRP (%)</b>
5000 - 10000 m AGL	30.8	20.5	+8.0		40.6
1000 - 5000 m AGL	16.1	12.9	- 2.4		47.0
58 - 1000 m AGL	27.4	18.1	- 1.2		64.8
Sfc. Layer (29 m AGL)	47.8	34.2	- 1.3		60.3
<b>Temperature (C)</b>	<b>RMSE (C)</b>	<b>MAE (C)</b>	<b>ME (C)</b>		<b>TRP (%)</b>
5000 - 10000 m AGL	1.15	0.94	+0.65		91.8
1000 - 5000 m AGL	1.23	1.01	+0.27		87.2
58 - 1000 m AGL	2.06	1.69	- 1.30		62.4
Sfc. Layer (29 m AGL)	2.62	2.03	- 0.52		62.2
<b>Mixing Ratio (g kg<sup>-1</sup>)</b>	<b>RMSE (g kg<sup>-1</sup>)</b>	<b>MAE (g kg<sup>-1</sup>)</b>	<b>ME (g kg<sup>-1</sup>)</b>		<b>TRP (%)</b>
5000 - 10000 m AGL	0.46	0.36	+0.18		75.5
1000 - 5000 m AGL	1.55	1.24	- 0.13		47.0
58 - 1000 m AGL	1.46	1.17	+0.12		51.4
Sfc. Layer (29 m AGL)	1.77	1.40	+0.41		42.9
<b>Pressure (mb)</b>	<b>RMSE (mb)</b>	<b>MAE (mb)</b>	<b>ME (mb)</b>		<b>TRP (%)</b>
Sfc. Layer (29 m AGL)	1.35	1.12	+0.84		81.1

statistics at that level. Mixing ratio errors for the surface and PBL are generally reduced relative to Exp. 2A, but there is further degradation of the moisture field in the middle and upper troposphere. This is likely due to more intense (over-predicted) vertical transport of moisture in deep convection, which also gives a hint as to how the physics may feed back to upper-level wind and temperature. Stronger convection, with its accompanying latent heat release, can induce ageostrophic adjustments that may alter the winds over hundreds of kilometers. Interestingly, Table 8 also shows that the *RMSEs* and *MAEs* for sea-level pressure in Exp. 2B have decreased along with the tropospheric temperature errors.

In Exp. 2C, FDDA was added on both domains of Configuration 2 by using analysis nudging above ~1500 m AGL. The statistical evaluation for this experiment is summarized below in Table 9. The surface wind-speed statistics in Table 9 show that, even though no surface or PBL wind data were assimilated in this experiment, the use of FDDA aloft did have a significant positive impact in the lower layers. The surface index of agreement for wind speed has risen to 0.66 in Exp. 2C. Generally, the speed errors aloft were reduced substantially at all levels, and the scores for the *RMSEs*, *MAEs*, *Is* and *TRPs* in Exp. 2C outperform all three previous experiments. The former bias (*ME*) in Exp. 2B toward fast PBL speeds was almost eliminated in Exp. 2C. Consistent with the obvious improvement in the wind speed accuracy aloft, the wind-direction errors in Exp. 2C were reduced greatly in free upper troposphere (above the PBL), as well. Even at the surface and in the PBL, directional errors were reduced somewhat relative to Exp. 2B, although winds were not assimilated in these two lower layers. Thus, the introduction of FDDA produced the most dramatic improvement in the wind statistics, especially for the layers where data assimilation was applied directly.

The temperature statistics for Exp. 2C in Table 9 also indicate that FDDA had a large

**Table 9. Statistical summary of MM5 performance for wind speed and direction in CAPTEX-83 Episode 1 (1200 UTC, 18 Sept. - 0000 UTC, 20 Sept. 1983) on the 12-km verification domain of EXP. 2C.**

<b>Wind Speed (ms<sup>-1</sup>)</b>	<b>RMSE (ms<sup>-1</sup>)</b>	<b>MAE (ms<sup>-1</sup>)</b>	<b>ME (ms<sup>-1</sup>)</b>	<b>I</b>	<b>TRP (%)</b>
5000 - 10000 m AGL	2.19	1.79	-0.96	0.99	83.6
1000 - 5000 m AGL	2.02	1.59	-0.98	0.95	78.0
58 - 1000 m AGL	2.78	2.29	-0.01	0.78	50.8
Sfc. Layer (29 m AGL)	2.46	2.03	+0.74	0.66	54.4
<b>Wind Direction (deg.)</b>	<b>RMSE (deg.)</b>	<b>MAE (deg.)</b>	<b>ME (deg.)</b>		<b>TRP (%)</b>
5000 - 10000 m AGL	15.1	10.8	+6.0		66.2
1000 - 5000 m AGL	11.3	8.7	+0.7		68.8
58 - 1000 m AGL	24.6	16.5	+1.1		65.8
Sfc. Layer (29 m AGL)	47.4	33.6	- 1.2		60.6
<b>Temperature (C)</b>	<b>RMSE (C)</b>	<b>MAE (C)</b>	<b>ME (C)</b>		<b>TRP (%)</b>
5000 - 10000 m AGL	0.67	0.54	+0.15		100.0
1000 - 5000 m AGL	0.77	0.61	- 0.19		93.9
58 - 1000 m AGL	1.85	1.57	- 1.01		64.4
Sfc. Layer (29 m AGL)	2.57	1.98	- 0.36		61.6
<b>Mixing Ratio (g kg<sup>-1</sup>)</b>	<b>RMSE (g kg<sup>-1</sup>)</b>	<b>MAE (g kg<sup>-1</sup>)</b>	<b>ME (g kg<sup>-1</sup>)</b>		<b>TRP (%)</b>
5000 - 10000 m AGL	0.45	0.33	+0.25		75.9
1000 - 5000 m AGL	1.44	1.13	+0.12		51.6
58 - 1000 m AGL	1.73	1.32	+0.85		49.0
Sfc. Layer (29 m AGL)	1.72	1.34	+0.56		46.3
<b>Pressure (mb)</b>	<b>RMSE (mb)</b>	<b>MAE (mb)</b>	<b>ME (mb)</b>		<b>TRP (%)</b>
Sfc. Layer (29 m AGL)	1.08	0.85	+0.20		94.3

positive impact above the PBL, where the data were assimilated. Even at the surface and in the PBL, the temperature errors are the lowest (or nearly so) of all the experiments examined so far. As in the other experiments, improvement of the temperature field in Exp. 2C produced a similar reduction in the errors for sea-level pressure. The mixing ratio statistics, however, did not show consistent improvement, except in isolated instances.

The last experiment for Configuration 2, Exp. 2D, was similar to Exp. 2C except that the FDDA design was extended to include three-hourly surface wind analyses. This experiment is similar to many of the analysis-nudging FDDA experiments reported for the MM5 in recent years (e.g., Shafran et al. 2000, Michelson and Seaman 2000). The statistics for Exp. 2D are summarized in Table 10. Since the only new data being assimilated in this experiment are the surface winds, it is expected that the surface and PBL wind simulations are the most likely to exhibit a noticeable change in the error statistics, with little change occurring in the other fields.

Examination of the wind speed and direction statistics in Table 10 shows that this is true, with the surface index of agreement rising to 0.70. In the rest of the atmospheric column, there were only minor changes, either positive or negative, but these are probably not significant because they are nearly random. However, the cumulative introduction of the various improvements in Exps. 2A-2D have resulted in great improvements in the wind speed errors at all levels and for all scores, compared to Exp. 1 (see Table 6). The largest remaining wind-speed errors are found in the PBL, again suggesting that additional development efforts focused on the PBL physics and/or FDDA strategies for this layer could be quite helpful.

**Table 10. Statistical summary of MM5 performance for wind speed and direction in CAPTEX-83 Episode 1 (1200 UTC, 18 Sept. - 0000 UTC, 20 Sept. 1983) on the 12-km verification domain of EXP. 2D.**

<b>Wind Speed (ms<sup>-1</sup>)</b>	<b>RMSE (ms<sup>-1</sup>)</b>	<b>MAE (ms<sup>-1</sup>)</b>	<b>ME (ms<sup>-1</sup>)</b>	<b>I</b>	<b>TRP (%)</b>
5000 - 10000 m AGL	2.17	1.77	- 0.85	0.99	85.5
1000 - 5000 m AGL	2.09	1.64	- 1.09	0.95	76.3
58 - 1000 m AGL	2.89	2.37	- 0.29	0.78	52.3
Sfc. Layer (29 m AGL)	2.13	1.71	+0.48	0.70	64.6
<b>Wind Direction (deg.)</b>	<b>RMSE (deg.)</b>	<b>MAE (deg.)</b>	<b>ME (deg.)</b>		<b>TRP (%)</b>
5000 - 10000 m AGL	14.8	10.7	+5.6		64.7
1000 - 5000 m AGL	11.3	8.6	+0.5		70.4
58 - 1000 m AGL	20.7	14.1	- 1.3		68.5
Sfc. Layer (29 m AGL)	42.5	29.2	- 3.5		65.1
<b>Temperature (C)</b>	<b>RMSE (C)</b>	<b>MAE (C)</b>	<b>ME (C)</b>		<b>TRP (%)</b>
5000 - 10000 m AGL	0.66	0.54	+0.13		100.0
1000 - 5000 m AGL	0.78	0.61	- 0.19		94.7
58 - 1000 m AGL	1.94	1.65	- 1.12		62.9
Sfc. Layer (29 m AGL)	2.57	1.96	- 0.33		62.7
<b>Mixing Ratio (g kg<sup>-1</sup>)</b>	<b>RMSE (g kg<sup>-1</sup>)</b>	<b>MAE (g kg<sup>-1</sup>)</b>	<b>ME (g kg<sup>-1</sup>)</b>		<b>TRP (%)</b>
5000 - 10000 m AGL	0.44	0.32	+0.23		77.3
1000 - 5000 m AGL	1.46	1.14	+0.09		51.8
58 - 1000 m AGL	1.65	1.28	+0.91		51.0
Sfc. Layer (29 m AGL)	1.70	1.31	+0.53		48.4
<b>Pressure (mb)</b>	<b>RMSE (mb)</b>	<b>MAE (mb)</b>	<b>ME (mb)</b>		<b>TRP (%)</b>
Sfc. Layer (29 m AGL)	1.07	0.83	+0.19		94.9

The wind direction errors shown in Table 10 for Exp. 2D also are among the lowest for all of the experiments. For example, this is the only experiment in which the surface *RMSE* is less than 45 degrees. The *MEs* (bias) are not quite the lowest of all, but they are nevertheless very small. Moreover, the *TRP* is the highest in Exp. 2D for all layers except in the upper troposphere. Overall, comparison of the wind speed and direction errors in this 12-km experiment to those published in the literature indicates that the statistics from Exp. 2D are among the best, both at the surface and aloft, of all FDDA experiments using analysis nudging reported in recent years. This is encouraging because the strong baroclinic forcing and vertical wind shear in this case make it, in some ways, a challenging episode.

Continuing with the evaluation of Exp. 2D, Table 10 shows that the temperature errors in the surface layer and in all levels above are changed only very little, compared to Exp. 2C. Nevertheless, the *TRP* shows that, overall, Exp. 2D has the lowest statistical error for temperature at all levels and for all experiments. The sea-level pressure errors also remain very low in Exp. 2D, with a *ME* = +0.19 mb and *RMSE* = 1.07 mb. Finally, we note that the mixing ratio statistics have changed very little as a result of all the changes introduced in the various experiments of Configuration 2. In fact, for the troposphere above the PBL, the *RMSEs* and *MAEs* actually are greater by a moderate amount than in Exp. 1A. In addition, the positive moist bias noted in the surface layer of Exp. 1A has increased in Exp. 2D. This suggests that the moisture errors in the upper layers are due to two factors. First, it is likely that the surface evaporation is excessive (possibly related to inaccurate definition of the soil moisture, which was held constant in these experiments). Moreover, the vertical transport of moisture in the deep convection may be excessive. Note that the introduction of FDDA for moisture occurs only above 1.5 km AGL and has relatively small impact because the nudging coefficient, *G*, used for

mixing ratio is very small ( $1 \times 10^{-5} \text{ s}^{-1}$ ), compared to that used for other variables (see Table 4). These results suggest that the FDDA strategy for moisture should be re-evaluated to determine a better approach that would reduce the water-vapor errors, while avoiding possible disruptions of rain processes.

Finally, Table 11 presents a statistical summary for Exp. 3A, which used the 4-km mesh over the entire region of the CAPTEX-83 monitoring network (1152 X 1220 km). Such large fine-mesh domains are becoming computationally practical as computer resources continue to expand rapidly. However, there is much to learn about whether or not current modeling techniques are adequate to produce accurate simulations at very fine scales and under what circumstances. This experiment (Configuration 3) is designed to learn whether simulations of regional-scale transport can be improved in future modeling studies by extending the use of 4-km resolution over large areas.

Examination of Tables 10 and 11 allows comparison of the wind-speed statistics for Exps. 2D and 3A. They reveal a very substantial *decrease* of accuracy for the winds in this case due to the introduction of the 4-km grid in Exp. 3A. The larger wind errors are consistently found in all layers. The *TRP* and index of agreement confirm that the 4-km mesh produces a net negative impact at all levels for both speed and direction.

A similar comparison of the temperatures for Exps. 2D and 3A indicates that errors are greater on the 4-km domain of Exp. 3A, but the effect is somewhat less dramatic than was found for the winds. Even so, the temperature statistics shown in Table 11 are comparable to or lower than the statistical errors found in many other recent air-quality cases. There is also a small increase of the errors for mixing ratio and sea-level pressure on the 4-km domain of Exp. 3A.

**Table 11. Statistical summary of MM5 performance for wind speed and direction in CAPTEX-83 Episode 1 (1200 UTC, 18 Sept. - 0000 UTC, 20 Sept. 1983) on the 4-km verification domain of EXP. 3A.**

<b>Wind Speed (ms<sup>-1</sup>)</b>	<b>RMSE (ms<sup>-1</sup>)</b>	<b>MAE (ms<sup>-1</sup>)</b>	<b>ME (ms<sup>-1</sup>)</b>	<b>I</b>	<b>TRP (%)</b>
5000 - 10000 m AGL	3.60	2.93	- 0.26	0.96	65.7
1000 - 5000 m AGL	3.92	3.04	- 1.11	0.84	51.6
58 - 1000 m AGL	3.38	2.64	-0.56	0.72	50.0
Sfc. Layer (29 m AGL)	2.73	2.17	+0.82	0.59	52.5
<b>Wind Direction (deg.)</b>	<b>RMSE (deg.)</b>	<b>MAE (deg.)</b>	<b>ME (deg.)</b>		<b>TRP (%)</b>
5000 - 10000 m AGL	30.2	20.6	+6.2		42.5
1000 - 5000 m AGL	17.7	14.2	- 0.6		41.5
58 - 1000 m AGL	23.9	17.5	- 0.3		56.0
Sfc. Layer (29 m AGL)	50.3	36.0	- 0.5		57.8
<b>Temperature (C)</b>	<b>RMSE (C)</b>	<b>MAE (C)</b>	<b>ME (C)</b>		<b>TRP (%)</b>
5000 - 10000 m AGL	1.00	0.82	+0.18		94.0
1000 - 5000 m AGL	1.21	0.99	- 0.61		84.6
58 - 1000 m AGL	1.98	1.69	- 1.25		66.3
Sfc. Layer (29 m AGL)	2.58	2.05	- 0.29		59.4
<b>Mixing Ratio (g kg<sup>-1</sup>)</b>	<b>RMSE (g kg<sup>-1</sup>)</b>	<b>MAE (g kg<sup>-1</sup>)</b>	<b>ME (g kg<sup>-1</sup>)</b>		<b>TRP (%)</b>
5000 - 10000 m AGL	0.45	0.32	+0.19		77.3
1000 - 5000 m AGL	1.62	1.25	+0.12		48.6
58 - 1000 m AGL	2.07	1.69	+0.79		34.2
Sfc. Layer (29 m AGL)	1.82	1.43	+0.49		43.3
<b>Pressure (mb)</b>	<b>RMSE (mb)</b>	<b>MAE (mb)</b>	<b>ME (mb)</b>		<b>TRP (%)</b>
Sfc. Layer (29 m AGL)	1.14	0.91	-0.19		93.2

Thus, it appears that adding the 4-km domain in this experiment had an overall negative impact on model accuracy for Episode 1 of CAPTEX-83. Assuming that the intended use of the meteorological fields is for input to an air-quality model, the most serious consequence is the growth of error in the wind fields. However, it is not justifiable to conclude on the basis of this one case that 4-km model resolution is counterproductive for air quality applications in general. In the strongly baroclinic environment encountered in Episode 1, the influence of small locally driven mesoscale circulations may be of lesser importance than would be likely in a mid-summer episode. For the latter situations, the added resolution possible with a 4-km grid has been shown in many studies to be important for simulating lake breezes, sea breezes and mountain-valley circulations known to be critical to the local and regional transport of pollutants. The important conclusion to be gained from the statistical evaluation presented here is that the use high resolution ( $\Delta x \leq 4$  km) in meteorological models does not automatically guarantee greater accuracy in all cases. More attention to the development of superior data assimilation strategies and physical sub-models certainly is warranted. Finally, it is recommended that careful comparison be made between the statistical accuracy produced on different grids of a given nested-domain experiment before meteorological model fields are used in air-quality modeling.

### **5.3 Evaluation of the Simulated Transport**

In this section, regional-scale transport simulated by the MM5 meteorological model solutions is investigated using a parcel trajectory model, TRAJEC. TRAJEC is a post-processor to the MM5 (see Sec. 3.3) that ignores effects due to turbulent dispersion, while calculating only the influence of the 3-D advection produced by the resolved wind fields in each experiment.

Recall that the tracer gas was released into the atmosphere at ground level from the Dayton, OH, site in the early afternoon between 1200 and 1500 LST, 18 September. That is, the tracer was injected into a convectively unstable PBL, where it would be rapidly mixed upward through that layer (~1.2-1.4 km deep). Next, we assume that there is no active mechanism by which a substantial percentage of the tracer can exit from the top of the convective boundary layer (such as deep convection or frontal lifting) *in the first several hours following the release*. In that case, TRAJEC can be used in a reasonably consistent manner to estimate subsequent transport of the plume in response to the MM5 winds. To do this, we initialize a set of parcels distributed in a vertical column above Dayton, from the surface to around 1300-1400 m AGL, and then follow those parcels as they are advected by the model's winds over the next 24 h.

Eight parcels were defined for each experiment and were released at 1700 UTC (1200 LST), 18 September 1983, at different levels in the Dayton grid column. In Exp. 1A, the parcel release levels correspond to the eight lowest sigma levels shown in Table 1 (36, 143, 326, 540, 777, 1012, 1308, and 1725 m AGL). Examination of soundings and model fields for the afternoon of 18 September indicates that the first seven should be in the PBL, while Parcel 8 at 1725 m was above the PBL. In Exps. 2A-3A (five experiments), the MM5 had greater vertical resolution in the boundary layer, so that TRAJEC was not initialized with a parcel in every model layer below 1700 m. The eight release levels for these experiments were chosen to coincide with the three lowest model levels (29, 86, and 143 m AGL), a layer near the middle of the afternoon mixed layer (472 m AGL), three layers near the top of the convectively unstable PBL (1047, 1206 and 1368 m AGL) and at one layer above the PBL (1533 m AGL). These coincide with model layers 32, 31,30, 25, 20, 19, 18, and 17 shown in Table 2.

Figure 58 shows the paths taken by the eight parcels released in Exp. 1A, as calculated by TRAJEC. The initial parcel release from Dayton is at 1700 UTC, 18 September (+5 h into the model run) and the termination time is at 1100 UTC, 19 September (+23 h), shortly before the parcels began to leave the 70-km model domain of Configuration 1. Before examining details of these results, some general comments are appropriate to understand the calculated trajectories. Because the winds in the lowest 2 km normally exhibit considerable speed and directional shear, a set of parcels advected by those winds should display differences in speed and direction, as well. Thus, Parcel 1 in Figure 58 travels close to the surface where friction decelerates the winds, so that its trajectory terminates along the northern shore of Lake Ontario at 1100 UTC, 19 September. The other parcels traveling at higher altitudes terminate much further downwind. Also, recall that winds near the surface are rotated to the left of the geostrophic (that is, toward lower pressures) wind due to frictional forces. In Figure 58, the parcels released close to the surface (Parcels 1-3) take paths that are more northerly (to the left), compared to the rest of the parcels that were released further aloft. Those released at or above the top of the mixed layer (Parcels 7 and 8) are found along the southern limit of the parcel family.

It should also be noted that the turbulent mixed layer does not have the same depth at all locations and at all times through the study period. The PBL is expected to be rather shallow at night over land and probably at most times over large water bodies. Even over land during the daytime, the mixing depth tends to be lower over NY and New England on 19 September due to increasing cloudiness as the cold front approached. Thus, a parcel released near, say, 500 m may be in the middle of the mixed layer at one time, but may be above it at a later time and location. Moreover, we note that the interaction of the parcels with frontal vertical motions can be represented in TRAJEC because those motions are part of the MM5's resolved-scale wind

MM5V3-SCIPUFF Exp1A-70km (36,143,325,549,777,1011,1308,1724)

Trajectories are released at 5.0 hours

Terminated at 23.0 hours

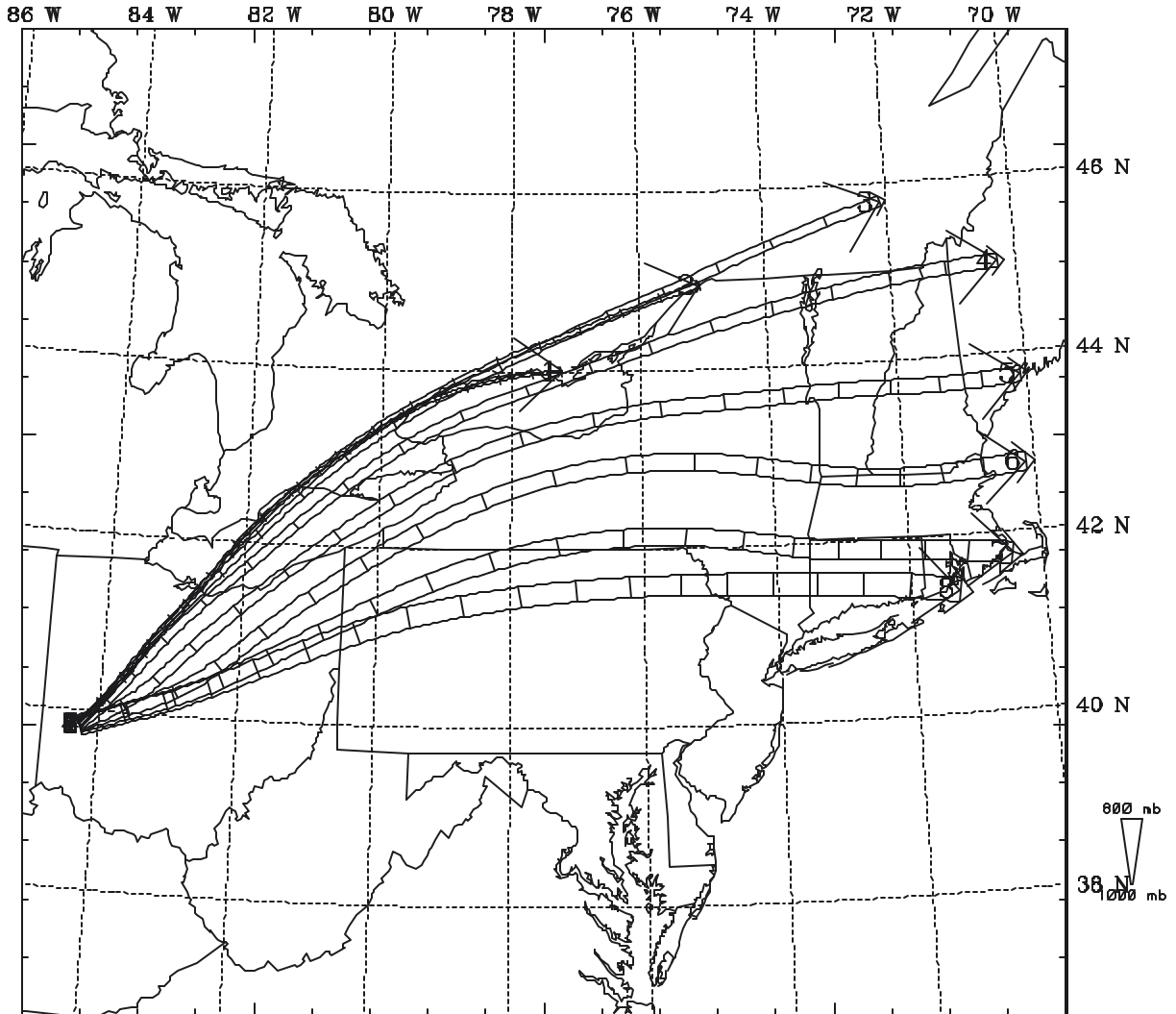


**Figure 58.** Parcel trajectories calculated for Exp. 1A using TRAJEC. Release time at Dayton is 1700 UTC, 18 September; termination time is 1100 UTC, 19 September 1983. Release heights as follows: Parcel 1 = 36 m, Parcel 2 = 143 m, Parcel 3 = 326 m, Parcel 4 = 540 m, Parcel 5 = 777 m, Parcel 6 = 1012 m, Parcel 7 = 1308 m, and Parcel 8 = 1725 m. All trajectories are plotted with two lines, the separation of which corresponds to the pressure level following the parcel (key is at lower right of the figure). Tick marks along the trajectories represent 1 h intervals.

circulations. However, vertical transport due to deep convection cannot be resolved in Exps. 1A-2D because in those experiments the convection occurs below the scale of the MM5's grid mesh. In Exp. 3A, the vertical motions in deep convection are resolved by the model grid (no cumulus parameterization). Vertical transport due to eddy fluxes are unresolved in all the experiments.

At the final time, 1100 UTC, 19 September, the distribution of Parcels 1-6 in Figure 58 (those likely to be in the mixed layer on both days) extends from the north shore of Lake Ontario to western ME. Comparison of this predicted parcel distribution with the measurements of the surface tracer at 1000 UTC on this day (Figure 14c) shows generally fair agreement. (Note that the two positive measurements on the north shore of Lake Erie in Fig. 14c are likely to be in error because they imply an unrealistically slow wind speed.) TRAJEC calculations indicate that the leading edge of the tracer cloud (represented by the fastest Parcels 3-6) has already begun to leave the monitoring network by this time, while the trailing edge (represented by Parcel 1) is still in the vicinity of northern NY. Note that Parcel 1 has turned to the right (to the south) of the paths taken by Parcels 2 and 3 during the final few hours of the period. This change of direction at the lowest levels seems to coincide with the arrival of the surface cold front along northern Lake Ontario. Because the frontal surface slopes northwestward with height, the surface layer should be the first to feel the effects of the wind rotation as the cold air arrives.

Next, we note that the slowly growing separation of the quasi-parallel pairs of lines representing Parcels 3-7 in Exp. 1 reveals that these parcels experience gentle rising motion over the period of the calculations. For example, Parcel 5 has risen from 777 m at the time of the release to nearly 1200 m by the end of the period, which corresponds to a mean vertical velocity of  $\sim 0.6 \text{ cm s}^{-1}$ . This very slow lifting is reasonable for a warm air mass that lies under the influence of an approaching cyclonic storm, but which has not yet encountered the

accompanying frontal boundaries. The rising motion is too weak to be discernable in the vertical cross sections showing modeled winds (e.g., Figure 32), but nevertheless the cumulative effect over time can be important. If a large fraction of the tracer cloud in Exp. 1A is slowly lifted by hundreds of meters during the course of the integration, then it can be carried above the mean top of the PBL. Thus, on the second day that lofted material can no longer be mixed down to the surface. In that event, the surface footprint of the plume probably would not include the area beneath the higher parcels, Parcels 6-8. Moreover, where positive surface concentrations are detected, they may be smaller than would have occurred if all of the plume was still in contact with the ground through turbulent transport. Closer inspection of Figure 14c confirms that there is no indication of tracer material in MA or south of Albany, NY (the path taken by Parcel 6), with positive readings limited mostly to the zone beneath Parcels 1-5.

Next, Figure 59 shows a similar set of parcel trajectories calculated by TRAJEC on the 12-km domain for Exp. 2B during the period from 1700 UTC, 18 Sept. (+5 h) to 1700 UTC, 19 Sept. (+29 h). The final time shown in this figure corresponds to the observed surface tracer footprint shown in Figure 14d. The model-predicted fronts, which traveled faster in this experiment than in Exp. 1A, are shown at this final time in Figure 35. Careful examination of the paths taken by the low-level Parcels 1-3 in Exp. 2B shows that they were influenced by the passage of the cold front, sometimes in ways that are not easy to anticipate. Parcel 1, released closest to the surface at 29 m AGL, turned sharply to the right of its early path when it was just north of Lake Erie (in southwest Ontario) about 0300 UTC, 19 September. Thereafter, it remained in the leading edge of the frontal zone as it moved across northern NY into southern NH. However, note that the change in the spacing of the two parallel lines for Parcel 1 indicates

MM6V3-SCIPUFF Exp2B-12km (29.87,146.462,1071,1234,1400,1669)

Trajectories are released at 5.0 hours

Terminated at 29.0 hours

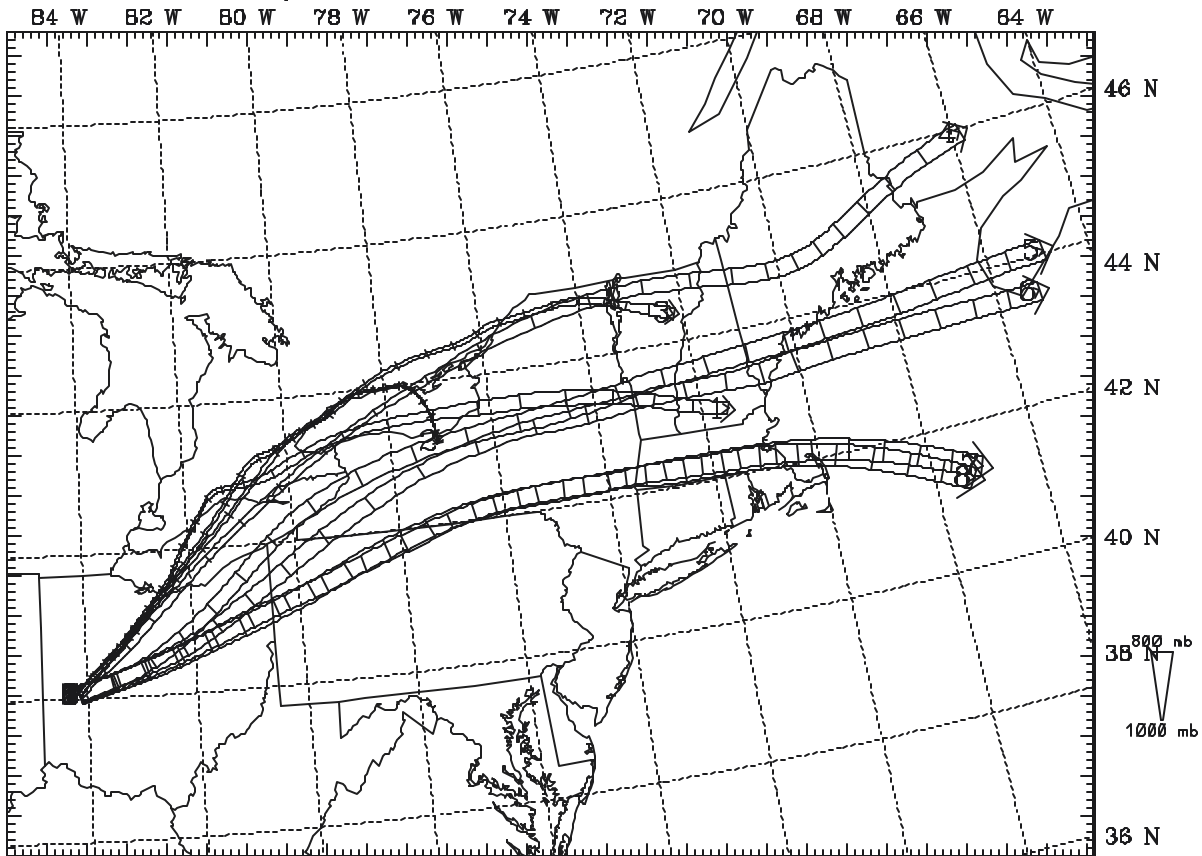


**Figure 59.** Parcel trajectories calculated for Exp. 2B using TRAJEC. Release time at Dayton is 1700 UTC, 18 September; termination time is 1700 UTC, 19 September 1983. Release heights as follows: Parcel 1 = 29 m, Parcel 2 = 86 m, Parcel 3 = 143 m, Parcel 4 = 472 m, Parcel 5 = 1047 m, Parcel 6 = 1206 m, Parcel 7 = 1368 m, and Parcel 8 = 1533 m. All trajectories are plotted with two lines, the separation of which corresponds to the pressure level following the parcel (key is at lower right of the figure). Tick marks along the trajectories represent 1 h intervals.

that this parcel was lifted substantially following 0300 UTC, so that it ended the period at nearly 1250 m. This represents a mean vertical velocity of about  $2.0 \text{ cm s}^{-1}$  over the final 14-h of the simulation due to rising motion near the frontal zone. Parcels 3-6 also show indications of vertical advection, on the order of  $0.5\text{-}1.0 \text{ cm s}^{-1}$ .

By contrast Figure 59 shows that, before 0300 UTC, Parcel 2 had been following a course slightly to the right (southeast) of Parcel 1, as expected. But as a result, Parcel 2 was overtaken by the cold front a bit later at  $\sim 0430$  UTC, 19 September, after which it encountered sinking motion along the northern shore of Lake Ontario. That forced Parcel 2 to travel close to the surface where it experienced frictional deceleration and was left slightly behind the front in the cold air. As it moved with the cold air mass, it encountered increasingly northerly winds late in the period, which carried it southward across Lake Ontario near the surface. This path appears to define the trailing end of the surface plume in Figure 14d (the positive measurements near Toronto may be spurious). Finally, Parcel 3 seems to have come under the influence of the northwesterly winds behind the cold front very late in the period. Parcels 4-8 remain ahead of the front. Comparison of Figures 59, 14 and 35 suggests that Parcels 4-8 may have overtaken the surface position of the warm front by the end of the trajectory calculation period at 1700 UTC, 19 September. However, by then these higher parcels are at or above 850 mb, which is well above the gently sloping warm front.

To conclude the trajectory analysis for Exp. 2B, it appears that only Parcels 1-4 are at low enough altitudes at the end of the period to be associated with a surface tracer plume (directly or through turbulent mixing). The region covered by these four parcels stretches from central Lake Ontario to eastern ME. Parcel 2 suggests that some pollutant material may be injected into the low layers of the cold air mass, although clean Canadian air should prevail further behind the

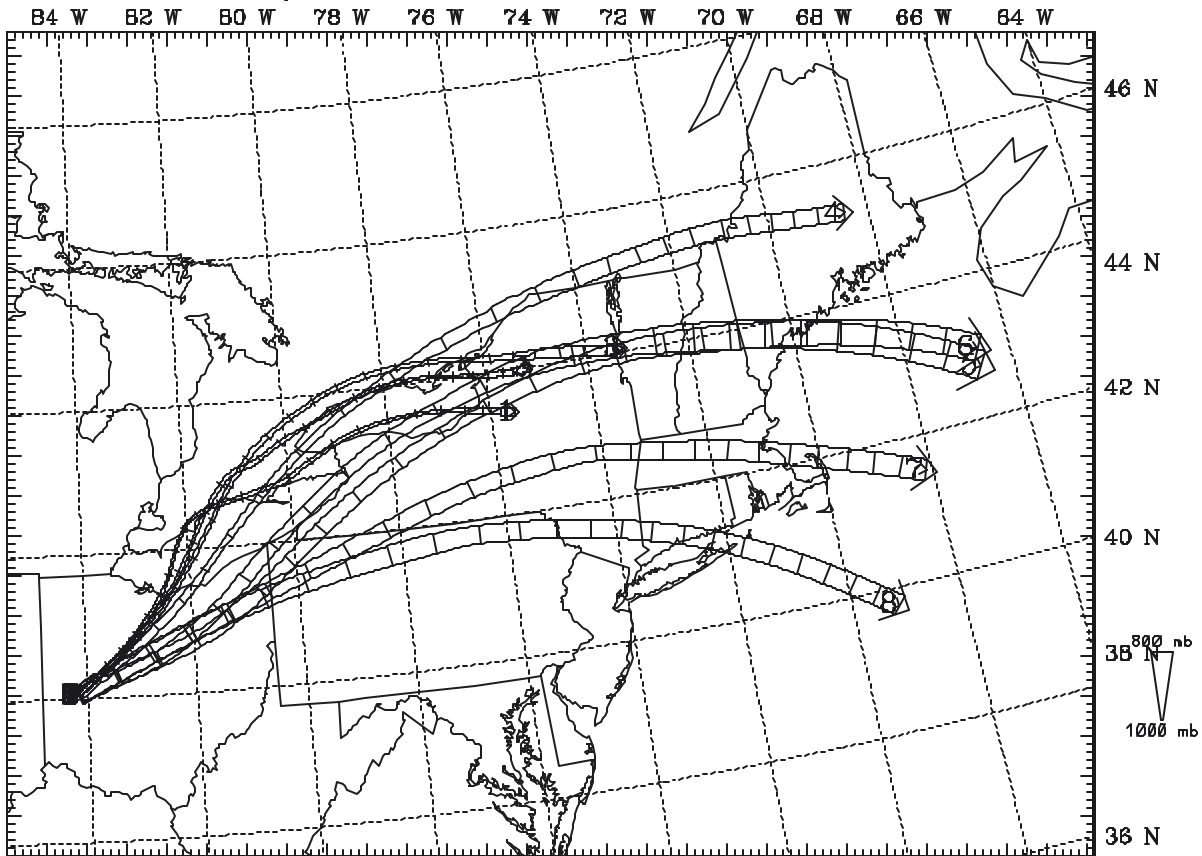
cold front. The trajectory taken by Parcel 1 may actually allow some material to enter southern New England late in the period. Moreover, much of the fastest moving tracer mass (represented by Parcels 4-6) should have already left the region of the monitoring network by 1700 UTC, 19 September. This would result in lower concentrations in the rearward part of the cloud remaining over the monitoring network. Thus we conclude that the trajectories for Exp. 2B support a final surface plume footprint from the southern shore of Lake Ontario across northern NY, VT and NH, with the possibility of some concentrations as far south as CT and MA. Figure 14d appears to confirm this general analysis of the trajectories shown in Figure 59. However, the strong lifting of Parcel 1 and the sharp rightward turn of Parcel 2 in the cold air behind the front, while possible, represent a somewhat unlikely response in Exp. 2B.

Figure 60 shows the trajectory plot for Exp. 2D covering the same 24-h period as in Figure 59. The pattern is mostly similar to that shown in Figure 59, but there are some important differences. First, the trajectories of the middle and upper parcels (Parcels 4-8) show greater anticyclonic turning late in the period. Parcels 4-6 (released in the upper half of the daytime PBL) travel somewhat slower in this experiment, indicating that the FDDA has decelerated the boundary-layer winds somewhat. This finding is confirmed in Tables 8 and 10, where the biases (mean errors) of wind speed in the PBL are reduced from  $+1.48 \text{ ms}^{-1}$  in Exp. 2B to  $-0.29 \text{ ms}^{-1}$  in Exp. 2D. Also, the low-level trajectories for Parcels 1-3 in the vicinity of Lakes Erie and Ontario show less erratic turning and more uniform vertical motions in Exp. 2D than in Exp. 2B. Parcels 5 and 6 have the greatest mean upward motion ( $\sim 1 \text{ cm s}^{-1}$ ). On the other hand, Parcels 7 and 8, which have the most southerly trajectories, temporarily experience some weak subsidence around 0700 UTC, 19 September, as they crossed southern NY. Recall that Parcel 7 was initially

MM6V3-SCIPUFF Exp2D-12km (29.87,146.462,1071,1234,1400,1669)

Trajectories are released at 5.0 hours

Terminated at 29.0 hours



**Figure 60.** Parcel trajectories calculated for Exp. 2D using TRAJEC. Release time at Dayton is 1700 UTC, 18 September; termination time is 1700 UTC, 19 September 1983. Release heights as follows: Parcel 1 = 29 m, Parcel 2 = 86 m, Parcel 3 = 143 m, Parcel 4 = 472 m, Parcel 5 = 1047 m, Parcel 6 = 1206 m, Parcel 7 = 1368 m, and Parcel 8 = 1533 m. All trajectories are plotted with two lines, the separation of which corresponds to the pressure level following the parcel (key is at lower right of the figure). Tick marks along the trajectories represent 1 h intervals.

released low enough (~1368 m) to have acquired some of the tracer material early on the afternoon of 18 September through turbulent mixing processes. By 0700 UTC, 19 September, this parcel had subsided to about 1100 m. So, as it passed over southern New England, the renewed daytime mixing on 19 September may have allowed some elevated tracer in Parcel 7 to be fumigated to the surface before being advected over the Atlantic Ocean. In summary, the trajectories of Exp. 2D suggest that the surface plume footprint at 1700 UTC, 19 September, is likely to extend from the eastern end of Lake Ontario to VT, NH and ME. There is also at least some possibility (indicated by the path of Parcel 7) that small concentrations of the tracer could reach the surface as far south as MA and CT. Therefore, among all of the trajectory calculations conducted for Configurations 1 and 2 (Exps. 1A - 2D), this experiment appears to produce results that are the most consistent overall with the observed surface tracer plume and with expected behavior of the parcels in the vicinity of the fronts.

Finally, the trajectories for Exp. 3A are shown in Figure 61. The initial time is, of course, the same (1700 UTC, 18 September), but the final time shown in the figure is curtailed to 1200 UTC, 19 September, because the 4-km model domain of Configuration 3 is smaller than the 12-km domain of Configuration 2. The trajectories for Parcels 1-4 in Exp. 3A are somewhat irregular. Parcels 1-3 fail to exhibit the strong clockwise turning that should occur with the approach of the cold front, so that these parcels travel farther north into southern Canada on 19 September. Also, Parcel 4 suddenly experiences very strong upward acceleration around 0500 UTC, 19 September. In ~90 minutes the parcel rises from ~500 m to ~2500 m, representing a mean vertical motion during that period of  $\sim 37 \text{ cm s}^{-1}$ . This strong vertical velocity suggests that the parcel must have encountered an area of resolved-scale convection on the 4-km grid in the vicinity of the cold frontal boundary. The direction taken by Parcels 1-3 down the St. Lawrence

MM5V3-SCIPUFF Exp3A 4km (29.87,146.482,1071,1234,1400,1569)

Trajectories are released at 5.0 hours

Terminated at 22.0 hours

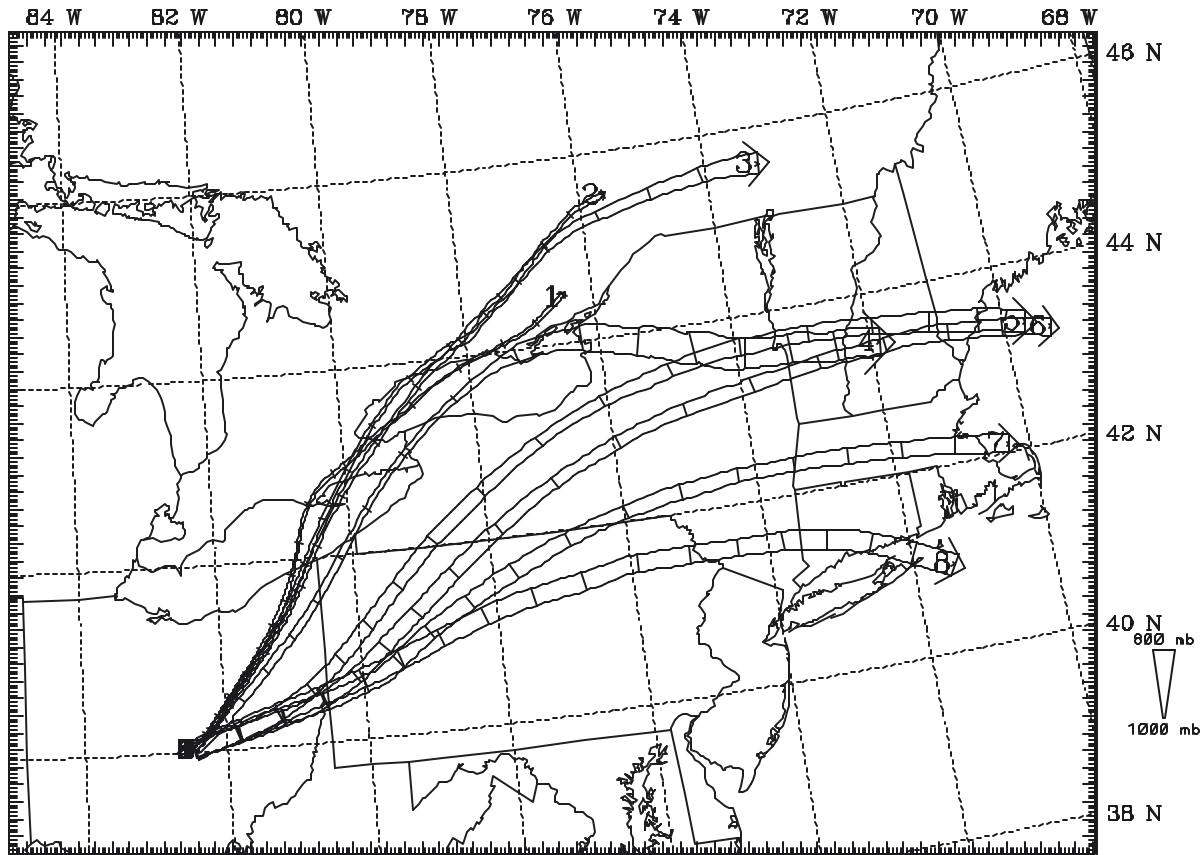


**Figure 61.** Parcel trajectories calculated for Exp. 3A using TRAJEC. Release time at Dayton is 1700 UTC, 18 September; termination time is 1200 UTC, 19 September 1983. Release heights as follows: Parcel 1 = 29 m, Parcel 2 = 86 m, Parcel 3 = 143 m, Parcel 4 = 472 m, Parcel 5 = 1047 m, Parcel 6 = 1206 m, Parcel 7 = 1368 m, and Parcel 8 = 1533 m. All trajectories are plotted with two lines, the separation of which corresponds to the pressure level following the parcel (key is at lower right of the figure). Tick marks along the trajectories represent 1 h intervals.

River Valley into Quebec, Canada, (instead of turning eastward into northern NY) appears to be inconsistent with the expected influence of the advancing cold front and the observed surface tracer cloud in Figure 14c. Therefore, it is concluded that Exp. 3A failed to produce a set of trajectories that is likely to explain tracer measurements in this case.

#### **5.4 Evaluation of the Simulated Plume Dispersion**

The final step in evaluating the performance of the MM5 mesoscale model for regional-scale transport is to calculate the dispersion of a tracer using a plume dispersion model (SCIPUFF) and to compare the simulated tracer concentrations with those observed during the CAPTEX Episode 1. Since the tracer release is identical in each of the six SCIPUFF experiments and SCIPUFF performance has been evaluated extensively in other studies, any differences in performance among the experiments in this case are expected to be primarily due to the meteorological fields used to drive the dispersion model.

First, Table 12 gives maximum surface concentrations simulated at 6-h intervals following the mid-time of the tracer release and corresponding to times at which concentrations are observed (see Fig. 14). Table 12 also gives the average ratios of modeled-to-observed concentrations to better compare MM5-SCIPUFF performance (perfect score is a ratio of 1.0). For example, the table shows that on average, Exp. 1A (70-km grid resolution) over-predicted the surface tracer concentrations by a factor of 2.65. Over-predictions of the surface concentration occurred at all four verification times. Also, the table gives the mean-absolute error of the 6-h modeled-to-observed ratios (*MAER*), which gives the most typical error for each experiment, where a perfect score is 0.0. Thus, in Exp. 1A the *MAER* is 1.65.

**Table 12. Maximum concentrations ( $\text{fl l}^{-1}$ ) of  $\text{C}_7\text{F}_{14}$  tracer at the surface during the CAPTEX-83 Episode 1. Numbers in parentheses are the ratio of modeled to observed concentrations at the specified times. Case-averaged ratios of modeled to observed concentrations (perfect score = 1.0) and mean absolute errors of the ratios (perfect score = 0.0) are shown in the two right-hand columns.**

Exp. Number	Hours Following Middle of Tracer Release				Average Model/Obs. Ratio	Mean Abs. Error of Ratio (Model/Obs)
	+5 h	+11 h	+17 h	+23 h		
<b>Exp. 1A</b>	1985.6 (1.25)	462.6 (3.82)	304.0 (3.45)	97.6 (2.08)	<b>2.65</b>	<b>1.65</b>
<b>Exp. 2A</b>	1702.3 (1.07)	531.2 (4.39)	179.5 (2.04)	56.4 (1.20)	<b>2.18</b>	<b>1.18</b>
<b>Exp. 2B</b>	1756.0 (1.11)	170.3 (1.41)	67.9 (0.77)	15.2 (0.32)	<b>0.90</b>	<b>0.36</b>
<b>Exp. 2C</b>	1517.2 (0.96)	138.9 (1.15)	69.1 (0.79)	0.60 (0.01)	<b>0.73</b>	<b>0.35</b>
<b>Exp. 2D</b>	1416.3 (0.89)	178.4 (1.47)	69.2 (0.79)	25.8 (0.55)	<b>0.93</b>	<b>0.31</b>
<b>Exp. 3A</b>	1919.6 (1.21)	25.2 (0.21)	0 (0.00)	0 (0.00)	<b>0.36</b>	<b>0.75</b>
<b>Observed</b>	1586	121	88	47	--	--

When the 12-km grid is introduced in Exp. 2A, the statistical performance of the SCIPUFF-MM5 concentrations immediately show significant improvement compared to Exp. 1A. Maximum concentrations are closer to the observed values for three of the four verification times, so that the average concentration ratio and the *MAER* are both improved by ~40%. Substantial errors remain in Exp. 2A, however. The maximum concentrations average a bit more than twice the observed values and there are over-predictions at all four verification times. Thus, the introduction of higher resolution grids alone is not a sufficient solution.

When more modern physics is added to the 12-km configuration in Exp. 2B, Table 12 indicates that the errors in the plume concentration maximums were reduced greatly. The predicted maximum concentrations were a bit too high in the first half of the period, but became somewhat lower than observed in the second half of the period. Thus, the average of the ratio for modeled versus observed concentrations is 0.90 in Exp. 2B, while the *MAER* was reduced to 0.36 (reduction by more than two thirds, compared to Exp. 2A). This improvement in SCIPUFF concentrations is consistent with the reduction of MM5 wind speed and direction errors at the surface and in the PBL noted earlier in Tables 7 and 8.

Next, Table 12 shows that introduction of FDDA in Exp. 2C (nudging toward upper-air data only) produced some mixed results in terms of the predicted maximum tracer concentrations. Even though Tables 8 and 9 show that the FDDA greatly reduced the remaining speed and direction errors for the surface and PBL winds, the average ratio of the modeled versus observed concentrations dropped to 0.73 in Exp. 2C, with the *MAER* reduced only very slightly to 0.35. Closer inspection of the results from Exps. 2B and 2C at each verification time reveals that introduction of FDDA in the MM5 led to more accurate SCIPUFF concentration maximums at the first three verification times, but by the final time (+23 h), there was almost no

tracer predicted at the surface in Exp. 2C. Since we have already shown that the introduction of FDDA reduced the MM5's tendency to over-predict the mean wind speed in the surface layer and PBL, it is clear that the very low tracer concentration at +23 h is not due to stronger advection that could cause the tracer to rapidly leave the domain. It is more likely that the parts of the tracer plume remaining in the 12-km domain at +23 h are isolated aloft and are not being fumigated to the ground.

In Exp. 2D, the MM5's FDDA strategy assimilated both surface and upper-air observations. Table 12 indicates that the addition of surface FDDA had fairly minor impact at most times, except that the predicted maximum concentration at the final time (+23 h) rose substantially. As a consequence, the average modeled-to-observed ratio became 0.93 and the *MAER* was reduced further to 0.31. In summary, this FDDA strategy produced wind and temperature fields that, when used to drive SCIPUFF, generated the best overall statistical skill for the maximum tracer concentrations at the surface. This result is consistent with the generally small errors found for the MM5's statistics in Exp. 2D (see Table 10).

Finally, Table 12 shows that the SCIPUFF concentrations predicted using the winds from Exp. 3A were comparatively poor. Maximum concentrations dropped well below observed values by the second verification time (+11 h) and SCIPUFF produced zero concentrations at the final two times. Thus, the case-averaged statistics are degraded badly compared to those found in the 12-km experiments. Tables 10 and 11 above showed that the *RMSE* and *MAE* for the wind speed and direction also were degraded significantly (at least in this case) when the 4-km fine grid was used. While the previous MM5 statistics gave some insights into the possible causes of the poor tracer concentrations in Exp. 3A, they do not tell the whole story, especially since there

are no useful tracer observations aloft. Thus, for more information, we turn to surface and cross section plots of tracer concentrations simulated by SCIPUFF.

At the surface, we shall concentrate primarily on the tracer plume areas (or, "footprints") simulated by SCIPUFF using the MM5's 3-D wind and temperature fields at 1000 UTC (+17 h) and 1600 UTC (+23 h), 19 September, during the latter part of the study period. This focuses attention on regional-scale plume transport over distances of 1000-1200 km and the role of meteorological modeling to affect that transport. The observed concentrations and frontal positions at these times are shown in Figures 14c and 14d, when the cold front was crossing the lower Great Lakes and entering northern New England. The tracer release-point at Dayton is shown as an inverted triangle over southwest OH in each of the SCIPUFF plots.

First, Figures 62 and 63 show that the SCIPUFF tracer footprints simulated at +17 and +23 h in Exp. 1A appear to be displaced too far to the northwest, with the axis of maximum predicted concentrations lying along the observed frontal positions. Thus, about half of the plume appears to lie north of the actual front in the cold air mass. In this experiment, the extent of the plume simulated behind the observed cold front is an obvious error caused by the under-prediction of the speed of the cold front and weakening of the nocturnal LLJ in Exp.1A (see Sections 5.1.1 and 5.2). Also, as noted in Table 12, the surface concentrations are much too high, compared to the observed values in Figure 14.

Next, Figures 64 and 65 present corresponding surface tracer footprints from Exp. 2B at +17 h and + 23 h, respectively, using 12-km resolution and improved physics to generate the meteorological inputs (but without FDDA). In this experiment, the plume has traveled much farther eastward due to the much stronger LLJ, so that the maximum predicted concentration at

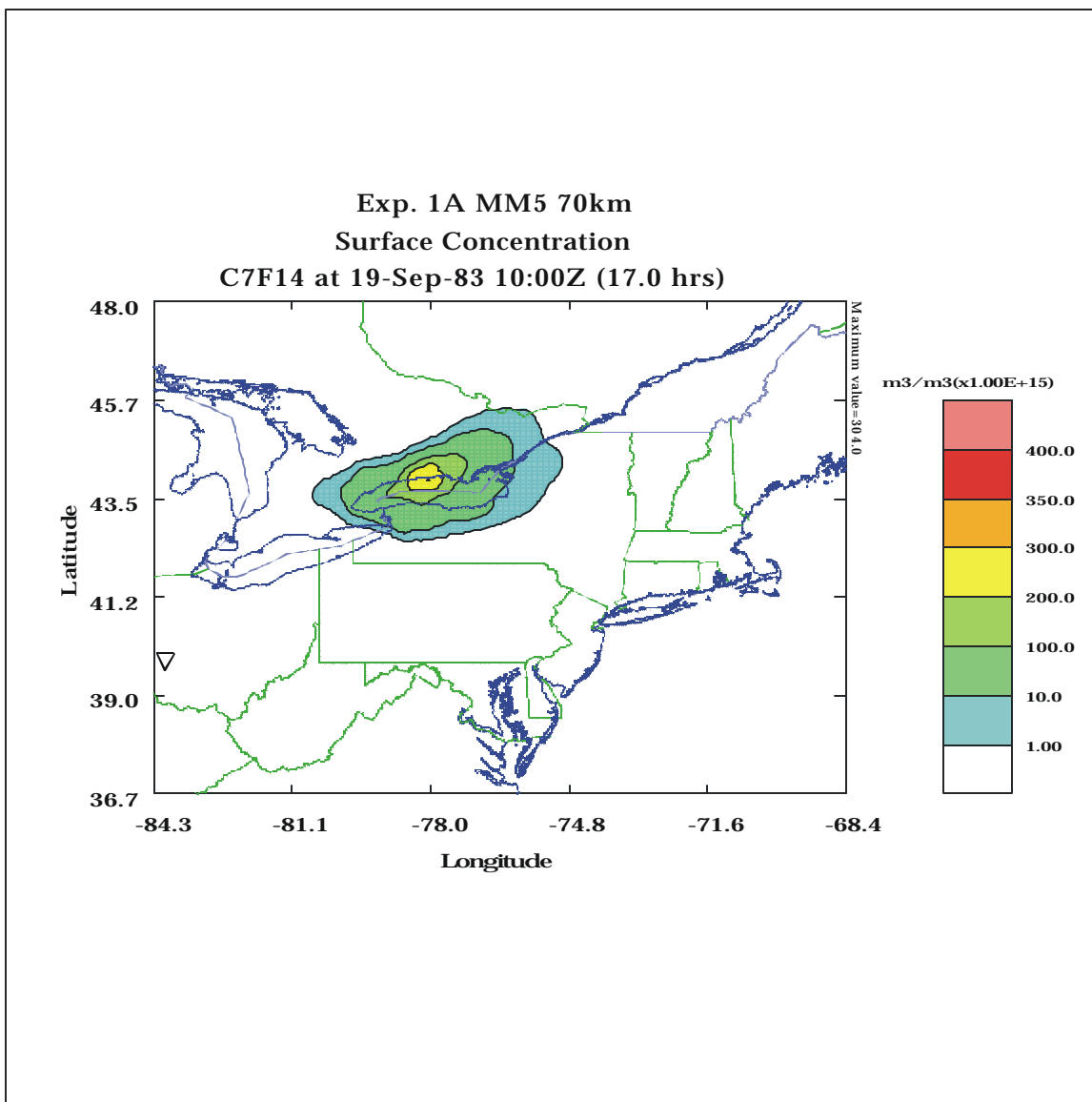


**Figure 62.** SCIPUFF surface concentrations of inert tracer ( $\text{fl l}^{-1}$ ) released from Dayton, OH, on the 70-km domain of Exp. 1A during CAPTEX-83, Episode 1. Concentrations are valid at 1000 UTC, 19 September 1983 (+17 h).

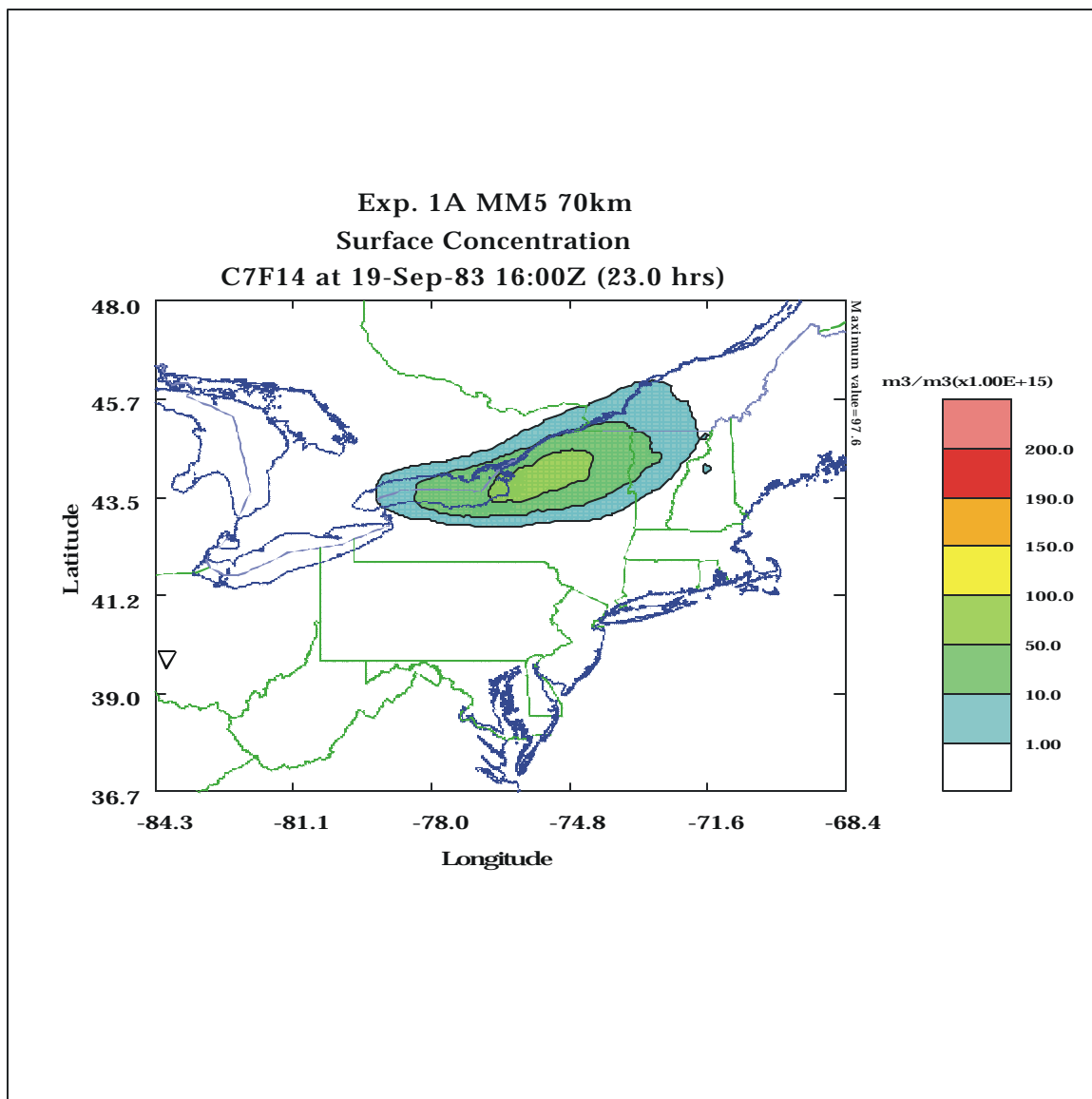


**Figure 63.** SCIPUFF surface concentrations of inert tracer ( $\text{fl l}^{-1}$ ) released from Dayton, OH, on the 70-km domain of Exp. 1A during CAPTEX-83, Episode 1. Concentrations are valid at 1600 UTC, 19 September 1983 (+23 h).

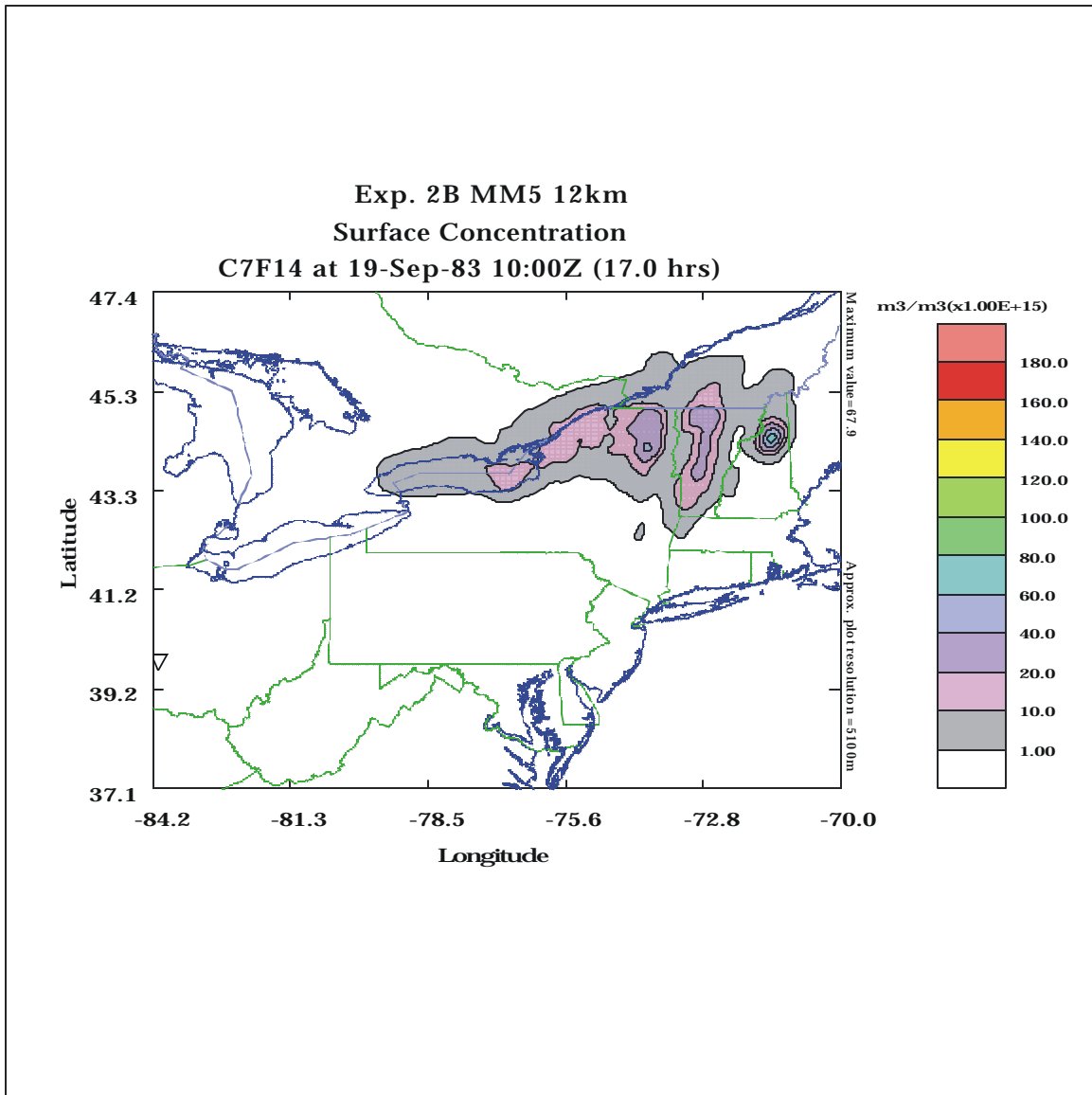


**Figure 64.** SCIPUFF surface concentrations of inert tracer ( $\text{fl l}^{-1}$ ) released from Dayton, OH, on the 12-km domain of Exp. 2B during CAPTEX-83, Episode 1. Concentrations are valid at 1000 UTC, 19 September 1983 (+17 h).

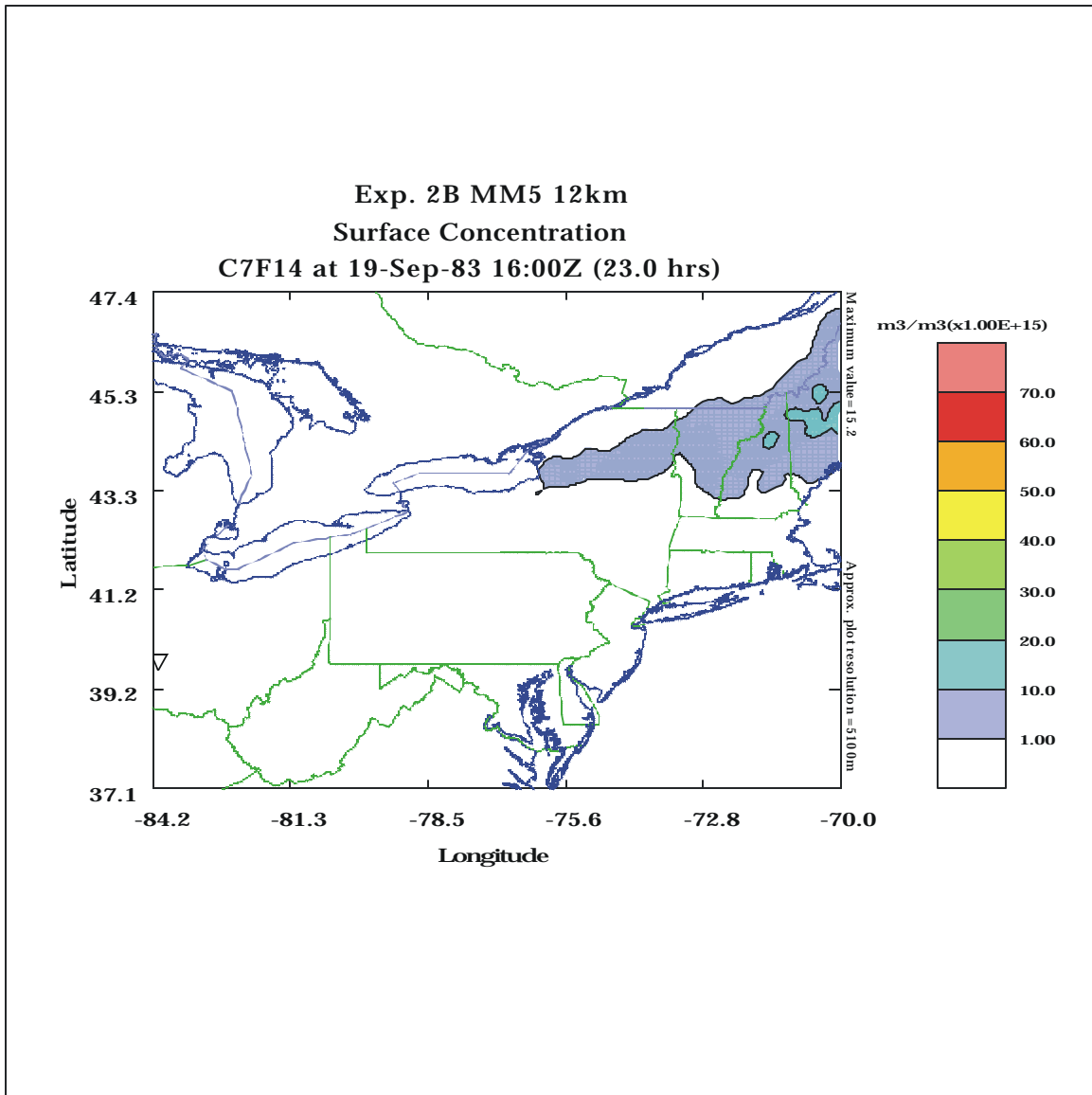


**Figure 65.** SCIPUFF surface concentrations of inert tracer ( $\text{fl l}^{-1}$ ) released from Dayton, OH, on the 12-km domain of Exp. 2B during CAPTEX-83, Episode 1. Concentrations are valid at 1600 UTC, 19 September 1983 (+23 h).

+17 h is over Mt. Washington in NH (Figure 64). However, Figure 14c indicates that the observed maximum at this time was farther west in northern NY east of Lake Ontario. Since the MM5's PBL winds were shown to be too strong in Exp. 2B, the eastward displacement of the maximum is easily understood. Also, note that in Figure 64 especially high concentrations are found over the peaks of the Adirondack, Green and White Mountains, which suggests that the core of the plume at 1000 Z (before dawn) is above the height of all but the highest terrain. This is consistent with the hypothesis that much of the tracer cloud was mixed upward on the previous afternoon over OH and then was transported rapidly east-northeastward during the night by the LLJ at considerably faster speeds than can be explained by the surface winds. Another problem with the surface concentrations predicted at +17 h in Exp. 2B is that they are very low just east of Lake Ontario, where the observed concentrations were greatest. Six hours later at +23 h, Figure 65 indicates that most of the tracer had left the domain, with low concentrations simulated in the tail of the plume that remains visible from northern NY to ME. The most obvious explanation for this result is that the LLJ winds were too strong in Exp. 2B.

Similar plots of the surface concentrations at +17 h and +23 h from the 12-km Exp. 2D, which added surface and upper-air FDDA to the MM5, are shown in Figures 66 and 67. Comparison between Figures 64 and 66 reveals that application of FDDA has slowed the plume's eastward progress considerably, so that in Exp. 2D the concentrations are greater in northern NY than in NH. This pattern agrees much better with the observed tracer at the same time (Figure 14c). The only serious problem apparent in Figure 66 is that SCIPUFF has also predicted fairly high concentrations north of Lake Ontario in the cold air mass just behind the observed frontal position, where the monitoring network shows no concentrations. Unlike Exp. 1A, it was shown in Section 5.1.2 that the simulated speed of the cold front was fairly accurate in Exp. 2D.

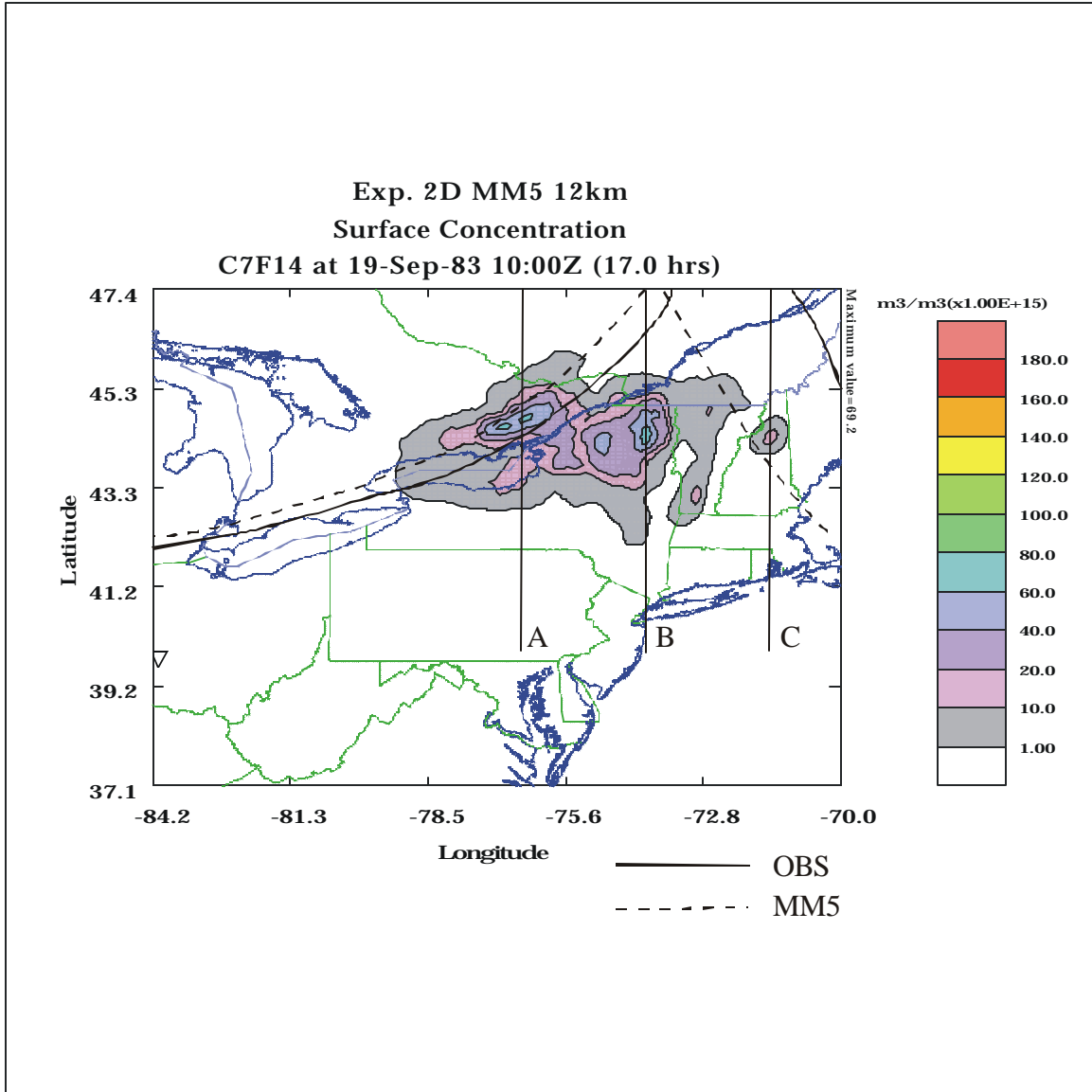


**Figure 66.** SCIPUFF surface concentrations of inert tracer ( $\text{fl l}^{-1}$ ) released from Dayton, OH, on the 12-km domain of Exp. 2D during CAPTEX-83, Episode 1. Concentrations are valid at 1000 UTC, 19 September 1983 (+17 h).

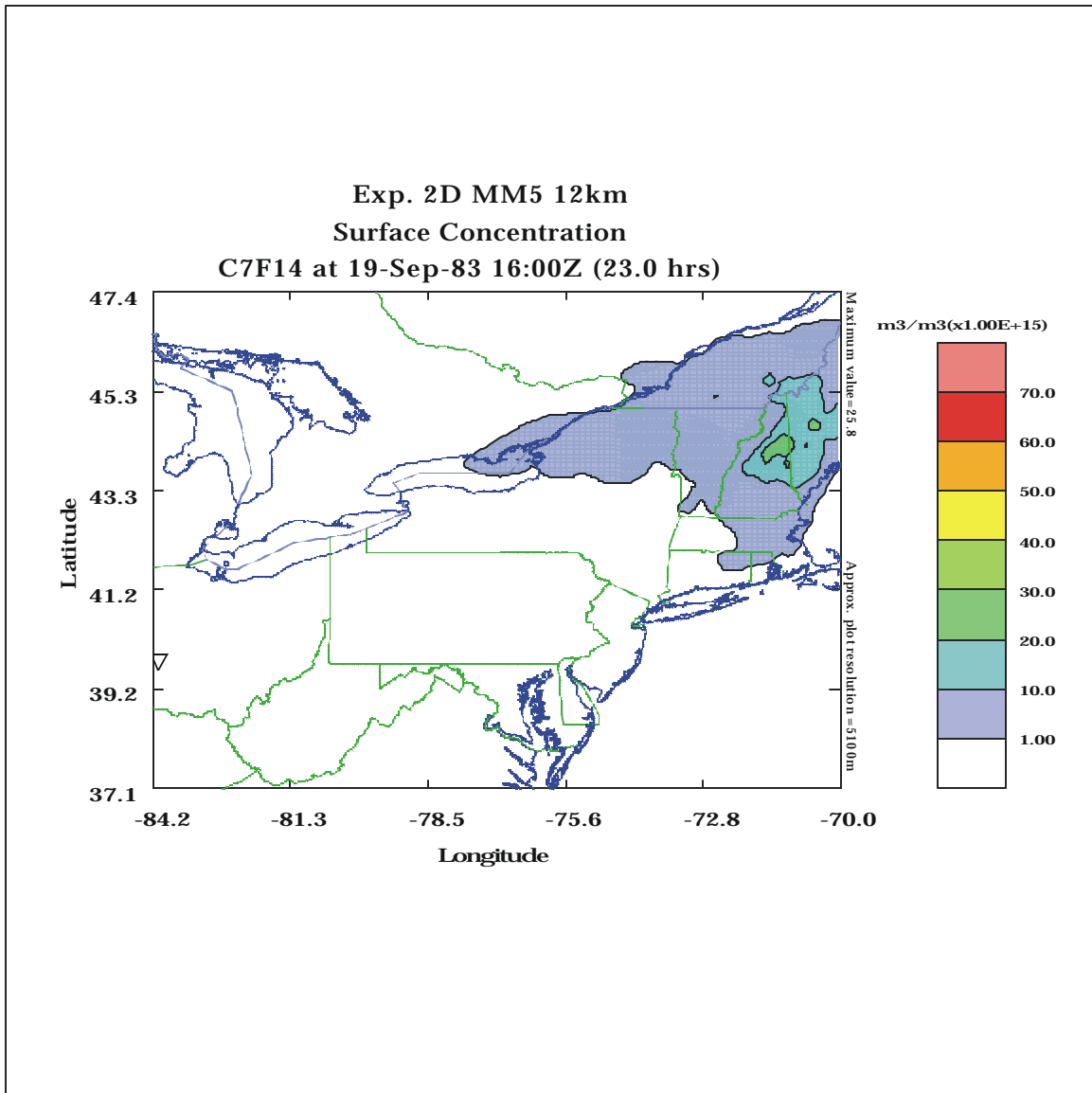


**Figure 67.** SCIPUFF surface concentrations of inert tracer ( $\text{fl l}^{-1}$ ) released from Dayton, OH, on the 12-km domain of Exp. 2D during CAPTEX-83, Episode 1. Concentrations are valid at 1600 UTC, 19 September 1983 (+23 h).

However, the overlay of the model-simulated (dashed) and observed (solid) frontal positions in Figure 66 indicates that in Exp. 2D the front is still a bit too slow at 1000 UTC. Thus, the erroneous high surface concentrations predicted by SCIPUFF just north of Lake Ontario are due primarily to the MM5's slightly slow frontal advance. Also, some of the monitoring sites north of Lake Ontario did not report during this episode, so the real position of the northern edge of the plume is somewhat uncertain. (Note that the high concentration reported in Figure 14c at the monitor just west of Niagara Falls, north of Lake Erie, is almost certainly spurious.) Six hours later, at +23 h, Figure 67 shows a considerably broader tracer footprint in Exp. 2D with higher surface concentrations over New England than were found in Figure 65 for Exp. 2B. Thus, except for the impact of the somewhat slower-than-observed front at 1000 UTC, 19 September (Figure 66), the pattern of the concentrations in this experiment is in mostly good agreement with the surface observations shown in Figure 14c and 14d.

Lastly, Figure 68 shows surface concentrations predicted by SCIPUFF at 0400 UTC, 19 September (+11 h) based on MM5's solutions in Exp. 3A (4-km grid). This plot is compared to the observations shown in Figure 14b. Here, it is seen that the predicted concentrations are much too low, even at this early time in the study period. Therefore, almost all of the tracer material released in SCIPUFF must remain in the domain, but trapped aloft. At subsequent times during Exp. 3A, the plume at the surface disappears completely in the SCIPUFF results (not shown).

The SCIPUFF surface concentrations are clearly very important for evaluating the regional-scale transport simulated by the MM5 mesoscale model in the CAPTEX-83 Episode 1. However, as discussed earlier, we expect much of the tracer material to be carried aloft due to vertical advection and mixing. Because of differential horizontal advection, particularly at night when the LLJ is strongest and intermittent shear-induced turbulence is expected, the morphology

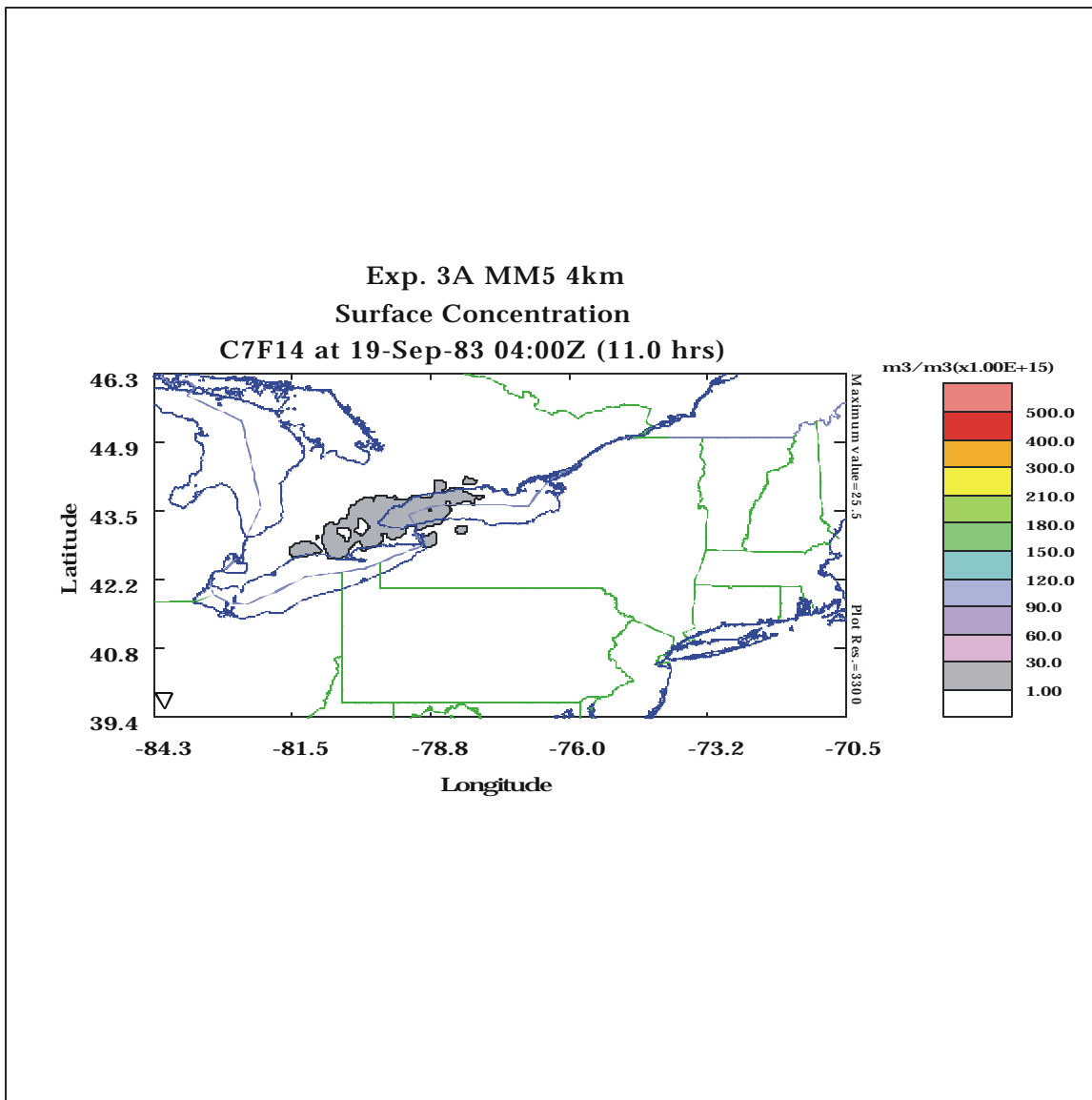


**Figure 68.** SCIPUFF surface concentrations of inert tracer ( $\text{fl l}^{-1}$ ) released from Dayton, OH, on the 4-km domain of Exp. 3A during CAPTEX-83, Episode 1. Concentrations are valid at 0400 UTC, 19 September 1983 (+11 h).

of the elevated plume may be considerably different from the surface footprint. Thus, a full understanding of the model's transport requires examination of the elevated plume concentrations, as well.

To understand the elevated plume structure, we will concentrate on three north-south vertical cross sections taken through the plume in Exp. 2D. The locations of these cross sections are shown in Figure 66. Section A is drawn along 76.8 W through the eastern end of Lake Ontario, Section B is along 74.0 W through the Adirondack Mountains of NY, and Section C is along 71.4 W through the White Mountains of NH. Each cross section extends from 40.0 N to 47.4 N to concentrate on the latitudes containing the plume. Investigation of the 3-D plume structure is limited to Exp. 2D because the meteorological statistics, trajectories and surface-plume evaluations given above consistently indicate that this experiment has the lowest overall error among the six experiments. Moreover, to focus on regional transport we will focus on 1000 UTC and 1600 UTC, 19 September, (+17 and +23 h), when the plume had been transported ~1000-1200 km downwind and had interacted with the LLJ and the fronts.

We begin with Figures 69-71, which show plume concentrations at 1000 UTC, 19 September, along the three vertical cross sections. Figure 69, corresponding to Section A, shows the plume structure over and just north of Lake Ontario at this time (see Figure 66). The most important characteristics of the plume in this section are that the maximum concentration is located at the surface ( $\sim 62 \text{ fl } \Gamma^1$ ) and that all concentrations greater than  $10 \text{ fl } \Gamma^1$  lie below 500 m MSL ( $\sim 200\text{-}400 \text{ m AGL}$ ). This is consistent with expected plume behavior, since trajectories of parcels confined close to the surface should experience relatively weaker mean wind speeds (see Parcels 1-3 in Figure 60). Thus, this part of the plume should correspond to the rear of the 3-D tracer distribution at this time. Also, air flowing over the relatively cool lake should experience

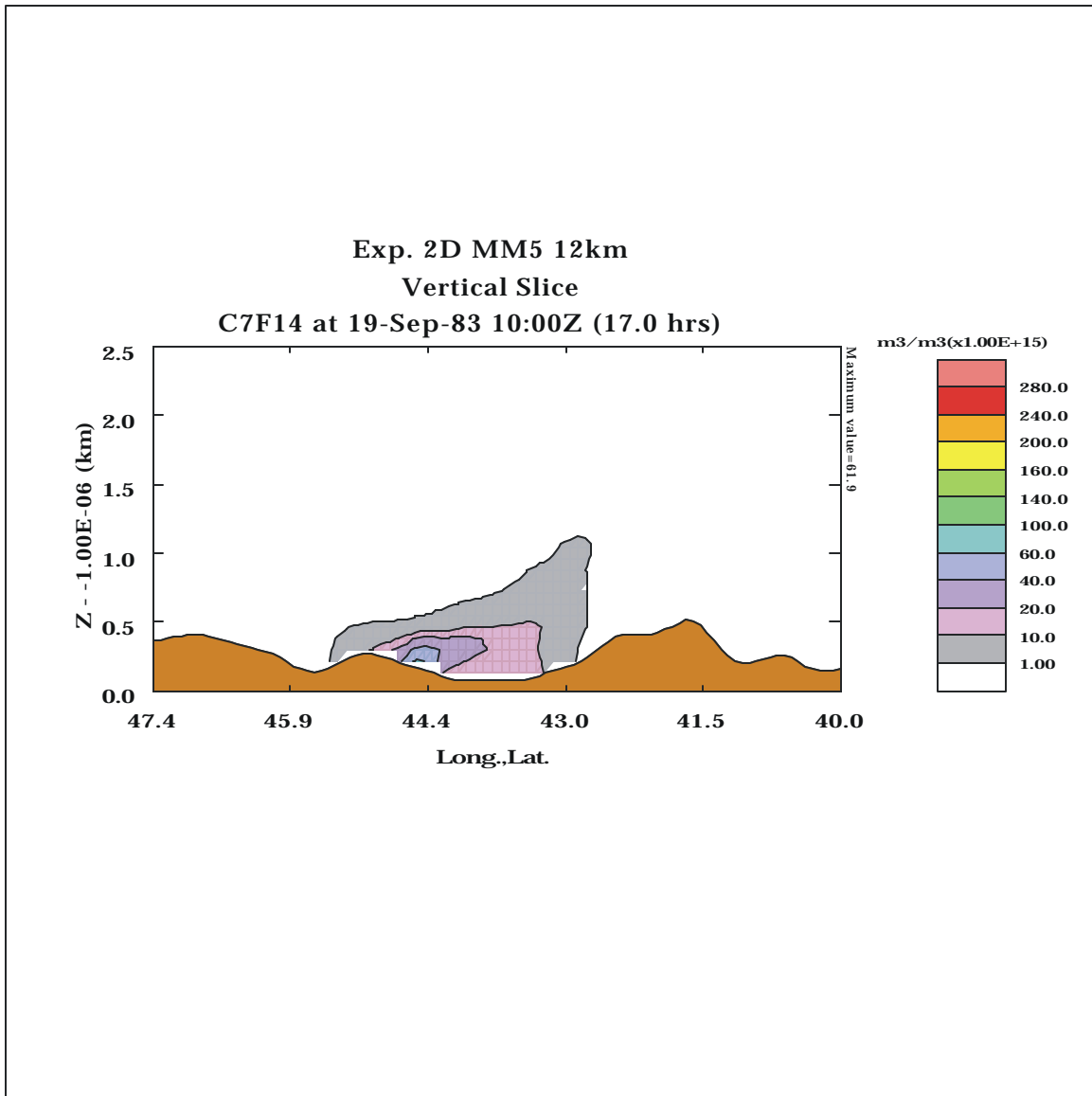


**Figure 69.** SCIPUFF surface concentrations of inert tracer ( $\text{fl l}^{-1}$ ) released from Dayton, OH, shown along cross section A (Lake Ontario) on the 12-km domain of Exp. 2D during CAPTEX-83, Episode 1. Concentrations are valid at 1000 UTC, 19 September 1983 (+17 h).

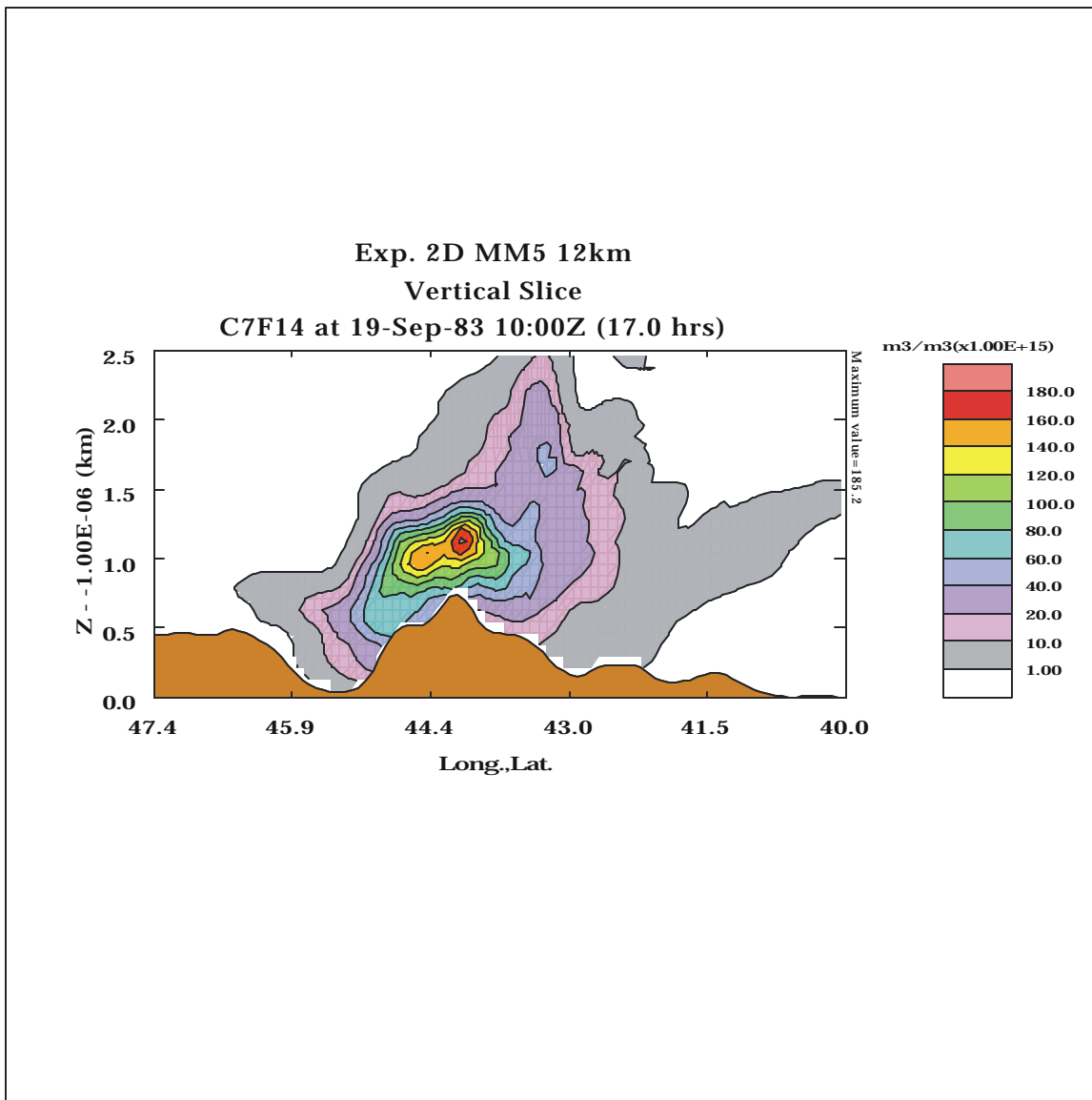


**Figure 70.** SCIPUFF surface concentrations of inert tracer ( $\text{fl l}^{-1}$ ) released from Dayton, OH, shown along cross section B (Adirondack Mountains) on the 12-km domain of Exp. 2D during CAPTEX-83, Episode 1. Concentrations are valid at 1000 UTC, 19 September 1983 (+17 h).

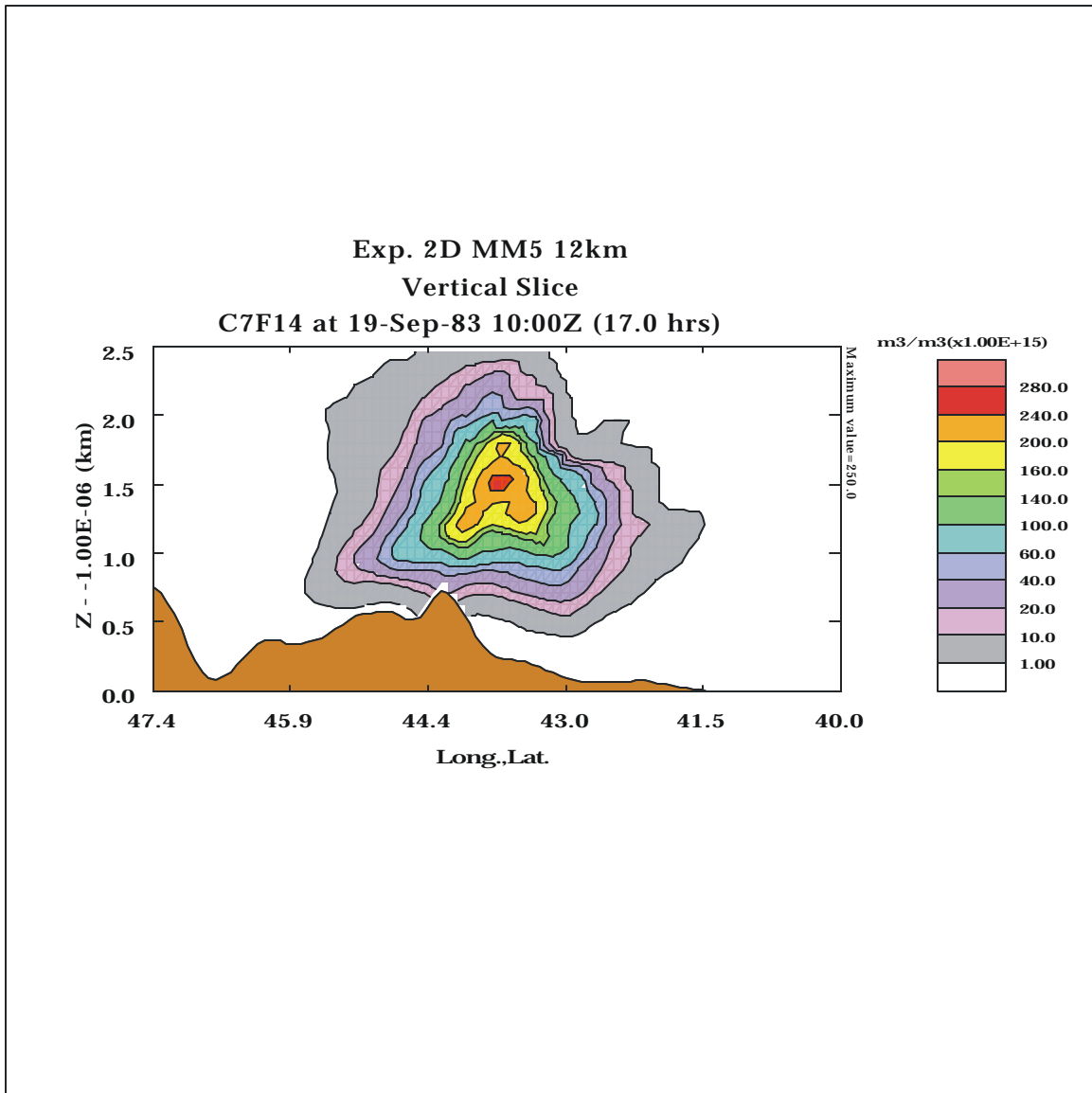


**Figure 71.** SCIPUFF surface concentrations of inert tracer ( $\text{fl l}^{-1}$ ) released from Dayton, OH, shown along cross section C (White Mountains) on the 12-km domain of Exp. 2D during CAPTEX-83, Episode 1. Concentrations are valid at 1000 UTC, 19 September 1983 (+17 h).

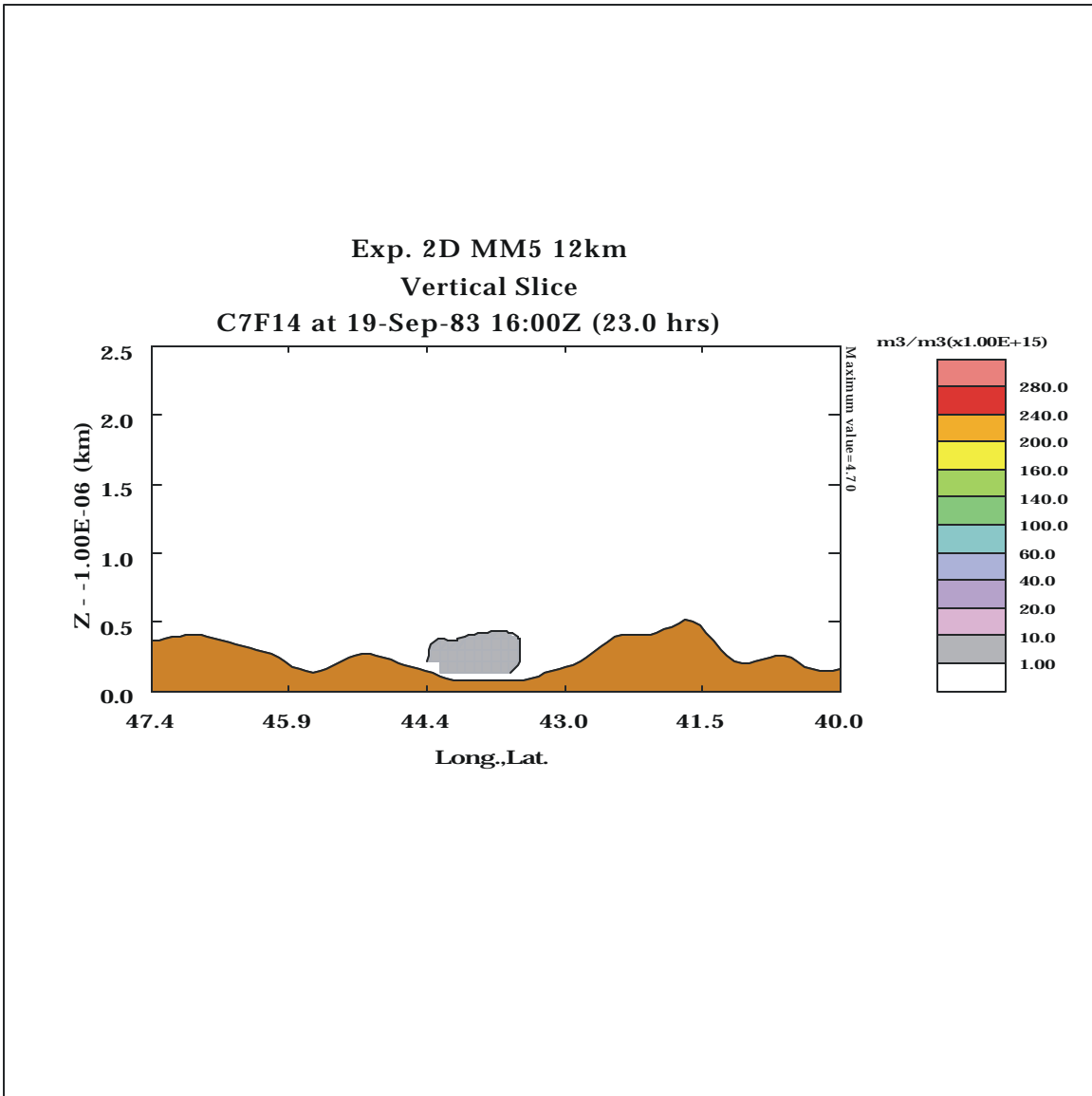
weaker turbulence and lower PBL depths, especially during the daytime, so the tracer material in this area ought to be found at low levels. Very little of the SCIPUFF tracer is detected northward or above the simulated cold front, which intersects the surface at ~44.8 N in this cross section (see Figure 66). Therefore, if the simulated cold front had traveled a bit faster in the model, as observed, the surface tracer maximum simulated by SCIPUFF (shown in Figures 66 and 69) would almost certainly have been displaced from the north shore of Lake Ontario to the east end of the Lake near Watertown, NY. That change would agree well with the local maximum observed by the monitoring network (see Figure 14c). Lastly, Figure 69 reveals that the uppermost part of the simulated plume extends to ~900 m AGL at 43.0 N, near Syracuse, NY. This lies closer to the LLJ axis at this time, although tracer concentrations here are very small.

Figure 70 shows the tracer concentrations for Exp. 2D in the plane of Section B at the same time, 1000 UTC. Several important differences are immediately apparent, compared to Figure 69. First, the concentration maximum is much greater ( $\sim 185 \text{ fl } \Gamma^1$ ) and it is located at ~1150 m MSL instead of the surface. If we had to rely only on the observations from the CAPTEX surface monitoring network, or the SCIPUFF surface tracer predictions, it might be easy to assume that the bulk of the plume lay closer to Lake Ontario. However, Figure 70 makes it clear that the greatest part of the plume mass has been traveling more rapidly eastward in the LLJ, as hypothesized earlier in this report. The latitude of the simulated maximum (~44.0 N) corresponds well with the path taken by TRAJEC parcels 5 and 6 (see Figure 60), which were released over Dayton at ~1000-1200 m AGL. Furthermore, note the horizontal extent of the plume is much broader in Section B, compared to Section A, with the southern edge located higher (~1500 m MSL) than the northern edge (~800 m MSL). Notably, a substantial amount of the tracer has been carried farther aloft to ~2500 m MSL in the vicinity of 43.3 N near Albany,

NY. Since this area lies in the vicinity of the leading edge of the pre-frontal convective showers generated by the MM5, it appears likely that some of the tracer in this cross section is being lifted by the vertical motions associated with the convection.

The easternmost transect along Section C at 1000 UTC is shown in Figure 71. Although the position of the warm front is rather uncertain at this time, the most likely position diagnosed from the model simulation in Exp. 2D intersects Section C near 43.5 N (Figure 66), so that the northern half of the transect lies east of the surface front. Figure 71 indicates that the maximum concentration aloft is  $\sim 250 \text{ fl } \Gamma^1$  at 1500 m MSL, while the maximum concentration at the surface this far eastward is only  $\sim 20 \text{ fl } \Gamma^1$  on top of Mt. Washington. Otherwise, the entire plume at this longitude is elevated, indicating that the leading part of the plume is indeed being lifted over the warm front as hypothesized earlier. The top of the plume extends just above 2500 m MSL, but its cross section is fairly symmetric, suggesting no unusual transport mechanisms are active in this area. The high tracer concentrations found in Section C, compared to Sections A and B, imply that much of the plume probably lies farther east and may already have left the SCIPUFF domain by +17 h. Finally, we note that at 1000 UTC the only two surface monitors in New England that observed concentrations greater than  $10 \text{ fl } \Gamma^1$  are located in the higher elevations of VT and NH (see Figure 14c). This confirms that almost all the actual along this eastern transect plume must exist aloft, as suggested by SCIPUFF and MM5.

Next, Figures 72-74 give simulated concentrations at 1600 UTC, 19 September (+23 h), along the same three transects. At 1000 UTC, the cross sections in Figures 69-71 indicated a 3-D plume that was close to the surface at its westernmost end (near the cold front) with its core rising steadily toward the east until almost the entire plume was above the ground over NH (ahead of the simulated position of the warm front). The results at 1600 UTC in Figures 72-74



**Figure 72.** SCIPUFF surface concentrations of inert tracer ( $\text{fl l}^{-1}$ ) released from Dayton, OH, shown along cross section A (Lake Ontario) on the 12-km domain of Exp. 2D during CAPTEX-83, Episode 1. Concentrations are valid at 1600 UTC, 19 September 1983 (+23 h).

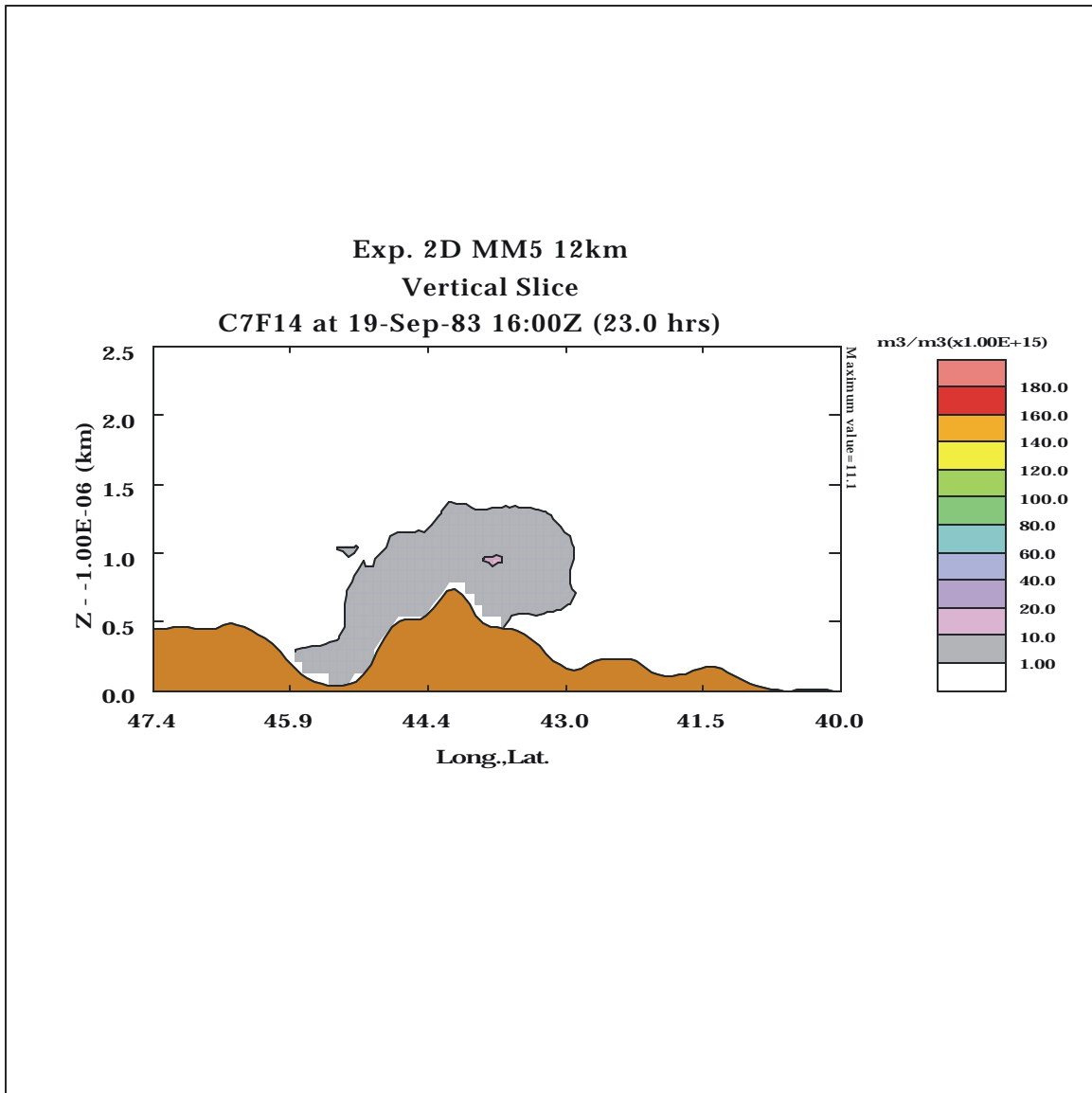


**Figure 73.** SCIPUFF surface concentrations of inert tracer ( $\text{fl l}^{-1}$ ) released from Dayton, OH, shown along cross section B (Adirondack Mountains) on the 12-km domain of Exp. 2D during CAPTEX-83, Episode 1. Concentrations are valid at 1600 UTC, 19 September 1983 (+23 h).

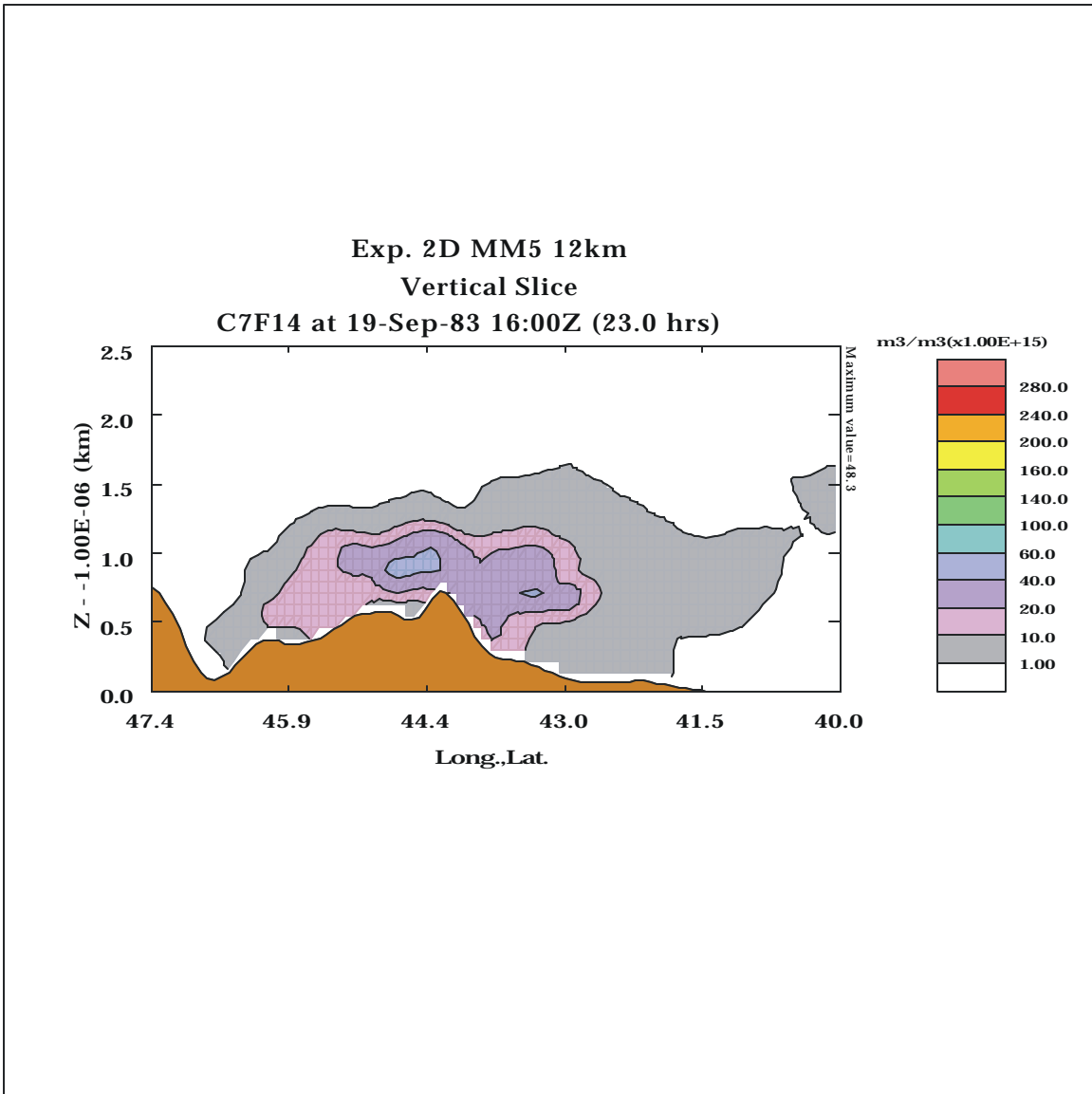


**Figure 74.** SCIPUFF surface concentrations of inert tracer ( $\text{fl l}^{-1}$ ) released from Dayton, OH, shown along cross section C (White Mountains) on the 12-km domain of Exp. 2D during CAPTEX-83, Episode 1. Concentrations are valid at 1600 UTC, 19 September 1983 (+23 h).

show, as expected, that the greatest part of the plume had been advected east of the monitoring network and out of the SCIPUFF domain. Figure 72 indicates that only very low concentrations remained in Section A in a shallow stable layer over eastern Lake Ontario (maximum  $\cong 5 \text{ fl } \Gamma^1$ ). In a similar way, Section B (Figure 73) reveals that most of the plume had passed well east of the Adirondack Mountains, as well. The maximum concentration in Section B at 1600 UTC is only  $11 \text{ fl } \Gamma^1$  at  $\sim 900 \text{ m MSL}$ . Comparison with Figure 70 in the same transect at 1000 UTC shows that by 1600 UTC, the horizontal extent of the plume over the Adirondacks had contracted a great deal, which is consistent with the bulk of the plume having moved well to the east of this longitude. Only along Section C (Figure 74) is there still a broad plume at 1600 UTC (+23 h) with moderate concentrations and a maximum of  $48 \text{ fl } \Gamma^1$  at  $\sim 900 \text{ m MSL}$ . Due to this relatively low altitude for the maximum, we conclude that Section C represents the trailing end of the main plume, even though this is the most easterly of the three transects. We note, incidentally, that the maximum concentration of  $48 \text{ fl } \Gamma^1$  is just  $\sim 200 \text{ m}$  above the MM5's representation of Mt. Washington, where the maximum observed concentration at this time was measured as  $47 \text{ fl } \Gamma^1$ . However, due to the 12-km horizontal grid used in Exp. 2D, the model's terrain is substantially lower than the actual height of the mountain. So, within the accuracy limitations of the model's terrain, there is actually rather good agreement between the simulated and observed plume characteristics in Exp. 2D, even late in the study period.

## 6. CONCLUSIONS

The main objectives of Study A-28 have been to investigate inter-regional transport capabilities of a mesoscale meteorological model and to develop specific estimates of how model skill has changed over the past decade due to improvements in various modeling procedures. These can be represented as three classes: (1) greater model resolution in the horizontal and vertical directions, (2) enhanced physical parameterizations to better represent sub-grid processes such as turbulence and convection, and (3) four-dimensional data assimilation to push model solutions toward observed states through the simulation period. The original investigation, as described in the proposal, envisioned using the MM5 mesoscale model and the TRAJEC parcel trajectory post-processor to estimate the transport of material parcels due to advection by the model's 3-D wind field. The CAPTEX-83 Episode 1 on 18-19 September 1983 was chosen for numerical experimentation because the meteorology of this case was fairly similar to synoptic conditions known to be associated with poor air quality in the Northeast U.S. and because the tracer data collected for this case was relatively complete. Of the many numerical experiments conducted by Penn State during this study, six have been presented in detail in this report.

However, as the investigation proceeded, it became clear that the meteorological observations alone would be insufficient to evaluate certain aspects of the mesoscale model simulations and how they are related to inter-regional transport. Advection by the resolved-scale winds is only part of the information needed to understand inter-regional transport of airborne constituents. Diffusion by turbulence is also extremely important. Examination of the meteorology in the 18-19 September case soon made it very clear that sub-grid vertical and horizontal mixing must have interacted strongly with major resolvable mesoscale features (fronts

and a low-level jet) to yield the observed downwind distributions of surface tracer concentrations. Upper-air measurements taken by aircraft during CAPTEX-83 were ineffective for revealing the 3-D morphology of the tracer in this case because the plume aloft traveled so rapidly that it had passed the pre-planned research flight paths before the airborne measurements were taken. Previous analysis and modeling studies in the literature acknowledged that complex scale interactions were likely to have occurred in this case, but they were unable to address these issues in a meaningful way.

Thus, the original scope of work for Study A-28 was expanded by Penn State to include plume dispersion modeling runs using the ARAP-Titan SCIPUFF model. By adding the SCIPUFF runs, it became possible to verify predicted surface tracer concentrations against observed surface concentrations collected during the CAPTEX-83 study. In this way the combined effects of diffusion and advection acting over time to produce inter-regional plume transport could be verified. Also, by combining results from MM5, TRAJEC and SCIPUFF, a much more complete picture emerged of the fate of the 3-D tracer plume as it traveled over 1200 km in less than 24 h. While the addition of SCIPUFF provided a more methodology and produced valuable insights into inter-regional transport issues, it led to a significant increase in the project work load that led to delays in the project's completion.

Investigation of the model solutions and observations revealed that most of the tracer mass had left the region of the monitoring network much earlier than anticipated at the time of the CAPTEX study. Some of the surface-level tracer was swept northeastward along the north shore of Lake Erie early on the evening of 18 September and then back southeastward across Lake Ontario during the night of September 18-19 as the cold front advanced across the lower Great Lakes. The front became the effective northern boundary of the surface tracer plume soon

after 0000 UTC, 19 September. More importantly, a nocturnal low-level jet ahead of the front was responsible for rapid advection of the upper part of the plume mass that had been mixed aloft by turbulence in the convective PBL over OH on the previous afternoon. Observed surface concentrations early on 19 September over northern NY and New England were primarily the result of shear-induced turbulence that mixed portions of the elevated jet-level plume down to the surface, especially over the higher elevations of the Adirondack, Green and White Mts. Newer, more advanced turbulence schemes such as the TKE-predicting scheme used here can be crucial in such cases because they are better able to simulate shear-induced turbulence than many older parameterizations available 15 years ago. The leading part of the plume was lifted over a warm front moving through New England at this time (although the exact position of the front during the night was indistinct). By 1200 UTC, 19 September, only the rear portion of the elevated plume remained over the CAPTEX monitoring network. Thus, at first glance the observed and modeled surface concentrations late in the episode did not appear consistent with the large mass of tracer that had been released from Dayton, OH. However, the more comprehensive modeling approach used in this study revealed important aspects of the inter-regional transport in 3-D than would otherwise have been apparent.

The study has resulted in a number of important specific conclusions about the use of mesoscale meteorological models for inter-regional transport problems:

- (8) The original model configuration in Exp. 1A that reflected modeling capabilities of the late 1980s (70-km horizontal resolution, 15 layers, older sub-grid physics, and no FDDA) was shown to produce very important errors in the simulated meteorology for the 18-19 September 1983 case. These errors included much

slower-than-observed frontal speeds and a weakened representation of the nocturnal low-level jet over the lower Great Lakes. The resultant surface tracer concentrations produced by the SCIPUFF dispersion model using the MM5 solutions for Exp. 1A were consistently too large, averaging 2.65 times the observed concentrations.

- (9) In Exp. 2A, simply improving the horizontal and vertical resolution of the mesoscale model to 12 km (about a factor of six) and 32 layers (more than a factor of 2) led to some improvements in the MM5 performance. Notably, phase speed errors of fronts noted in Exp. 1A were reduced. But overall, improvements in the mesoscale meteorology and dispersion calculations were fairly modest in this complex case. Over-predictions of the surface tracer concentrations were reduced, but on average they remained about 2.18 times the observed maximums. It is clear from this test that higher grid resolutions alone are not likely to be very effective for producing meteorological data sets with the accuracy needed for air-quality applications involving inter-regional transport.
- (10) The addition of more advanced physical parameterizations for boundary-layer turbulence, resolved-scale moist microphysics and sub-grid convection, coupled with finer 12-km grid resolution (Exp. 2B) produced much greater reductions of errors in MM5 and SCIPUFF than merely using fine grid resolution alone (Exp. 2A). Surface tracer concentrations and distributions became much like those observed.
- (11) Use of FDDA (surface and upper-air analysis nudging), along with 12-km resolution and improved physics in Exps. 2C and 2D produced the overall best

performance of all experiments. Frontal and low-level jet characteristics were represented fairly well and simulated tracer concentrations were in reasonable agreement with observations. Maximum surface concentrations in Exp. 2D averaged 0.93 times the observed maximums (7% bias), while the normalized mean absolute error of the model's maximums was only 0.31. This result, as well as other aspects of the meteorological and dispersion evaluations, showed that modeling capabilities for inter-regional transport indeed have improved substantially due to the combined effects of the three types of upgrades introduced into mesoscale models over the past 10-15 years.

- (12) Further reduction of the horizontal grid size in Exp. 3A to 4 km actually had a detrimental effect on meteorological and plume dispersion solutions in the case of 18-19 September 1983. The primary cause of poor mesoscale model performance was traced to the explicit representation of extensive convection accompanying a cold front advancing across the lower Great Lakes and into New England. Since no convective parameterization was used at this grid size, the convective updrafts were forced onto coarser-than-normal scales so that rainfall became too intense. This led cold downdrafts to be too vigorous also, causing widespread disruption of the low-level winds and spurious advection of the simulated tracer. Much more of the tracer was carried aloft by the vertical winds in Exp. 3A than in other experiments, so that the surface tracer concentrations in SCIPUFF became much too small (averaging only 36% of the observed maximum concentrations).
- (13) The results of Exp. 3A (4-km horizontal mesh) demonstrate that use of very fine grid resolution in mesoscale models sometimes can be counter-productive. This

result should not be interpreted to mean that 4-km grids are unsuitable for air-quality studies in general. However, model applications on grid of 4 km or less cannot be assumed automatically to be superior in all situations, especially if widespread deep convection is possible. Use of such fine resolutions may be more practical for predominantly dry cases. It is recommended that, when producing meteorological model solutions on a nested very fine grid, a comparison should be made between statistics calculated for the fine grid and similar statistics for its parent intermediate grid (say, ~12-km mesh size). This comparison should be made on a case-by-case basis before using model-generated meteorological fields in air-quality models.

- (14) Future research is recommended to broaden the applicability of very fine scale models (grids of 4 km or less) for cases in which widespread convection is possible. Improvements are necessary in the representation of boundary layer turbulence at fine scales so that spurious low-level convective instability does not develop so easily, causing excessive thunderstorm development by the explicit moist physics. It is also likely that the entrainment and detrainment of explicitly represented convection needs to be investigated to prevent updrafts and downdrafts from being over-accelerated. Furthermore, it actually may be less problematic to use even finer grids on the order of 1 km in cases having moist convection, since the updrafts and downdrafts would be better represented at approximately the correct scales. However, further experimentation is required before this option can be considered reliable for use in air-quality studies.

## REFERENCES

- Anthes, R.A., 1977: A cumulus parameterization scheme utilizing a one-dimensional cloud model. *Mon. Wea. Rev.*, **105**, 270-286.
- Arakawa, A., and V.R. Lamb, 1977: Computational design of the basic dynamical process of the UCLA general circulation model. *Methods in Comp. Physics*, **17**, 173-265.
- Benjamin, S.G. and N.L. Seaman, 1985: A Simple Scheme for Objective Analysis in Curved Flow. *Mon. Wea. Rev.*, **113**, 1184-1198.
- Blackadar, A.L., 1957: Boundary layer wind maxima and their significance for the growth of nocturnal inversions. *Bull. Amer. Meteor. Soc.*, **38**, 283-290.
- Bornstein, R.D., N.L. Seaman, D. Boucouvala, J. Wilkinson, A. Yadav, D.R. Stauffer, G.K. Hunter, and D. Miller, 2001: Development and Evaluation of the Mesoscale Meteorological Model MM5 for Air-Quality Applications in Southern California and the San Joaquin Valley. Final Report to CA Air Resources Board, CARB Contract No. 97-310, 78 pp.
- Chock, D.P. and Y.-H. Kuo, 1990: Comparison of wind-field models using the CAPTEX data. *J. Appl. Meteor.*, **29**, 76-91.
- Deng, A, N.L. Seaman and J.S. Kain, 2002a: A shallow-convection parameterization for mesoscale models Part I: Sub-model description and preliminary applications. Accepted for publication in *J. Atmos. Sci.*, **59**, 39 pp.
- Deng, A, N.L. Seaman and J.S. Kain, 2002b: A shallow-convection parameterization for mesoscale models Part II: Verification and sensitivity studies. Accepted for publication in *J. Atmos. Sci.*, **59**, 36 pp.
- Dudhia, J., 1989: Numerical study of convection observed during the Winter Monsoon Experiment using a mesoscale two-dimensional model. *J. Atmos. Sci.*, **46**, 3077-3107.
- Dudhia, J., 1993: A nonhydrostatic version of the Penn State-NCAR mesoscale model: Validation tests and simulation of an Atlantic cyclone and cold front. *Mon. Wea. Rev.*, **121**, 1493-1513.
- Fritsch, J.M., and C.F. Chappell, 1980: Numerical prediction of convectively driven mesoscale pressure systems. Part I: convective parameterization. *J. Atmos. Sci.*, **37**, 1722-1733.
- Gayno, G.A., N.L. Seaman, A.M. Lario, and D.R. Stauffer, 1994: Forecasting visibility using a 1.5-order closure boundary layer scheme in a 12-km non-hydrostatic model. 10<sup>th</sup> AMS Conf. on Num. Wea. Pred., Portland, OR, 18-22 July, 18-20.

- Grell, G.A., J. Dudhia, and D.R. Stauffer, 1994: A description of the fifth generation Penn State/NCAR mesoscale model (MM5). NCAR Tech. Note NCAR/TN-398+STR, 138 pp. [Available from NCAR Information Support Services, P.O. Box 3000, Boulder, CO 80397]
- Haagenson, P.L., Y.-W. Kuo, M. Skumanich and N.L. Seaman, 1987: Tracer verification of trajectory models. *J. Climate Appl. Meteor.*, **26**, 410-426.
- Haagenson, P.L., K. Gao and Y.-H. Kuo, 1990: Evaluation of meteorological analyses, simulations, and long-range transport calculations using ANATEX surface tracer data. *J. Appl. Meteor.*, **29**, 1268-1283.
- Hogrefe, C., S.T. Rao, P. Kasibhatla, G. Kallos, C.J. Tremback, W. Hao, D. Olerud, A. Xiu, J. McHenry and K. Alapaty, 2001a: Evaluating the performance of regional-scale photochemical modeling systems: Part I - Meteorological predictions. Accepted for *Atmos. Environ.*, **35**, 30 pp.
- Hogrefe, C., S.T. Rao, P. Kasibhatla, W. Hao, G. Sistla, R. Mathur and J. McHenry, 2001b: Evaluating the performance of regional-scale photochemical modeling systems: Part II - Ozone predictions. Accepted for *Atmos. Environ.*, **35**, 28 pp.
- Kain, J.S. and J.M. Fritsch, 1990: A one-dimensional entraining/detraining plume model and its application in convective parameterization. *J. Atmos. Sci.*, **47**, 2784-2802.
- Kao, C.-Y. and T. Yamada, 1988: Use of the CAPTEX data for evaluations of a long-range transport numerical model with a four-dimensional data assimilation technique. *Mon. Wea. Rev.*, **116**, 293-306.
- Kuo, H.-L., 1965: On formation and intensification of tropical cyclones through latent heat release by cumulus convection. *J. Atmos. Sci.*, **22**, 40-63.
- Kuo, H.-L., 1974: Further studies of the parameterization of the influence of cumulus convection on large-scale flow. *J. Atmos. Sci.*, **31**, 1232-1240.
- Lewellen, W.S. and R.I. Sykes (1986): Analysis of concentration fluctuations from lidar observations of atmospheric plumes. *J. Clim. & Appl. Met.*, **25**, 1145-1154.
- Lyons, W.A., C.J. Tremback, and R.A. Pielke, 1995: Applications of the Regional Atmospheric Modeling System (RAMS) to provide input to photochemical grid models for the Lake Michigan Ozone Study (LMOS). *J. Appl. Meteor.*, **34**, 1762-1784.
- McNider, R.T., Norris, W.B., Song, A., Mueller, S.F., and Bornstein, R., 1998: The role of convergence zones in producing extreme concentration events. Preprints. *10<sup>th</sup> AMS Conf. On the Applications of Air Pollution Meteor. with the A&WMA*. Phoenix, AZ, 11-16 January, 68-72.

- Michelson, S.A. and N.L. Seaman, 2000: Assimilation of NEXRAD-VAD Winds in Meteorological Simulations over the Northeast U.S. *J. Appl. Meteor.*, **39**, 367-383.
- Moeng, C.-H., and J.C. Wyngaard, 1989: Evaluation of turbulent transport and dissipation closures in second-order modeling. *J. Atmos. Sci.*, **46**, 2311-2330.
- Ray, S.D., T.S. Dye, P.T. Roberts, and D.L. Blumenthal, 1998: Analysis of nocturnal low-level jets in the northeastern United States during the summer of 1995. *10<sup>th</sup> AMS Conf. on the Applications of Air Poll. Meteor. with A&WMA*. 11-16 January, Phoenix, AZ, 177-181.
- Seaman, N.L., 2000: Meteorological Modeling for Air-Quality Assessments. *Atmos. Environ.*, **34**, 2231-2259.
- Seaman, N.L. and S.A. Michelson, 2000: Mesoscale Meteorological Structure of a High-Ozone Episode during the 1995 NARSTO-Northeast Study. *J. Appl. Meteor.*, **39**, 384-398.
- Seaman, N.L., D.R. Stauffer and A.M. Lario-Gibbs, 1995: A Multi-Scale Four-Dimensional Data Assimilation System Applied in the San Joaquin Valley During SARMAP: Part I: Modeling Design and Basic Performance Characteristics. *J. Appl. Meteor.*, **34**, 1739-1761.
- Shafran, P.C., N.L. Seaman and G.A. Gayno, 2000: Evaluation of Numerical Predictions of Boundary-Layer Structure during the Lake Michigan Ozone Study (LMOS). *J. Appl. Meteor.*, **39**, 412-426.
- Stauffer, D.R. and N.L. Seaman, 1990: Use of Four-Dimensional Data Assimilation in a Limited-Area Mesoscale Model. Part I: Experiments with Synoptic-Scale Data. *Mon. Wea. Rev.*, **118**, 1250-1277.
- Stauffer, D.R. and N.L. Seaman, 1994: On Multi-Scale Four-Dimensional Data Assimilation. *J. Appl. Meteor.*, **33**, 416-434.
- Stauffer, D.R. and N.L. Seaman, 1999: Intercomparison of turbulence parameterizations for simulating coastal-zone marine boundary layer structure. Preprints. *3<sup>rd</sup> AMS Conf. on Coastal Atmosphere and Ocean Predictions and Processes*. New Orleans, LA, 3-5 November, 7-12.
- Stauffer, D.R., R.C. Munoz, and N.L. Seaman, 1999: In-cloud turbulence and explicit microphysics in the MM5. *9<sup>th</sup> PSU/NCAR Mesoscale Model Users' Workshop*. Boulder, CO, 23-25 June, 177-180.
- Sykes, R.I., D.S. Henn, S.F. Parker and R.S. Gabruck, 1996: SCIPUFF- A generalized hazard dispersion model. *9<sup>th</sup> AMS Joint Conf. on Applications of Air Poll. Meteor. with A&WMA*, Atlanta, GA, 28 Jan - 2 Feb., 184-188.

- Sykes, R.I., W.S. Lewellen and S.F. Parker, 1984: A turbulent-transport model for concentration fluctuations and fluxes. *J. Fluid Mech.*, **139**, 193-218.
- Sykes, R.I., S.F. Parker, D.S. Henn, C.P. Cerasoli, and L.P. Santos, 1998: PC-SCIPUFF Version 1.2PD Technical Documentation. ARAP Report No. 718, Available for Titan Corp., Princeton, NJ, 170 pp.
- Wang, W. and N.L. Seaman, 1997: A Comparison Study of Convective Parameterization Schemes in a Mesoscale Model. *Mon. Wea. Rev.*, **125**, 252-278
- Warner, T.T., R.A. Petersen, and R.E. Treadon, 1997: A tutorial on lateral boundary conditions as a basic and potentially serious limitation on regional numerical weather prediction. *Bull. Amer. Meteor. Soc.*, **78**, 2599-2617.
- Weisman, L.M., J.B. Klemp, and W.C. Skamarock, 1997: The resolution dependence of explicitly-modeled convective systems. *Mon. Wea. Rev.* **125**, 527-548.
- Willmott, C.J., 1982: Some comments on the evaluation of model performance. *Bull. Amer. Meteor. Soc.*, **63**, 1309-1313.
- Willmott, C.J., S.G. Ackleson, R.E. Davis, J.J. Feddema, K.M. Klink, D.R. Legates, J. O'Donnell, and C.M. Rowe, 1985: Statistics for the evaluation and comparison of models. *J. of Geophys. Res.*, **90**, 8995-9005.
- Zhang, D.-L. and R.A. Anthes, 1982: A high resolution model of the planetary boundary layer: Sensitivity tests and comparisons with SESAME-79 data. *J. Appl. Meteor.*, **21**, 1594-1609.